UNIVERSITÀ DEGLI STUDI DI PADOVA

DIPARTIMENTO DI FISICA E ASTRONOMIA "GALILEO GALILEI"
Corso di Dottorato di Ricerca in Fisica
Ciclo XXXIII

APPLICATIONS OF CRYSTAL COLLIMATION TO THE CERN LARGE HADRON COLLIDER (LHC) AND ITS HIGH LUMINOSITY UPGRADE PROJECT (HL-LHC)

Coordinatore:
Ch.mo Prof. **Franco Simonetto**

Dottorando:
Marco D'Andrea
Matricola 1174616

Supervisore:
Ch.mo Prof. **Marco Zanetti**

Co-supervisori:
Dr. **Stefano Redaelli**
Dr. **Daniele Mirarchi**

A plan is only as good as those who see it through.

Abstract

Charged particles interacting with materials with a highly ordered structure can experience a variety of coherent processes, among which crystal channeling is of particular interest to applications to high-energy colliders. Bent crystals can be used to efficiently steer charged particles by trapping impacting particles in the potential well generated by adjacent crystalline planes. A crystal of a few millimeters can apply a deflection equivalent to the effect of a magnetic field of hundreds of Tesla, far beyond what can be achieved by state-of-the-art superconducting magnets. This impressive property stimulates accelerator physicists to make use of crystals for advanced beam manipulations.

A variety of possible applications were conceived in accelerators around the world in order to exploit the specific features of this process, including beam extraction, collimation and in-vacuum fixed target physics. Applications to beam collimation were the driving motivation for this effort at CERN in the last 15 years. The crystal collimation concept relies on bent crystals to deflect beam halo particles towards, in principle, a single absorber. Compared to the standard collimation system currently deployed at the Large Hadron Collider (LHC), this advanced technique promised to improve both the cleaning performance and the impedance of the machine. While the use with high-energy proton beams requires a dedicated absorber capable of withstanding the impact of the deflected particles, this system could potentially be deployed in operations with heavy-ion beams, where a standard secondary collimator is sufficient. Throughout Run 2, this concept has been extensively studied for the High-Luminosity upgrade of the machine (HL-LHC), which will increase the total energy stored by the circulating beams and pose serious challenges to the present collimation system.

Crystal channeling, however, can be applied to a variety of applications aside from beam collimation. In the context of Physics Beyond Colliders (PBC), the possibility to use the equivalent magnetic field experienced by channeled particles to measure the magnetic dipole moment of short-lived baryons has been first explored at the Fermi National Accelerator Laboratory (FNAL) in an extraction line of the Tevatron. The application of this complex setup at the LHC poses a number of challenges, but a feasible "double-crystal" layout has been conceived for the integration in the hierarchy of the LHC collimation system. Additionally, in 2018 bent crystals were deployed for the first time during a physics run with proton beams at the LHC, with the specific goal to minimize the observed background at the ALFA and TOTEM experiments. Other applications of bent crystals to particle accelerators at CERN include crystal-assisted slow-extraction schemes, explored at the Super Proton Synchrotron (SPS) and a two-crystal setup for the production of simultaneous particle beams at the NA48 experiment.

In this Ph.D. work, the main results gathered with the use of bent crystals at the high-energy frontier in the CERN accelerator complex are reported, with particular focus on crystal collimation tests carried out at the LHC in 2018 with Pb ion beams. These activities allowed to demonstrate the cleaning improvement provided by this collimation scheme, and were a key ingredient in the decision to include crystal collimation in the HL-LHC baseline for the run starting in 2022. The code development effort aimed at improving the available simulation tools for crystal collimation with proton beams is also described, using as case studies two important applications beyond ion beam collimation that were explored at CERN: the double-crystal setup at the SPS and the deployment of crystals for the reduction of background on forward physics detectors.

Contents

Chapter 1

Introduction

The Large Hadron Collider (LHC) [1] is the world's largest and highest-energy particle accelerator. Built by the European Organization for Nuclear Research (CERN) between 1998 and 2008, it is designed to accelerate and collide counter-rotating hadron beams at the unprecedented energy of 7 TeV. Since it was put into operation, the LHC has given a massive contribution to the research on fundamental topics of particle physics. The High-Luminosity upgrade project (HL-LHC) [2], officially approved by the CERN Council in 2016, will allow this machine to keep its place at the frontier of high-energy particle physics for the next two decades.

Superconducting magnets are placed along the 27-kilometer ring of the LHC in order to bend and focus the trajectory of the accelerated particles. In the present configuration, during proton operations each circulating beam is accelerated up to 6.5 TeV and routinely stores a total energy of more than 300 MJ, which, if not properly handled, has the potential to damage machine equipment or cause the magnets to lose their superconductive properties (an event called *quench*). Therefore, the machine is equipped with a sophisticated collimation system to dispose of unavoidable beam losses in a safe and controlled way [1,3]. After 10 years of activities, the LHC has surpassed by more than a factor 2 its design peak luminosity in its present configuration. The HL-LHC upgrade aims at achieving a baseline peak luminosity 5 times larger than the LHC design value. The goal of HL-LHC is to reach a total integrated luminosity of 3000 fb^{-1} in the 12 years of operations following the final installation. Such a massive upgrade calls for an improvement of the collimation system in order to withstand the new, extremely challenging operational conditions. Various innovative technologies have been explored to address these requirements.

Bent crystals have shown promising results for applications to beam collimation. Their ordered atomic structure allows, under certain conditions, to trap impinging particles inside the potential well generated by adjacent crystalline planes. Particles experiencing this process, called *crystal channeling*, are then forced to follow the curvature of the crystal. A crystal of 4 mm can deflect particles by 50 μrad at 7 TeV, an effect equivalent to that of a magnetic field of about 300 Tesla over the same length, far beyond what can be achieved by state-of-the-art superconducting magnets. This property has a large potential for different applications, from beam collimation [4] to halo extraction on targets, as envisaged by the Physics Beyond Colliders (PBC) study [5,6].

After careful design and preliminary studies carried out at the Super Proton Synchrotron (SPS), a prototype crystal collimation setup has been installed at the LHC between 2015 and 2017. Four bent crystals (one for each collimation plane of the two circulating beams) are used to deflect beam halo particles towards a single secondary collimator. Throughout the course of Run 2 (2015-2018), an extensive campaign of tests has been carried out in

order to assess the performance of this innovative system. In particular, this thesis reports the analysis of the experimental results gathered in 2018 with Pb ion beams, which were of crucial importance to determine the inclusion of crystal collimation in the baseline of the HL-LHC upgrade to improve collimation cleaning for heavy-ion beams.

Crystal channeling can be used for a variety of other applications to particle accelerators. In 2018, crystals were deployed for the first time in a dedicated physics run of the LHC, with the goal to reduce the background observed by the detectors of the ALFA and TOTEM experiments. Other proposed uses of bent crystals include the exploitation of the high equivalent magnetic field experienced by channeled particles to measure the magnetic dipole moment of short-lived baryons. The feasibility of such a setup in the LHC has been studied via proof-of-concept experiments carried out at the SPS, in a safer low-energy environment. Part of the work presented in this thesis involved active participation to these activities.

A complete analysis of the measurements requires careful benchmarking and comparison with predictions using simulation tools. A routine to reproduce the interaction of proton halo particles with crystals was developed based on SixTrack, a tracking code routinely used at CERN to simulate the dynamics of particles traveling through colliders and their interactions with the collimation system. Part of this thesis was dedicated to the migration of the crystal simulation routine to the most recent version of SixTrack, allowing to take advantage of the latest improvements of the code. The routine was also extensively used to study the various specific applications of bent crystals to proton beam manipulations mentioned above. A new model to treat the crystal miscut angle was implemented.

The theoretical framework required to understand the topics of this thesis and basic information on the layout of the LHC and its collimation system are given in the first chapters. In particular, **Chapter 2** recalls fundamental notions of accelerator physics and collimation theory, while **Chapter 3** describes in detail the interaction of charged particles with crystals and the scope for the applications treated in this thesis.

Chapter 4 presents a comprehensive overview of crystal collimation measurements at the LHC with proton beams, which allowed to characterize the crystal devices, address operational aspects in preparation for tests with ion beams, and study the performance of the system. These results also provided invaluable reference data for the development and benchmark of simulation tools.

Chapter 5 focuses on the results obtained in 2018 with Pb ion beams. The first demonstration of cleaning improvement for Pb ion beams is described, along with the very first crystal collimation tests performed with high-intensity ion beams. A possible operational configuration to be deployed during the first year of Run 3 is discussed, along with an outlook of further upgrades of the system.

Chapter 6 is dedicated to the work performed on the improvement of the crystal simulation routine and to its integration into the latest SixTrack release. An extensive benchmark campaign against the original version of the routine was carried out to verify that the physics results were maintained unaltered in the migration. The implementation of a new treatment of miscut angle effects is described in detail, together with some preliminary simulation results.

Chapter 7 focuses on other applications of bent crystals to particle accelerators. The simulation campaign that lead to the deployment of crystal collimation during the 2018 special physics run with proton beams at the LHC is reported, together with highlights from the experimental results. A double-crystal channeling layout explored at the SPS is described, along with the simulations that allowed to assess the achievable performance of this setup. Preliminary results of crystal channeling of higher order halos are also shown.

Finally, **Chapter 8** recalls the main outcomes of the work presented in this thesis, and gives a brief outlook of the next steps for studies involving bent crystals at CERN.

Chapter 2

Accelerator Physics and Collimation

In the past decades, circular colliders have been crucial to particle physics discoveries, allowing to explore known processes and observe new particles. This chapter introduces the fundamental concepts of particle accelerator physics which will be used throughout this thesis, with specific focus on circular colliders. A more comprehensive treatment can be found in [7–9].

2.1 Accelerator Physics

In first approximation, synchrotrons can be described as a composition of three types of elements:

- Dipole magnets, which are used to bend the trajectory of charged particles. The orbit defined by the dipoles is referred to as the *nominal orbit*.

- Quadrupole magnets, which counter the natural tendency of charged particles to diverge from the beam axis. Since each quadrupole focuses the beam in one plane but defocuses it in the orthogonal one, a sequence of orthogonal quadrupole fields is required, forming the so-called *FODO cell* [7, 10], the basic structure of a modern accelerator.

- Radiofrequency (RF) cavities, used to supply the energy lost by synchrotron radiation and also accelerate the particles. Ideal particles are perfectly synchronized with the cavities.

Although real colliders such as the LHC are not linear machines, this linear approximation [7] is commonly used for its simplicity and because it allows to deduce most of the functions that describe the motion of circulating particles. Higher order magnets, such as sextupoles, would be required for a more realistic model of the machine.
An *ideal particle* (or *synchronous particle*) steadily travels along the nominal orbit defined by the dipoles while also being synchronized with the accelerating radiofrequencies. In real conditions, however, beam particles always have a certain offset in terms of energy, momentum and phase-space coordinates with respect to the ideal particle. The resulting transverse amplitude is the composition of two contributions:

- A *betatronic* oscillation, caused by the focusing and defocusing effect of the quadrupole magnets.

- An *off-momentum* displacement, determined by the effect of the machine optics on a particle with a relative momentum offset with respect to the ideal one.
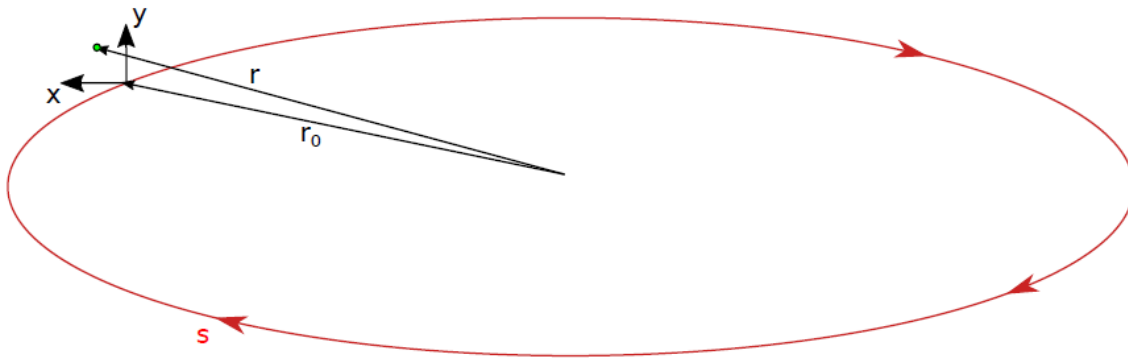
Figure 2.1: The Frenet-Serret reference system [11].

Particles with transverse amplitudes or energy deviations significantly larger than those of the ideal particle are referred to as *beam halo particles*.

2.1.1   Transverse Dynamics and Betatron Oscillations

The betatron motion is a consequence of the focusing magnets that keep the beam particles on the nominal trajectory, resulting in *betatron oscillations* on the transverse plane around the orbit of the ideal particle.

In order to derive the equation of motion for particles traveling in a circular collider, it is useful to define the *Frenet-Serret reference system*, shown in Fig. 2.1. The Lorentz force acting on the particles can be written as:

$$\frac{d\vec{p}}{dt} = q(\vec{E} + \vec{v} \times \vec{B}), \tag{2.1}$$

where $\vec{p}$, $\vec{v}$ and q are the particle momentum, velocity and electric charge respectively, while $\vec{E}$ and $\vec{B}$ are the electric and magnetic fields respectively. Assuming the transverse component of $\vec{E}$ to be negligible, eq. 2.1 can be rewritten in the Frenet-Serret reference system as:

$$\ddot{r} = \frac{q}{m}(\dot{r} \times \vec{B}). \tag{2.2}$$

For an ideal particle, this equation can be expanded and split in a system of equations of motion for the two transverse coordinates x and y:

$$x''(s) + \left(\frac{1}{R(s)^2} - k(s)\right)x(s) = 0, \tag{2.3}$$

$$y''(s) + k(s)y = 0, \tag{2.4}$$

where $\frac{1}{R(s)}$ and $k(s)$ are the energy invariant dipole and quadrupole strengths respectively. Eq. 2.3 and 2.4 can be recognized as Hill's equations, which describe a pseudo-harmonic oscillator. The general solution for $z \equiv (x, y)$ can be written as [12]:

$$z(s) = \sqrt{A\beta_z(s)}\sin\varphi_z(s). \tag{2.5}$$

$\beta_z(s)$ is the amplitude modulation coefficient, and the combination of eq. 2.5 with eq. 2.3 and 2.4 gives:
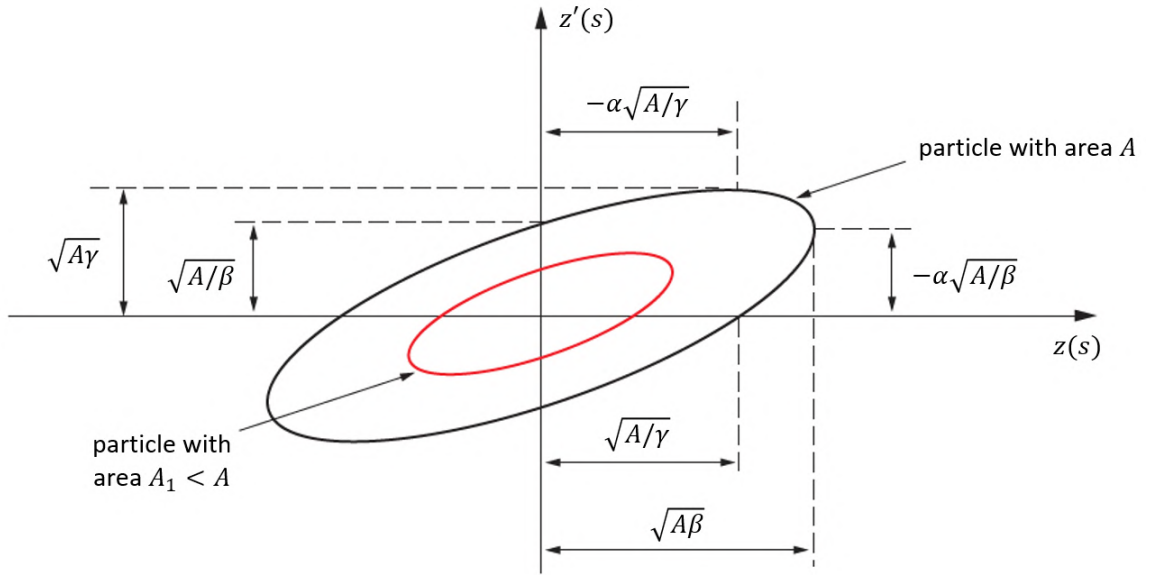
Figure 2.2: Phase-space ellipse that describes the particle motion at any machine location for given Twiss parameters.

$$\frac{\beta_z''(s)}{2} + K_z(s)\beta_z(s) - \frac{1}{\beta_z(s)}\left[1 + \frac{\beta_z'(s)^2}{4}\right] = 0, \tag{2.6}$$

with $K_x(s) = \left(\frac{1}{R(s)^2} - k(s)\right)$ and $K_y(s) = k(s)$. The betatron phase is also defined as:

$$\varphi_z(s) = \int_0^s \frac{ds'}{\beta_z(s')}. \tag{2.7}$$

Two additional quantities can be defined from $\beta(s)$:

$$\alpha_z(s) = -\frac{\beta_z'(s)}{2}, \tag{2.8}$$

$$\gamma_z(s) = \frac{1 + \alpha_z^2(s)}{\beta_z(s)}. \tag{2.9}$$

$\alpha_z(s)$, $\beta_z(s)$ and $\gamma_z(s)$ are the so-called *Twiss parameters* (or *Courant-Snyder parameters*), and are useful to describe the particle motion in phase-space at any machine point. In complete analogy with a harmonic oscillator, the particle trajectory in phase-space is represented by an ellipse like in Fig. 2.2, whose important points can be computed from the Twiss parameters. Additionally, the parameter A in eq. 2.5 can be recognized to be the area of the ellipse, which is defined as the *single particle emittance*:

$$\varepsilon_i = \gamma_z z^2 + 2\alpha_z z z' + \beta_z z'^2. \tag{2.10}$$

Under certain conditions, Liouville's theorem states that this quantity is a first integral of the particle motion for conservative systems. This is not the case for particle accelerators, in which various processes can lead to emittance growth [10, 13, 14], but this goes beyond the scope of this section.

The beam emittance ε is defined as the phase-space area that contains 95% of the beam particles. In the typical case of a Gaussian beam distribution in the transverse plane, the following quantities can be defined:

$$\sigma_z(s) = \sqrt{\varepsilon \beta_z(s)}, \tag{2.11}$$

$$\sigma_z'(s) = \sqrt{\varepsilon \gamma_z(s)}, \tag{2.12}$$

where $\sigma_z(s)$ and $\sigma_z'(s)$ are the betatronic r.m.s. size and divergence of the beam respectively. The emittance so far discussed depends on the beam momentum. Increasing the momentum of the beam reduces the emittance and hence the physical size of the beam, a process called *adiabatic damping*. For this reason, it is often more useful to define a *normalized beam emittance*:

$$\varepsilon_n = \beta \gamma \varepsilon, \tag{2.13}$$

where β and γ are the relativistic factors of the beam particles. This quantity can be used to define the normalized beam size $\tilde{\sigma}$ and normalized beam divergence $\tilde{\sigma}'$, in complete analogy to Eq. 2.11 and 2.12 respectively.

Finally, a fundamental parameter for beam stability is the *tune*, which is closely linked to betatron oscillations. It represents the number of oscillation periods in the phase-space in one revolution of the machine and it is defined as:

$$Q_z = \frac{1}{2\pi} \varphi(C) = \frac{1}{2\pi} \int_{s_0}^{s_0+C} \frac{ds}{\beta_z(s)}, \tag{2.14}$$

where C is the machine circumference. If this number was an integer or a rational number, it is easy to see that it could lead to beam instabilities. In complete analogy with a resonant oscillator, any imperfection in the magnetic lattice would be added up at each passage. For this reason, the tune should be as close as possible to an irrational number in order for the z-z' phase-space to be dense, i.e. for the particles to span the full range of possible phase-space coordinates in any passage through any location in the machine [10, 14]. This concept leads to multiturn processes that are very important for beam collimation.

Using the Twiss parameters, a matrix formalism to describe the motion of particles in a circular accelerator can be defined. The general trajectory solution given in eq. 2.5 can be rewritten as:

$$z(s) = a\sqrt{\beta_z(s)} \sin \varphi_z(s) + b\sqrt{\beta_z(s)} \cos \varphi_z(s). \tag{2.15}$$

Assuming knowledge of the coordinates (z, z') in a certain location s_1, it is possible to obtain a and b from eq. 2.15 and its derivative. Knowing these coefficients, it is then possible to evaluate the particle coordinates in any given location s_2, as:

$$\begin{pmatrix} z(s_2) \\ z'(s_2) \end{pmatrix} = M(s_1|s_2) \begin{pmatrix} z(s_1) \\ z'(s_1) \end{pmatrix}, \tag{2.16}$$

where M is the transport matrix from s_1 to s_2. Its elements can be written in terms of the Twiss parameters and phase advance φ_{21} between the two locations.:

$$M(s_1|s_2) = \begin{pmatrix} \sqrt{\frac{\beta_2}{\beta_1}}(\cos \varphi_{21} + \alpha_1 \sin \varphi_{21}) & \sqrt{\beta_2 \beta_1} \sin \varphi_{21} \\ -\frac{1+\alpha_1 \alpha_2}{\sqrt{\beta_2 \beta_1}} \sin \varphi_{21} + \frac{\alpha_1 - \alpha_2}{\sqrt{\beta_2 \beta_1}} \cos \varphi_{21} & \sqrt{\frac{\beta_1}{\beta_2}}(\cos \varphi_{21} - \alpha_2 \sin \varphi_{21}) \end{pmatrix}, \tag{2.17}$$

where the z subscript has been dropped from the optics functions for simplicity. This formalism is particularly useful when the full lattice optics (i.e. $\alpha(s)$, $\beta(s)$ and $\gamma(s)$) is known, as it allows evaluating the evolution of a given particle from one point to another in the machine.
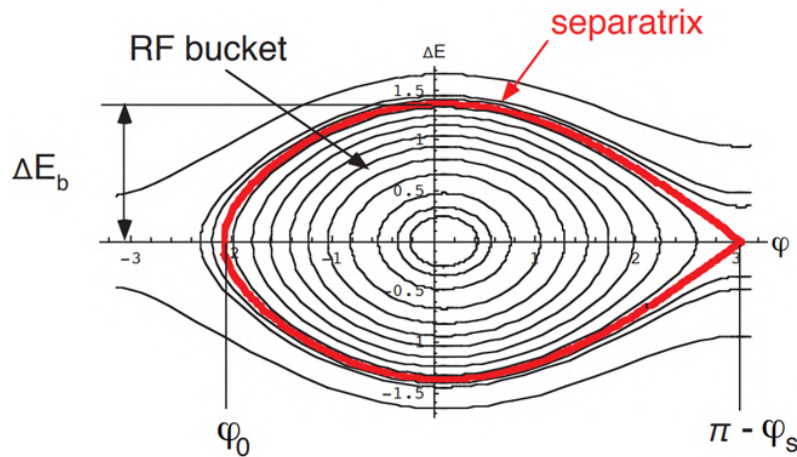
Figure 2.3: Longitudinal motion in ΔE-φ phase-space. The separatrix is shown in red [16].

2.1.2 Longitudinal Dynamics and Synchrotron Oscillations

The dynamics associated to the particle energy is a consequence of the presence of RF cavities, which accelerate the circulating particle and compensate for energy losses per single turn (e.g. synchrotron radiation) [15]. The voltage provided by an accelerating cavity can be expressed as:

$$V(t) = V_0 \sin(\varphi_s + \omega_{rf} t), \tag{2.18}$$

where φ_s is the *synchronous phase*. The frequency ω_{rf} is set up to be an integer multiple of the nominal revolution frequency ω_0:

$$\omega_{rf} = n_h \omega_0, \tag{2.19}$$

where n_h is the *harmonic number*. In this condition, a synchronous particle, which has the nominal energy and circulates on the nominal trajectory, always passes through the RF cavity with the synchronous phase φ_s and experiences the same energy gain:

$$\Delta E = q V_0 \sin \varphi_s, \tag{2.20}$$

where q is the particle electric charge. Particles with slightly higher or lower momentum, on the other hand, have a different phase advance and experience different RF kicks at each passage, resulting in *synchrotron oscillations* of the relative momentum offset $\delta = \frac{\Delta p}{p}$ around the synchronous particle. This effect is described by the following highly non-linear equation:

$$\ddot{\varphi} + \frac{\Omega_s^2}{\cos \varphi_s}(\sin \varphi - \sin \varphi_s) = 0, \tag{2.21}$$

where Ω_s is a constant, while φ and φ_s are the phase of the beam particle and of the synchronous particle respectively. The behaviour of the solutions to this equation can be observed in the ΔE-φ phase-space, as shown in Fig. 2.3, where a stable region usually referred to as *RF bucket* is clearly visible. Outside the limit of this region, called *separatrix*, particles lose energy at every passage through the RF and get lost.

Considering the effect of a dipole on a particle with momentum offset δ, eq. 2.3 is modified as:

$$z''(s) + \left[\frac{1}{R^2(s)} \frac{1-\delta}{1+\delta} - k(s) \frac{1}{1+\delta} \right] z(s) = \frac{1}{R(s)} \frac{\delta}{1+\delta}. \tag{2.22}$$

A possible solution for this equation can written in the form:

$$z(s) = z_\beta(s) + D(s)\delta, \tag{2.23}$$

where $z_\beta(s)$ is the general solution of Hill's equations as described in Sec. 2.1.1, while $D(s)\delta$ is the equilibrium path followed by a particle with momentum offset δ and no betatron oscillations (i.e. a special solution of the equation of motion with the added perturbation δ). The coefficient $D(s)$ is called *dispersion function*.

2.2   Collimation and Beam Cleaning

Each circulating beam of the LHC stores a total energy of hundreds of MJ. The unavoidable losses generated by such highly energetic beams need to be properly handled and safely disposed of, in order to avoid critical damage on sensitive components. For this reason, the role of the beam collimation system has progressively grown in importance in order to ensure the operational efficiency of the machine.
A collimation system typically fulfills several roles:

- **Cleaning of betatron and off-momentum beam halos**. This is especially challenging for superconductive machines, since losses need to be kept below certain limits in order to prevent a quench of the cold magnets. In particular, the typical quench limits of the LHC magnets are of a few tens of $\mathrm{mW/cm^3}$, to be compared to the design stored energy of 362 MJ [17] and the foreseen value of 700 MJ for the HL-LHC upgrade.

- **Passive machine protection**. Collimators are the closest devices to the beam and as such are the first line of defense against abnormal loss scenarios. Given the highly destructive power of hadron beams, this is one of the most crucial aspects of beam collimation [18, 19].

- **Cleaning of collision products**. Dedicated collimators intercept collision debris and scattered beam particles emerging from the collision points of high-luminosity experiments.

- **Optimization of the experiment background**. Collimators can provide beam tail scraping and local shielding at the detector locations to reduce spurious signal. Contrary to other accelerators, such as Tevatron or RHIC, this is not the main aim of the LHC collimation system. Nevertheless, a very special condition is explored in Chap. 7.

- **Concentration of radiation doses**. An essential design requirement for a collimation system is the capability to localize beam losses in controlled areas, in order to avoid having many activated areas along the machine and allow easier access for maintenance.

- **Local protection of equipment for improved lifetime against radiation effects**. Dedicated movable or fixed collimators provide local shielding to improve the lifetime of the equipment in the high-radiation enviroment foreseen during operations.

- **Beam halo scraping and halo diagnostics**. Collimators can be used to scan the beam distribution, for example to probe the population of beam tails [20, 21].

The relative importance of each task depends on the specific design requirements of the machine. In the case of the LHC, the most crucial aspect was halo cleaning, to protect the superconductive magnets. However, the presently deployed collimation system [3], while extremely complex and challenging to operate, is capable of fulfilling all roles previously listed.

2.2.1 Particle Interaction with Matter

When a beam particle interacts with the material of a collimator jaw, a wide series of events may take place. For LHC beams, the spectrum of phenomena extends from particle-nucleon interactions at hundreds of GeV in the center-of-mass reference system down to low-energy nuclear interactions in the meV energy range.

One of the main sources of energy loss of a massive charged particle (such as a proton or an ion) traveling through matter is given by collisions with the atomic electrons of the medium. The mean energy loss per unit path length, called *stopping power*, is described by the Bethe-Bloch equation [22]:

$$-\left\langle \frac{dE}{dx} \right\rangle = Kz^2 \frac{Z}{A} \frac{1}{\beta^2} \left[\frac{1}{2} \ln \frac{2m_e c^2 \beta^2 \gamma^2 T_{max}}{I^2} - \beta^2 - \frac{\delta(\beta\gamma)}{2} \right], \qquad (2.24)$$

which depends on the properties of both the impacting particle (charge z, relativistic factors β and γ) and the material (atomic number Z, atomic mass A, mean ionization potential I). T_{max} is the maximum kinetic energy that can be transferred to a free electron in a single collision, and δ represents the effect of the polarization of the material, which becomes the dominating term for very high values of the momentum of the particle. Finally, K is a constant defined as:

$$K = 4\pi N_A r_e^2 m_e c^2, \qquad (2.25)$$

where N_A is Avogadro's number, r_e and m_e are the classical radius and mass of the electron and c is the speed of light.

On top of this, the impacting particle can experience multiple deflections due to Coulomb scattering onto atomic nuclei, as schematically shown in Fig. 2.4. The final angular distribution of the particles exiting the medium is described by the Molière theory of Multiple Coulomb Scattering (MCS) and it has a Gaussian core with larger tails due to single Rutherford scattering events at big deflection angles [23].

Nuclear scattering events produce the largest variations in energy and direction of the primary beam particle and can also lead to its absorption and to the generation of secondary particle showers. In the case of nuclear *elastic* scattering, the impacting particle survives the interaction with the material and emerges from the collimator with modified direction. Surviving particles continue their path along the machine following a different orbit and are eventually lost at a downstream location, determining the loss patter around the beam line. In the case nuclear *deep inelastic* scattering, on the other hand, the interacting particle is lost at the collimator and multiple new particles with lesser energy are produced. Each of these can then interact in the same way, in a sort of chain reaction. The end result is the production of a shower of secondary particles that propagates through the impacted area, inducing thermal loads, mechanical stresses and radioactivity.

A particular kind of inelastic nuclear interaction which is relevant for protons at LHC beam energies is *single diffractive scattering* (SD). In this process, the impacting proton
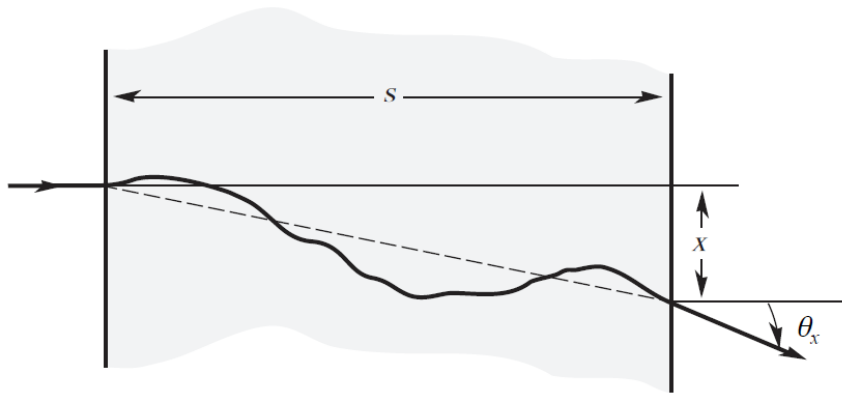
Figure 2.4: Example trajectory of a particle experiencing Multiple Coulomb Scattering while crossing a block of material. The particle exits from the block with a deflection angle θ_x [24].

undergoes an inelastic interaction with a nucleus. This event is characterized by a large value of momentum transfer. Both the target nucleus and the impacting proton can survive the interaction. In particular, the surviving proton can emerge from the collimator with a small change in direction, but much different energy. The proton is then possibly lost at the nearest dispersion peak due to its high momentum offset, making single diffractive processes particularly concerning for collimation purposes.

Fragmentation and *electromagnetic dissociation* events are, on the other hand, the main limitation for collimation of ion beams. As a result of the interaction with a collimator, the impacting ion "breaks" into a number of ions with smaller atomic and mass number. These products behave very differently than the primary beam because of their different q/m ratio (see Eq. 2.2) and many are quickly lost on the machine aperture.

2.2.2   Loss Modeling

The expected beam losses during the operation of a circular collider can be divided in two main categories [9]:

- *Continuous beam losses*, which include all the mechanisms that lead to emittance growth and to the population of the beam halo (intra-beam scattering, transverse resonances, collisions at IPs...). Typically they are multi-turn losses with constant rate over time.

- *Accidental beam losses*, which include single-turn losses generated when a fraction of the beam is sent on an abnormal orbit. These kind of losses have high destructive power and can be caused by a variety of reasons (errors during injection, asynchronous beam dumps, dynamic changes during transitions between different configurations of the machine, wrong operations...).

The cleaning performance of a collimation system is quantified by the *cleaning efficiency*, i.e. the fraction of particles lost from the beam that were actually caught by the system. A perfect beam collimation provides 100% cleaning. However, throughout this thesis the *local cleaning inefficiency* will be more commonly used instead. This quantity is a function of the longitudinal coordinate s and is defined as:

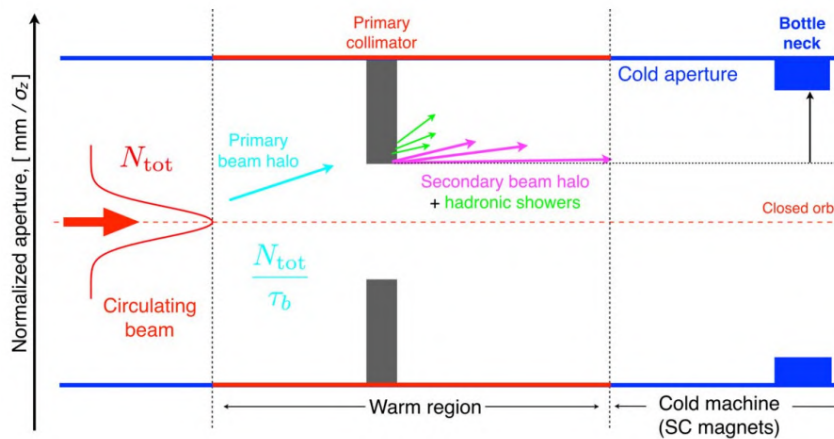$$\eta_c(s) = \frac{N(s \to s + \Delta s)}{N_{\text{abs}}} \frac{1}{\Delta s},$$

(2.26)

Figure 2.5: Schematic representation of a single-stage collimation system [9].

where $N(s \to s + \Delta s)$ is the number of particles lost over the distance Δs, and N_{abs} the total number of particles absorbed by the collimation system.

Continuous beam losses lead to a decrease of the beam intensity, which can be described by an exponential decay:

$$I(t) = I_0 e^{-\frac{t}{\tau_b}}, \tag{2.27}$$

where I_0 is the initial intensity of the beam and the time constant τ_b defines the *beam lifetime*. This quantity is actually a function of time and changes throughout the operational cycle. A conservative value of minimum lifetime must be assumed in order to ensure the required cleaning in any machine conditions (for example, $\tau_{min} = 0.2$ h for the LHC [25]). Knowing the quench limit of the superconducting magnets, R_q, and the cleaning inefficiency at the limiting location, the maximum circulating intensity for which safe operations are assured can be calculated as [3]:

$$I_{max} \leq \frac{R_q \tau_{min}}{\eta_c}. \tag{2.28}$$

Eq. 2.28 can also be reversed in order to set the maximum acceptable local cleaning ineffi- ciency knowing the maximum intensity needed to achieve the required performance of the accelerator, a condition that should drive the design of the collimation system.

2.2.3   Multistage Collimation Systems

A collimator is essentially composed of blocks of material, called *collimator jaws*, placed close to the circulating beam in order to intercept halo particles that stray far away from the beam core. In principle, a simple *single-stage collimation system* could be built by placing a single primary collimator per plane to intercept beam losses, preferably as far away as possible from superconducting magnet, as schematically depicted in Fig. 2.5. The amplitude of the collimator is usually expressed in terms of the betatronic beam size defined in Eq. 2.11:

$$n_\sigma = \frac{h}{\sigma_z}, \tag{2.29}$$

where h is the distance in mm between the collimator jaw and the circulating beam. Such a system would work if the collimator was a black absorber, capable of stopping all the halo
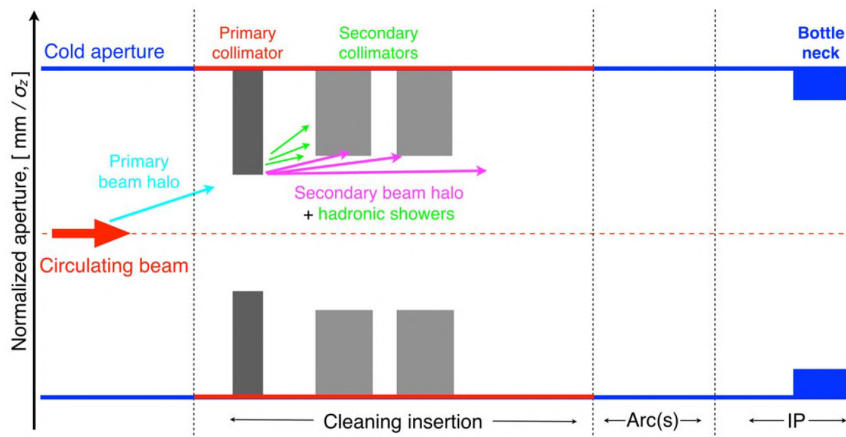
Figure 2.6: Schematic representation of a multistage collimation system obtained by adding a set of secondary collimators to the single-stage system shown in Fig. 2.5 [9].
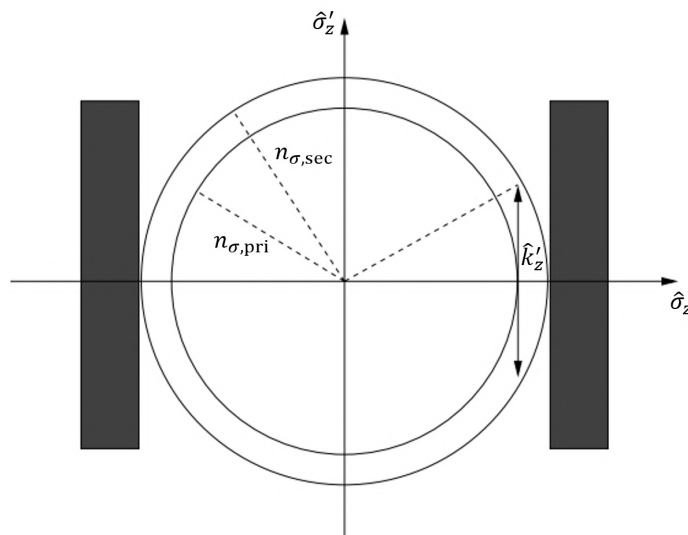
Figure 2.7: Normalized phase-space with circumferences corresponding to the primary ($n_{\sigma,\mathrm{pri}}$) and secondary ($n_{\sigma,\mathrm{sec}}$) collimators. The normalized kick $\hat{k}'_z$ required for halo particles to reach the secondary after hitting the primary is given by Eq. 2.30 [9].

particles that hit its surface. However, the expected impact parameter (i.e. the distance between the impact point and the edge of the collimator facing the beam) is between a few tens of nm and a few μm [26, 27]. At this scale, halo particles do not interact with the full length of the collimator because of jaw flatness and surface roughness errors, and are outscattered at larger amplitudes and modified energies before being absorbed. These particles populate the so-called *secondary beam halo* and risk getting lost in the machine before interacting again with the collimator in subsequent turns. Additionally, the interaction of beam halo particles with the primary collimator produces hadronic showers whose products can reach the cold magnets downstream of the cleaning insertion. It is clear that a single-stage collimation system is not adequate for high-energy superconducting accelerators.

Additional collimators downstream of the primaries can be used to catch the secondary halo particles, building a *multistage collimation system* like the one schematically shown in Fig. 2.6. The aperture of the secondary collimators needs to be larger than that of the primary, to avoid the risk of hierarchy breaking, while at the same time be small enough

to maximize the efficiency in catching the secondary halo. The angular kick necessary for a particle impinging on the primary collimator to reach the secondary can be calculated as:

$$\hat{k}'_z = \frac{k'_z}{\sigma'_z} = \sqrt{n^2_{\sigma,\text{pri}} - n^2_{\sigma,\text{sec}}}, \tag{2.30}$$

and is typically accumulated over the course of multiple passages through the primary stage of collimation. The process is schematically shown in Fig. 2.7. The longitudinal position of the secondary also needs to be adjusted in order to have the proper phase advance to intercept secondary halo particles. It is important to note that particles hitting the primary collimator on a specific plane are actually scattered in all directions. It can be demonstrated that an arrangement of primary and secondary collimators in three planes (horizontal, vertical and skew) can provide satisfactory coverage and multiturn cleaning [28]. Collimators are among the main sources of machine impedance, since they are usually the closest devices to the beam and the resistive wall impedance scales as g^{-3} (where g is the gap between the two jaws) [29]. A collimation system composed of a large number of stages will allow to spread beam loads over a large area, reducing their impact, but will also contribute significantly to the total impedance of the machine, which may lead to beam instabilities. It is important to find the right compromise between these two opposite needs.

In Sec. 2.1, the description of betatron and off-momentum dynamics was separated, neglecting the coupling between the two contributions. This allows to split the collimation system in two sections, dedicated to the cleaning of particles with high betatron amplitude and high momentum offset respectively. This is particularly convenient because of the conflicting requirements of these two tasks:

- Betatron cleaning requires regions with low dispersion, so that high transverse displacement corresponds to high betatron displacement.

- Momentum cleaning requires regions with high dispersion, so that high transverse displacement is mainly caused by high momentum offset.

This is the reason why, for example, the collimation system of the LHC includes two separate cleaning insertions with different features to accomplish both tasks. It is important to remember, however, that the two systems are not completely decoupled, in particular with the tight collimator settings required during operations at the LHC and the non-zero dispersion in the dispersion suppressor region downstream of the betatron insertion.

2.2.4   The LHC Layout and Collimation System

The LHC layout and the positions of the collimators around the ring are schematically shown in Fig. 2.8. The accelerator is composed of eight arcs, which house the equipment required to bend the trajectory of the beams, and eight *Long Straight Sections* (LSSs), also called *Insertion Regions* (IRs), where devices with dedicated tasks are installed. Each of them is dedicated to a specific function:

- IR2 and IR8 are the injection locations for Beam 1 and Beam 2 respectively.

- IR3 and IR7 are dedicated to beam collimation, with specific focus on off-momentum and betatron cleaning respectively.

- IR4 houses the accelerating RF cavities.

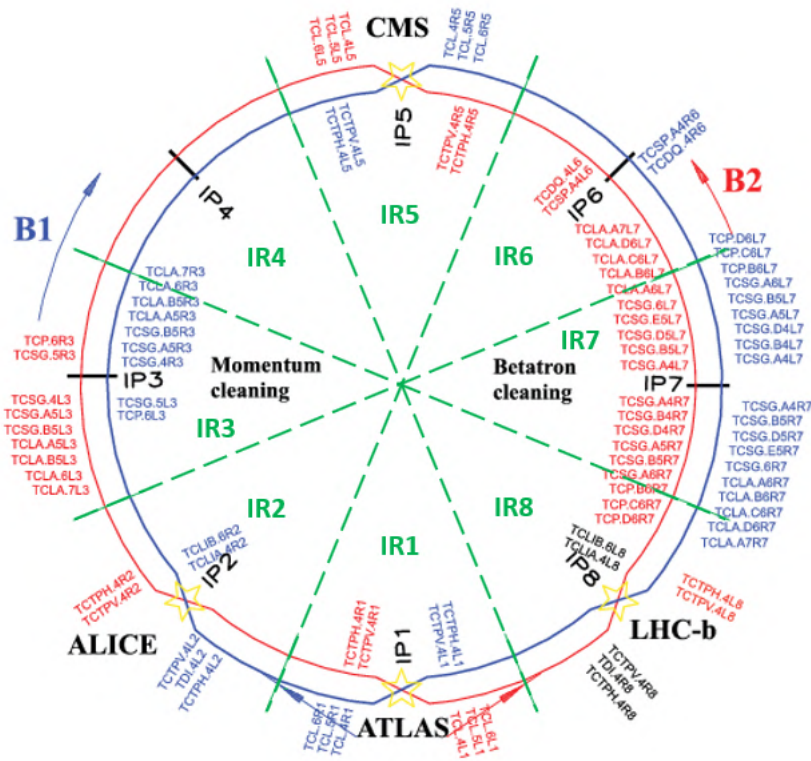- IR6 is where the beam extraction and dump system is located.

Figure 2.8: Schematic representation of the LHC layout, showing the IRs and the collimator locations around the ring [9].

The beams are brought into collisions at the four *Interaction Points* (IPs), located in IR1, IR2, IR5 and IR8. This is where the four major high-energy physics detectors (ATLAS, ALICE, CMS and LHCb) are housed.

Including the dump protection devices (e.g. TCDQs, Target Collimators Dump Quadrupole) and the injection protection devices (e.g. TDI, Beam Absorber for Injection), the LHC collimation system includes 110 [9] movable collimators installed around the ring and in its transfer lines. Additionally, 10 fixed-aperture absorbers are installed in front of the most exposed warm magnets of each collimation insert, in order to reduce the radiation doses to magnet coils and increase their lifetime. Such a complex collimation system is very versatile and allows to fulfill a variety of tasks, but is also among the largest impedance contributors of the machine [30].

Collimators are organized in families based on their functional positions and settings, and together they provide multiple cleaning steps in order to ensure high efficiency of halo particle disposal. The settings used during LHC operations with protons at injection (450 GeV) and flat top (6.5 TeV) are reported in Tab. 2.1. It is important to note that even though the normalized beam emittance is not actually constant in a real accelerator, the collimator settings are usually given assuming its nominal value (which corresponds to 3.5 μm for the LHC). The same convention will be used throughout this thesis.

This thesis will mainly focus on the IR7 betatron cleaning insertion, which houses a three-stage collimation system schematically depicted in Fig. 2.9. The primary collimators (TCPs, Target Collimators Primary) are the closest to the beam and they represent the aperture bottleneck during regular operations. Beam tail particles interact with these collimators when they first enter the collimation system. The secondary collimators (TCSGs, Target
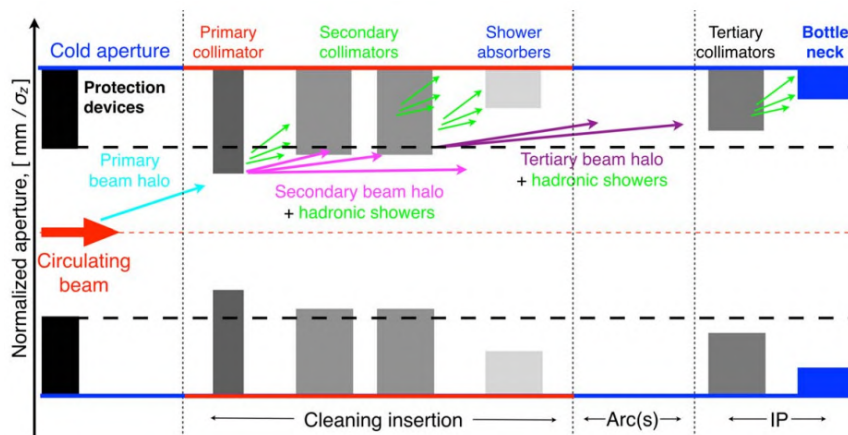
Figure 2.9: Schematic representation of the LHC multistage collimation system [9].

Collimators Secondary Graphite) collect what leaks from the primaries. Being the closest to the beam, primary and secondary collimators are made of a robust carbon fiber composite (CFC), in order to withstand large beam losses. Active absorbers (TCLAs, Target Collimator Long Absorbers) are installed towards the end of the insertion, to catch secondary showers before entering the arcs. These collimators are made of a tungsten alloy in order to maximize the energy absorption, while sacrificing their robustness. For this reason they should never intercept primary beam losses, a condition which is ensured by the setting hierarchy.

Two tertiary collimators (TCTPs, Target Collimators Tertiary with Pick-up) made of a tungsten alloy are installed upstream of the collision points for all experimental IRs, in order to provide background control for the experiments and local protection of the quadrupole triplets in the final focusing system. Downstream of the high-luminosity experiments (ATLAS and CMS) there are three more collimators (TCLs, Target Collimators Long) to intercept the collision debris and minimize the leakage of collision debris to the downstream arc. Additional collimators are installed in the injection and extraction regions in order to provide protection against failures (such as miskicked beams).

The LHC collimators (with the exception of the TCDQs) are composed of two movable jaws that are kept centered with respect to the center of the beam envelope, such that a symmetric cut of the beam is achieved. The aperture of the jaws is adjusted according to the beam energy, machine optics and operational mode.

Table 2.1: 2018 operational LHC collimator settings for proton beams. The values are expressed in units of the betatronic beam size σ, assuming the nominal normalized beam emittance of 3.5 μm. H, V and S stand for horizontal, vertical and skew respectively.

Device name	IR	Plane	450 GeV Settings [σ]	6.5 TeV Settings [σ]
TCL.4[R/L]1.B[1/2]	1	H	OUT	OUT
TCL.5[R/L]1.B[1/2]	1	H	OUT	OUT
TCL.6[R/L]1.B[1/2]	1	H	OUT	OUT
TCTPH.4[L/R]2.B[1/2]	2	H	13.0	37.0
TCTPV.4[L/R]2.B[1/2]	2	V	13.0	37.0
TDI.4[L/R][2/8].B[1/2]	2/8	V	6.8	OUT
TCLIA.4[L/R][2/8].B[1/2]	2/8	V	6.8	OUT
TCLIB.6[L/R][2/8].B[1/2]	2/8	V	6.8	OUT
TCP.6[L/R]3.B[1/2]	3	H	8.0	15.0
TCSG.5[L/R]3.B[1/2]	3	H	9.3	18.0
TCSG.4[R/L]3.B[1/2]	3	H	9.3	18.0
TCSG.A5[R/L]3.B[1/2]	3	S	9.3	18.0
TCSG.B5[R/L]3.B[1/2]	3	S	9.3	18.0
TCLA.A5[R/L]3.B[1/2]	3	V	12.0	20.0
TCLA.B5[R/L]3.B[1/2]	3	H	12.0	20.0
TCLA.6[R/L]3.B[1/2]	3	H	12.0	20.0
TCLA.7[R/L]3.B[1/2]	3	H	12.0	20.0
TCTPH.4[L/R]5.B[1/2]	5	H	13.0	8.5
TCTPV.4[L/R]5.B[1/2]	5	V	13.0	8.5
TCL.4[R/L]5.B[1/2]	5	H	OUT	OUT
TCL.5[R/L]5.B[1/2]	5	H	OUT	OUT
TCL.6[R/L]5.B[1/2]	5	H	OUT	OUT
TCDQ.4[R/L]6.B[1/2]	6	H	8.0	7.4
TCSP.A4[R/L]6.B[1/2]	6	H	7.5	7.4
TCP.D6[L/R]7.B[1/2]	7	V	5.7	5.0
TCP.C6[L/R]7.B[1/2]	7	H	5.7	5.0
TCP.B6[L/R]7.B[1/2]	7	S	5.7	5.0
TCSG.A6[L/R]7.B[1/2]	7	S	6.7	6.5
TCSG.B5[L/R]7.B[1/2]	7	S	6.7	6.5
TCSG.A5[L/R]7.B[1/2]	7	S	6.7	6.5
TCSG.D4[L/R]7.B[1/2]	7	V	6.7	6.5
TCSG.B4[L/R]7.B[1/2]	7	H	6.7	6.5
TCSG.A4[L/R]7.B[1/2]	7	S	6.7	6.5
TCSG.A4[R/L]7.B[1/2]	7	S	6.7	6.5
TCSG.D5[R/L]7.B[1/2]	7	S	6.7	6.5
TCSG.E5[R/L]7.B[1/2]	7	S	6.7	6.5
TCSG.6[R/L]7.B[1/2]	7	H	6.7	6.5
TCLA.A6[R/L]7.B[1/2]	7	V	10.0	10.0
TCLA.B6[R/L]7.B[1/2]	7	H	10.0	10.0
TCLA.C6[R/L]7.B[1/2]	7	V	10.0	10.0
TCLA.D6[R/L]7.B[1/2]	7	H	10.0	10.0
TCLA.A7[R/L]7.B[1/2]	7	H	10.0	10.0
TCTPH.4[L/R]8.B[1/2]	8	H	13.0	15.0
TCTPV.4[L/R]8.B[1/2]	8	V	13.0	15.0
TCTPH.4[L/R]1.B[1/2]	1	H	13.0	8.5
TCTPV.4[L/R]1.B[1/2]	1	V	13.0	8.5

Chapter 3

Crystal Collimation at the LHC

In Chap. 2, the working principles of circular colliders were explained along with the importance of a collimation system to properly dispose of the energy losses caused by the circulating beams, which is especially true in the case of superconductive machines. In the past years, an advanced collimation technique that makes use of crystal collimators to steer beam halo particles with high efficiency has been extensively studied at the CERN accelerator complex.

This chapter describes coherent processes that particles can experience when interacting with bent crystals, focusing on planar channeling. The working principles of crystal-assisted collimation and its applications to the LHC are also introduced. A wider overview can be found in [31, 32].

3.1   Crystal Channeling and Coherent Phenomena

Charged particles can experience a wide variety of interactions when hitting a block of material, as described in Sec. 2.2.1. In the case of a crystal, however, specific interactions are suppressed or enhanced depending on the impact conditions, such as the relative orientation between the particle trajectory and the target.

A crystal is a solid material whose atoms are arranged in a highly ordered microscopic structure, called *crystalline lattice*. This peculiar property was hypothesized to be the explanation for the observations made in early 20th century of charged particle beams being able to emerge from crystal targets, rather than being absorbed as in any other amorphous material [33]. If the crystal is well oriented with respect to the trajectory of the impinging particle, the crystalline lattice is seen as ordered planes or rows of atoms. The particle can then get trapped inside the electrostatic potential generated by two adjacent planes (*planar channeling*) or by an axis (*axial channeling*), and be forced to travel in essentially empty space for the full length of the crystal [31, 32, 34, 35], as schematically depicted in Fig. 3.1.

Given the larger achievable deflection, planar channeling is the process that lends itself the most to beam collimation purposes. If a particle is channeled by a bent crystal, its trajectory will be forced to follow the curvature of the crystalline planes. A few millimeter long crystal can thus be used to efficiently steer beam halo particles by tens of μrad, an effect corresponding to an equivalent magnetic field of hundreds of Tesla over the same length. This offers two main benefits:

- The probability of inelastic interactions in a crystal collimator is much lower than in a standard collimator, since channeled particles travel through the relatively empty space between planes. As a result, losses caused by single diffractive events in the case
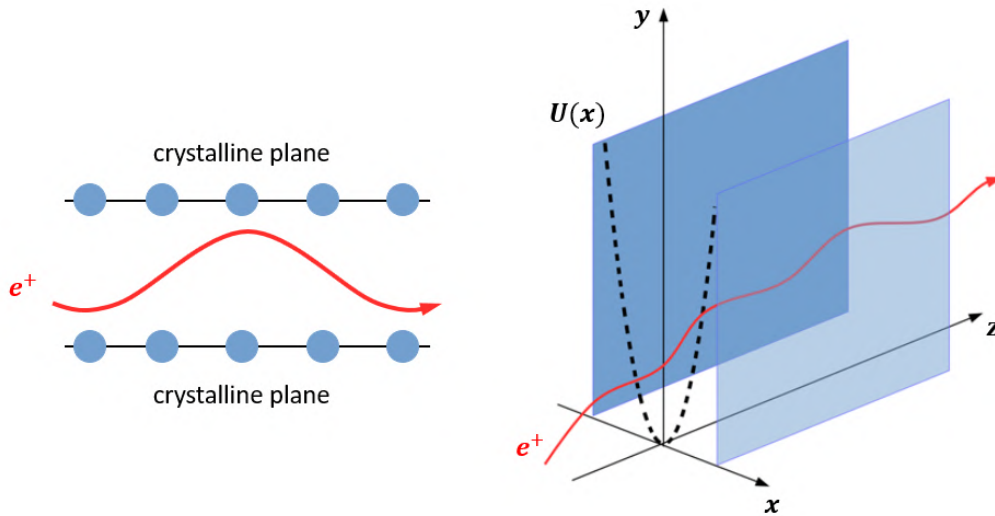
Figure 3.1: Illustration of the planar channeling concept. The trajectory of a positively charged particle (solid red) within the potential well generated by two adjacent crystalline planes is shown from the top (left frame) and from the side (right frame).

of protons and by fragmentation or dissociation in the case of ions, which constitute the main limitations of the present collimation system, can be significantly mitigated.

- The channeled beam can in principle be directed towards a single absorber, allowing to reduce the number of stages of the collimation system and concentrate losses in a smaller area. Futhermore, a more compact system would reduce contribution to the impedance budget of the machine.

In the following sections, the mathematical description of planar channeling will be presented. The treatment will focus on Si crystals, which are presently the most suitable candidates to be used for particle deflectors, given their well developed manufacturing process that allows to produce highly pure crystalline structures.

3.1.1   Potential Generated by Crystalline Planes

The description of planar channeling starts with the potential field that describes the interaction between a charged particle and an atom. This is in general a very challenging problem to solve, as it involves many different parameters. A good approximation is however given by the *Thomas-Fermi model* [36, 37]:

$$V(r) = \frac{Z_i Z e^2}{r} \phi\left(\frac{r}{a_{TF}}\right), \tag{3.1}$$

where $Z_i e$ is the charge of the impinging particle, Z is the atomic number of the target atom and r is the relative distance between the two. The factor $\phi\left(\frac{r}{a_{TF}}\right)$ is the *Molière screening function*, a correction required by the Thomas-Fermi model to take into account the effect of the electronic cloud around the nucleus [38]. a_{TF} is the Thomas-Fermi screening length of the ion-atom interaction, calculated as [39]:

$$a_{TF} = 0.8853 \cdot a_0 Z^{-1/3}, \tag{3.2}$$

where $a_0 = 0.529$ Å is the Bohr radius. In particular, $a_{TF} = 0.194$ Å for Si atoms ($Z = 14$).
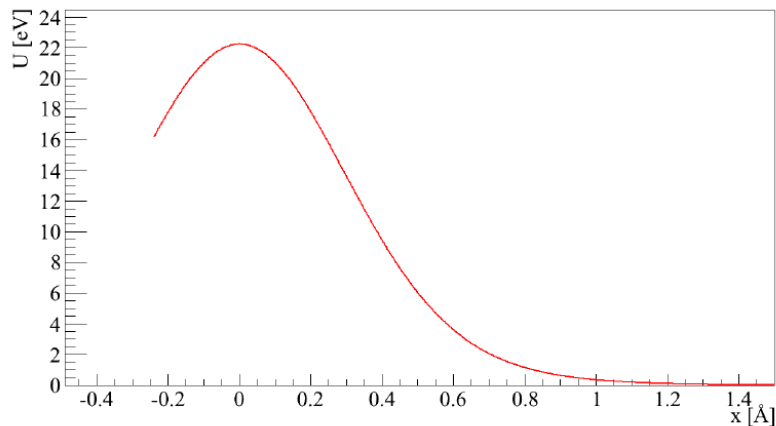
Figure 3.2: Potential generated by a single (110) silicon crystal plane in the Molière approximation at room temperature [16].

The average potential generated by the whole crystalline plane can be considered as a continuous potential in the hypothesis, proposed by Lindhard [34], of small impact angle between the impinging particle direction and the plane. The resulting function is:

$$U_p(x) = Nd \iint_{-\infty}^{+\infty} V(x,y,z) dy dz, \tag{3.3}$$

where d is the distance from the plane, N is the atomic density of the crystal, $V(x,y,z)$ is the potential in eq. 3.1. The reference system shown in Fig. 3.1 has been used, with z being the longitudinal direction and x being the direction perpendicular to the crystalline plane. Thermal agitation must also be taken into account and can be approximated with a spatial Gaussian distribution. The final potential is thus the average of eq. 3.3 over this distribution. An example is reported in Fig. 3.2.

Superimposing the potential generated by two adjacent planes, it is easy to see that the combined shape is a potential well. Assuming that particles are influenced only by the closest planes, the resulting potential can be approximated as:

$$U(x) \approx U_p\left(\frac{d_p}{2} - x\right) + U_p\left(\frac{d_p}{2} + x\right) \approx U_{max}\left(\frac{2x}{d_p}\right)^2, \tag{3.4}$$

where d_p is the distance between the two planes, i.e. the width of the channel.

3.1.2 Planar Channeling in Straight Crystals

In this section, a theoretical treatment of particle dynamics in channeling will be presented. A classical approach of the interactions between particles and crystals will be followed, rather than using quantum mechanics, for two main reasons:

- As described in Sec. 3.1.1, particles trapped in crystalline planes oscillate in a potential well that can be approximated with an harmonic potential. The transverse energy of the particles is therefore quantized and the number of energy levels in a channel is given by:

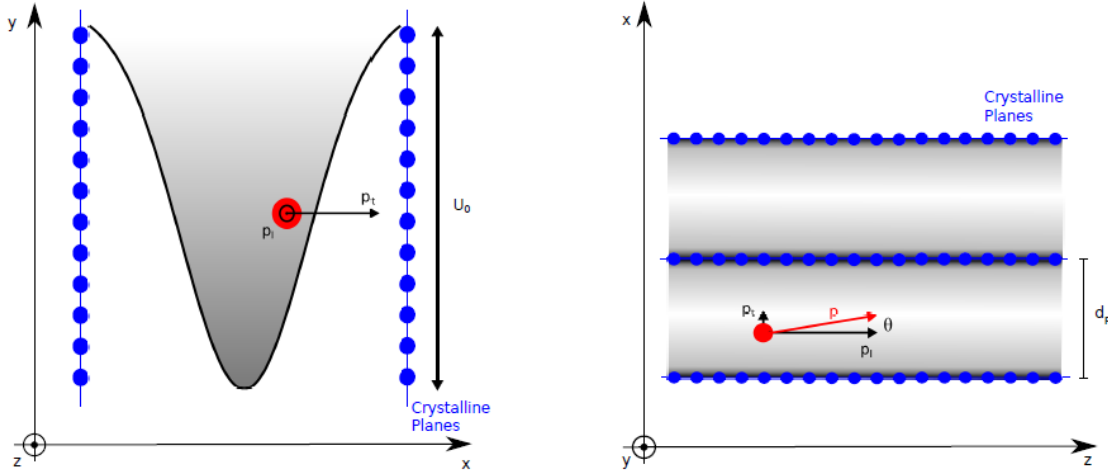$$n = \frac{d_p}{\hbar\sqrt{8}}\sqrt{U_{max}m\gamma}, \tag{3.5}$$

Figure 3.3: Reference frame for positively charged particles traveling through crystalline planes. The momentum p (red) and the momentum components p_t and p_l (black) are shown. On the left is the front face view, while on the right is the view from the top [11].

where U_{max} is the maximum of the potential well and $m\gamma$ is the relativistic mass of the particle. If $n \gg 1$ the spectrum can be considered continuous. This is always the case for applications to the LHC.

- If the transverse de Broglie wavelenght $\lambda_{dB} = \frac{h}{p}$ (where p is the particle momentum) is much smaller than the channel width, the tunneling effect can be neglected. This condition is also always fulfilled in applications to the LHC.

For a particle to get trapped between crystalline planes, its transverse momentum must be lower than the height of the potential well. This condition can be expressed as a function of the impact angle θ of the particle with respect to the crystalline plane. In the small angle approximation:

$$\theta = \tan \frac{p_t}{p_l} \simeq \frac{p_t}{p_l}, \tag{3.6}$$

where p_t and p_l are the transverse momentum and longitudinal momentum of the particle respectively, shown in Fig. 3.3. Since the potential only acts on the transverse direction, the total energy of the particle, which is conserved, can be rewritten in order to separate the longitudinal and transverse contribution:

$$E = \sqrt{p_t^2 + p_l^2 + m^2c^4} + U(x) \simeq \frac{p_t^2 c^2}{2E_l} + E_l + U(x), \tag{3.7}$$

where $E_l = \sqrt{p_l^2 c^2 + m^2 c^4}$ is the longitudinal energy, which is also conserved, since forces act only on the transverse direction. It follows that a conserved transverse energy can be defined as:

$$E_t = \frac{p_t^2 c^2}{2E_l} + U(x) \simeq \frac{p^2 c^2}{2E}\theta^2 + U(x) = \text{constant}, \tag{3.8}$$

using the approximations $\theta \simeq \frac{p_t}{p_l}$, $p \simeq p_l$ and $E \simeq E_l$, which follow from eq. 3.6. Thus, a particle can undergo planar channeling if the following condition is satisfied:

Table 3.1: Critical angle, oscillation wavelength and critical bending radius at different energies for positive charged particles traveling through silicon strip crystals (110 planes).

Energy [GeV]	θ_c [μrad]	λ [μm]	R_c [m]
120	18.3	33.0	0.3
180	18.0	40.5	0.4
270	12.2	49.6	0.6
400	10.0	60.3	1.0
450	9.4	64.0	1.1
6500	2.5	240.0	15.6
7000	2.4	250.0	16.8

$$\frac{p^2c^2}{2E}\theta^2 + U(x) \leq U_{max}. \tag{3.9}$$

Under the assumption that the particle enters in the center of the channeling, where $U(0) = 0$, and noting that $pc^2 = vE$, where v is the particle velocity ($v \sim c$ for LHC applications), the above equation can be rewritten as:

$$\frac{pv}{2}\theta^2 \leq U_{max}. \tag{3.10}$$

This relation allows to define a *critical channeling angle* θ_c as the maximum impact angle a particle can have in order to undergo planar channeling:

$$\theta_c = \sqrt{\frac{2U_{max}}{pv}}. \tag{3.11}$$

This quantity depends on the momentum of the particle and the height of the potential well, which is determined by the crystal material.
The equation of motion of a particle experiencing planar channeling can be obtained from the second derivative of eq. 3.8:

$$pv\frac{d^2x}{dz^2} + \frac{8U_{max}}{d_p^2}x = 0, \tag{3.12}$$

with $\theta = \frac{dx}{dz}$, with z being the longitudinal coordinate, and using the harmonic approximation in eq. 3.4. The solution to this equation is a sinusoid described by:

$$x(z) = \frac{d_p}{2}\sqrt{\frac{E_t}{u_{max}}}\sin\left(\frac{2\pi z}{\lambda} + \phi\right), \tag{3.13}$$

where ϕ is the oscillation phase determined by the initial conditions when the particle enters the crystal, while $\lambda = \sqrt{\frac{pv}{2U_{max}}}$ is the oscillation wavelength. Values of critical angle and oscillation wavelength at various energies for silicon crystals ($U_{max} \simeq 20$ eV) are listed in Tab. 3.1. As opposed to what happens in amorphous materials, particles experiencing planar channeling oscillate between crystalline planes in relatively empty space and in principle can travel through the entire crystal length without energy loss or any large-angle (or inelastic) scattering.
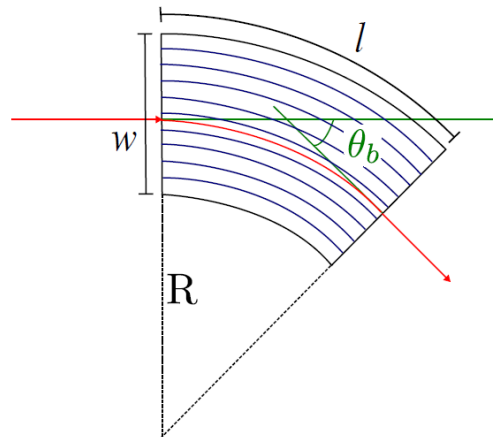
Figure 3.4: Schematic representation of channeling in a bent crystal. The bending angle θ_b is shown in green, while the trajectory of the channeled particle is shown in red [11].

3.1.3 Planar Channeling in Bent Crystals

A crystal can be bent along a specific direction by applying a mechanical stress. If the curvature radius R is much larger than the crystal thickness w, the internal structure of the crystal is not significantly modified and the charge distribution generated by the crystalline planes remains continuous. In this approximation, the interaction of particles with the crystal can be treated similarly to what was done in Sec. 3.1.2. The bending angle of the crystal is defined as:

$$\theta_b = \frac{l}{R}, \tag{3.14}$$

where l is the crystal length, as shown in Fig. 3.4. Particles channeled by such a crystal will be forced to follow the curvature of the crystalline planes and their direction will be steered by θ_b.

The effect of a bent crystal can thus be simulated by adding a centrifugal force to eq. 3.12, which is modified as follows:

$$pv\frac{d^2x}{dz^2} + U'(x) + \frac{pv}{R} = 0. \tag{3.15}$$

The centrifugal force affects the trajectory of the particle, which is still a sinusoid but it ranges around a new equilibrium point. An effective potential which depends on the particle energy and the crystal bending radius can then be defined:

$$U_{eff}(x) = U(x) + \frac{pv}{R}x, \tag{3.16}$$

and is shown in Fig. 3.5. The centrifugal component causes an asymmetry between the two sides of the potential well and an effective reduction of its depth. Furthermore, the lower the distance from the center of curvature, the higher the density of nuclei along the plane. This progressively increases the height of the potential barriers, as can be seen in Fig. 3.6. Therefore, there is a *critical bending radius* R_c, depending on the particle energy, under which the potential well becomes not deep enough to allow planar channeling. This critical point is reached when the centrifugal term is equal to the interplanar field at the location of the potential barrier x_{max}:
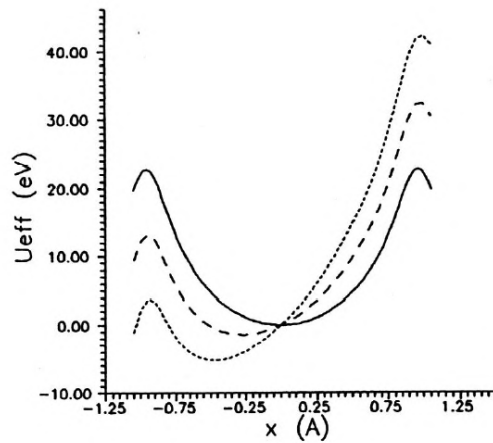
Figure 3.5: Effective potential in bent silicon crystals. The solid line represents a straight crystal, while the dashed and dotted lines correspond to $\frac{pv}{R} = 1$ and 2 [GeV/cm] respectively [16].
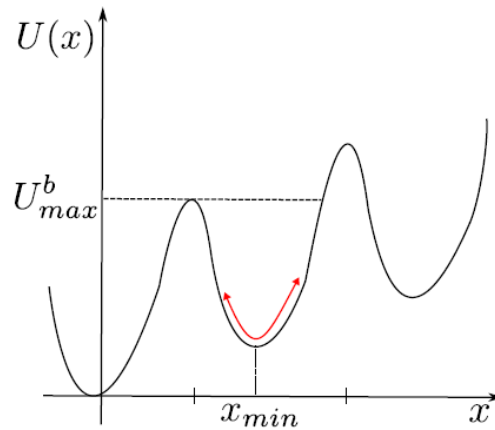
Figure 3.6: Crystalline plane potential in a bent crystal. The height of the potential barriers increases when moving towards the center of curvature, as the density of nuclei along the bent planes increases [11].

$$\frac{pv}{R_c} = U'(x_{max}). \tag{3.17}$$

Using the harmonic approximation, it follows that:

$$R_c = \frac{pv}{U'(x_{max})} \simeq \frac{pv x_{max}}{2U_{max}}. \tag{3.18}$$

Typical values for silicon crystals are reported in Tab. 3.1. The solution of eq. 3.15 is:

$$x(z) = -x_{min} + x_{max} \sqrt{\frac{E_t}{U_{max}^b}} \sin\left(\frac{2\pi z}{\lambda} + \phi\right). \tag{3.19}$$

Comparing this expression with eq. 3.13, the differences are the following:

- In order to take into account the finite charge distribution, the potential barrier is calculated at:

$$x_{max} = \frac{d_p}{2} - a_{TF}. \tag{3.20}$$

- The new equilibrium point of the oscillation is:

$$x_{min} = -\frac{pvx_{max}^2}{2RU_{max}} = -x_{max}\frac{R_c}{R}. \tag{3.21}$$

- The reduced potential well is calculated as:

$$U_{max}^b = U_{eff}(x_{max}) - U_{eff}(x_{min}) = U_{max}\left(1 - \frac{R_c}{R}\right)^2. \tag{3.22}$$

Finally, the critical angle of a bent crystal can also be expressed in terms of the critical radius, the bending radius and the original, straight critical angle:

$$\theta_c^b = \theta_c\left(1 - \frac{R_c}{R}\right). \tag{3.23}$$

3.1.4   Other Coherent Phenomena in Bent Crystals

Planar channeling is not the only coherent process that a charged hadron can experience when interacting with a bent crystal.
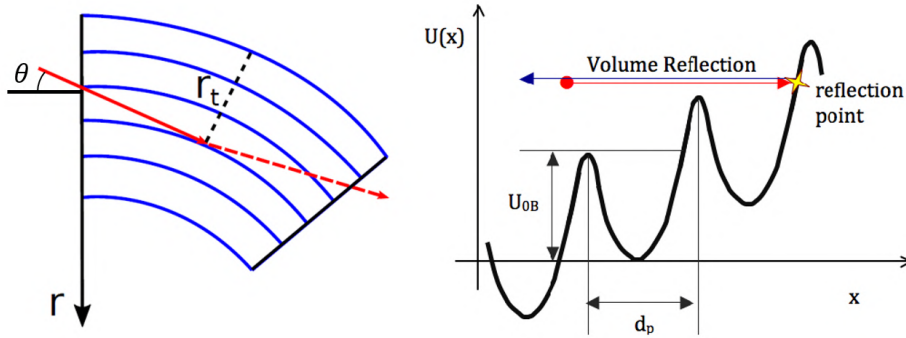

Figure 3.7: Graphic representation of the volume reflection process [16].

Volume reflection (VR) [40, 41] is a process in which a particle is deflected by elastic scattering with the potential barrier generated by crystalline planes. If the impact angle of the particle, θ, is lower than the crystal bending angle, θ_b, but larger than the critical angle, θ_c, its transverse energy will be too large to allow channeling by the first layer. Sec. 3.1.3 briefly mentioned that the atomic density of the bent crystalline planes increases when moving towards the center of curvature, and as a result they will generate progressively higher potential barrier. This means that the non-channeled particle will traverse the crystal crossing crystalline planes until it encounters a potential barrier that is as high as its transverse energy. As can be seen from the schematic representation in Fig. 3.7, the angle between the particle direction and the crystalline planes progressively decreases. The transverse energy of the particle can be expressed as:

$$E_t \propto pv\psi^2 + U_{eff}(x), \tag{3.24}$$

where ψ is the angle formed by the particle trajectory with the crystalline plane that is being crossed. It is easy to see that the above condition will be met when $\psi = 0$, i.e. at the point r_t where the particle trajectory is tangent to the crystalline plane and $U_{eff}(r_t) = E_t$. The motion is then inverted by the elastic interaction with the barrier and the particle may escape the crystal with a deflection given by:

$$\theta_{VR} = k_{VR}\sqrt{\frac{2U(r_t)}{pv}}, \tag{3.25}$$

where $k_{VR} \simeq 1.6$ is a coefficient that was tuned to match experimental data [42].
The efficiency of this process (around 90% for particles with $\theta_c < \theta < \theta_b$) is much larger than
that of channeling, thanks to the larger angular acceptance given by the crystal bending
angle and to the large number of crystalline planes in the crystal volume, which makes it
likely for a particle to find itself in the correct conditions to be reflected at some point.
Because of its high efficiency, volume reflection was initially considered for applications to
beam collimation. However, channeling was preferred for two main reasons:

- Particles experiencing volume reflection cross crystalline planes and as a result have a
  higher probability of interacting with lattice nuclei than particles experiencing chan-
  neling, an undesirable scenario for collimation since nuclear interactions are among
  the main limitations for hadron cleaning.

- Deflection angles achievable with channeling are much larger than those given by
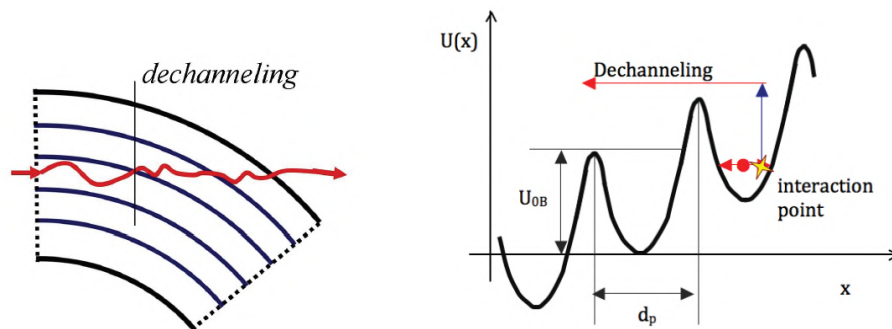 volume reflection, which are also determined by the energy.

Figure 3.8: Graphic representation of the dechanneling process [16].

Dechanneling (DC) [43] happens when a channeled particle interacts with the crystalline
lattice and loses channeling conditions. In bent crystals, a dechanneled particle escapes the
potential well before having traveled through the full length of the crystal, and the resulting
deflection is lower than the bending angle. Channeled particles are in fact not entirely free
in their motion. If the oscillations in the potential well are wide enough to bring the particle
close to the edge of the barrier, the probability of elastic scattering with the electrons of
the lattice atoms or even with the nuclei themselves increases [44]. As a result of these
interactions, the transverse momentum of the particle is modified, making it possible to
escape channeling. This process can be experimentally described as an exponential decay
of the initial population of channeled particles:

$$N(z) = N_0 e^{-\frac{z}{L_D}}, \tag{3.26}$$

where z is the length of the path in the crystal and L_D is a characteristic *dechanneling length*.
A graphic representation of the process is given in Fig. 3.8. Two separate contributions must
be considered in order to describe this process in a complete way:

- A "slow"dechanneling regime described by scattering with electrons, which causes small
  momentum variations.

- A "fast" dechanneling regime described by scattering with nuclei, which can cause significant momentum variation with a single interaction.

Using diffusion theory, the *electronic dechanneling length* can be calculated as [32]:

$$L_D^e = \frac{256}{9\pi^2} \frac{pv}{\ln\left(2m_e c^2 \gamma / I\right) - 1} \frac{a_{TF}}{Z_i r_e m_e c^2},$$

(3.27)

where I is the ionization potential while, m_e and r_e are the rest mass and classical radius of the electron respectively. The *nuclear dechanneling length*, on the other hand, can be derived by appropriate scaling of the electronic value based on fine tuning with experimental data. In bent crystals, the different atomic density of the crystalline planes when moving towards the center of curvature and the different oscillation center with respect to straight crystals need to be taken into account. It can be demonstrated that the dechanneling length of a bent crystal can be written as a function of the bending radius R:

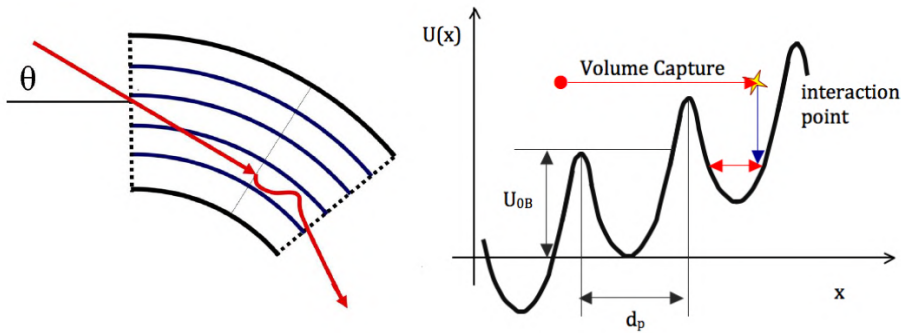$$L_D^b = L_D\left(\frac{R_c}{R}\right).$$

(3.28)

Figure 3.9: Graphic representation of the volume capture process [16].

Volume capture (VC) [45] is the opposite process that allows a non-channeled particle to fall within channeling conditions as a result of elastic interactions with atoms of the crystalline lattice. The probability of this process for a bent crystal can be written as a function of the particle energy E and the bending radius R:

$$P_{VC} = k_{VC}\left(\frac{R}{R_c} - 0.7\right)E^{0.2},$$

(3.29)

where k_{VC} is a constant tuned to experimental data [46]. The process is graphically represented in Fig. 3.9. When a particle is captured, it is treated as a channeled particle and the possibility of it later experiencing a dechanneling interaction should also be taken into account.

3.2   Crystals for Improved Hadron Beam Collimation and Plans for HL-LHC

Crystal channeling has shown promising results for applications to beam collimation at the LHC [11]. In a crystal-assisted collimation system, the primary collimators are replaced by bent crystals placed at the edge of the beam envelope, and oriented so that the crystalline planes at the crystal entry point are aligned to the beam envelope, i.e. to the direction of

the individual halo particles at that amplitude (typically between 5 and 6 σ). In such a configuration, halo particles are channeled and deflected by the crystal towards an absorber. This concept would provide various advantages with respect to the standard multi-stage system:

- Bent crystals can coherently deflect halo particles by tens of μrad, much more than what is achievable with an amorphous collimator (about 3 μrad for particles that see the full length of the jaw), requiring less tight settings for the downstream collimators. As a result, the contribution to the machine impedance is reduced, a particularly desirable feature for operations with proton beams.

- All channeled particles acquire the same deflection, given by the bending angle of the crystal, requiring in principle a single absorber to be effectively intercepted.

- Channeled particles have a low probability of interacting with lattice nuclei, reducing the rate of single diffractive events for protons and of fragmentation and dissociation for ions [47]. This mitigates significantly some of the main sources of losses that limit the performance of the standard system. The following chapters will show that the crystal collimation test stand currently installed at the LHC allows to significantly reduce losses at the dispersion suppressor area of the betatron cleaning insertion and to achieve a faster cleaning process.

The action of channeling from a crystal collimator on a circulating particle can be modeled as a kick θ in the transverse phase-space, and the effect on the particle motion can easily be described using the matrix formalism introduced in Sec. 2.1.1. Considering a particle that experiences channeling for the full length of the crystal without losing energy in the process, if the kick is applied in the z direction at location s_1, the coordinates change as:

$$\begin{pmatrix} z(s_1) \\ z'(s_1) \end{pmatrix} = \begin{pmatrix} z(s_1) \\ z'(s_1) + \theta \end{pmatrix} \tag{3.30}$$

Applying the matrix in eq. 2.17 to transport the new coordinates to location s_2, it is possible to show that:

$$z(s_2) = \sqrt{\frac{\beta_z(s_2)}{\beta_z(s_1)}}(\cos\varphi_{21} + \alpha_z(s_1)\sin\varphi_{21})z(s_1) + \sqrt{\beta_z(s_1)\beta_z(s_2)}\sin\varphi_{21}(z'(s_1)+\theta), \tag{3.31}$$

where the first term is the standard betatron oscillation term, while the second is the deviation from the reference orbit due to the kick. This formalism allows to trace the trajectory of the channeled halo around the machine and verify if a collimator placed at a certain aperture is able to safely intercept it.

This description is however an approximation which is valid for particles that are fully channeled at the first passage through the crystal. In reality, contributions coming from multi-turn effects, particles that experience other interactions inside the crystal and the energy spread of the beam need to be considered for a complete treatment. For this reason, the real assessment of the crystal collimation concept needs to come from full tracking simulations and from direct experience in the machine. However, a simplified approach is essential to the design phase of the layout and to check the basic dynamics.

3.2.1   Layout of the Crystal Collimation Test Stand at the LHC

Even though crystal collimation tests were carried out at the SPS with promising results, they could not be considered exhaustive enough to propose this system as a baseline for future upgrades of the LHC. A performance assessment under LHC conditions was considered mandatory to demonstrate a cleaning improvement for both proton and ion beams in a superconductive machine, where an efficiency higher than 99.99% is needed. Furthermore, tests at the SPS were carried out only in static conditions (coasting beams), whereas operational aspects related to dynamical phases of the LHC cycle (injection, ramp, squeeze, collisions) needed to be addressed. Lastly, the small acceptance of the channeling process at higher energy calls for a solid validation of the controls of the devices.

Table 3.2: Chronology of the installation of crystal collimators in the LHC. The technology and producer is reported for each crystal. The new devices installed in each operational year are shown in bold. ST and QM stand for strip and quasi-mosaic respectively.

Year	Beam 1		Beam 2	
	Horizontal	**Vertical**	**Horizontal**	**Vertical**
2015-2016	**ST-INFN**	**QM-PNPI**	n.a.	n.a.
2017	ST-INFN	QM-PNPI	**QM-PNPI**	**QM-PNPI**
2018	ST-INFN	QM-PNPI	**ST-PNPI**	QM-PNPI

Table 3.3: Name, collimation plane, installation position and main optics parameters for the crystal devices presently installed in the LHC. The name of the secondary collimator used to absorb the channeled halo is also reported.

	Beam 1		Beam 2	
Name	TCPCH.A4L7	TCPCV.A6L7	TCPCH.A5R7	TCPCV.A6R7
Plane	Horizontal	Vertical	Horizontal	Vertical
s **[m]**	19918	19842	20090	20145
β_x **[m]**	342.1	30.5	201.6	30.5
β_y **[m]**	64.9	281.1	135.0	281.1
α_x **[rad]**	-2.05	0.24	-3.53	0.24
α_y **[rad]**	0.84	-2.63	2.36	-2.63
D_x **[m]**	0.03	0.15	-0.28	0.01
D_y **[m]**	0.10	0.12	0.22	0.32
Absorber	TCSG.B4L7	TCSG.D4L7	TCSG.B4R7	TCSG.D4R7

Due to time restrictions and limited possibility to change the IR7 layout, a minimal prototype crystal system was deployed by installing four bent crystals and by relying only on existing collimators to intercept channeled halo particles. A careful analysis was carried out in order to identify the optimal parameters for the devices and strike the right compromise between the various needs of the setup [16]. Silicon was chosen as the most suitable material for crystal collimators, given its well consolidated manufacturing technique that allows to produce crystalline lattice almost without imperfections [48]. Through a campaign of simulations and semi-analytical studies, a length of 4 mm and a bending angle of 50 μrad (resulting in a bending radius of 80 m, well above the critical value both at injection ad flat top energy, see Tab. 3.1) were identified as optimal parameters.
Several crystal collimators were produced and installed in the IR7 insertion of the LHC,

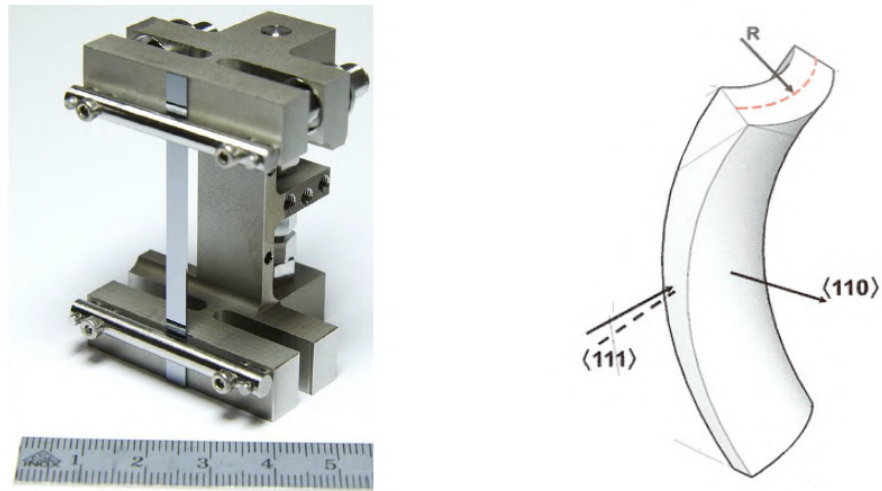Figure 3.10: On the left side, a picture of a strip crystal for the LHC with its titanium holder. On the right side, a scheme of how the the bending of the crystal is mechanically produced [11].
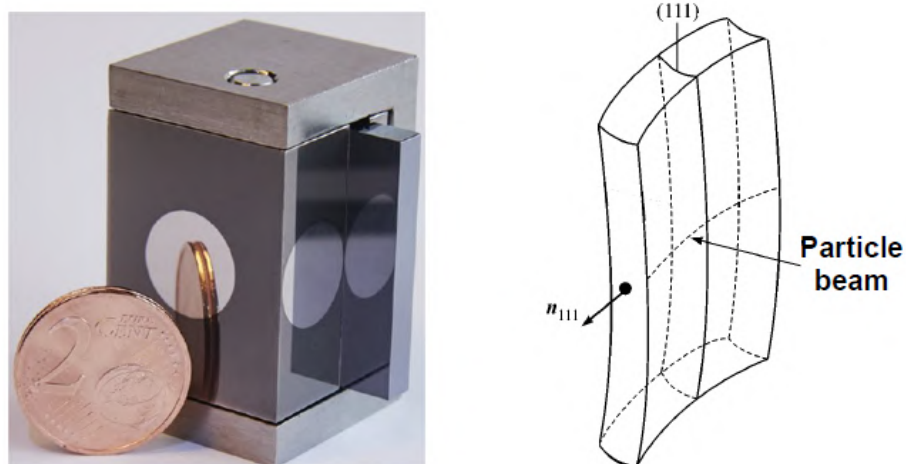

Figure 3.11: On the left side, a picture of a quasi-mosaic crystal for the LHC with its titanium holder. On the right side, a scheme of how the the bending of the crystal is mechanically produced [11].
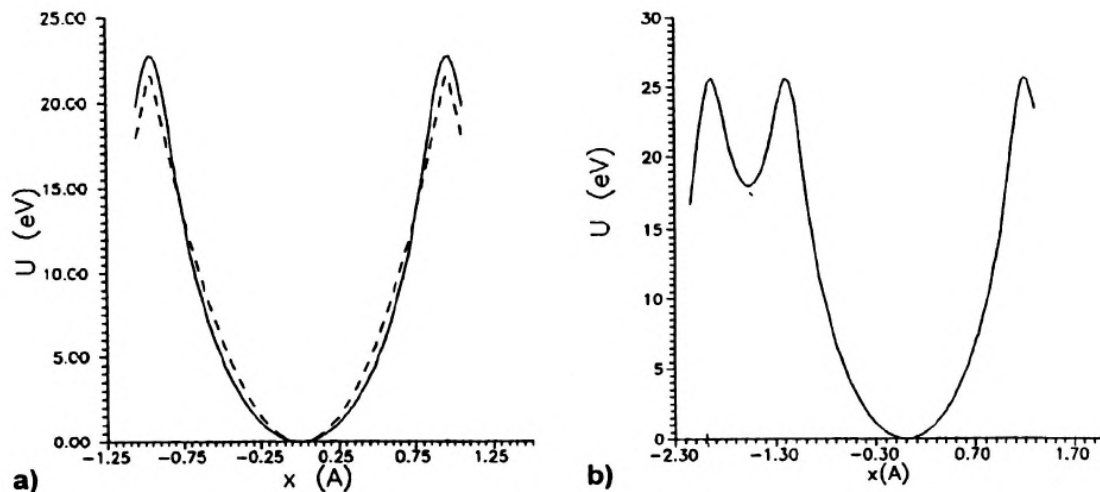
Figure 3.12: Potential seen by a proton entering between crystalline planes at a small angle. On the left, silicon strip crystals (110 planes) are used and the harmonic approximation is also showed (dashed line). On the right side, silicon quasi-mosaic crystals (111 planes) are used and the characteristic 1:3 ratio between subsequent planes can be seen [16].

following the timeline reported in Tab. 3.2. These devices are composed of a metal holder that applies a curvature to a silicon crystal, and were provided by the Petersburg Nuclear Physics Institute (PNPI), Russia, and the section of Ferrara of the Istituto Nazionale di Fisica Nucleare (INFN), Italy, in the framework of the UA9 collaboration [49,50]. The main parameters of the four crystals used for crystal collimation tests in 2018 are reported in Tab. 3.3.

The installed devices essentially consist of a holder that clamps the crystal in order to induce a secondary curvature on the plane selected for particle steering, and can be divided in two categories which use different technologies:

- *Strip crystals* (ST), shown in Fig. 3.10, are silicon strips mechanically bent at their extremities. As a result, an anticlastic curvature is induced along the (110) planes, which are used for channeling [49].

- *Quasi-mosaic crystals* (QM), shown in Fig. 3.11, are thick silicon tiles clamped by a holder along their axis. This generates an anticlastic curvature along the larger face and, at the same time, a quasi-mosaic curvature along the (111) planes, which are used for channeling [50].

Aside from the macroscopic structure, the main difference between the two types of devices is the fact that (110) planes are equidistant, while (111) planes are in a 1:3 ratio, producing the characteristic shape of the potential wells that can be seen in Fig. 3.12. In both cases, a piezogoniometer is used to measure and adjust the crystal orientation. The full assembly installed in the LHC is called TCPC (Target Collimator Primary Crystal) and is described in detail in [51, 53]. A schematic drawing of the goniometer for a horizontal crystal is shown in Fig. 3.13. The TCPC positioning control system is derived from that of the LHC collimation system [54], whereas the angular controls are based on a novel interferometer technology deployed for the first time in accelerators [55]. These devices are designed in order to comply with the requirements for LHC operations summarized in Tab. 3.4. In
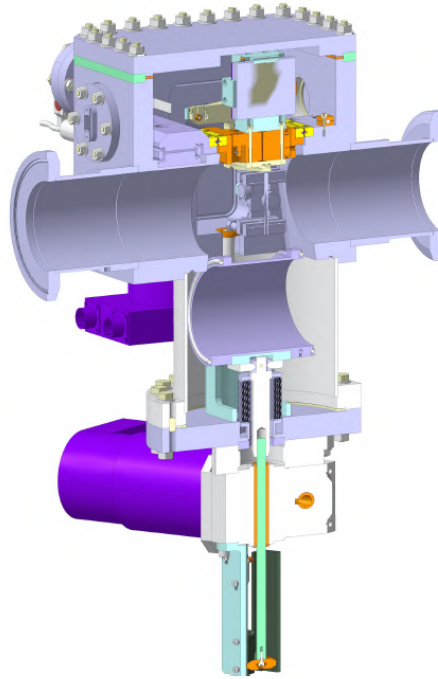
Figure 3.13: Schematic drawing of the main part of the goniometer for a horizontal crystal. A section of the beam pipe is retractable, in order to allow the insertion of the crystal mounted on the chamber above the pipe [51].

Table 3.4: TCPC position and angle control requirements [52].

Property	Specification
Linear stroke	>50 mm
Stroke across zero (center of beam pipe)	>5 mm
Linear resolution	5 μm
Linear accuracy	$\pm$50 μm
Linear reproducibility	$\pm$20 μm
Total angular range	$\pm$10 mrad
Yaw angular resolution	0.1 μrad
Yaw angular precision over the entire linear range	$\pm$1 μrad
Yaw angular overshoot	10%
Yaw angular settling time	20 ms
Yaw angular max speed in scan mode	50 mrad/s
Pitch angular accuracy over last 10 mm travel	Few μrad
Roll angular accuracy over last 10 mm travel	Few tens of μrad

particular, a sub-μrad precision is required for the angular controls in order to achieve and maintain channeling conditions at the LHC.

An extensive campaign of crystal collimation tests at the LHC were carried out throughout Run 2. All devices were fully characterized and the cleaning performance of the system was evaluated with proton beams and with Xe ion beams with promising results [11]. This thesis mainly focuses on measurements that were carried out in 2018, with the goal of demonstrating an improvement in cleaning efficiency with Pb ion beams and conclude on the feasibility of crystal collimation in operations with ions in the future upgrades of the LHC.

3.2.2   Upgrade Scope for Crystal Collimation at the HL-LHC

Throughout Run 2, which lasted from 2015 to 2018, the LHC operated with 13 TeV center-of-mass proton collisions, reaching and eventually surpassing by more than a factor 2 the design peak luminosity of 10^{34} cm^{-2}s^{-1}. This excellent performance allowed to achieve a total integrated luminosity of 190 fb^{-1} by the end of 2018. At this point, the machine has reached its peak performance in its present configuration, and the statistical gain in running the accelerator beyond Run 3 would become marginal. In order to explore the full capacity of the machine, a significant increase in luminosity beyond the original design value is required. The High-Luminosity LHC (HL-LHC) [2, 56] upgrade was first set up in 2010, and has become a major construction project for the next decade after the approval of the CERN Council in 2016. The main objective of this upgrade is to reach the impressive goal of a total integrated luminosity of 3000 fb^{-1} (about 10 times the total integrated luminosity estimated reach of the LHC at the end of Run 3) in the 12 years after the upgrade at a pace of about 250 fb^{-1} per year. The four main experiments located around the LHC ring will be upgraded in different phases starting in the Second Long Shutdown (LS2), in order to take full advantage of the new capability of the machine, following the baseline schedule shown in Fig. 3.14. In particular, the ALICE and LHCb experiments will be fully upgraded already during LS2, requiring collisions with high-intensity ion beams to be delivered already during the first year of Run 3.

Such a massive upgrade requires the improvement of a number of systems, such as magnets, cryogenics and machine protection equipment, which were not designed for the upgraded beam parameters and conditions and would otherwise be particularly vulnerable to breakdown and wear out. In particular, the requirement to operate efficiently and safely with the unprecedented energy stored by high-intensity hadron beams at small colliding beam sizes provides significant challenges, which drive the key design aspects of the collimation system at the HL-LHC [57,58]. A potential performance limitation was identified in the Dispersion Suppressor (DS) around the betatron collimation insertion, a region where the high dispersion value can cause significant off-momentum leakage. Extensive tracking and shower simulations, as well as experimental quench tests, were carried out in order to determine the expected power loads and quench margins for both proton and heavy-ion operation [17]. The results indicates that upgrades of the collimation cleaning hardware in the DS are needed as part of the HL-LHC upgrade. To mitigate the risk of quenches due to IR7 leakage, especially for operations with ion beams, it is foreseen to add a new set of tungsten collimators (TCLDs, Target Collimator Long Dispersion) in the DS, where the dispersion has already started rising. In order to make space for the new collimators, it is envisaged to replace, for each TCLD, an existing main dipole with two shorter 11 T dipoles. This was the chosen baseline upgrade solution for HL-LHC, with the plan to integrate it in LS2. The main goal is to ensure a successful heavy-ion run in Run 3. The HL-LHC intensity upgrade for proton beams will take place in Run 4, with no limitations expected during Run 3 [58].
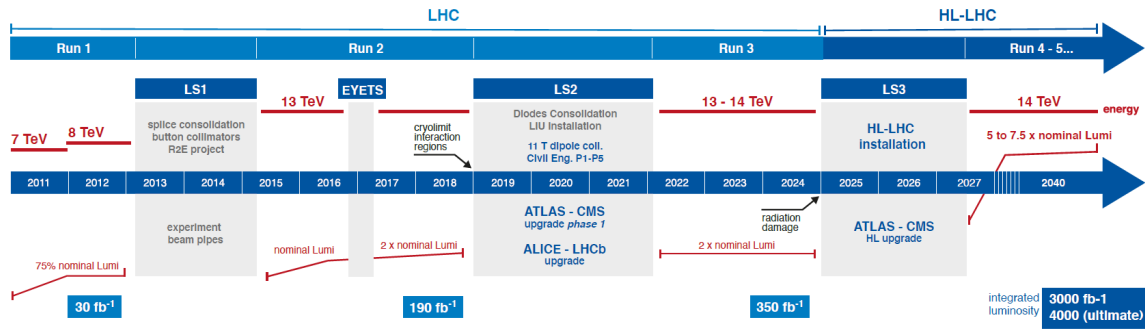
Figure 3.14: LHC/HL-LHC baseline program as of August 2020 [59].

Crystal collimation was studied in parallel as an alternative solution to improve ion cleaning in Run 3. The direct deployment of crystal collimation with proton beams in operational scenarios is not envisaged, since a special absorber capable of handling losses of up to 1 MW during 10 seconds is required to intercept the channeled beam halo. However, the planned TCLD upgrade is satisfactory for the HL-LHC proton beam parameters in Run 4. On the other hand, ion collimation does not present such prohibitive conditions, since a peak power deposition below 1 kW/cm^3 and a total beam loss power of 28.5 kW is expected for Pb ion beams with a lifetime of 12 minutes [60]. As such, the channeled halo can be safely caught by a standard secondary collimator even in the extreme environment of the HL-LHC. After various studies and also thanks to the experimental results achieved in this thesis work with Pb ion beams, in December 2019 it was decided to integrate crystal collimation in the upgrade baseline in order to mitigate risks of delays in the planned schedule for the 11 T dipole project.

At present, crystal collimation has become the main plan for the improvement of ion collimation cleaning in Run 3, since the installation of the 11 T dipoles will not be possible during LS2 [61] given the recent status of the project [62]. This proposal was approved thanks to the possibility to build the new required hardware through an in-kind contribution by Russia. The detailed scope of this upgrade consists in preparing 4 new crystal primary collimators that can replace the existing 4 devices in IR7, which were conceived as a test bench rather than for regular operations. The controls also need to be upgraded in order to adapt the operational modes to the standards used by the rest of the collimation system for operations with high intensity beams.

Crystal collimation tests performed during 2018, the last year of Run 2, were the first opportunity to test the full implementation of this innovative collimation technique with Pb ion beams. Demonstrating the ability to improve the cleaning efficiency of the collimation system was crucial in view of the possible deployment of crystals during Run 3 and beyond. A potential configuration for use in operation with high-intensity ion beams, based on result gathered during the 2018 ion run, will be proposed in Chap. 5.

3.3 Other Applications of Bent Crystals to Hadron Accelerators under Study

Crystal channeling can be used for a variety of other applications to physics at particle accelerators. In 2018, two specific setups for proton beams were explored at the CERN accelerator complex, namely at the LHC and at the SPS.

3.3.1   Bent Crystals for Reduced Detector Background

The extreme reliability and versatility of the LHC is often exploited in *special runs*, during which unusual configurations of beam optics, collimator settings and detector configurations are deployed for specific purposes. Crystal collimation proved to be an additional assets to improve the flexibility and performance of the machine. Following a request by the ATLAS (ALFA) [63] and TOTEM [64] experiments, the 2018 special physics run at the LHC involved low-intensity proton beams (up to about $6 \cdot 10^{11}$ protons per beam) at injection energy and a special optics with a larger beam size at the interaction points compared to normal operations [65]. The physics motivations of this run were the measurement of the proton-proton elastic cross section and the extrapolation of its nuclear part to low values of four-momentum transfer squared t [66]. The preparation of this run posed several challenges from the accelerator physics point of view, including the development of specific collimation layouts and settings (featuring the tightest normalized apertures ever used in operations at the LHC) [67]. Crystal collimation, with a faster cleaning process and potentially reduced multi-turn halo, was proposed as an alternative to the standard collimators. This was possible thanks to the relaxed machine protection constraints with low-intensity beams. The simulation campaign that demonstrated the feasibility of this setup, as well as some highlights from the measurements gathered during the special physics run, will be shown in Sec. 7.1

3.3.2   Applications of Bent Crystals to Physics Beyond Colliders

Beam collimation is far from the only application of bent crystals to hadron accelerators. Over the course of the years, crystal-assisted beam steering has been investigated in a variety of machines and context. For example, a two-crystal setup was applied for the production of simultaneous particle beams at the NA48 experiment [68], and a crystal-assisted slow-extraction scheme was explored at the SPS [69]. Both of these configurations were explored as a test stand for potential applications at the LHC.

More recently, in the context of Physics Beyond Colliders (PBC) [70], the idea of using crystal channeling to measure the magnetic moment of short-lived baryons produced at the LHC was proposed. This concept exploits the strong equivalent magnetic field provided by a bent crystal to induce the precession of the polarization vector [5, 6]. Since no external beam exists yet at the LHC, a double-crystal setup was conceived. The first crystal deflects beam halo particles towards a fixed target, while the second crystal rotates the polarization vector of the baryons produced in the collision and steers them towards a detector [71]. Before proceeding with the installation of this setup in the LHC, it is crucial to verify the feasibility of such a complex beam manipulation in a safer, low-energy environment. For this reason, a simplified version of the double-crystal setup was implemented by the UA9 collaboration as part of the collimation hierarchy of the SPS [72, 73], and a number of tests were carried out in the past years to evaluate its performance. Some of the results gathered in 2018 will be discussed in more detail in Sec. 7.2.

Chapter 4

Crystal Collimation Studies with Proton Beams

At the present time, the usage of bent crystals for halo collimation in LHC operations with high-intensity proton beams is severely hampered by the need to design a special absorber, capable of withstanding an impacting beam loss power of the order of 1 MW over a few mm^2 caused by the high-intensity channeled beam. Furthermore, proton beams are not expected to cause significant issues during the gradual intensity ramp up over the course of Run 3, and Run 4 will see the implementation of 11 T dipoles in the DS, which are foreseen to provide a satisfactory upgrade to the cleaning efficiency of the system.

Nevertheless, activities with low-intensity proton beams are an extremely important test bench to prove the crystal collimation concept, allowing to achieve a variety of goals:

- Gain experience with the setup of the crystal collimation system.

- Verify the reliability and reproducibility of the installed devices.

- Have a first assessment of the performance of the system in terms of cleaning improvement.

- Study operational-oriented aspects of crystal collimation (such as the deployment during dynamical phases of the machine) in a safe and controlled environment.

- Fully characterize the crystal devices in view of future applications not only to beam collimation at the LHC but to other contexts as well.

Given the low intensity allowed in these tests (up to $3 \cdot 10^{11}$ circulating protons), the jaw of a TCSG can be safely used to intercept the channeled beam halo coming from a crystal collimator.

After an overview of the experimental methodology used to assess the performance of crystal collimation at the LHC, this chapter presents the results gathered during Run 2 with proton beams. These observations were instrumental in preparation for crystal collimation tests with ion beams, for which a very limited time is allocated every year.

4.1 Methods and Procedures for Crystal Collimation Tests at the LHC

Local losses around the LHC ring are measured using Beam Loss Monitors (BLMs) [74], a series of more than 3900 ionization chambers installed at likely or critical loss locations to
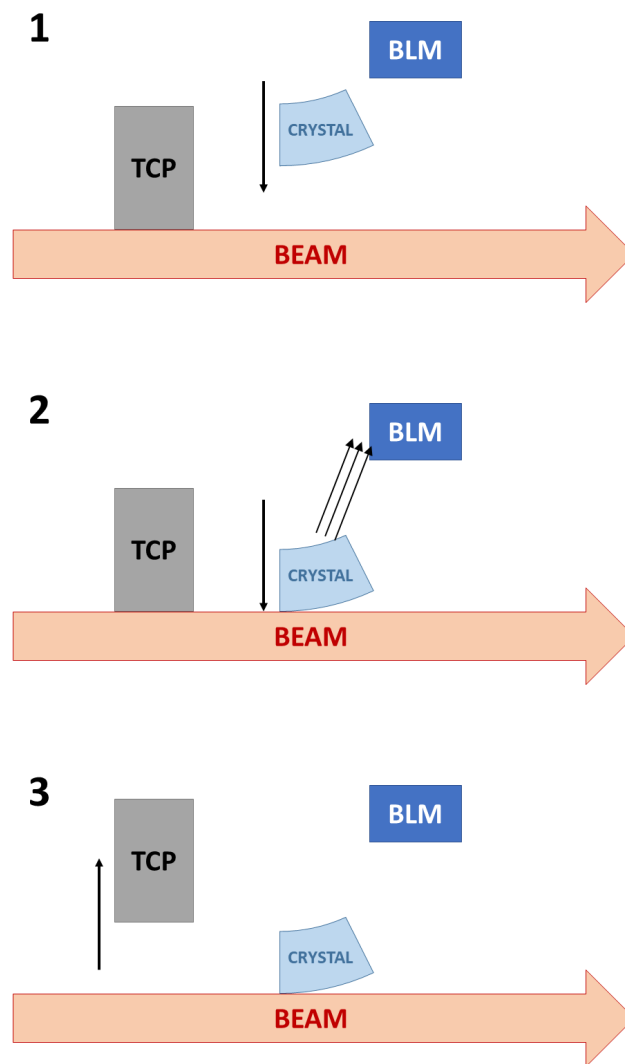
Figure 4.1: Main steps of the beam-based alignment procedure used to set a crystal as the primary collimation stage.

detect products of showers generated by nuclear interactions. In order to study crystal properties in a circular accelerator and to setup a crystal-based collimation system, it is necessary to observe losses at the crystal position and at other locations around the ring, such as the secondary collimator used to absorb the channeled halo or selected other collimators in IR7. The distribution of beam losses shows specific features when particles interact coherently with a crystal, allowing to evaluate the performance of the device. This section presents the key methods for evaluating crystal channeling that have been developed throughout the years [11].

4.1.1   Beam-based Alignment of Crystal Collimators

In order to set crystal collimators as the primary bottleneck of the collimation system, a well established procedure called *beam-based alignment* [75] is used. This method is routinely used at the LHC to determine the optimal jaw positions of the standard collimators and to

ensure that the precise hierarchy of the collimation system is respected.

The key steps of the procedure are schematically shown in Fig. 4.1. The beam halo is first shaped with a primary collimator, closed to its nominal gap of 5 σ (1). This reference halo is then used to cross-align the crystal, by moving it towards the beam in small steps of 5-20 μm until it touches the beam halo, causing a signal spike in the closest BLM (2). For tests with low-intensity beams, the primary collimator is then retracted to its parking position, leaving the crystal as the primary collimation stage (3). Additionally, all secondary collimators located between the crystal and the absorber of the channeled halo are also opened.

This procedure is needed in particular for crystal devices because they use the parking (i.e. fully retracted) position as reference for the transverse alignment, rather than the center of the beam like a standard double-sided collimator. The beam-based alignment allows to place them at the correct aperture settings, which are measured in units of the beam r.m.s. width from the beam center.

4.1.2 Angular Scan

After the crystal has been set as the primary bottleneck, it needs to be aligned with the beam divergence to maximize the probability of halo particles to be channeled. This is done by a procedure called *angular scan*, during which the crystal is rotated at constant speed along the deflection plane. The behavior of the BLM signal recorded at the crystal location and at the location of the absorber has distinct features that allow to identify the optimal channeling orientation.

As described in Chapter 3, channeled particles travel through essentially empty space between crystalline planes, and the probability of them experiencing nuclear inelastic interactions is reduced. It follows that, when the crystal is well aligned with respect to the beam envelope so that halo particles are likely to be channeled, the signal recorded by the closest BLM is reduced compared to amorphous orientation, when no coherent processes are possible and the crystal behaves like a standard scatterer. On the other hand, the signal at the location of the collimator used to catch the channeled halo increases when the crystal is in optimal channeling conditions, as more and more particles are deflected onto the absorber.

In order to clearly observe the above mentioned features of the BLM signal, the beam is excited by introducing white noise via the Active Transverse Damper (ADT). This procedure allows to increase the diffusion speed of beam particles of selected bunches, causing high but controlled beam losses during the angular scan. However, it is impossible to maintain a constant rate of lost particles for the whole duration of the scan as the bunches are progressively consumed. Since the BLM signal is proportional to the number of lost particles per unit of time, a normalization is required to analyze the signal profile. To take this into account, the measured beam intensity during the scan as a function of time is fitted with a $3^{\rm rd}$ order polynomial, and its derivative (i.e. the flux of lost particles) is used to normalize the BLM signal at each given time.

The characteristic shape of an angular scan is shown in Fig. 4.2, where the horizontal crystal on Beam 1 at injection energy has been chosen as an example. In the left frame, the opposite behavior of the raw BLM signal recorded at the crystal and at the absorber can clearly be seen. The right frame shows the normalized signal at the crystal, and three different regions where different coherent processes dominate can be distinguished:

1. The **channeling well** (1615-1635 μrad), the width of which is determined by the critical angle (9.4 μrad for Si crystals at 450 GeV).

2. The **volume reflection plateau** (1530-1615 μrad), the width of which is related to the bending angle of the crystal.
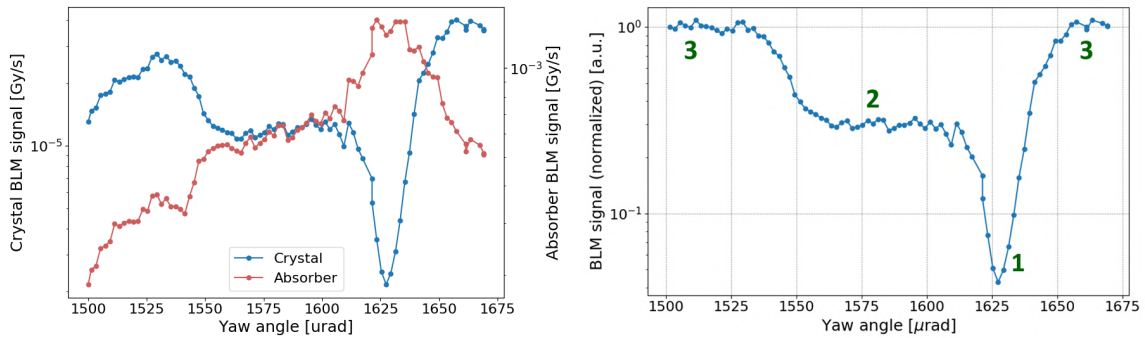
Figure 4.2: Characteristic BLM signal profile during an angular scan of the horizontal crystal on Beam 1, performed with proton beams at 450 GeV. The left frame shows the raw signal recorded at the crystal and at the absorber. The right frame shows the BLM signal at the crystal after it has been normalized to the flux of lost particles and to the amorphous level.

3. The **amorphous shoulders** on both sides of the scan.

The signal is further normalized by the average losses recorded in amorphous orientation. The optimal channeling orientation is identified by fitting the channeling well with a second order polynomial and used as a reference for future tests. The corresponding value is an estimate of the *reduction factor* of local losses when the crystal is in optimal channeling. This quantity is affected by the settings of the machine. However, for activities performed in the same configuration, its measurement can give a good indication of the reproducibility of the results. The uncertainty on this value is evaluated in a statistical approach by calculating the mean and r.m.s. around the minimum of the channeling well and then performing the average over all angular scans performed in the same conditions.

4.1.3   Linear Scan

When the crystal is in optimal channeling orientation, halo particles are coherently steered towards a selected absorber, which in the case of crystal collimation tests at the LHC is the jaw of a secondary collimator. The channeled beam gets separated from the primary beam envelope and follows its own distinct dynamics and can be studied via a *linear scan* with a collimator jaw. The jaw of the absorber is retracted and then progressively moved towards the core of the primary beam. During this procedure, the channeled halo is intercepted by the downstream collimators, which are kept at their nominal settings. As the jaw moves towards the primary beam, the channeled halo will be intercepted first, generating an increase in beam losses recorded at the collimator location. The scan is stopped as soon as the jaw touches the envelope of the primary beam, generating a massive loss spike. An example of the resulting signal profile is shown in Fig. 4.3.

The BLM signal recorded during the scan is proportional to the integral of the channeled beam crossed by the jaw. By fitting the rise in signal with an error function, it is possible to extract a measure of the width of the channeled beam and of its transverse position [76], while the primary beam envelope is assumed to be located at the start of the signal spike at the end of the linear scan (see $x \sim 1$ mm in Fig. 4.3). This information can then be used to reconstruct the effective deflection θ given to the particles by the crystal, i.e. the bending angle of the crystal.

Using Eq. 3.31, the transverse position z of a deflected particle can be calculated in any given point of the machine. In this specific case, s_1 indicates the location of the crystal,
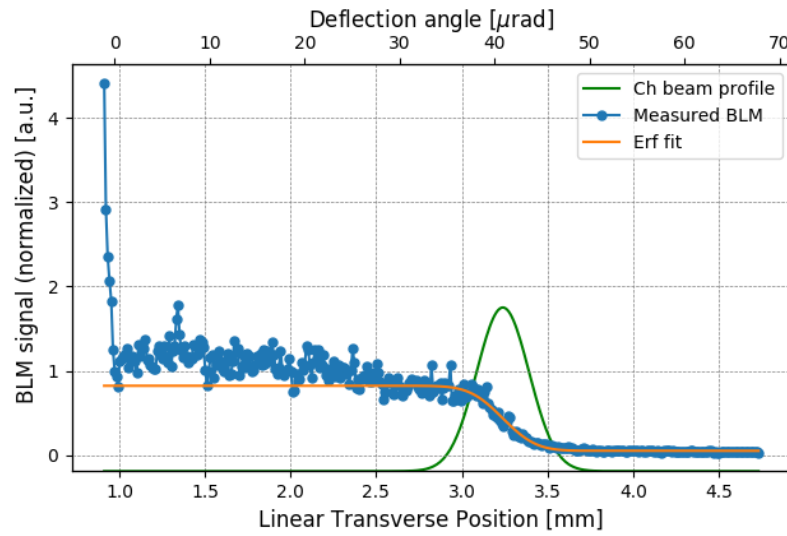
Figure 4.3: BLM signal as a function of the absorber transverse position during a linear scan. The values are normalized to the signal recorded at the position of the primary beam envelope. The error function fit and the resulting channeled beam profile are also shown. On the top axis, the transverse position is converted into angular deflection using Eq. 4.5.
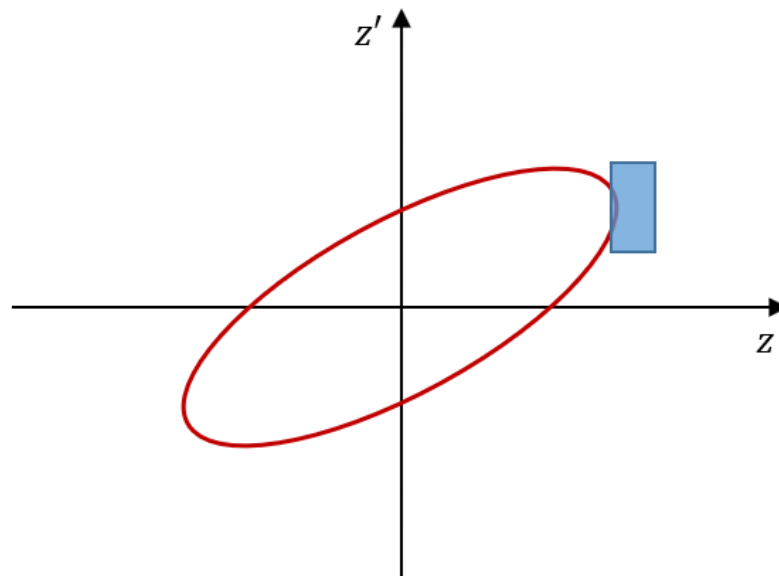

Figure 4.4: A crystal collimator, represented as a blue box, is positioned in order to touch the edge of the primary beam.

where the deflection is applied, while s_2 indicates the location of the absorber used to intercept the channeled beam. Assuming that the crystal is positioned in order to touch the primary beam (as schematically shown in Fig. 4.4) and oriented in optimal channeling, the phase-space coordinates of the channeled particles when hitting the crystal are given by the beam envelope at that location, which can be calculated using the beam emittance ε and the Twiss parameters introduced in Sec. 2.1.1:

$$z(s_1) = n_\sigma \sqrt{\varepsilon \beta_z(s_1)}, \tag{4.1}$$

$$z'(s_1) = -n_\sigma \alpha_z(s_1) \sqrt{\frac{\varepsilon}{\beta_z(s_1)}}, \tag{4.2}$$

where n_σ is the distance of the crystal from the primary beam core, expressed as a multiple of the beam r.m.s. width. In complete analogy, the transverse position of the primary beam envelope at the absorber location is:

$$z_{env}(s_2) = n_\sigma \sqrt{\varepsilon \beta_z(s_2)}, \tag{4.3}$$

where n_σ is the same as in Eq. 4.1 and 4.2 because the crystal constitutes the primary stage of collimation and as such it defines the width of the beam envelope. Using these formulas in Eq. 3.31, the distance between the center of the channeled beam and the primary beam envelope at the absorber location is given by:

$$\Delta z(s_2) = z(s_2) - z_{env}(s_2) = n_\sigma \sqrt{\varepsilon \beta_z(s_2)}(\cos \varphi_{21} - 1) + \theta \sqrt{\beta_z(s_2)\beta_z(s_1)} \sin \varphi_{21}. \tag{4.4}$$

Knowing the relative position between the channeled beam and the primary beam envelope, Eq. 4.4 can be inverted to extract the crystal bending angle:

$$\theta = \frac{\Delta z(s_2) - n_\sigma \sqrt{\varepsilon \beta_z(s_2)}(\cos \varphi_{21} - 1)}{\sqrt{\beta_z(s_2)\beta_z(s_1)} \sin \varphi_{21}}. \tag{4.5}$$

This estimation is useful to verify that the crystal device actually falls within the required specifics for operations in the LHC. However, it is important to note that this calculation is very sensitive to the value of the optics functions, which in reality may not coincide exactly with the nominal parameters of the machine. Uncertainties on the closed orbit at the crystal and at the absorber can also influence the result. In order to take this into account, a systematic uncertainty of 5 μrad is assumed.

Finally, the BLM signal as a function of the absorber position during an angular scan is normalized to the value recorded at the location of the primary beam envelope. In this condition, the saturation value of the error function used to fit the rise caused by the intercepted channeled beam is actually a measure of the channeling efficiency, i.e. the percentage of particles hitting the crystal that actually experience channeling [76]. The uncertainty on this measurement is dominated by the point of the scan chosen to normalize the BLM profile. This translates into a systematic error which can be assumed to correspond to 5% of the measured value [76].

4.1.4   Loss Maps

One of the most important means of assessing the halo cleaning performance of the LHC collimation system is by using the ADT to intentionally excite the beam and generate controlled losses around the machine. The resulting signal is detected by the BLMs installed

all around the ring. The loss pattern is displayed in what is commonly referred to as a *loss map*, an example of which can be seen in Fig. 4.5, and allows to measure the *cleaning inefficiency* of the system, i.e. the fraction of particles entering the collimation system that are lost at particularly sensitive locations. This quantity can be used to easily compare the performance of the standard and crystal collimation system.
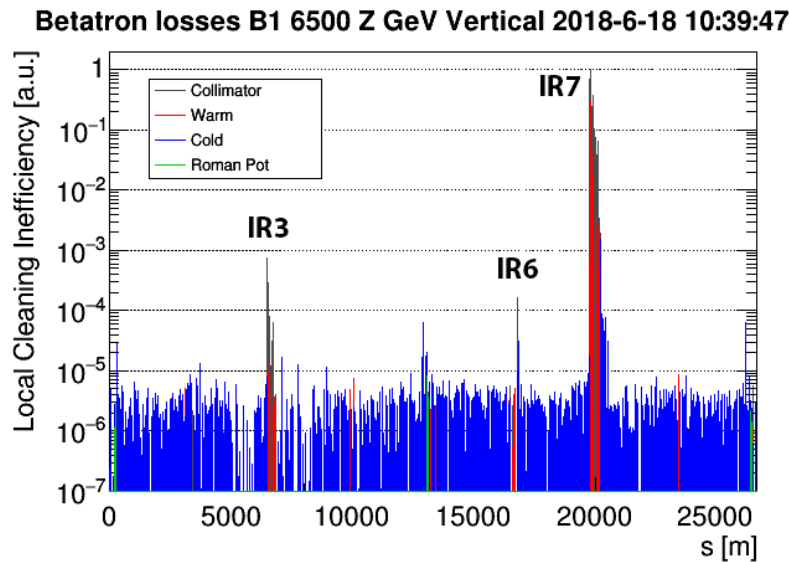

Figure 4.5: Full LHC ring loss map for the vertical plane of Beam 1 with the standard collimation system, measured with protons at 6.5 TeV. BLM signals are normalized to the highest peak.

In standard collimation, the cleaning inefficiency is measured by normalizing the signal profile by the highest signal recorded among the BLMs close to the primary collimators. This value is proportional to the number of particles intercepted by the collimation system and therefore such a normalization allows to directly estimate the cleaning inefficiency at any location of the machine. The location of interest to evaluate the performance of the system is the IR7 Dispersion Suppressor (DS), a region downstream of the first main dipoles after the straight insertion where high off-momentum leakage is recorded. However, the BLM response behaves very differently for crystal collimation. As previously explained, the probability of inelastic interactions with the atoms of the crystalline lattice is reduced when a particle experiences crystal channeling. Therefore, losses at the crystal location actually decrease when in channeling, and are not proportional to the number of impacting particles like for a standard TCP. In order to compare the two systems, a different kind of normalization that can be applied in both cases is needed. The chosen normalization factor is the flux of lost particle calculated from the decrease in intensity over time observed during the beam excitation.

As an example, normalized loss maps for the horizontal plane of Beam 1 are shown in Fig. 4.6. In the left frame, the usual IR7 hierarchy of the standard collimation system can be seen, with the highest loss peak localized at the primary collimator. In the right frame, on the other hand, a very different loss pattern can be observed when crystal collimation is deployed. In this case, the highest peak is instead located at the secondary collimator that intercepts the channeled halo.

The local cleaning inefficiency comparison between the two systems is performed by dividing the cold IR7-DS region into four different sections, which are for simplicity identified by the
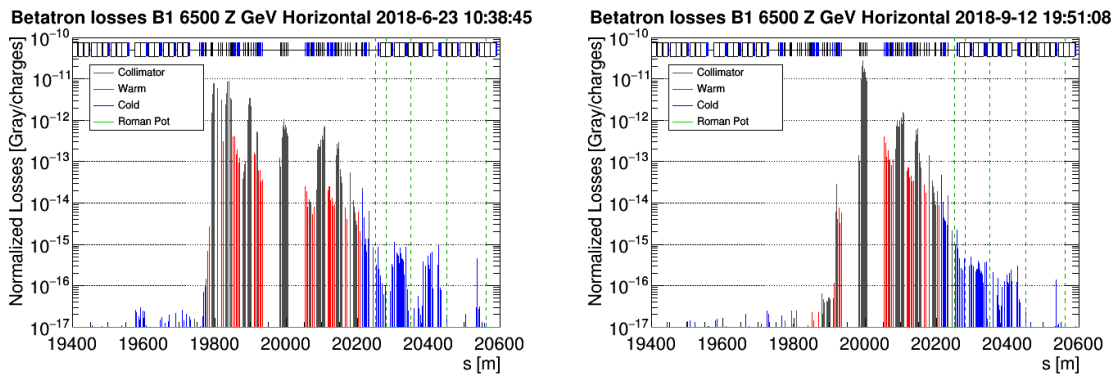
Figure 4.6: Typical IR7 loss pattern with the standard (left) and crystal (right) collimation system, measured on the horizontal plane of Beam 1 with protons at 6.5 TeV. Losses are normalized to the beam flux.
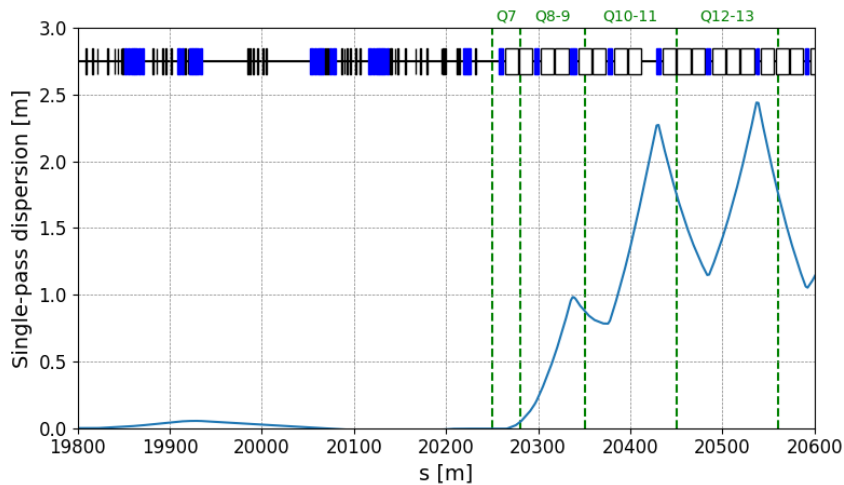

Figure 4.7: Single-pass dispersion experienced by particles that interacted with the primary collimator on the horizontal plane on Beam 1. The cold aperture regions investigated during collimation measurements are delimited by green dashed lines. The layout of the LHC is schematically shown at the top, with collimators, dipoles and quadrupoles represented by black, white and blue boxes respectively.

quadrupoles they respectively enclose (Q7, Q8-9, Q10-11 and Q12-13, with the respective longitudinal range shown in Fig. 4.7 for Beam 1). The Q7 region is considered because crystal collimation tests show increased losses in this location even though the single-pass dispersion is zero, and as such no off-momentum leakage is expected. This behaviour could be explained by losses coming from the nearby tungsten TCLAs. The following regions are all characterized by a peak in the dispersion function, leading to off-momentum losses which are predicted to be reduced when crystal collimation is deployed. It is worth mentioning that the Q12-13 region is only relevant for collimation tests with ion beams, since no significant losses are recorded there during operations with protons.

The Q6 region (upstream of Q7) is not considered for the local cleaning inefficiency comparison, even if noticeable losses can be observed in this area when crystals are deployed, as shown in the right frame of Fig. 4.6. As can be seen in Fig. 4.8, the highest loss signal in a BLM labeled as "cold" (blue lines in the loss map graphs) is located at $s = 20215$ m,

upstream of the Q6 quadrupole modules (represented as blue boxes in the schematic layout shown at the top). This means that this BLM is actually detecting showers coming from upstream collimators, rather than losses on the magnets. Note that this BLM is used to protect the Q6 region against losses caused by the counter-rotating Beam 2, thus it is installed downstream of the quadrupole modules following the direction of this beam. For this reason, this area is not considered to be at risk of quench and is not included in the cleaning inefficiency measurements.
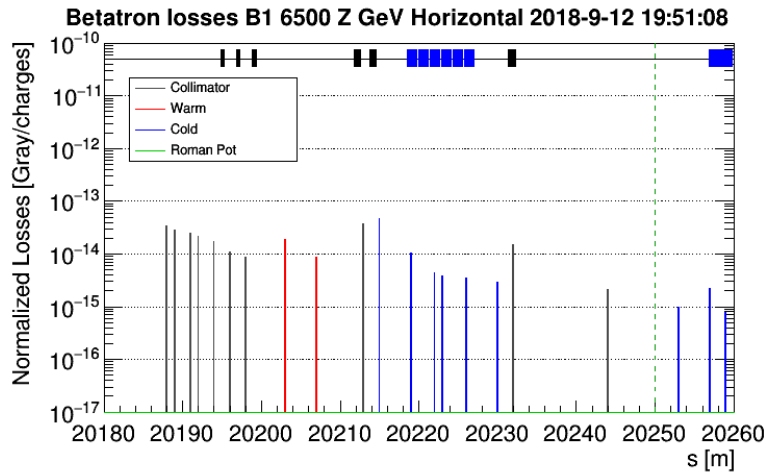

Figure 4.8: Losses measured in the Q6 region using the crystal collimation system on the horizontal plane of Beam 1 with protons at 6.5 TeV. BLM signals are normalized to the beam flux.

The cleaning inefficiency η_c in each of the above defined IR7-DS regions is evaluated as the highest normalized BLM signal in the respective longitudinal range. In order to compare the performance of the crystal-based system to that of the standard system, a *local leakage ratio* is defined for each region:

$$LLR_i = \frac{\eta_c^{\text{STD}}(i)}{\eta_c^{\text{CRY}}(i)}, \qquad (4.6)$$

where i indicates the specific IR7-DS region considered, while STD and CRY stand for standard and crystal system respectively. With this definition, if $LLR_i > 1$ for a certain region i, then the cleaning inefficiency is reduced in that region when crystals are deployed, leading to a performance improvement of the collimation system.

Evaluating the leakage ratio region by region is extremely useful to understand how different settings of the collimation system affect the loss pattern. However, for the purpose of evaluating the performance of the system in view of potential use in operations with ion beams, a more interesting aspect is the global cleaning improvement achieved across the whole IR7-DS. A *global leakage ratio* can be defined:

$$GLR = \frac{\max \eta_c^{\text{STD}}(i)}{\max \eta_c^{\text{CRY}}(i)}. \qquad (4.7)$$

This quantity allows to immediately evaluate the overall improvement provided by crystal collimation over the standard system.

4.1.5   Channeling during Dynamical Phases of the Machine

In order to use crystal collimation during operations at the LHC, the capability to maintain channeling conditions continuously during dynamical phases of the machine, such as the energy ramp, is essential. During these phases, the beam size is naturally reduced as the energy increases (*adiabatic damping*), and collimator settings need to be progressively adjusted in order to follow this change. The beam divergence also decreases with the energy, which means that the orientation of the crystal must also change in order to keep channeling conditions. This is particularly challenging because, as previously described, the angular acceptance of the crystal is defined by the critical angle θ_c, which scales as the inverse of the square root of the beam energy. Tab. 3.1 shows that its value decreases from 9.4 μrad at 450 GeV to 2.5 μrad at 6.5 TeV. It follows that an extremely precise control system is required in order to change the crystal orientation to accommodate the change in beam divergence, while also maintaining channeling conditions with a progressively smaller acceptance.

To operate standard collimators during the ramp and adjust their settings, functions based on an interpolation of key beam-based parameters measured at injection and at flat top, such as the beam position and r.m.s. width [77] are deployed. Crystals can be treated as single-sided primary collimators with the addition of a rotational stage, so a linear and a rotational function need to be used to operate them [11]. Following the approach used for standard collimators, the linear stage function is:

$$x(t) = x_c - \left[n_{inj} + \frac{n_{ft} - n_{inj}}{\gamma_{ft} - \gamma_{inj}}(\gamma(t) - \gamma_{inj}) \right] \left[\tilde{\sigma}_{inj} + \frac{\tilde{\sigma}_{ft} - \tilde{\sigma}_{inj}}{\gamma_{ft} - \gamma_{inj}}(\gamma(t) - \gamma_{inj}) \right] \frac{1}{\sqrt{\gamma(t)}}, \quad (4.8)$$

where n are the settings in units of the beam r.m.s. width, $\tilde{\sigma}$ is the normalized beam r.m.s. width, γ is the relativistic parameter and x_c is the beam position at the crystal location at flat top. It is important to note that the beam position changes during the ramp, and a linear interpolation with the energy is assumed to generate ramp functions for the standard collimators. However, only the estimated beam center at flat top is taken as a reference for the crystal. This choice was justified by two reasons [78]:

- The crystal channeling acceptance is much smaller at flat top due to the dependence of the critical angle on the beam energy. As such, maintaining optimal channeling conditions at the end of the ramp is a much more delicate operation compared to lower energy values.

- For standard collimators, the linear settings are measured from the beam center. However, the zero of the crystal linear stage corresponds to the parking position (i.e. when the device is completely retracted). As a result, the beam center at the crystal location can only be estimated as:

$$x_c = x_{cry} + n_{\sigma,cry}\sigma_{cry}, \quad (4.9)$$

  where $n_{\sigma,cry}$ are the crystal settings determined via the beam-based alignment, and σ_{cry} is the betatronic beam size at the crystal location calculated with the optics functions. The optics in particular is usually more under control at flat top, making this estimate more reliable than at injection.

The dependence of the beam center with the beam energy is partly "absorbed" in a redefinition of the other parameters of the ramp function performed via a script, in order to fix the
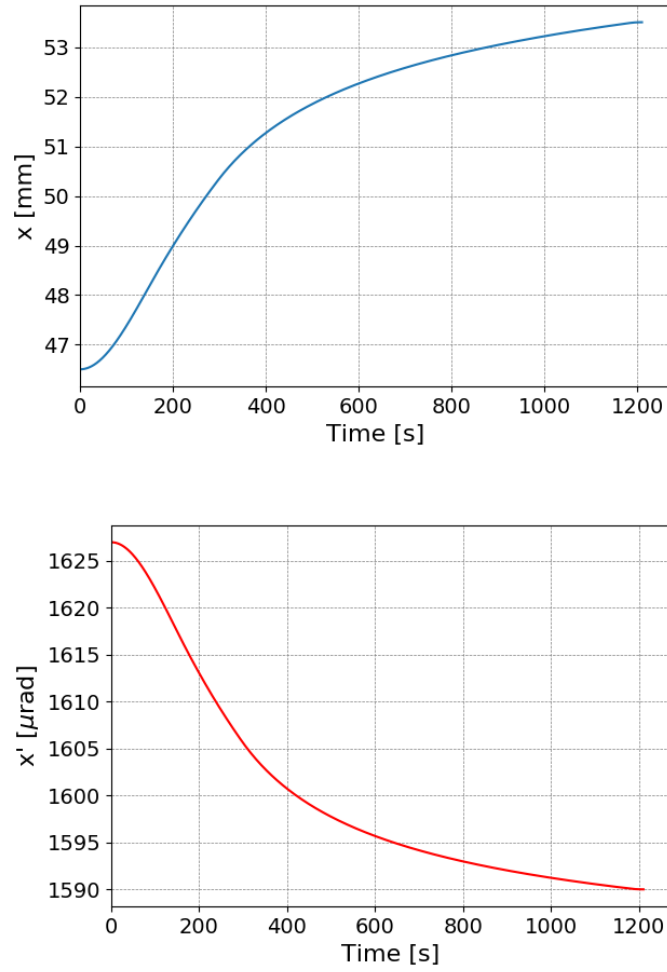
Figure 4.9: Linear (top) and rotational (bottom) ramp functions generated for the horizontal crystal on Beam 1.
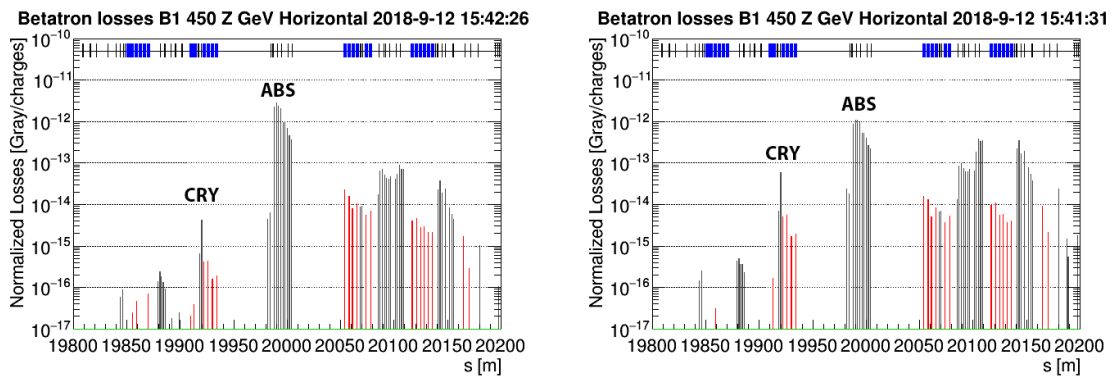

Figure 4.10: Measured loss pattern during an angular scan of the horizontal crystal on Beam 1 with proton beams at 450 GeV. Losses in IR7 are shown when the crystal is oriented in channeling (left) and in amorphous orientation (right). Losses are normalized to the beam flux. The location of the crystal (CRY) and of the secondary collimator used to absorb the channeled halo (ABS) are shown on the plots.

initial and final points to the transverse alignment found during measurements at injection and at flat top respectively. It is however planned to refine this procedure in view of future operational tests.

The same approach can be followed for the angular stage function:

$$x'(t) = x'_{CH} - \left[n_{inj} + \frac{n_{ft} - n_{inj}}{\gamma_{ft} - \gamma_{inj}} (\gamma(t) - \gamma_{inj}) \right] \left[\tilde{\sigma}'_{inj} + \frac{\tilde{\sigma}'_{ft} - \tilde{\sigma}'_{inj}}{\gamma_{ft} - \gamma_{inj}} (\gamma(t) - \gamma_{inj}) \right] \frac{1}{\sqrt{\gamma(t)}} - \delta,$$
(4.10)

where $\tilde{\sigma}'$ is the normalized beam divergence, x'_{CH} is the optimal channeling orientation experimentally found at flat top and δ is the beam divergence at flat top. As discussed above, the orientation at flat top is taken as a reference, and the parameters of the function are adjusted to set the initial and final points to the channeling orientation found in measurements at injection and at flat top respectively. It is worth noting that these formulas are valid for the general case where in principle the settings and optics at the device position are not necessarily the same at the beginning and at the end of the energy ramp. As an example, the ramp functions generated for the horizontal crystal on Beam 1 are shown in Fig. 4.9.

In order to verify if channeling conditions are continuously kept, multiple loss maps are taken as the beam energy increases (typically one every 500 GeV). The ratio between the BLM signal at the crystal and at the absorber of the channeled halo is used as a figure of merit. As shown in Fig. 4.10, if channeling conditions are lost during measurements for any reason, losses increase at the crystal, which is now behaving like a very thin standard collimator, and decrease at the absorber, which is not intercepting any channeled particle anymore. Thus, the BLM signal at these two locations can be used as a figure of merit to determine if channeling conditions are being maintained. In particular, the crystal can be safely assumed to be in optimal channeling if this ratio is lower than the empirically defined value of 10^{-2}, while it is considered in amorphous orientation otherwise [11].

4.2   Summary of Crystal Performance with Proton Beams

Crystal collimation with proton beams has been extensively studied throughout the entirety of Run 2 in Machine Development (MD) sessions. These dedicated runs are carefully planned in specific periods of the LHC operation schedule (usually five days long occurring three or four times a year) to carry out activities aimed at assessing and optimizing the performance of the machine. Due to high demand, beam time allocated to individual studies is often limited. Over the course of three years, a total of 58 hours of MD time were dedicated to crystal collimation studies with proton beams [79–85].

All crystal collimation MDs were performed using the standard machine setup (optics and collimator settings) of the corresponding year [86, 87]. For machine protection reasons, the maximum beam intensity allowed in the machine for these tests was fixed to $3 \cdot 10^{11}$ protons both at injection and at flat top. Nominal bunches (10^{11} protons each) could only be used at injection while still respecting the above mentioned limit. At flat top, filling schemes with up to 30 pilot bunches of abut 10^{10} protons each were used instead.

Single, non-colliding bunches at the LHC are very stable, with a typical lifetime of over 100 hours. Losses naturally produced by such beams would have been too low to carry out the proposed measurements, so the beams are excited by introducing white noise with the ADT to produce controlled losses on crystals and collimators, similarly to what is done during standard collimation loss maps. Since the allowed low-intensity bunches quickly get

consumed during this kind of procedure, the ADT was set to excite three bunches at the same time in order to ensure a steady loss regime for the entire duration of each measurement. The procedure for crystal collimation MDs includes the following steps for each crystal:

1. Beam-based alignment of the crystal to set it at the same aperture as the primary collimator on the corresponding plane.

2. Opening all collimators upstream the crystal and all collimators located between the crystal and the secondary used to absorb the channeled halo.

3. Angular scan to find the optimal channeling orientation.

4. Linear scan of the channeled beam with a secondary collimator, while the crystal is kept in optimal channeling.

5. Other activities depending on the scope of the MD and on time constraints (loss maps to compare the performance of standard and crystal collimation, channeling during the energy ramp, etc.).

The first step is performed following the procedure described in Sec. 4.1.1. After the crystal has been set as the primary stage of the collimation system, its position in mm can be measured for reference in future tests.

In the second step, the above mentioned collimators are retracted to their respective parking positions, in order to remove any possible source of perturbation that could hide the signature features of the coherent interactions of beam halo particles with crystal collimators. This procedure is allowed by the limited beam intensity allowed during these tests, which ensures the safety of the equipment even in such an unusual configuration.

The other steps have already been described in detail in Sec. 4.1. The methods used to carry out these measurement have been developed and defined after years of experience since the first installation of crystal collimators in the LHC in 2015 [11].

### 4.2.1   Characterization of Crystal Devices with Proton Beams

Thanks to the experience gathered over the years and to the high precision of the goniometers, the angular scans allowed to identify the optimal channeling orientation very efficiently for all crystals, including the newly installed one. Fig. 4.11 and 4.12 show the measured BLM signal (normalized to the beam flux and to the amorphous level) as a function of the angular orientation (expressed as the *yaw angle* read by the goniometer) for the four crystals, at injection and flat top respectively. In each plot, both the dip corresponding to the optimal channeling orientation and the volume reflection plateau can be clearly seen. The reference optimal channeling orientation and the reduction factor of local losses at the crystal location are reported in Tab. 4.1. Due to time constraints, only a fast angular scan could be performed for the vertical crystal on Beam 2 at injection, and as a result the uncertainty on the reduction factor calculated for this case is particularly large. The performance of the horizontal crystal on Beam 2 was of particular interested during 2018 tests, since this device was changed for a new one during at the end of 2017 (as shown in Tab. 3.2). The original device presented a problematic behavior shown in Fig. 4.13. The peculiar shape of this profile was attributed to the effect of the axial orientation of the crystal. In this condition, particles can be channeled by the so-called *skew planes* of the crystalline lattice, which present themselves as additional, smaller wells located symmetrically around the main planar channeling dip [11]. This issue made finding the optimal channeling orientation for this crystal particularly challenging, and could not be solved by changing the crystal orientation

Table 4.1: Measured reduction factor of local losses, optimal channeling orientation, bending angle and multiturn channeling efficiency for all four crystals, both at injection (450 GeV) and at flat top (6.5 TeV) for proton beams. Values marked with * correspond to measurements that could not be performed in 2018 due to time constraints, and are taken from earlier tests [78]. All other values are taken from 2018 measurements.
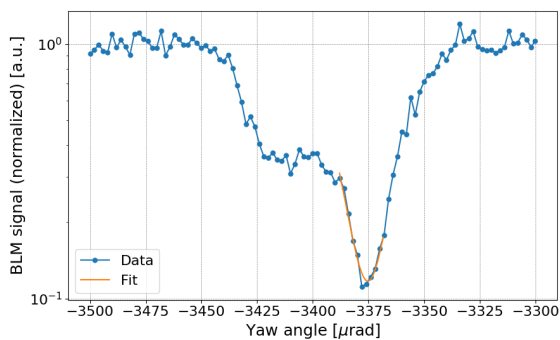
	Reduction factor		Optimal channeling orientation [μrad]		Bending angle [μrad]		Multiturn CH efficiency	
	Inj	FT	Inj	FT	Inj	FT	Inj	FT
B1H	20.9 ± 1.7	13.8 ± 2.3	1627.5 ± 0.3	1590.2 ± 0.1	57.7 ± 5	61.6 ± 5	$97 \pm 5\%$	$29 \pm 2\%$
B1V	10.6 ± 1.1	24.8 ± 1.9	2649.4 ± 0.2	2599.6 ± 0.1	$39.8 \pm 2.3^*$	38.4 ± 5	$87 \pm 5\%^*$	$85 \pm 4\%$
B2H	8.7 ± 0.4	22.7 ± 1.8	-3375.3 ± 0.3	-3467.2 ± 0.1	43.2 ± 5	33.5 ± 5	$86 \pm 4\%$	$74 \pm 4\%$
B2V	12.1 ± 7.0	11.2 ± 3.8	-6.3 ± 0.2	-52.9 ± 0.2	$56.5 \pm 1.8^*$	55.2 ± 5	$83 \pm 5\%^*$	$81 \pm 4\%$
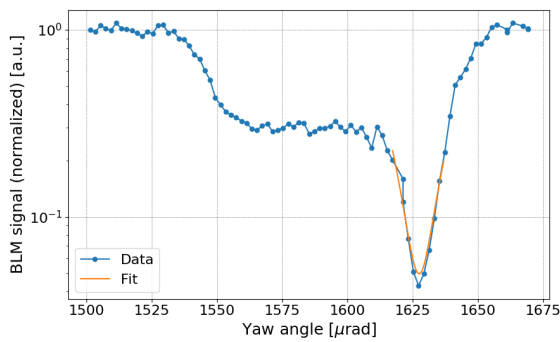
(a) B1H.
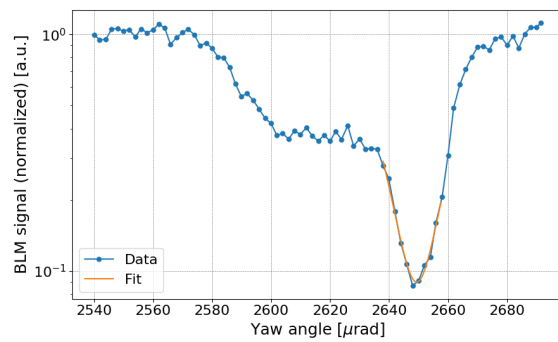
(b) B1V.

(c) B2H.

(d) B2V.

Figure 4.11: Angular scans performed with proton beams at 450 GeV. The BLM signal has been normalized to the flux of lost particles and to the amorphous level.
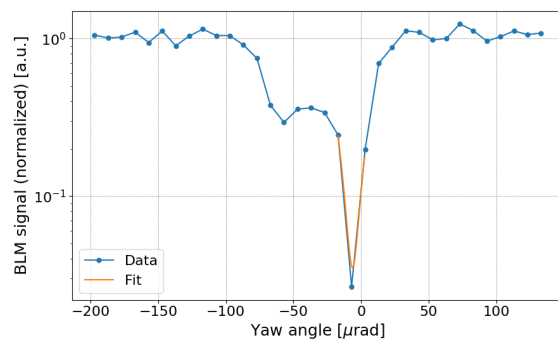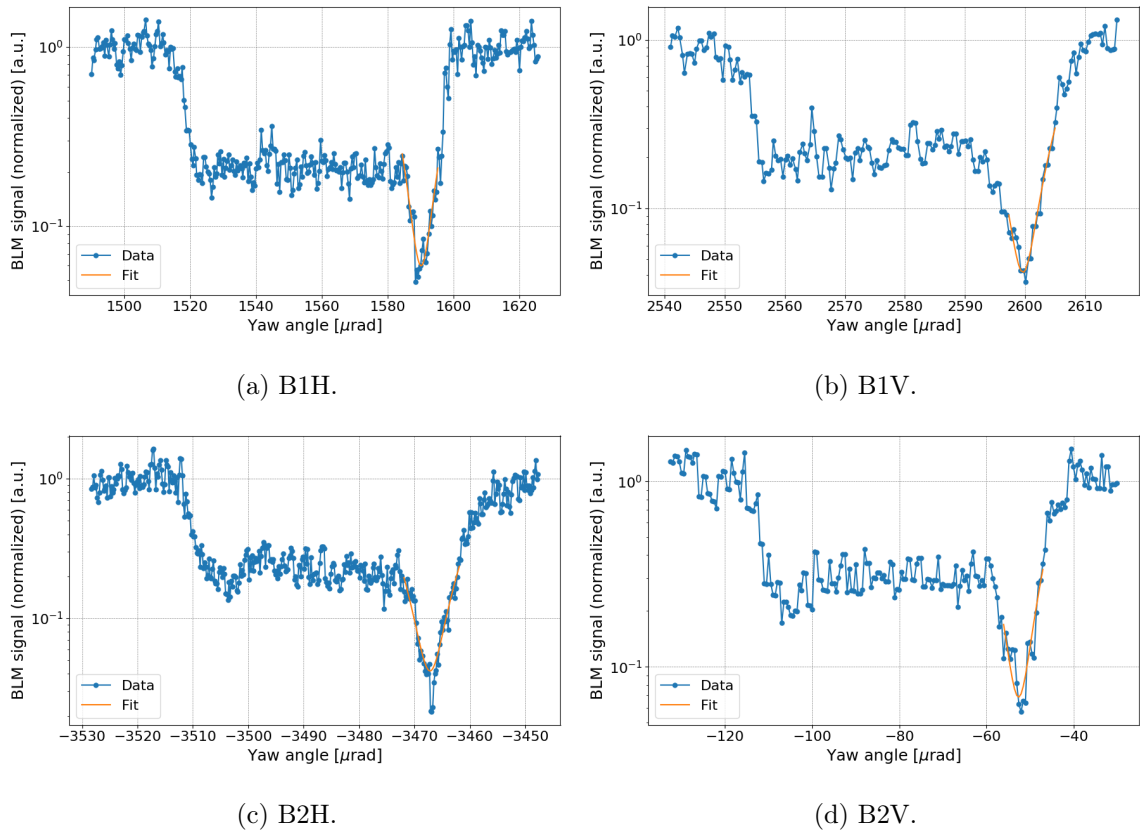
(a) B1H.

(b) B1V.

(c) B2H.

(d) B2V.

Figure 4.12: Angular scans performed with proton beams at 6.5 TeV. The BLM signal has been normalized to the flux of lost particles and to the amorphous level.
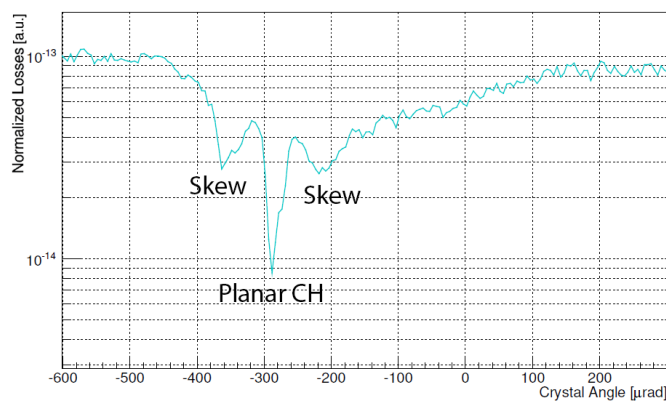

Figure 4.13: Angular scan performed with the horizontal crystal on Beam 2 before it was replaced [11]. The BLM signal has been normalized to the flux of lost particles. The additional wells caused by the effect of the skew planes are visible on the left and right side of the planar channeling well.
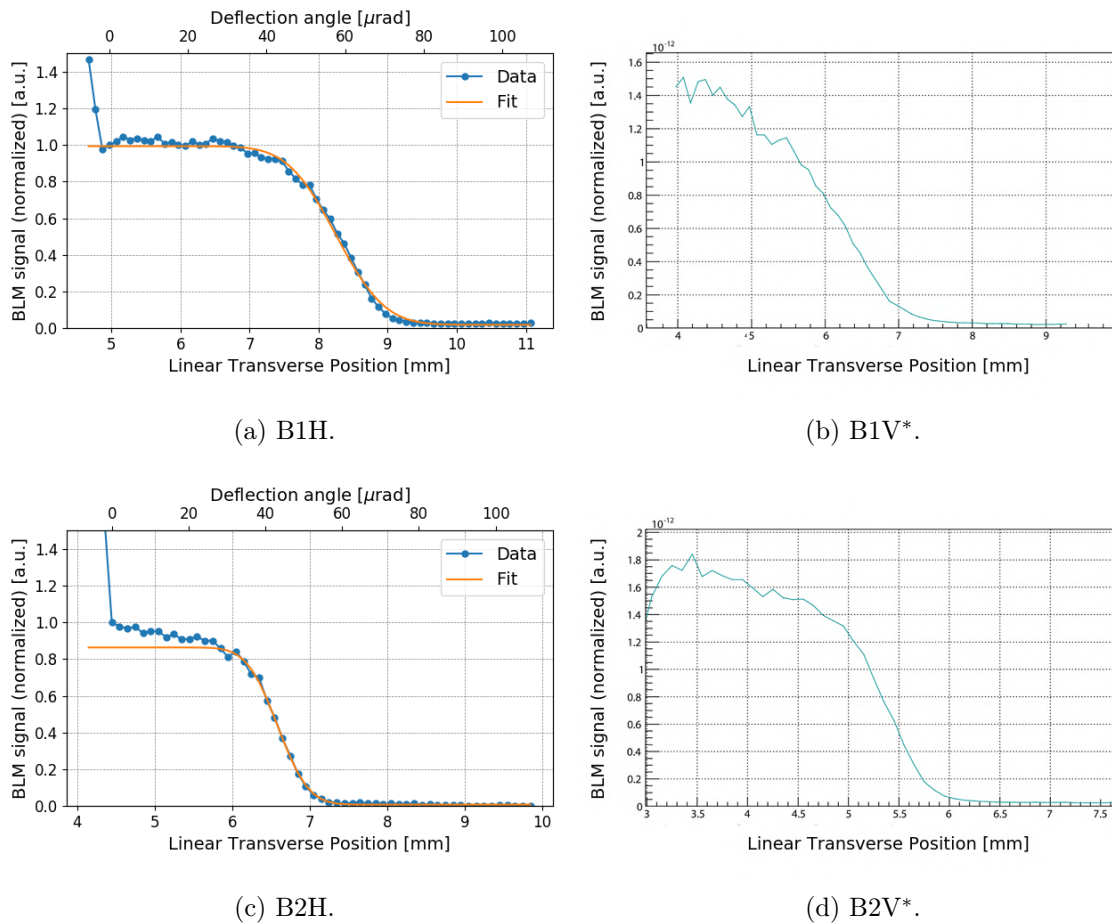
(a) B1H.

(b) B1V*.

(c) B2H.

(d) B2V*.

Figure 4.14: Linear scans performed with proton beams at 450 GeV. The BLM signal has been normalized to the flux of lost particles and to the signal recorded when touching the primary beam. The error function fit used to estimate the bending angle and the channeling efficiency is shown as an orange line. Scans marked with * correspond to measurements that could not be performed in 2018 due to time constraints, and are taken from earlier tests [78]. For these, only the BLM signal normalized to the flux of lost particles is shown.

remotely. As such it was decided to replace the entire device with a new one which, as expected, did not show the same features.

The linear scans were used to measure the channeling efficiency as well as the effective bending angle of each crystal. The recorded BLM signal (normalized to the value corresponding to the point when the primary beam is hit) as a function of the transverse position of the moving secondary collimator is shown in Fig. 4.14 and 4.15 for injection and flat top respectively. The results are summarized in Tab. 4.1. The first observation is the significant difference in the profile at injection and flat top for the Beam 1 horizontal crystal. This was already observed in previous measurements at the LHC [11] and is primarily due to the fact that the bending angle of this crystal does not respect the required specifics of 50 μrad due to an instability of the holder. The actual bending angle is of $\sim$63 μrad, which for a 4 mm long crystal corresponds to a bending radius of $\sim$63.5 m. This value is only about four times larger than the critical radius at flat top energy, which may lead to an increase in the probability of dechanneling and a reduction of the channeling efficiency. Dechanneled particles experience a lower effective deflection and this can be seen in the profile as a continuous rise
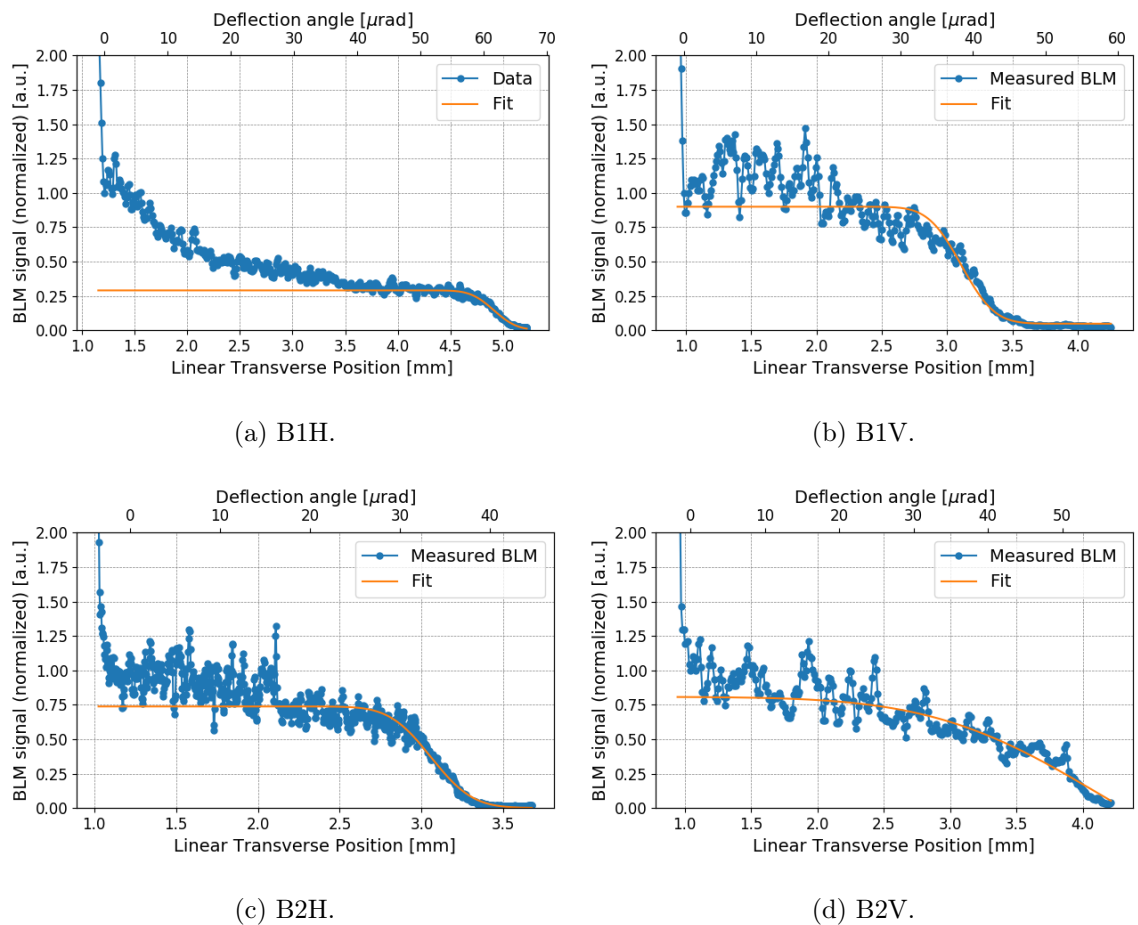
(a) B1H.

(b) B1V.

(c) B2H.

(d) B2V.

Figure 4.15: Linear scans performed with proton beams at 6.5 TeV. The BLM signal has been normalized to the flux of lost particles and to the signal recorded when touching the primary beam. The error function fit used to estimate the bending angle and the channeling efficiency is shown as an orange line.

of the signal when the absorber moves beyond the location of the channeled beam. On the other hand, this issue does not manifest itself at injection because the critical radius scales with the energy, putting the crystal outside of this problematic situation at 450 GeV. Furthermore, the measured bending angle for the Beam 2 horizontal crystal is not only smaller than the required specifics, but is also significantly different between injection and flat top. It is speculated that both these effects could be at least partly caused by a misalignment between the crystal entrance face and the crystalline planes (a so-called *miscut angle*), to be verified in dedicated simulations. The implementation of the treatment of these effects in simulations is described in detail in Chap. 6.

4.2.2 Halo Cleaning Measurements with Proton Beams

The evaluation of beam cleaning efficiency through loss maps focused mainly on flat top energy, since it is the most constraining condition for LHC operations. Various settings of the downstream secondary collimators and absorbers were tested, in order to compare different kinds of setup to intercept the channeled halo particles. The settings of all relevant collimators are reported in Tab. 4.2, while the standard configuration was maintained for

Table 4.2: IR7 collimators positions (in units of the beam r.m.s. width σ) used for loss map measurements with proton beams at 6.5 TeV during MD tests.

Configuration	Standard	Crystal		
	Nominal	1	2	3
TCPs	5.0	Out	Out	Out
Upstream TCSGs	6.5	Out	Out	Out
Crystal	Out	5.0	5.0	5.0
Downstream TCSGs	6.5	6.5	6.5	6.5
TCLAs	10.0	10.0	8.0	6.5

(a) B1H
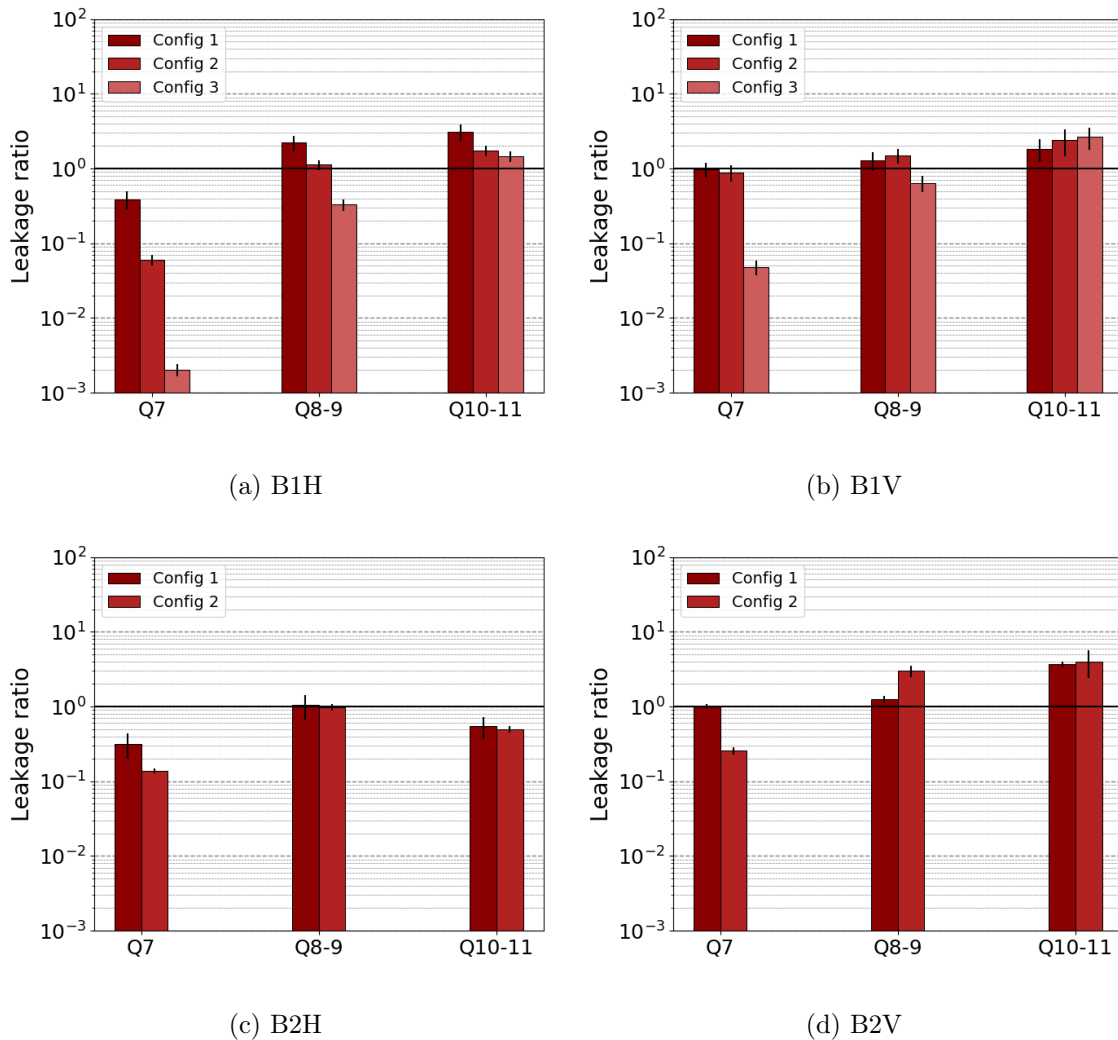
(b) B1V

(c) B2H

(d) B2V

Figure 4.16: Local leakage ratio measured with proton beams at 6.5 TeV. The standard system in the nominal configuration is compared to the crystal system in configurations 1-3 (see Tab. 4.2). Only configurations 1 and 2 could be tested for Beam 2 because of a beam dump that prevented further measurements.

the rest of the collimation system.

Loss maps were performed in each configuration both with the standard and crystal collimation system, and the cleaning inefficiency in the IR7-DS region was compared. Only the first three areas of the IR7-DS region are considered in the analysis, since the Q12-13 area is only relevant for operations with ion beams. The resulting values of local leakage ratio are shown in Fig. 4.16. A clear improvement in the Q8-9 and Q10-11 regions can be seen on Beam 1, while results for Beam 2 are not as conclusive. The measurements of cleaning inefficiency were affected by a trip of an orbit corrector (as described in Sec. 4.2.3), which nearly caused a beam dump at flat top because of large closed orbit errors. The orbit on the horizontal plane of Beam 2 was corrected at best to its references, but not optimally. This might explain why the crystal system on this plane shows a worse performance than what was measured for Beam 1. It is noted that no other measurements are available for this specific crystal with proton beams, as it was installed in 2018 and further measurements were only carried out with Pb ion beams. Further tests with proton beams are however planned to take place during Run 3.

It is important to note that the Q7 region consistently shows a worsening of the cleaning inefficiency when crystals are deployed. The current working hypothesis attributes this behavior to showers coming from upstream collimators and is currently under study via energy deposition simulations, which are beyond the scope of this thesis.

4.2.3 Crystal Channeling during the LHC Energy Ramp

The first attempt at deploying crystal collimation during the LHC energy ramp took place in a dedicated MD in 2016 [11]. During that test, it was demonstrated that the horizontal crystal could successfully be kept in channeling conditions for the entire time using ramp functions generated following the procedure described in Sec. 4.2.3.
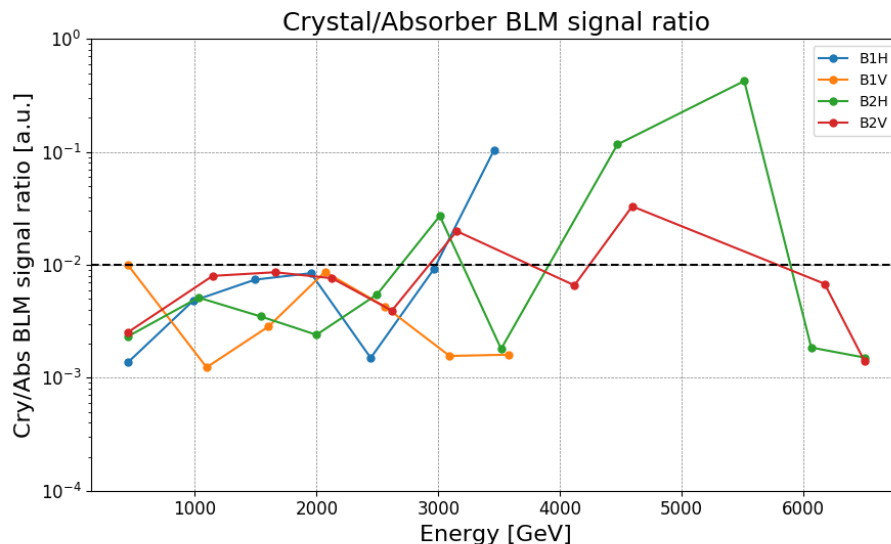

Figure 4.17: Ratio between losses at each crystal and at the corresponding absorber measured during the energy ramp.

2018 marked the first attempt at maintaining all four crystals in channeling orientation at the same time during the energy ramp. Loss maps were taken roughly every 500 GeV for all beams and planes, and the ratio between BLM signals recorded at the crystal and at

the absorber was used to assess if channeling conditions were being kept. Unfortunately, a trip of the orbit corrector magnets about halfway through the ramp altered the orbit of the beams. From this point on, the position of the beams became difficult to predict and could not be accurately followed with the previously generated ramp functions. As a result, measurements performed during the second half of the ramp were unreliable. Nonetheless, the results in Fig. 4.17 show that the ratio stayed well under 10^{-2} for all four crystals for the first half of the ramp, indicating that channeling conditions were kept up until that point. Furthermore, the crystals were correctly in channeling once flat top energy was reached. This is due to the fact that the trip of the corrector only affected the compensation of orbit drifts during the ramp, while in stable conditions the reference orbit could be kept by the feedback. As a result, the reference positions and angular orientations for optimal channeling at flat top were still valid after the ramp.

This is a very promising result considering the complexity of the setup, which requires a control system of extremely high precision.

Chapter 5

Demonstration of Cleaning Improvement for Pb Ion Beams

As part of the upgrade of the collimation system for HL-LHC, new 11 T dipoles will be installed in the IR7-DS region. This improvement will allow the machine to withstand losses generated by the beams of progressively increasing intensity that will be delivered at the LHC over the course of Run 3. Proton beams are not expected to pose significant challenges during the first year of Run 3. Heavy ion beams, on the other hand, are much more delicate to handle, since losses generated by them were already close to quench limit during the final year of Run 2. Collisions of high-intensity ion beams are planned to take advantage of the upgrade of the ALICE experiment. For this reason, the improvement of the collimation system is crucial to guarantee safe operations with ions during the first year of Run 3.

As mentioned in Chap. 4, crystal collimation cannot be deployed during LHC operations with proton beams due to the lack of a special absorber capable of safely intercepting the channeled beam halo and withstanding the expected peak power deposition of 1 MW over a few mm^2. However, this is not the case for heavy ion beams. Numerical studies show that the present collimators can be safely used to dispose of channeled particles even in accidental scenarios with heavy ion beams of high energy and intensity, where a peak power deposition below 1 kW/cm^3 and a total beam loss power of 28.5 kW is expected for Pb ion beams with a lifetime of 12 minutes [60]. This allows to use the jaw of a TCSG to intercept halo particles, much like what is currently done in tests with low-intensity beams. For this reason, crystal collimation was considered to be integrated in the HL-LHC upgrade baseline in order to cope with potential schedule issues with the production of the 11 T dipoles. Extensive studies with ion beams have been carried out over the years in order to assess the performance of this advanced collimation scheme.

After giving an overview of the activities carried out in this context since the first installation of crystal collimators in the LHC in 2015, this chapter mainly focuses on the results gathered during crystal collimation tests with Pb ion beams in 2018. In particular, the two main milestones achieved in these studies are reported:

- The first demonstration of improved beam halo cleaning with Pb ion beams.

- The first use and validation of crystal collimation with high-intensity Pb ion beams during the intensity ramp-up.

Finally, settings for potential use of crystal collimation in operations are discussed. Thanks to these promising results, crystal collimation has been officially included in the HL-LHC upgrade baseline program [56].

5.1   Overview of Crystal Collimation Studies with Ion Beams

Over the course of the years, 34 hours of total MD time were dedicated to crystal collimation studies with ion beams [11, 88–90]. Crystal channeling was observed for the first time with Pb ion beams in 2016, with a setup that included only two crystals, one for each plane of Beam 1. However, only a handful of IR7 collimator configurations could be explored, and cleaning measurements did not show a clear improvement with respect to the standard system [11]. Following the installation of two additional crystals on Beam 2, a fully realized crystal collimation system was deployed for the first time in 2017, during the special run with Xe ion beams [91]. Much more promising results were gathered in this occasion, and a clear reduction of IR7-DS losses could be observed using a number of different arrangements of collimator settings that allowed to improve the performance of the system compared to previous measurements [11]. In all cases, only low-intensity beams could be used for machine protection reasons.

The 2018 ion run was crucial, as it was the first time the full system could be tested with Pb ion beams, and the last opportunity to assess its performance before LS2 and the final decision on the use of crystal collimation in Run 3. 12 hours of MD time were used to fully characterize the four crystal devices with Pb ion beams and perform cleaning measurements with configurations similar to those tested with Xe ion beams the previous year. Finally, the 2018 intensity ramp-up offered the chance to deploy crystal collimation for the first time with high-intensity Pb ion beams (up to 648 circulating bunches), allowing to verify the stability of the system in these challenging conditions as well as explore and define operational settings for potential use in Run 3.

5.2   Crystal Cleaning Performance with Pb Ion Beams

Crystal collimation tests with low-intensity Pb ion beams were carried out in dedicated MD sessions, following a similar program to activities with proton beams:

1. Beam-based alignment of all four crystals.

2. Opening of primary collimators and all secondary collimators located between each crystal and the corresponding absorber.

3. Angular and linear scans to characterize each device both at injection and flat top energy ($450Z$ GeV and $6.37Z$ TeV respectively, where Z is the atomic number of the ion species used).

4. Loss maps with varying collimator settings for cleaning measurements at flat top.

All these measurements are performed using the standard machine configuration for the 2018 ion run [87, 92]. The settings of the standard collimation system, carefully optimized during dedicated commissioning activities, are reported in Tab. 5.1. The results gathered during these activities are described in detail in the following sections.

### 5.2.1   Multiturn Crystal Performance

Angular (Fig. 5.1 and 5.2) and linear (Fig. 5.3 and 5.4) scans were performed for all crystals both at injection and at flat top, allowing for the first time a complete and comprehensive characterization with Pb ion beams. The measured reduction factor of local losses, optimal channeling orientation, bending angle and multiturn channeling efficiency are reported in

Table 5.1: 2018 ion run collimator settings for a normalized emittance of $\varepsilon_n = 3.5\ \mu$m. L and R indicate the left and right jaw respectively [87].

| Collimator	Beam	IR	Injection	FT (β*=1 m)	Physics (β*=50 cm)
TCPs/TCSGs/TCLAs	B1	7	5.7/6.7/10	5.5(L)-5.0(R)/6.5/10	5.5(L)-5.0(R)/6.5/10
TCPs/TCSGs/TCLAs	B2	7	5.7/6.7/10	5/6.5/10	5/6.5/10
TCPs/TCSGs/TCLAs	B1/2	3	8/9.3/10	15/18/20	15/18/20
Horizontal TCTs	B1	1/2/5	13	15/15/15	11/9/9
Horizontal TCTs	B2	1/2/5	13	15/15/15	9/9/9
Vertical TCTs	B1/2	1/2/5	13	15/15/15	9/9/9
TCTs	B1/2	8	13	15	15
TCDQ	B1/2	6	8	7.4	7.4
TCSP	B1	6	7	7.4	7.4
TCSP	B2	6	7	7.4	7.4(L)-11.2(R)
TCL.4/5/6	B1/2	1/5	OUT	OUT	15/15/OUT
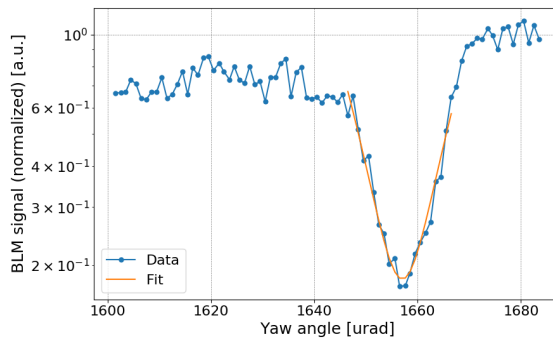
(a) B1H
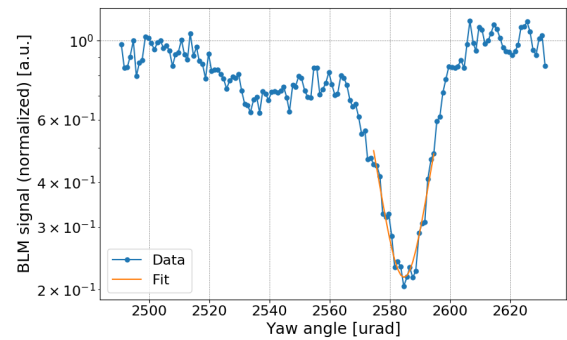
(b) B1V
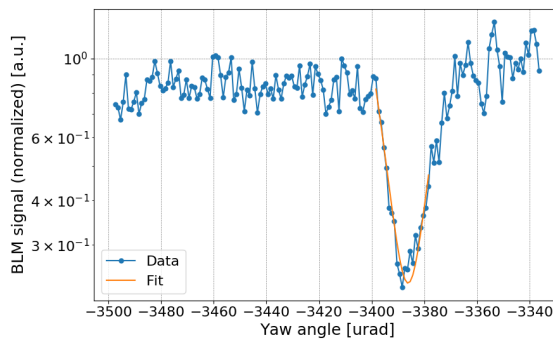
(c) B2H
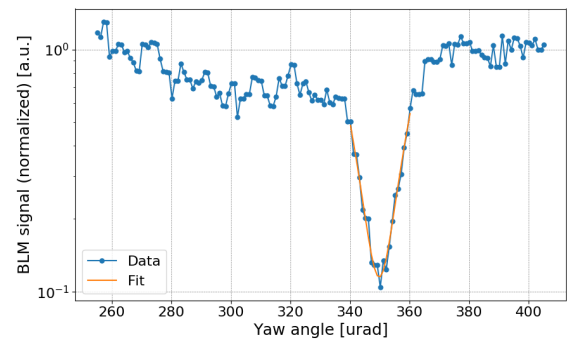
(d) B2V

Figure 5.1: Angular scans at $450Z$ GeV performed during MD tests with Pb ion beams. The BLM signal has been normalized to the particle flux and to the amorphous level.
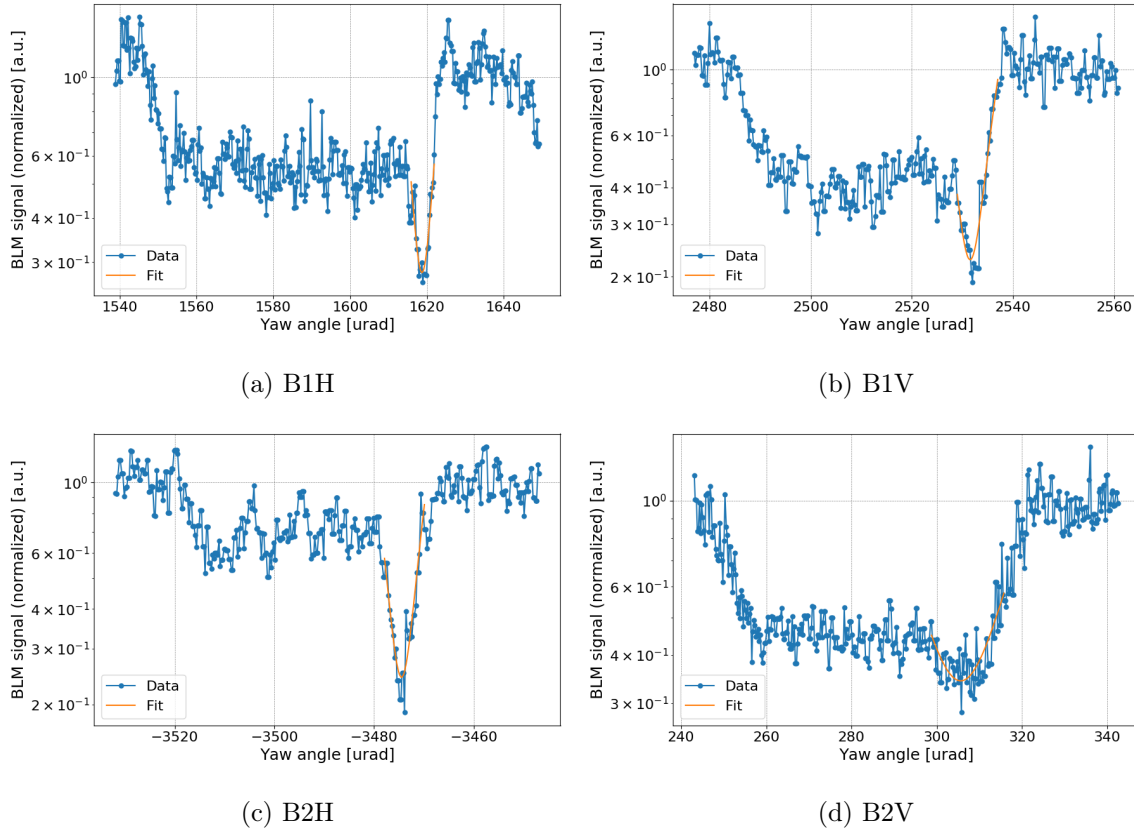
(a) B1H

(b) B1V

(c) B2H

(d) B2V

Figure 5.2: Angular scans at $6.37Z$ TeV performed during MD tests with Pb ion beams. The BLM signal has been normalized to the particle flux and to the amorphous level.

Table 5.2: Measured reduction factor of local losses, optimal channeling orientation, bending angle and multiturn channeling efficiency for all four crystals, both at injection and at flat top energy for Pb ion beams.

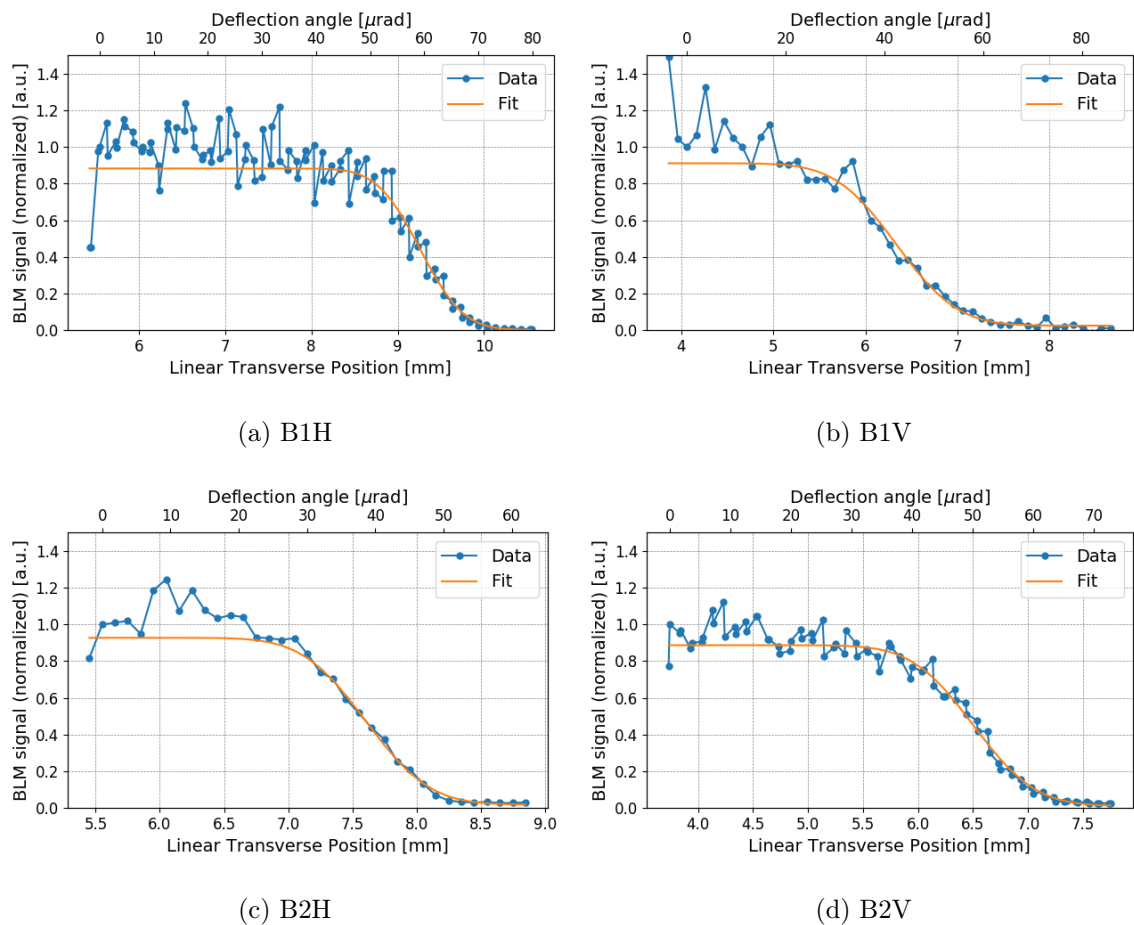|	Reduction factor		Optimal channeling orientation [μrad]		Bending angle [μrad]		Multiturn CH efficiency	
	Inj	FT	Inj	FT	Inj	FT	Inj	FT
B1H	5.4 ± 0.5	3.5 ± 0.2	1657.0 ± 0.2	1618.7 ± 0.1	64.7 ± 5	64.5 ± 5	$88 \pm 4\%$	$17 \pm 1\%$
B1V	4.6 ± 0.3	4.3 ± 0.4	2584.7 ± 0.2	2531.5 ± 0.1	45.7 ± 5	40.9 ± 5	$90 \pm 5\%$	$82 \pm 4\%$
B2H	3.7 ± 0.2	4.5 ± 0.5	-3386.2 ± 0.2	-3474.5 ± 0.2	41.8 ± 5	36.4 ± 5	$93 \pm 5\%$	$91 \pm 5\%$
B2V	8.2 ± 0.1	2.9 ± 0.5	349.8 ± 0.1	305.6 ± 0.4	54.3 ± 5	53.1 ± 5	$89 \pm 5\%$	$85 \pm 4\%$

(a) B1H

(b) B1V

(c) B2H

(d) B2V

Figure 5.3: Linear scans at $450Z$ GeV performed during MD tests with Pb ion beams. The BLM signal has been normalized to the particle flux and fitted with an error function to derive the bending angle of each crystal.

Tab. 5.2. These values are extremely useful references to verify the stability of the crystal devices and the reproducibility of the results.

They key features highlighted by these measurements are consistent with what was observed with proton beams. In particular, all crystals show an excellent multiturn channeling efficiency of more than 80%. The only exception is the horizontal crystal on Beam 1, for which a significant reduction is observed when going from injection to flat top. As already mentioned in Sec. 4.2.1, this peculiar behavior is believed to be related to the large bending angle of this crystal, which may increase the probability of dechanneling at high energy values. The possibility of this feature being linked to a miscut angle between the crystalline planes and the entrance face of the crystal will be explored in simulations as a follow up of this thesis work. More details are mentioned in Chap. 6.

The measured bending angle of the horizontal crystal on Beam 2 appears to be smaller at flat top than at injection. Qualitatively, a similar effect was observed in measurements with proton beams (see Sec. 4.2.1), although for Pb ion beams the difference is significantly smaller. This behavior is currently being investigated, as the available data do not allow to reach a conclusion.
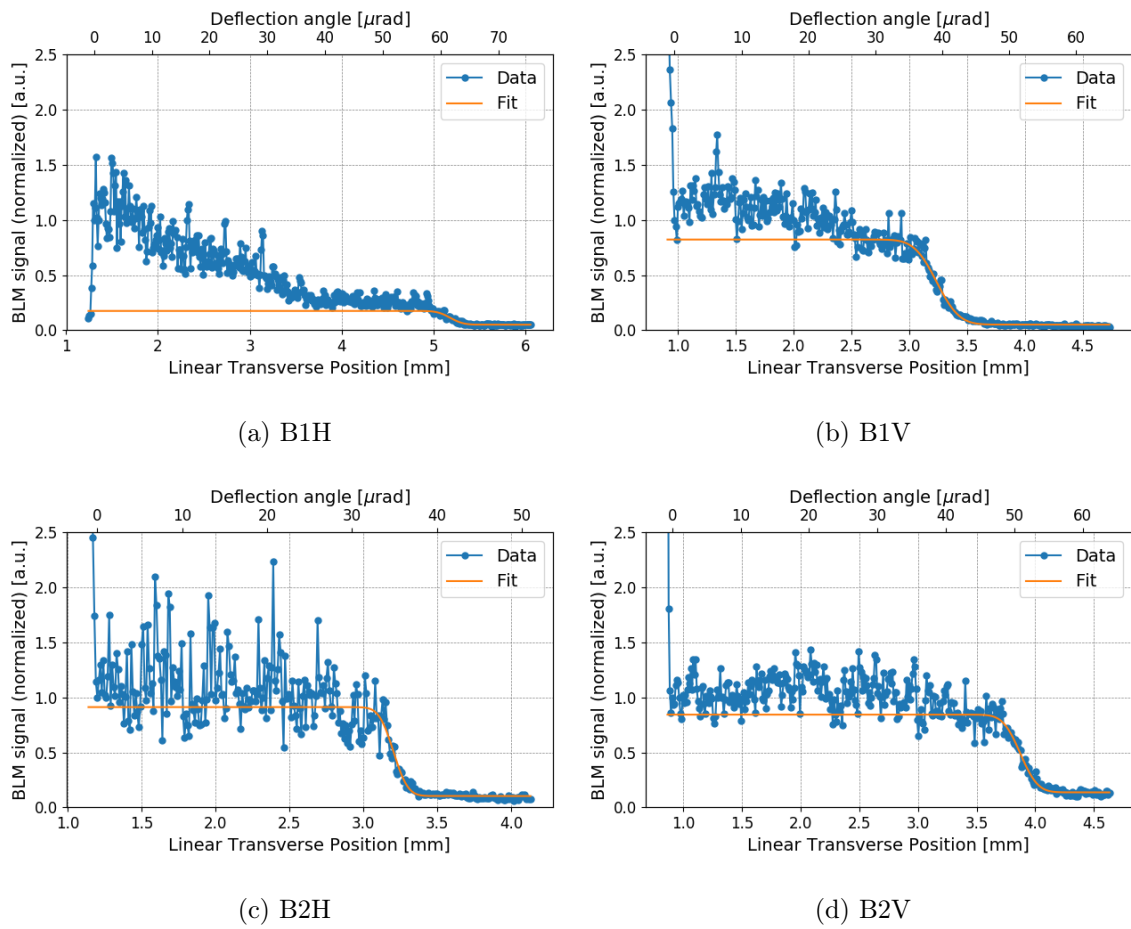
(a) B1H

(b) B1V

(c) B2H

(d) B2V

Figure 5.4: Linear scans at $6.37Z$ TeV performed during MD tests with Pb ion beams. The BLM signal has been normalized to the particle flux and fitted with an error function to derive the bending angle of each crystal.

5.2.2 Collimation Cleaning Measurements

An extensive campaign of loss maps was carried out at flat top energy in order to compare the cleaning performance of the standard and crystal collimation system with different IR7 collimator settings, reported in Tab. 5.3 and 5.4 respectively. In particular:

1. Configuration 1, also referred to as *nominal* for the standard system, is the "base" configuration used as a starting point for cleaning measurements both in MDs and in operational tests.

2. Configuration 2-4 are obtained from configuration 1 by setting the TCLAs at progressively tighter apertures (from 9 to 7 σ).

3. Configurations 5-8 are obtained from configuration 1 by setting the TCLAs and the TCSGs downstream the absorber of the channeled beam at the same aperture, which is then progressively reduced (from 9 to 6 σ).

Table 5.3: IR7 collimator positions (in units of the beam r.m.s. σ) used for flat top loss map measurements with Pb ion beams for the standard collimation system during MD tests. Configuration 1 is also referred to as the *nominal* configuration.

Configuration	1	2	3	4	5	6	7	8
TCPs	5.0	5.0	5.0	5.0	5.0	5.0	5.0	5.0
Upstream TCSGs	6.5	6.5	6.5	6.5	6.5	6.5	6.5	6.5
Crystal	Out	Out	Out	Out	Out	Out	Out	Out
Downstream TCSGs	6.5	6.5	6.5	6.5	9.0	8.0	7.0	6.0
TCLAs	10.0	9.0	8.0	7.0	9.0	8.0	7.0	6.0

Table 5.4: IR7 collimator positions (in units of the beam r.m.s. σ) used for flat top loss map measurements with Pb ion beams for the crystal collimation system during MD tests.

Configuration	1	2	3	4	5	6	7	8
TCPs	Out	Out	Out	Out	Out	Out	Out	Out
Upstream TCSGs	Out	Out	Out	Out	Out	Out	Out	Out
Crystal	5.0	5.0	5.0	5.0	5.0	5.0	5.0	5.0
Downstream TCSGs	6.5	6.5	6.5	6.5	9.0	8.0	7.0	6.0
TCLAs	10.0	9.0	8.0	7.0	9.0	8.0	7.0	6.0

These are the same configurations that were explored in 2017 during crystal collimation tests with Xe ion beams, in order to verify if the settings of downstream collimators can affect and further improve the cleaning efficiency of the system [11]. In particular, it is speculated that tighter settings of the TCLAs allow to better intercept off-momentum particles generated in the interaction of the channeled beam with the secondary collimators, disposing of them before they are lost in the first dispersive area (Q8-9). Reducing the aperture of the downstream TCSGs, on the other hand, should allow to catch fragments produced at the crystal location before they generate losses at the second dispersive peak (Q10-11). This is of particular interest for the Beam 1 horizontal crystal, since its large bending angle
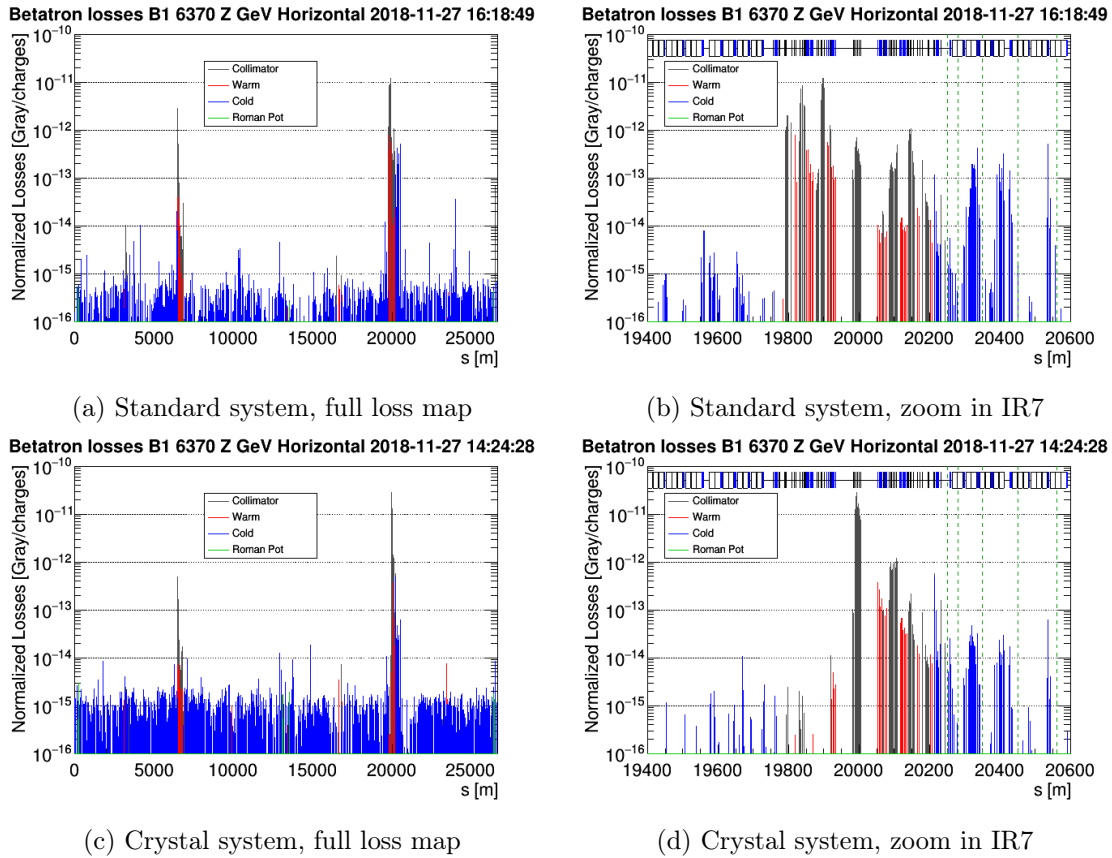
(a) Standard system, full loss map

(b) Standard system, zoom in IR7

(c) Crystal system, full loss map

(d) Crystal system, zoom in IR7

Figure 5.5: Beam 1 horizontal loss maps performed at $6.37Z$ TeV with the standard (top) and crystal (bottom) collimation system respectively during MD studies. The BLM signal is normalized to the flux of lost particles. The four regions in which the IR7-DS area is divided are delimited by green dashed lines. Losses observed in Q6 when crystals are deployed are not considered to be at risk of quench, as discussed in Sec. 4.1.4.

may lead to an increased population of dechanneled particles at low deflection angles. Testing these configurations with Pb ion beams is extremely useful to find the conditions that maximize the performance of the crystal collimation system, and define suitable settings for operations.

Loss maps are performed with the standard and crystal collimation system in the same configuration, and the cleaning inefficiency is compared by calculating the local leakage ratio defined in Eq. 4.6 for each region of the IR7-DS. As opposed to proton beams, for ion beams the Q12-13 region is also considered. As an example, Beam 1 horizontal loss maps for the two systems in configuration 1 are shown in Fig 5.5. This comparison already shows a generally cleaner pattern when crystal collimation is used, with reduced losses in various locations of the machine.

Fig. 5.6 and 5.7 show the measured local leakage ratio for the tested configurations. Overall, the cleaning inefficiency is clearly improved by all crystals. In particular, the horizontal crystal of Beam 1 is able to reduce losses in the IR7-DS by a factor ∼10. The horizontal crystal of Beam 2 shows a slightly lower gain in the Q8-9 and Q10-11 regions, but the leakage ratio reaches ∼100 in the Q12-13 regions, indicating a very effective reduction of the highest loss peak usually observed in standard operations with Pb ion beams. Both vertical crystals show lower local gains compared to the horizontal crystal on the same beam. A possible
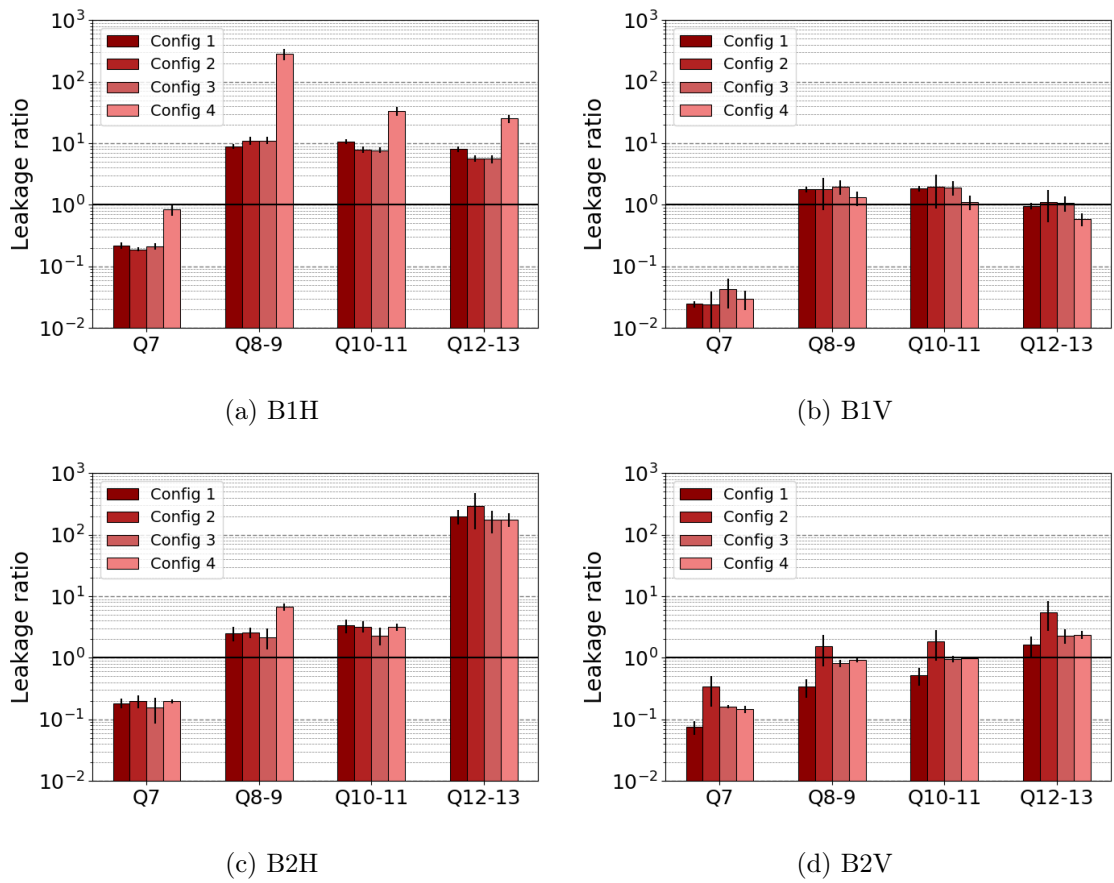
Figure 5.6: Local leakage ratio measured in the IR7-DS during MD tests with Pb ion beams at $6.37Z$ TeV. The standard system in configurations 1-4 is compared to the crystal system with the same configurations of downstream collimators (see Tab. 5.3 and 5.4 respectively).
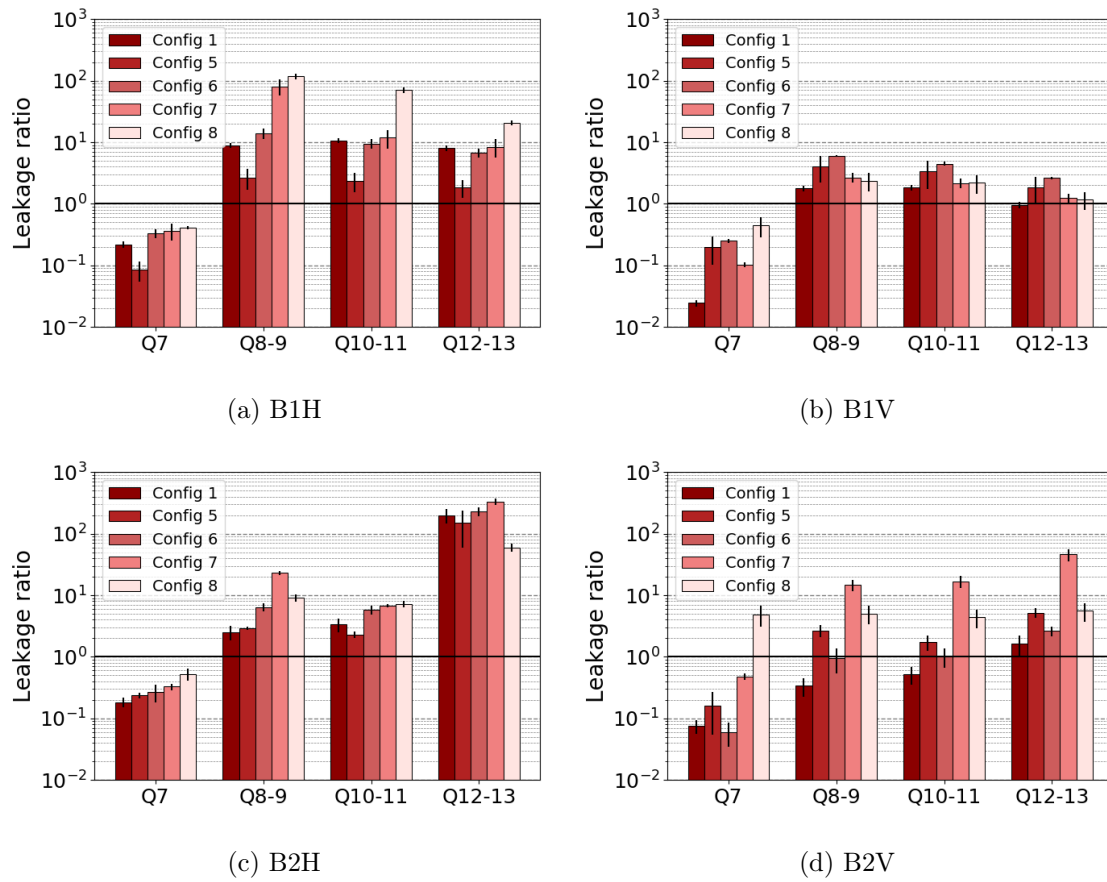
(a) B1H

(b) B1V

(c) B2H

(d) B2V

Figure 5.7: Local leakage ratio measured in the IR7-DS during MD tests with Pb ion beams at $6.37Z$ TeV. The standard system in configurations 1 and 5-8 is compared to the crystal system with the same configurations of downstream collimators (see Tab. 5.3 and 5.4 respectively).

explanation is given by the different production technologies, since strip crystals are installed on the horizontal plane and quasi-mosaic crystals on the vertical plane of both beams. In quasi-mosaic crystals, the potential wells between crystalline planes do not have all the same width and depth, as shown in Fig. 3.12. This is not an issue for protons, which are small enough to be well captured and deflected in any case. When the larger Pb ions are channeled by the smallest wells, however, the probability of nuclear interactions is much higher than for protons, generating higher losses [11, 16]. This hypothesis needs to be verified in dedicated simulations. However, different arrangements of downstream collimators can mitigate this and improve the performance of the vertical crystals.

A common feature of all beams and planes is the increase in losses recorded at the Q7 location. As previously mentioned, leakage in this area cannot be caused by off-momentum losses, as particles escaping the crystal have yet to experience any diffusion. The current working hypothesis attributes this behavior to showers coming from upstream collimators, to be verified with extensive simulations that are beyond of the scope of this thesis.
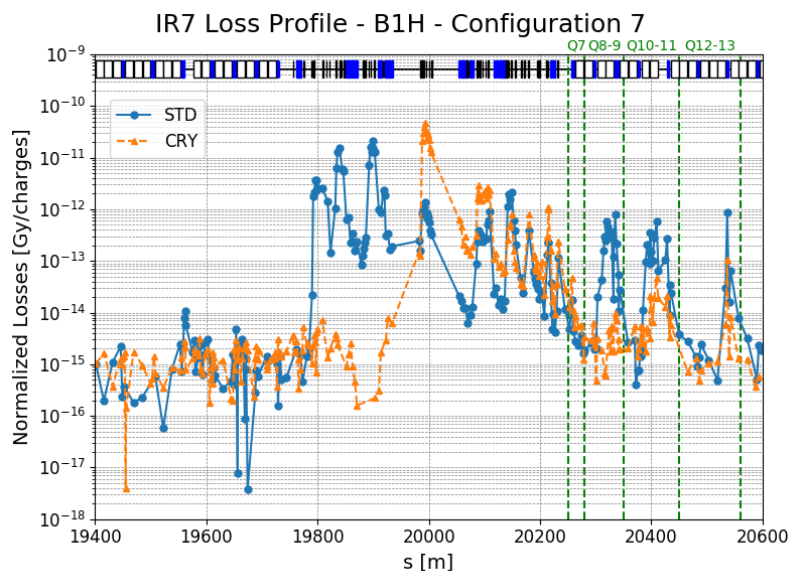

Figure 5.8: Comparison of the BLM signal recorded during loss maps on the horizontal plane of Beam 1 with Pb ion beams at $6.37Z$ TeV during MD tests, for the standard and crystal system in configuration 7 (see Tab. 5.3 and 5.4 respectively). The signal is normalized to the flux of particles lost during the loss map.

A direct comparison of the recorded BLM signal in IR7 is extremely useful to assess if the relatively increased losses in the Q7 region could cause any machine protection concerns. Fig. 5.8 shows the normalized BLM signal with both systems in configuration 7. The comparison shows that losses at the Q7 region, while increased with respect to the standard system, are not to be considered a potential issue because they are still lower in absolute than losses recorded at downstream locations, even when collimator settings are pushed to the extreme (the only exception being the horizontal plane of Beam 1 with the very tight settings of configuration 8). Furthermore, the comparison with losses recorded at the Q8-9 location with the standard system is particularly interesting for this discussion. A quench test was performed in 2015 in order to validate the quench limit at $6.37Z$ TeV in the IR7-DS region with the standard system. The limiting location was identified as the dipole magnet MBB.9L7, located in the Q8-9 area, which quenched at a peak power loss of 15 kW [93]. Fig. 5.8 shows that losses at the Q7 with the crystal system are well below the maximum
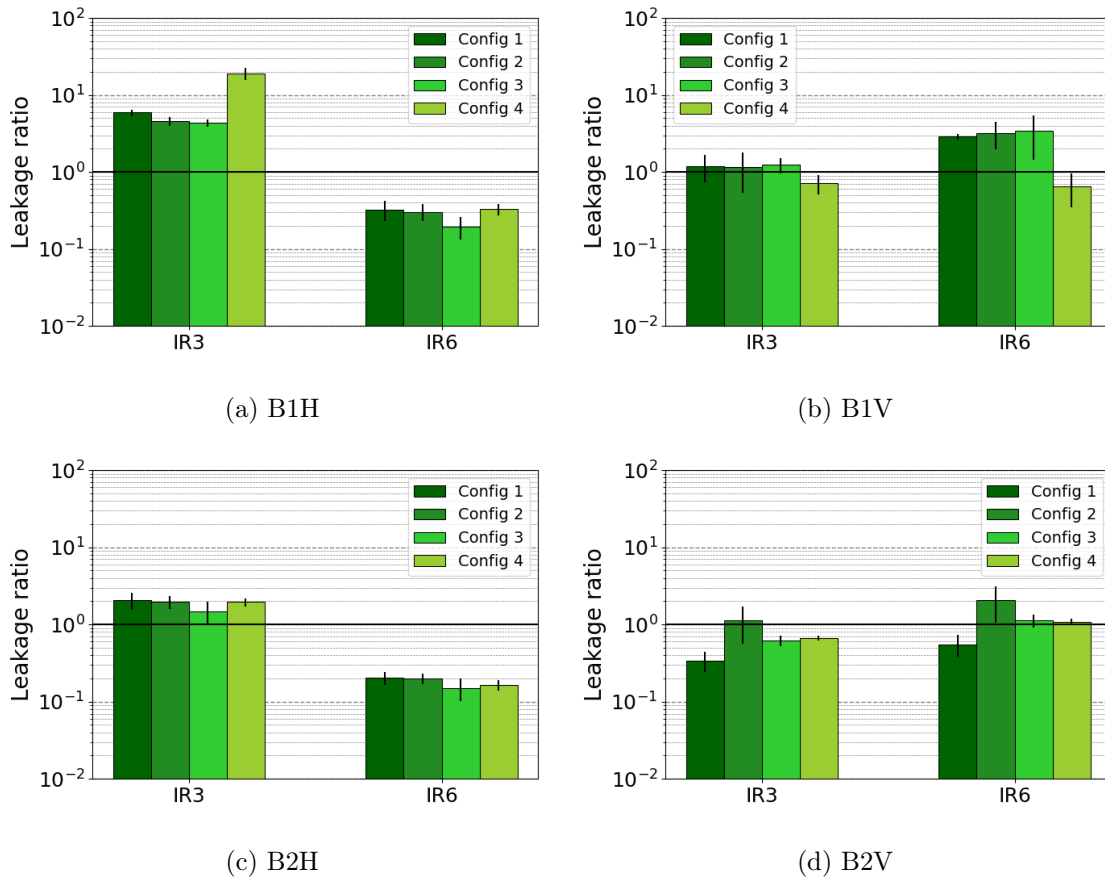
Figure 5.9: Local leakage ratio measured in IR3 and IR6 during MD tests with Pb ion beams at $6.37Z$ TeV. The standard system in configurations 1-4 is compared to the crystal system with the same configurations of downstream collimators (see Tab. 5.3 and 5.4 respectively).

signal recorded at the Q8-9 with the standard system. This is true for all beams and planes and for all configurations. Thus, the observations reported above can be translated into potential performance reach. If quenches were the only limitations, the gain factors would correspond to an increase in the total beam current allowed in the machine.

Another region of particular interest for operations with ion beams is the Q12-13 location. This area was found to be the bottleneck of the machine during the 2018 Pb ion run instead of the Q8-9 region, for reasons that are currently being investigated. Fig. 5.6 and 5.7 show that a reduction of local losses of a factor 10 or larger could be achieved in almost all beams and planes with appropriate collimator settings. The only exception is the vertical crystal on Beam 1, for which a maximum reduction of a factor 2.6 was measured.

In order to evaluate the effect of crystal collimation in other areas of the ring, the local leakage ratio has been calculated for IR3 and IR6 too, using the highest BLM signal recorded in these areas. The results are shown in Fig. 5.9 and 5.10. The cleaning in IR3, which houses the momentum cleaning portion of the collimation system, is improved in almost all configurations. This observation is consistent with the reduction of off-momentum leakage that is expected when using crystal collimation, compared to the standard system. Losses in IR6, on the other hand, are increased on the horizontal plane, and especially when the IR7 TCSGs are retracted to the same aperture of the TCLAs. This is related to the fact that particles escaping from the secondary collimators used to catch the channeled halo end
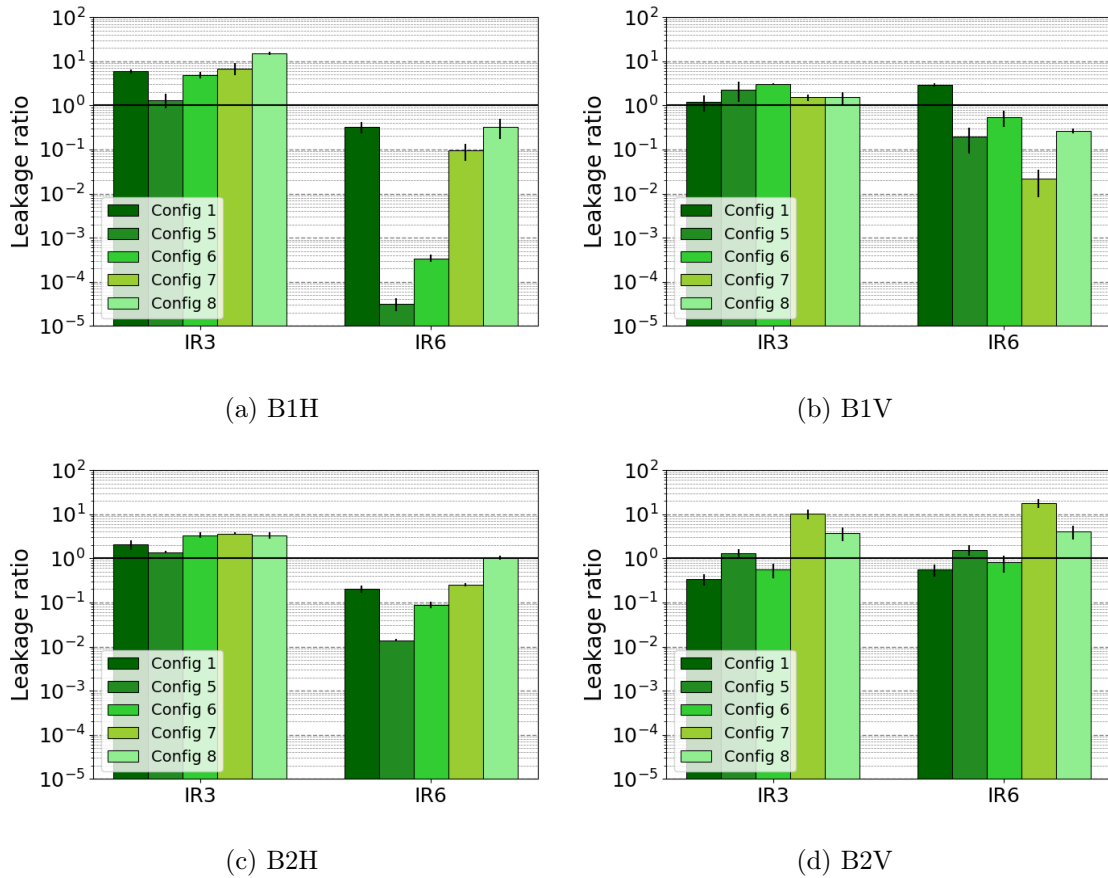
(a) B1H

(b) B1V

(c) B2H

(d) B2V

Figure 5.10: Local leakage ratio measured in IR3 and IR6 during MD tests with Pb ion beams at $6.37Z$ TeV. The standard system in configurations 1 and 5-8 is compared to the crystal system with the same configurations of downstream collimators (see Tab. 5.3 and 5.4 respectively).
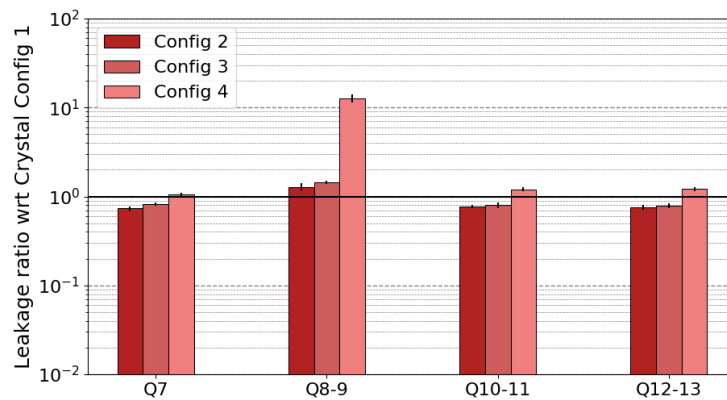

Figure 5.11: Local leakage ratio for the horizontal crystal on Beam 1, calculated by comparing the crystal system in configurations 2-4 to the crystal system in configuration 1 (see Tab. 5.4) during MD tests at $6.37Z$ TeV.
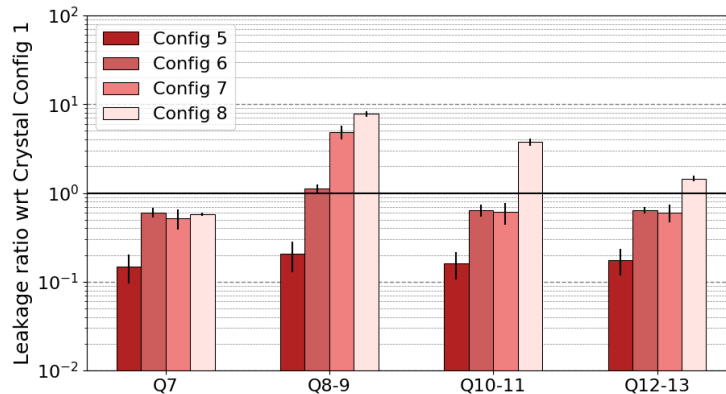
Figure 5.12: Local leakage ratio for the horizontal crystal on Beam 1, calculated by comparing the crystal system in configurations 5-8 to the crystal system in configuration 1 (see Tab. 5.4) during MD tests at $6.37Z$ TeV.

up being lost in IR6 due to the relative phase advance between the two locations. However, setting both the downstream TCSGs and the TCLAs at tight apertures allows to intercept these particles and to reduce the increase in losses observed at this location. These findings allow to better define the range of collimator settings that can be considered for the safe use of crystal collimation in operations.

A dedicated discussion can be done on the effects of specific collimator arrangments. Fig. 5.6 shows that, for the horizontal crystal in Beam 1, the leakage ratio in the Q8-9 region improves when the TCLAs are progressively closed, while the performance in the other regions remains roughly the same. This is an indication that particles with a large momentum offset are produced by the interaction of the channeled halo with the secondary collimator used to catch it, and are lost at the first dispersion peak. Closing the TCLAs further allows to better intercept these particles, reducing losses in the region. This can be seen more clearly in Fig. 5.11, where the leakage ratio for the horizontal crystal on Beam 1 has been calculated by comparing the crystal system in configurations 2-4 to the crystal system in configuration 1, in order to directly see how the different downstream settings affect the performance of the system. The same behavior can be observed for the horizontal crystal on Beam 2, although less clearly, while for the vertical crystals it is completely masked by the already high losses.

On the other hand, closing at the same time both the TCLAs and the TCSGs downstream the collimator used to catch the channeled halo allows to better intercept and dispose of off-momentum particles produced by the interaction with the crystals themselves. As a result, the cleaning in all regions of the IR7-DS is affected. Fig. 5.7 shows the clearest results for the horizontal crystal of Beam 1, for which the leakage factors increase up to several hundreds as the collimators are set at progressively tighter apertures. A more clear picture is shown in Fig. 5.12, where the leakage ratio for the horizontal crystal on Beam 1 has been calculated by comparing the crystal system in configurations 5-8 to the crystal system in configuration 1. A similar behavior can be seen for the horizontal crystal on Beam 2, while the two vertical crystals show less clear results. This is consistent with the hypothesis that, on the vertical plane, losses are dominated by particles coming from the QM crystals. The observed behavior is similar to what happens with the standard system, where losses are essentially defined by fragments escaping from the TCPs.

Table 5.5: Maximum normalized BLM signal recorded during MD tests in each plane with configuration 5, along with the corresponding region where it is located. The calculated global leakage ratio is reported in the rightmost column.

Crystal	Maximum normalized BLM signal [a.u.]		Global leakage ratio
	Standard	Crystal	
B1H	$(6.63 \pm 0.19) \cdot 10^{-13}$ Q12-13	$(3.56 \pm 1.14) \cdot 10^{-13}$ Q12-13	1.9 ± 0.6
B1V	$(5.47 \pm 2.12) \cdot 10^{-13}$ Q8-9	$(2.42 \pm 0.67) \cdot 10^{-13}$ Q12-13	2.3 ± 1.1
B2H	$(3.15 \pm 0.05) \cdot 10^{-13}$ Q8-9	$(1.07 \pm 0.07) \cdot 10^{-13}$ Q8-9	2.9 ± 0.2
B2V	$(7.31 \pm 1.44) \cdot 10^{-13}$ Q8-9	$(2.74 \pm 0.23) \cdot 10^{-13}$ Q8-9	2.7 ± 0.6

Table 5.6: Maximum normalized BLM signal recorded during MD tests in each plane with configuration 7, along with the corresponding region where it is located. The calculated global leakage ratio is reported in the rightmost column.

Crystal	Maximum normalized BLM signal [a.u.]		Global leakage ratio
	Standard	Crystal	
B1H	$(8.74 \pm 2.14) \cdot 10^{-13}$ Q12-13	$(1.04 \pm 0.22) \cdot 10^{-13}$ Q12-13	8.4 ± 2.7
B1V	$(3.58 \pm 0.42) \cdot 10^{-13}$ Q12-13	$(2.88 \pm 0.28) \cdot 10^{-13}$ Q12-13	1.2 ± 0.2
B2H	$(6.40 \pm 0.36) \cdot 10^{-13}$ Q12-13	$(6.63 \pm 0.25) \cdot 10^{-14}$ Q10-11	9.6 ± 0.7
B2V	$(5.33 \pm 1.15) \cdot 10^{-12}$ Q8-9	$(3.62 \pm 0.05) \cdot 10^{-14}$ Q8-9	14.7 ± 3.2

While the configurations reported in this section need further validation before being considered for operational use, since they feature particularly "aggressive" collimator settings, they still give a good idea of the performance reach of crystal collimation at the LHC. In particular, Tab. 5.5 reports the global leakage ratio for configuration 5, calculated using the maximum BLM signal recorded in the IR7-DS with the two collimation systems as defined in Eq. 4.7. These settings yielded the highest minimum global leakage ratio among all beams and planes. However, using other configurations it was possible to push the global leakage ratio up to a factor 10 and beyond for selected beams and planes. An example is given by configuration 7, which is particularly promising since it allowed to reduce local losses of up to a factor ~100 in specific locations of the IR7-DS, without causing Q7 to become the limiting location. Tab. 5.6 reports the global leakage measured with these settings. These configurations can be further explored in the future, in view of the deployment of crystal collimation during Run 3. In particular, since crystals are single-sided devices, there is the possibility that channeling conditions could be lost if an orbit perturbation causes the beam to drift away from the device until it becomes too close to the jaw of a secondary collimator. One way to mitigate potential risks in this situation is to use a standard collimator jaw to protect the other side of the beam pipe with respect to the crystal. In this way, if the orbit moved away from the crystal, the collimation process would occur in a similar way as in the

present system without crystals. This configuration would provide a qualitatively similar cleaning performance to that of 2018, and is expected to be sufficient if this – in principle rare – event happens during a fill at lower beam intensity than in collisions. Dedicated settings need to be defined and tested to verify the viability of this option. Other specific loss scenarios (such as beam dump failures) also need to be evaluated from the machine protection point of view, although at this stage no evident drawback is expected as the settings of the secondary collimators downstream of the TCPCs and of the collimators in IR6 are foreseen to remain the same as in 2018. Finally, a review of the BLM thresholds that trigger beam dumps, which are currently optimized for the standard collimation system, is required before the deployment of crystals in operations with ion beams.

5.3 Operational Tests with Pb Ion Beams

Increasing the total beam intensity of the circulating beams poses a number of operational challenges. Great care must be taken with many important aspects, ranging from well-optimized injection to sufficiently good control of the key beam parameters such as tune, chromaticity and closed orbit. For this reason, LHC operations with the high-intensity beams required by the experiments are always preceded by a careful testing phase called *intensity ramp-up*, during which the number of circulating bunches is progressively increased. Before moving to the next step up in number of bunches, the full and proper functioning of all systems (e.g. magnet protection, radiofrequency, beam instrumentation, collimation, feedback, beam dump and injection, etc.), must be verified.

At the end of each step, when all the system checks have been successfully performed, a few hours can be dedicated to specific tests before the beams are dumped and replaced with fresh ones. These *end-of-fill* tests offered the opportunity to successfully deploy crystal collimation with up to 648 circulating bunches, for a maximum total intensity of $3.76 \cdot 10^{12}$ charges. Being able to verify the stability of the system in such challenging and never before attempted conditions was an extremely important milestone on the path towards the validation of crystal collimation for use in operations.

During these tests, the standard collimation system was kept in place with the usual settings used for LHC operations in order to guarantee the required passive machine protection. However, crystal collimators were *adiabatically* inserted in the system and set as the primary bottleneck of the machine, with an aperture tighter than that of the primaries by 0.25 σ. In this configuration, all beam losses impinge on the crystal for classical loss mechanisms. Various aspects relevant for operations were evaluated, including:

- Impedance checks, which showed no signs of dangerous heating;

- Reproducibility of the settings (in terms of alignment position and channeling orientation), in view of long term use of the system;

- Cleaning assessment with high losses.

5.3.1 Cleaning Evaluation in Operational Settings

A fill with 20 bunches, for a total intensity of $2.20 \cdot 10^{11}$ charges, was used to evaluate the cleaning efficiency of the crystal collimation system in this configuration. The collimator settings used during these tests are reported in Tab. 5.7. As opposed to what was done during the MD, the settings of the standard system were not changed to reflect the various configurations used for cleaning measurements with the crystal system, and the performance comparison was instead done with respect to the nominal standard system in all cases. As

Table 5.7: IR7 collimator positions (in units of the beam r.m.s. σ) used for flat top loss map measurements during operational tests with 20 bunches of Pb ions at $6.37Z$ TeV.

	Standard	Crystal			
Configuration	Nominal	1	2	3	4
TCPs	5.0	5.0	5.0	5.0	5.0
Upstream TCSGs	6.5	6.5	6.5	6.5	6.5
Crystal	Out	4.75	4.75	4.75	4.75
Downstream TCSGs	6.5	6.5	6.5	6.5	6.5
TCLAs	10.0	10.0	9.0	8.0	7.0

(a) Standard system, full loss map

(b) Standard system, zoom in IR7

(c) Crystal system, full loss map
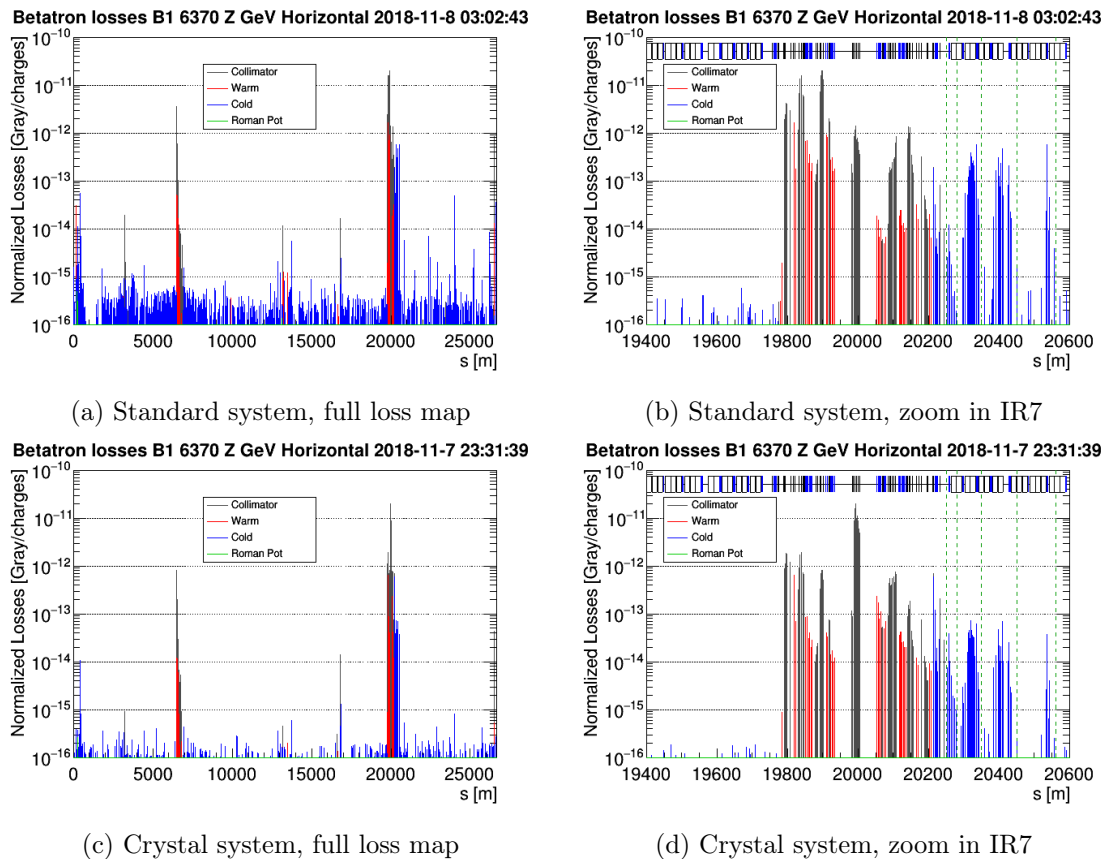
(d) Crystal system, zoom in IR7

Figure 5.13: Beam 1 horizontal loss maps performed at flat top with the standard (top) and crystal (bottom) collimation system respectively during operational tests with 20 bunches of Pb ions at $6.37Z$ TeV. The BLM signal is normalized to the flux of lost particles. The four regions in which the IR7-DS area is divided are delimited by green dashed lines. Losses observed in Q6 when crystals are deployed are not considered to be at risk of quench, as discussed in Sec. 4.1.4.
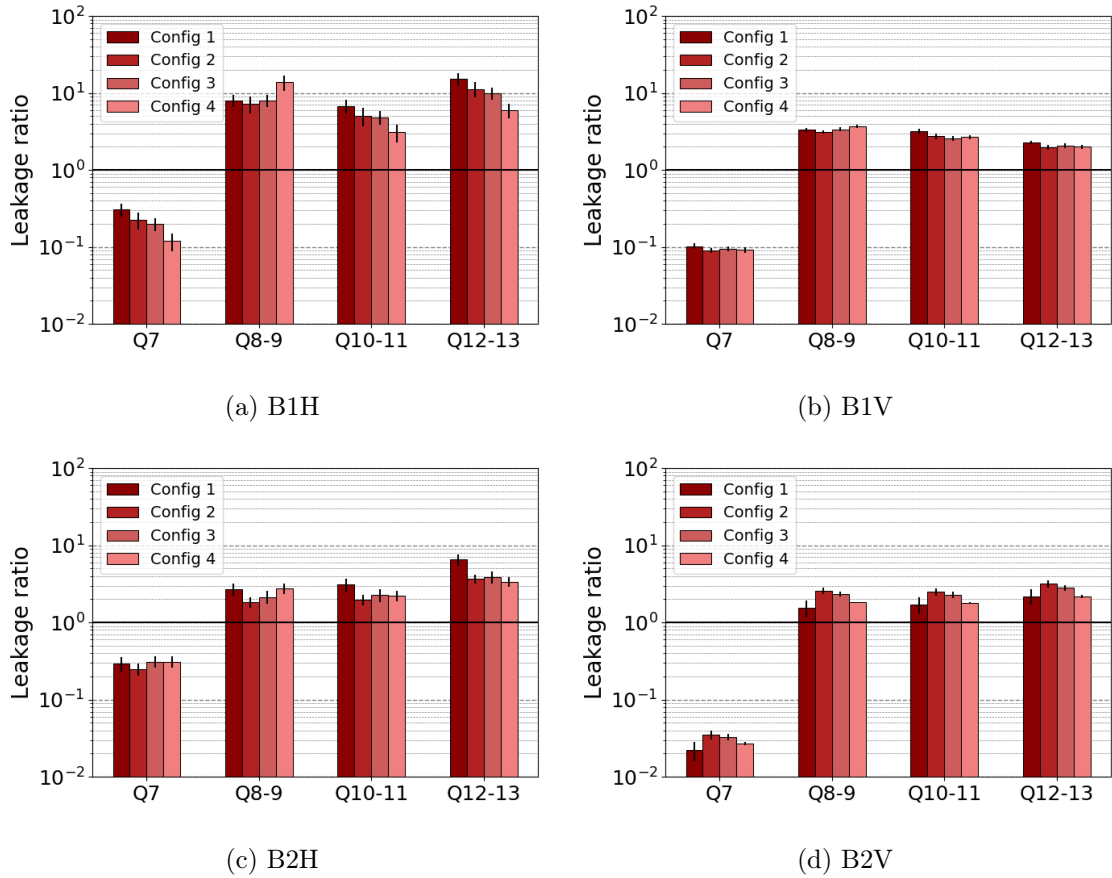
(a) B1H

(b) B1V

(c) B2H

(d) B2V

Figure 5.14: Local leakage ratio measured in the IR7-DS during operational tests with 20 Pb ion bunches at $6.37Z$ TeV. The standard system in the nominal configuration is compared to the crystal system in configurations 1-4 (see Tab. 5.7).

an example, loss maps performed for Beam 1 horizontal with the nominal standard system and with the crystal-assisted system in configuration 1 are shown in Fig. 5.13.

The measured leakage factor is reported in Fig. 5.14 for each IR7-DS region. Overall, aside from the already described worsening in the Q7 region, all crystals show a clear improvement in cleaning inefficiency when used in conjunction with the standard system. Most notably, losses are reduced by a factor ~10 and by a factor ~2-3 by the horizontal crystals on Beam 1 and Beam 2 respectively. The direct comparison of the BLM signal as a function of the longitudinal position for the horizontal crystal on Beam 1 can be seen in Fig. 5.15, showing that Q7 does not become the limiting location despite the increased losses. The vertical crystal on Beam 1 shows a comparable performance to the horizontal crystal on Beam 2 for the IR7-DS area, but losses at the Q7 region are further increased. Finally, the vertical crystal on Beam 2 exhibits the worst results, with an increase in losses in the Q7 region of almost a factor ~50. However, the direct comparison of the BLM signal, shown in Fig. 5.16, demonstrates that losses at the Q7 region are still lower than in the other limiting locations of the IR7-DS. This is true for all beams and planes and for all configurations.

With regards of the leakage ratio calculated for IR3 and IR6, shown in Fig. 5.17, similar considerations to Sec. 5.2.2 can be made. The low rate of inelastic interactions in crystal collimators reduces the production of off-momentum particles in IR7, allowing to improve the leakage to IR3. While this cannot be considered a figure of merit of the performance
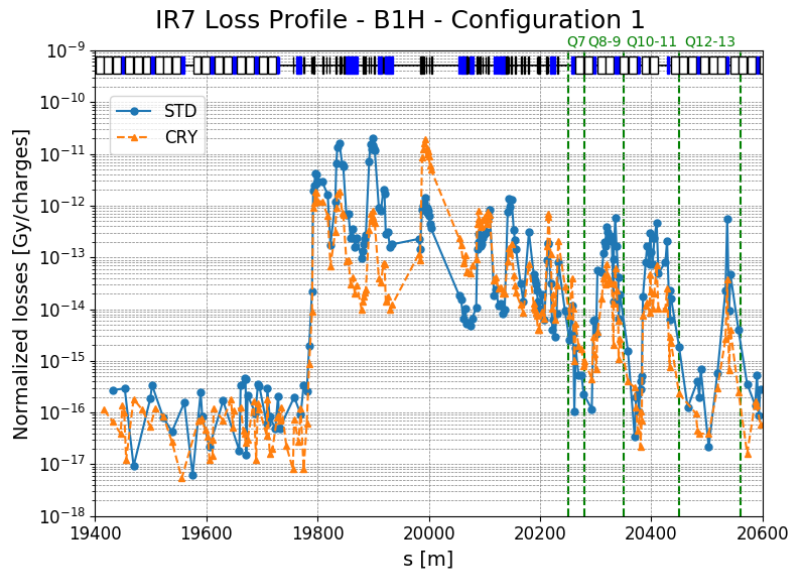
Figure 5.15: Comparison of the BLM signal recorded during loss maps on the horizontal plane of Beam 1 with 20 bunches of Pb ions at $6.37Z$ TeV, for the standard system in the nominal configuration and the crystal system in configuration 1 (see Tab. 5.7). The signal is normalized to the flux of particles lost during the loss map.
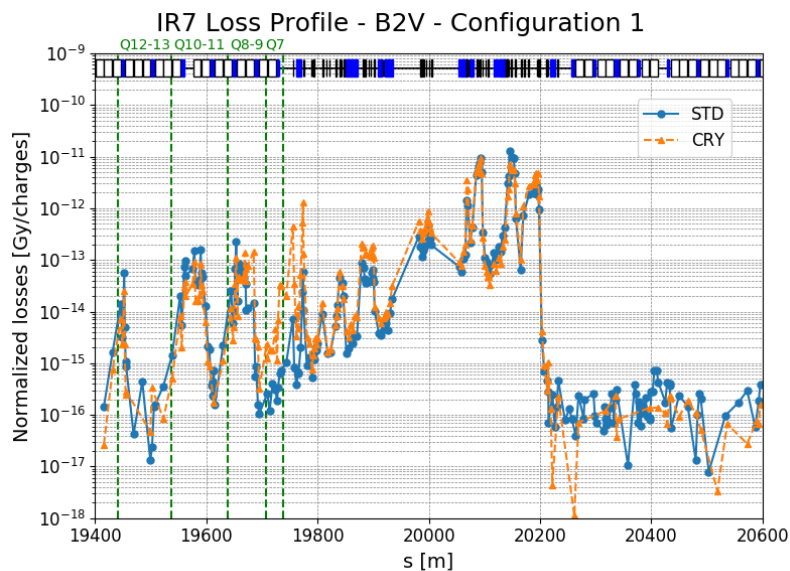

Figure 5.16: Comparison of the BLM signal recorded during loss maps on the vertical plane of Beam 2 with 20 bunches of Pb ions at $6.37Z$ TeV, for the standard system in the nominal configuration and the crystal system in configuration 1 (see Tab. 5.7). The signal is normalized to the flux of particles lost during the loss map.
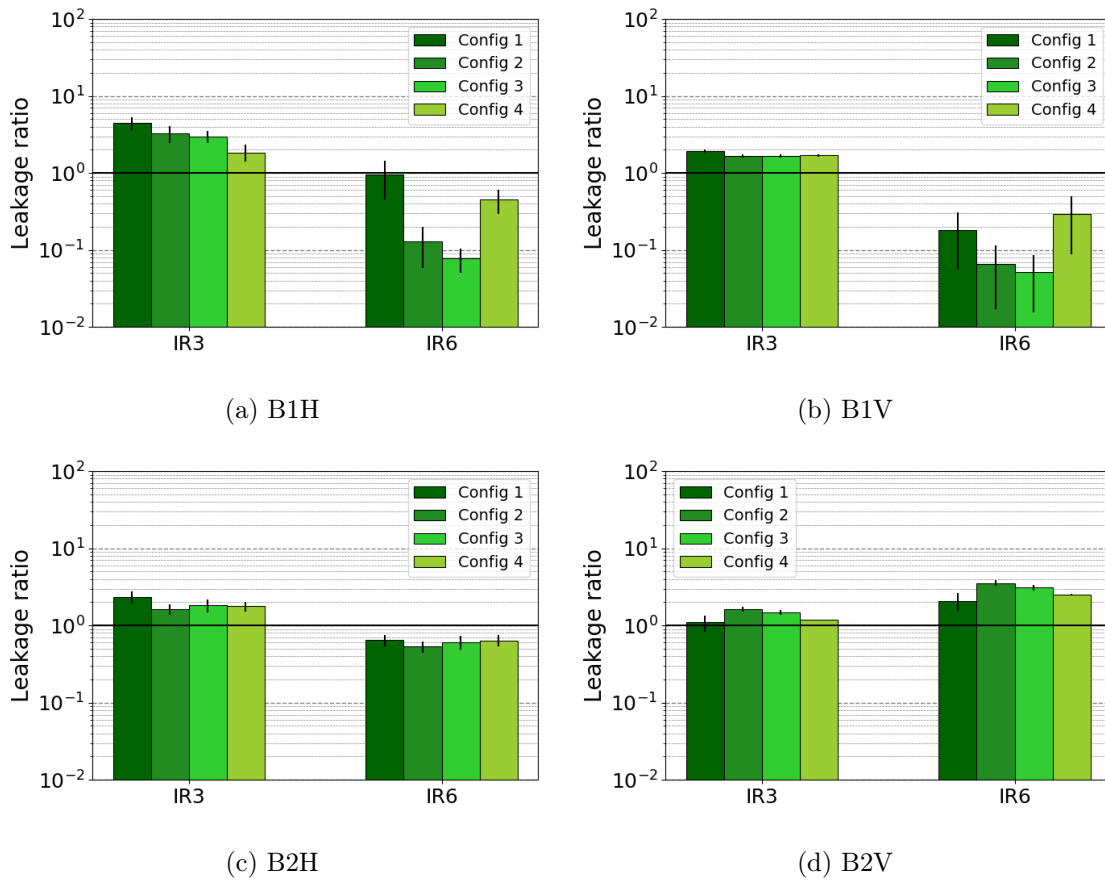
(a) B1H

(b) B1V

(c) B2H

(d) B2V

Figure 5.17: Local leakage ratio measured in IR3 and IR6 during operational tests with 20 Pb ion bunches at $6.37Z$ TeV. The standard system in the nominal configuration is compared to the crystal system in configurations 1-4 (see Tab. 5.7).
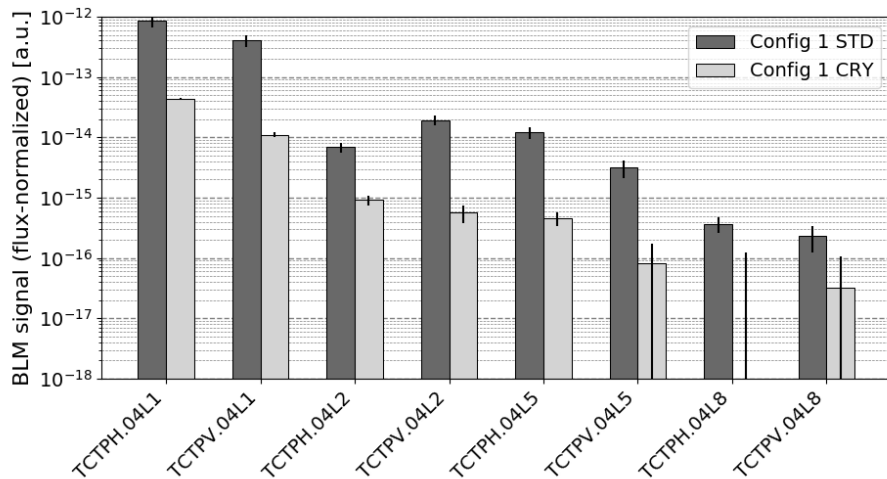

Figure 5.18: Normalized BLM signal recorded at TCTs with the standard and crystal collimation system during loss maps on the horizontal plane of Beam 1 with 20 bunches of Pb ions at $6.37Z$ TeV (configuration 1).

of the system, it gives an indication that the collimation process is "cleaner", with less off-momentum particles generated in the first stages. The leakage to IR6, however, is affected by the settings of the IR7 downstream collimators, limiting the range of configurations to be considered for operations.

The BLM signal recorded at TCTs was also monitored during loss maps. These collimators are made of tungsten, which maximizes their absorption power at the expense of their durability. For this reason, the threshold to trigger a beam dump is lower at these locations compared to other areas of the machine. In fact, throughout Run 2 a number of accidental beam dumps were triggered by TCTs. Fig. 5.18 reports the normalized signal recorded during loss maps on the horizontal plane of Beam 1 with the standard and crystal collimation system. This example shows that the load on TCTs is reduced when crystal collimation is deployed, limiting the risk of triggering a beam dump. Furthermore, lower losses on the TCTs also allow to reduce the background observed by the experiments. It is worth noting that the signal recorded with crystal collimation at the TCTs in IR5 and IR8 is close to the background noise, hence the large error bars.

5.3.2 Crystal Insertion with High-Intensity Beams

During the intensity ramp-up in preparation for the 2018 Pb ion run, crystals were inserted in the beam line with high-intensity ion beams for the very first time since their installation in the LHC. It is important to note that the setup of the crystal collimation system for these studies was very efficient, thanks to the high reproducibility of the devices. In most cases, the optimal channeling orientation found during the initial setup for end-of-fill tests could be used as a reference starting point. The only exception was the vertical crystal on Beam 2, as the goniometer lost its reference position between subsequent measurement sessions. An automated sequence for the insertion of crystal collimators, originally implemented for the 2018 special physics run with proton beams described in Chap. 7, was tested for the first time in ion beam fills with 20 bunches and 260 bunches respectively. While the first attempt was successful, the second one needed to be interrupted because of high losses due to too fast movements. Rather than a fundamental limitation of crystal collimation, this is a known
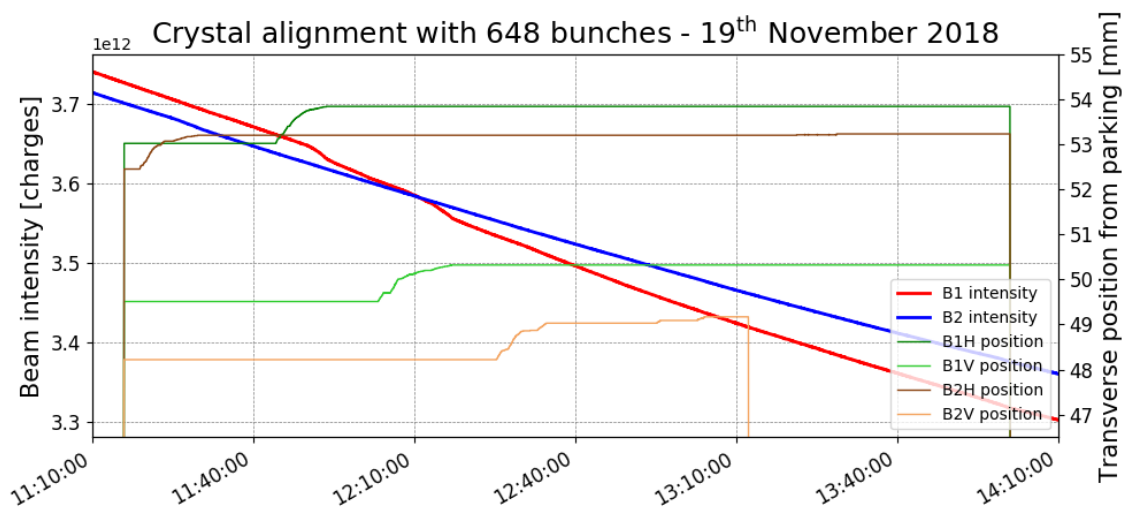

Figure 5.19: Overview of the alignment of the crystal collimators during a fill with 648 bunches of Pb ions at $6.37Z$ TeV.

issue related to the population of beam tails. As a result, high loss spikes are generated when the crystals are inserted too quickly in the beam line. However, the necessity to insert the crystals directly at flat top is not expected to present itself in operational scenarios, and instead channeling conditions are maintained from injection all the way through the energy ramp via dedicated ramp functions (see Sec. 4.1.5). Furthermore, it is important to note that the BLM thresholds that trigger beam dumps are inherited from the standard system, and as such are not optimized for the peculiar loss pattern of crystal collimation. Indeed, the main limitation during these activities comes from the BLM signal approaching dump thresholds on secondary collimators, which is not expected to be a real limitation of the system. The following activities relied on manual insertion of the devices at a lower speed, in order to limit the height of the loss spikes generated in the process. An overview of the alignment process during the fill with 648 bunches is shown in Fig. 5.19. Each crystal was kept in channeling conditions for up to 2 hours with no signs of deterioration or other issues.

5.4   Proposed Crystal Collimation Settings for Run 3

The activities described in Sec. 5.3 marked the first use of crystal collimation in a potentially operational configuration with high-intensity Pb ion beams. The very promising results provided a key ingredient to the decision to include crystal collimators in the baseline of the LHC upgrade. This will spark a new campaign of tests with Pb ion beams for Run 3, during which more configurations could be explored in view of the definition of operational settings for potential use in HL-LHC. Based on the experience accumulated so far, a starting configuration is defined in this section for the ion commissioning in 2022.

5.4.1   Settings baseline for Run 3

Among the various configurations tested with high-intensity beams, configuration 1 seems to be the most promising, allowing to achieve a satisfactory cleaning improvement in the IR7-DS region, without increasing the loads on the Q7 region and in IR6 by too large a margin. The corresponding IR7 collimator settings are listed in Tab. 5.8. Tab. 5.9 reports the measured local leakage ratio for each relevant region, while Tab. 5.10 reports the measured global leakage ratio for each plane. The latter, in particular, can be considered an estimation of the performance reach of the machine when the crystal system is used in operations. Configuration 1 was also subject to a number of additional tests aimed at ensuring that safe operations can be guaranteed in these conditions, including:

- Channeling with high losses in all planes at the same time (shown in Fig. 5.20) with 20 circulating bunches, without abnormal loss spikes and generally a very clean pattern all around the ring.

- An asynchronous beam dump test, which was later confirmed to pose no particular dangers for the machine.

- Stable channeling for all crystals for up to 2 hours with 648 bunches, even during orbit corrections.

The good outcome of all these tests cements configuration 1 as a good starting point for crystal collimation in Run 3, to be worked upon in future studies.

Table 5.8: IR7 collimator positions (in units of the beam r.m.s. σ) for the proposed operational configuration for crystal collimation in Run 3.

TCPs	5.0
Upstream TCSGs	6.5
Crystal	4.75
Downstream TCSGs	6.5
TCLAs	10.0

Table 5.9: Leakage ratio measured during operational tests with the proposed configuration.

Crystal	Q7	Q8-9	Q10-11	Q12-13
B1H	0.31±0.06	7.96±1.42	6.78±1.34	15.24±2.68
B1V	0.10±0.01	3.33±0.18	3.17±0.26	2.27±0.12
B2H	0.30±0.06	2.71±0.48	3.09±0.61	6.55±1.13
B2V	0.02±0.01	1.54±0.38	1.72±0.42	2.19±0.49

Table 5.10: Maximum normalized BLM signal recorded during operational tests in each plane for the proposed configuration, along with the corresponding region where it is located. The calculated global leakage ratio is reported in the rightmost column.

Crystal	Maximum normalized BLM signal [a.u.]		Global leakage ratio
	Standard	Crystal	
B1H	$(5.81 \pm 1.03) \cdot 10^{-13}$ Q8-9	$(7.30 \pm 0.15) \cdot 10^{-14}$ Q8-9	8.0 ± 1.4
B1V	$(1.95 \pm 0.07) \cdot 10^{-13}$ Q8-9	$(6.39 \pm 0.05) \cdot 10^{-14}$ Q12-13	3.1 ± 0.1
B2H	$(2.76 \pm 0.39) \cdot 10^{-13}$ Q12-13	$(7.89 \pm 0.78) \cdot 10^{-14}$ Q8-9	3.5 ± 0.6
B2V	$(2.25 \pm 0.01) \cdot 10^{-13}$ Q8-9	$(1.46 \pm 0.36) \cdot 10^{-13}$ Q8-9	1.5 ± 0.4
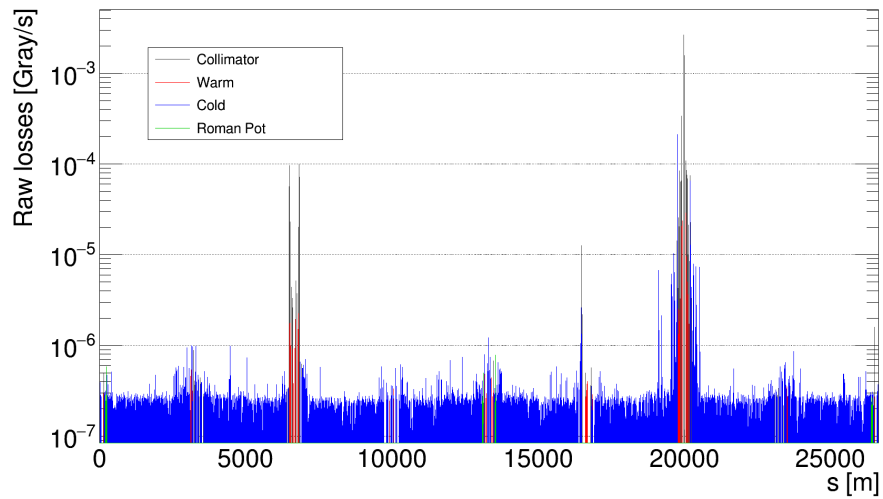
(a) Full loss map.
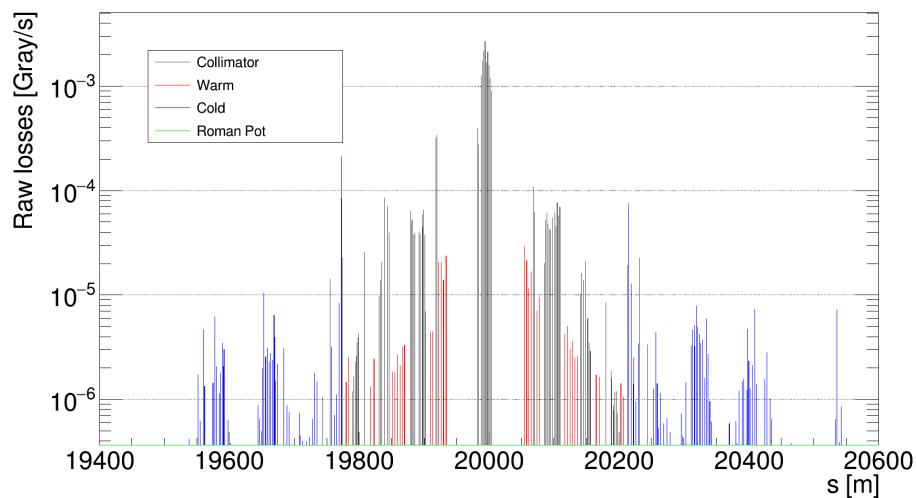
(b) IR7 close-up.

Figure 5.20: Loss map with all four crystals in optimal channeling with Pb ion beams at 6.37Z TeV. The ADT was used to generate sustained losses on both planes of both beams at the same time. The full loss pattern (top) and a close-up of IR7 (bottom) are shown. Losses observed in Q6 on both sides of IR7 are not considered to be at risk of quench, as discussed in Sec. 4.1.4.

5.4.2 Double-Sided Crystal Collimation Concept Layout

The crystal collimators currently installed in the LHC are single-sided devices. The horizontal crystals are placed on the external side of the beam pipe, while the vertical ones are located at the top. This positioning was chosen as the only option capable to accommodate the goniometer assembly that holds the crystal. While this system is already able to provide a significant cleaning improvement, as demonstrated in this chapter, there are specific beam loss scenarios that cannot be effectively covered by single-sided collimators. As mentioned earlier, orbit perturbations can change the position of the beam center at the collimator location, leading to two different scenarios:

- If the beam drifts towards the side where the crystal collimator is installed, the beam halo can still be intercepted and, if the perturbation did not push the beam divergence outside of the acceptance of the crystal, channeling conditions can be kept.

- If the beam moves towards the opposite side and the size of the drift is larger than the margin between the crystal and a secondary collimator, the crystal is not the primary collimator anymore and cannot intercept the beam halo.

In the present scenario, where TCPs are kept at nominal settings and crystals are adiabatically inserted at tighter settings by a fraction of σ, events like these should not constitute a fundamental risk. The primary collimators still provide passive protection to the machine, and the overall performance is not expected to be worse than the standard collimation system. However, the statistics of the reasons for premature beam dumps, as well as the direction of orbit drifts, need to be carefully monitored throughout Run 3.

As part of this thesis, some options were explored to address this issue for a potential crystal-only collimation system. In order to cover the event of an orbit drift, two crystals, ideally host by the same goniometer assembly, should be installed at the opposite sides of each plane, for a total of 4 crystals per beam. However, such a configuration would require a complete redesign of the device. Another option that can be considered is to have the two crystals installed on separate goniometers. This would still require a redesign of the goniometer assembly in order to fit two devices on opposite sides of the beam pipe (which is not possible with the current design), but in principle it could be less challenging. If the two crystals cannot be installed at the same longitudinal location due to the presence of other equipment, alternative suitable positions have been identified.

The location of the horizontal crystals presently installed in the LHC with respect to IP7 is not the same between the two beams due to constraints on the available slots [11, 94]. In order to restore the symmetry of the system, the longitudinal position for the two crystals on the other side of the beam pipe can be swapped. The vertical crystals, on the other hand, are currently installed at the same relative position on the two beams [11, 94]. The two additional ones can then be placed at the closest available locations on the opposite side. The identified slots for both beams are reported in Tab. 5.11.

Table 5.11: Location of the LHC slots identified for the possible installation of an additional device on the opposite side of the beam pipe.

Beam	Plane	Slot name	s [m]
B1	Vertical	TCSM.A6L7.B1	19834
B1	Horizontal	TCSM.A5L7.B1	19898
B2	Horizontal	TCSM.D6R7.B2	20069
B2	Vertical	TCSM.A6R7.B2	20153

Using Eq. 3.31, the trajectory of the channeled halo can be predicted for both sides of the beam, in order to verify that they can be safely intercepted without changing the already tested collimator configuration. As an example, the predictions at injection and at flat top are shown in Fig. 5.21 and 5.22 for the horizontal and vertical crystals on Beam 1 respectively.

While the adiabatic insertion of crystals in the existing collimation system is expected to provide a suitable cleaning improvement during Run 3, the setup explored in this section can be considered as a reasonable starting point for future upgrades of the crystal collimation system.
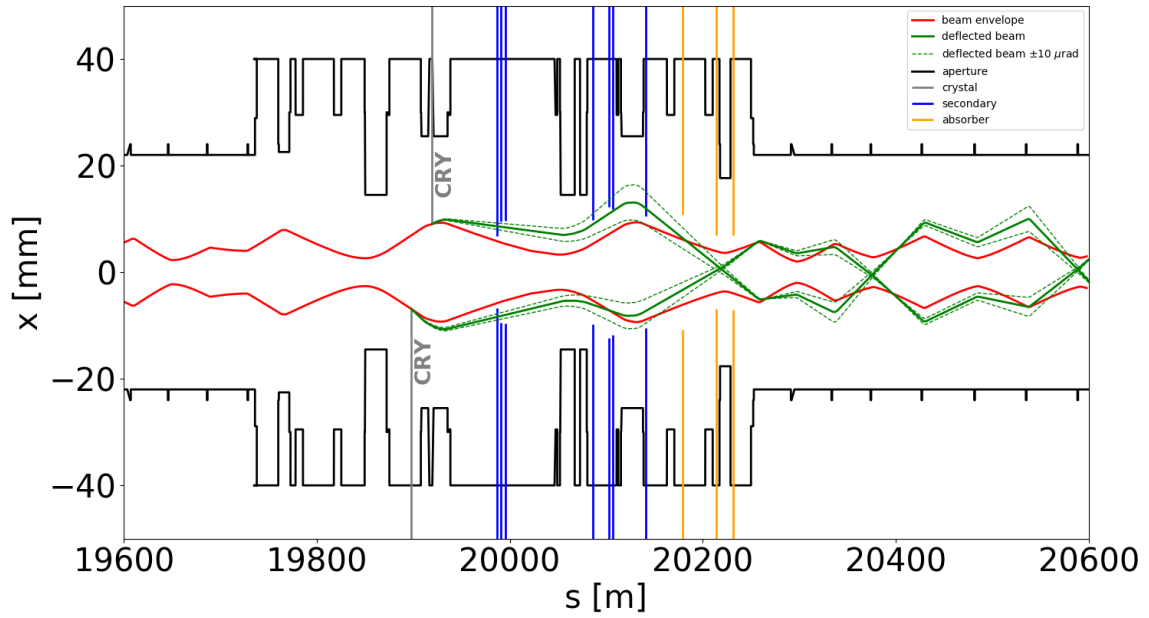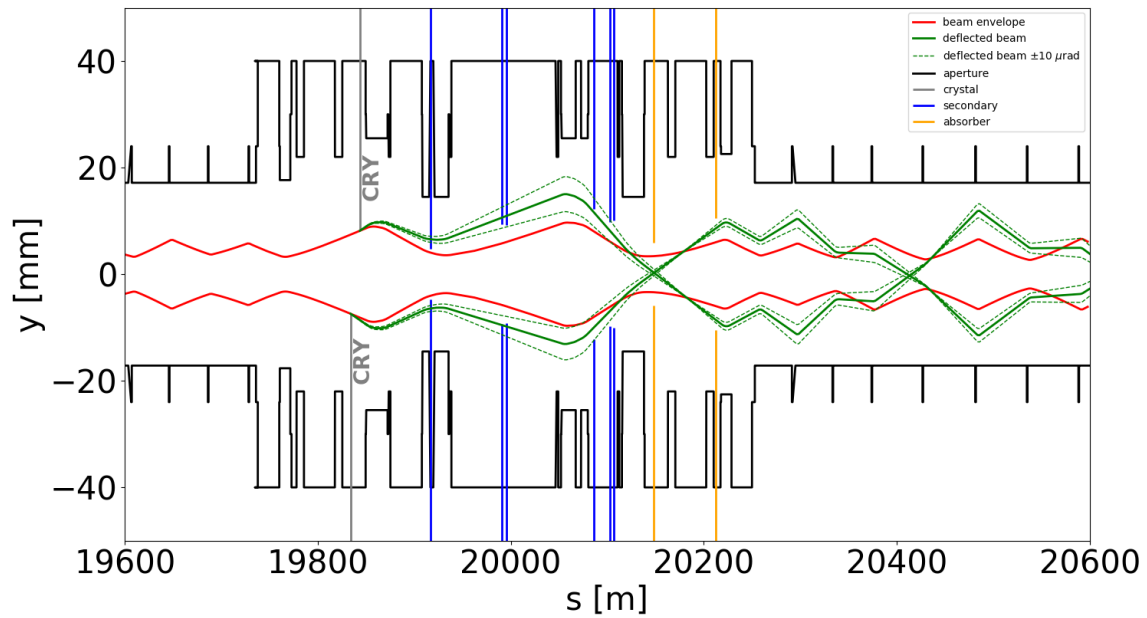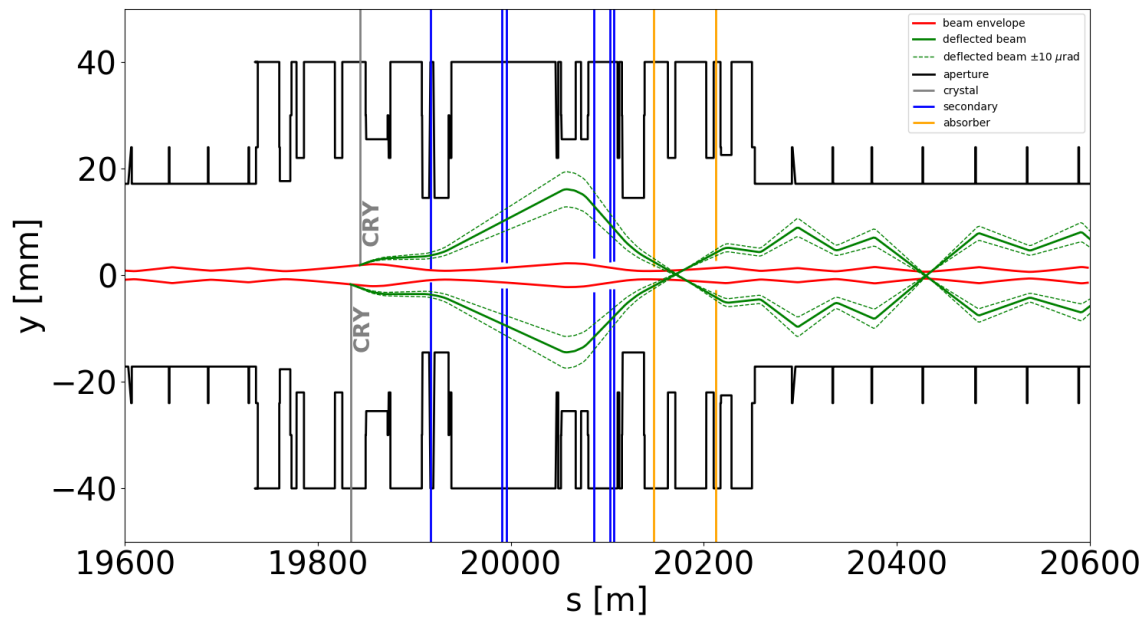
(a) 450 GeV.
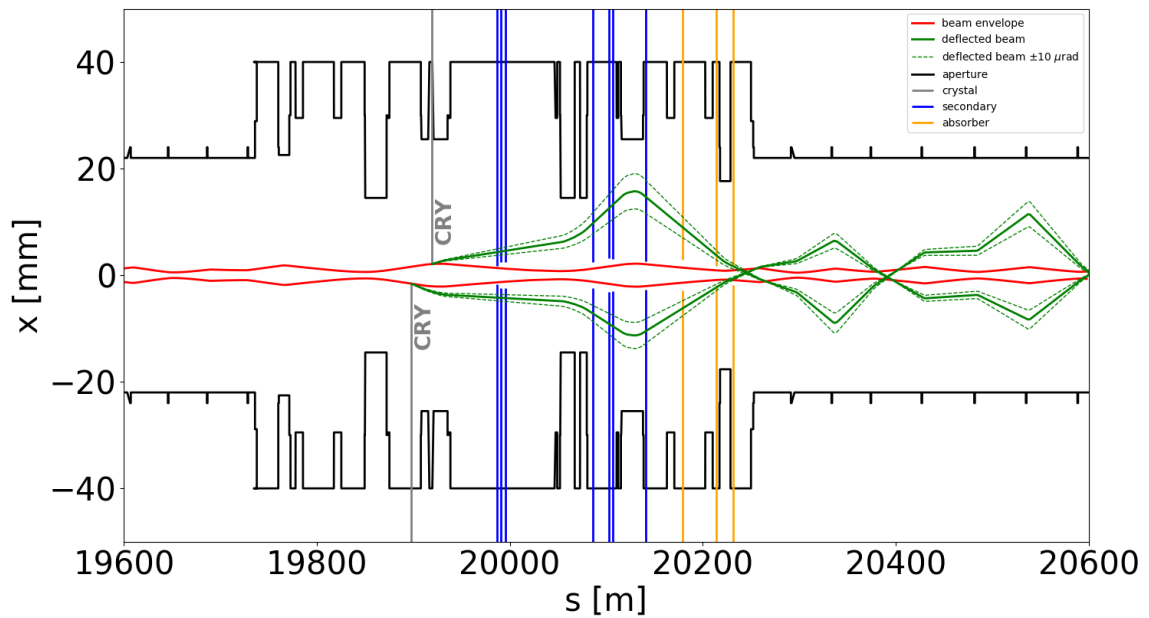
(b) 6.5 TeV.

Figure 5.21: Predicted trajectory of the channeled beam halos for a double-sided crystal collimation system on the horizontal plane of Beam 1.

(a) 450 GeV.

(b) 6.5 TeV.

Figure 5.22: Predicted trajectory of the channeled beam halos for a double-sided crystal collimation system on the vertical plane of Beam 1.

Chapter 6

Updated Crystal Simulation Routine

The development of simulation tools is an essential part of crystal collimation studies. Their range of applications spans from the design phase, to predicting the performance of this advanced collimation system in the LHC and extrapolating the results to other machines and working conditions, to the reproduction and interpretation of key experimental findings. The standard tool used at CERN for collimation studies is based on the single particle tracking code SixTrack, which performs a six-dimensional tracking of charged particles through a magnetic lattice. Crystal collimators, however, require a dedicated simulation routine which was originally developed by Igor Yazynin. The routine was later implemented in Six-Track 4 by Valentina Previtali [76] along with upgraded physics models provided by Daniele Mirarchi [16]. Part of the work described in this thesis was dedicated to the migration of the crystal routine in SixTrack 5. As of version 5.4.1, the routine is part of the official SixTrack release [95]. The physics model of the routine was also integrated with an updated treatment of the crystal miscut angle, which is currently not part of the official release.

After an introduction on SixTrack and on the structure of the original routine, the motivation and the main improvements gained with the implementation of the crystal routine in SixTrack 5 are described in this chapter. The new treatment of the miscut angle is also discussed in detail with some preliminary applications.

6.1 SixTrack for Collimation Studies

SixTrack [96–98] is a single particle tracking code widely used at CERN for simulating beam dynamics in circular accelerators. It performs a symplectic and fully chromatic tracking of protons and, as of recently, ions [99, 100] through a magnetic lattice which includes all the different elements of the machine that affect the beam dynamics (such as magnets, RF cavities, collimators, etc.).

Two main input files are required to set up a SixTrack simulation:

- The `fort.2` file specifies the machine lattice and structure and the settings of the magnetic elements. This file is usually automatically generated by MADX [101], a code for optics design and optimization largely used at CERN.

- The `fort.3` file provides the settings of the simulation and needs to be manually edited by the user.

Collimation studies require a specific version of SixTrack, which implements essential physics to treat the interaction of beam particles with the constituting material of machine elements. An additional input file, the *collimator database*, is required to provide this version of
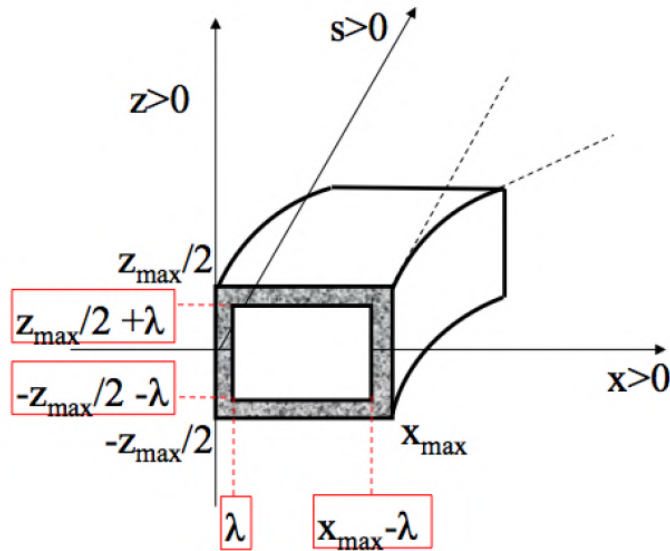
Figure 6.1: Crystal reference system used in the routine. An amorphous layer of thickness λ is considered [76].

SixTrack with all the relevant information regarding the collimators, such as their material and length. The code is routinely used to predict the distribution of losses in the ring, which can be compared to the loss distribution measured in operations.

6.2   The Monte-Carlo Crystal Simulation Routine

The dedicated crystal routine [102, 103] models the interaction between proton beams and crystal collimators via a Monte-Carlo simulation based on the theoretical framework presented in Chap. 3. Only simulations of proton beams are supported by this routine. An infrastructure to treat the interactions of ion beams with crystal collimators through the coupling of SixTrack with other codes (such as FLUKA and Geant) is currently under development.

In order to standardize the mathematical treatment of coherent processes no matter the aperture, orientation and collimation plane of the crystal, the routine makes use of a specific reference system referred to as the *crystal reference frame* $(x_{cry}, z_{cry}, s_{cry})$, shown in Fig. 6.1. The entrance face of the collimator is located on the transverse (x_{cry}, z_{cry}) plane $s_{cry} = 0$, while the bulk of the crystal lays in the $s_{cry} > 0$ volume. The positive x_{cry} axis corresponds to the direction of the deflection applied by the crystal to a channeled particle. It is clear that a particle can interact with the crystal if its impact coordinates fall between the limits of the entrance face:

$$0 < x_{cry} < x_{cry}^{max}, \tag{6.1}$$

$$-\frac{z_{cry}^{max}}{2} < z < \frac{z_{cry}^{max}}{2}, \tag{6.2}$$

where x_{cry}^{max} and z_{cry}^{max} are specified in the collimator database. The routine also allows to define an *amorphous layer* of thickness λ, a region surrounding the crystal bulk where only amorphous interactions can happen, although this feature will not come into play for the scope of this thesis.

What is depicted above, however, is not the same reference system used by SixTrack, which tracks particles in the *machine reference frame* (x, y, s). For this reason, the implementation in SixTrack 4 required an intermediate step to transport the particle coordinates from one frame to the other [76].

Different processes can take place when a particle hits the crystal, depending on the energy, orientation with respect to the crystal planes, and crystal material. The effects considered in the routine are the following:

- **Amorphous**: the particle is not aligned with the crystal planes, or hits the amorphous layer, and interacts with the crystal as an amorphous material.

- **Planar channeling**: the particle is trapped in the potential well between crystalline planes and follows the curvature of the crystal.

- **Volume reflection**: the particle is reflected by the bulk of the crystal, resulting in a deflection of about $1.5\theta_c$.

- **Volume capture**: while initially not aligned with the crystalline planes, the particle loses energy while traveling through the crystal and eventually enters the potential well, being channeled from that point onward.

- **Dechanneling**: while in channeling, the particle experiences a point-like elastic interaction with a nucleus or multiple scattering with electrons and escapes the potential well, interacting with the crystal as an amorphous material from that point onward.

Fig. 6.2 depicts the logic of the crystal routine through a functional flowchart. All the quantities required for the calculation of the probability are either defined as input variables of the routine itself or read as global (common) parameters from parent routines. It is important to recall the main limitations of this model:

- Axial channeling and torsion effects are not treated.

- No secondary curvature on other directions is considered.

- The crystal holder geometry is not implemented.

- The shower of secondary particles emitted in the event of an inelastic interaction is not calculated.

The routine was later improved with upgraded physics models [16] and the benchmark against experimental data has shown remarkable results in a variety of configurations, both at the SPS and at the LHC [11, 102, 104–106].

6.3   Implementation of the Crystal Routine in SixTrack 5

Since the first implementation of the original crystal simulation routine, many features were added to SixTrack over the years, such as:

- The *online aperture check*, i.e. the capability to check if particles are lost on the machine aperture while the simulation is running, instead of saving their trajectories for an offline check by a separated program and removing them in the postprocessing.

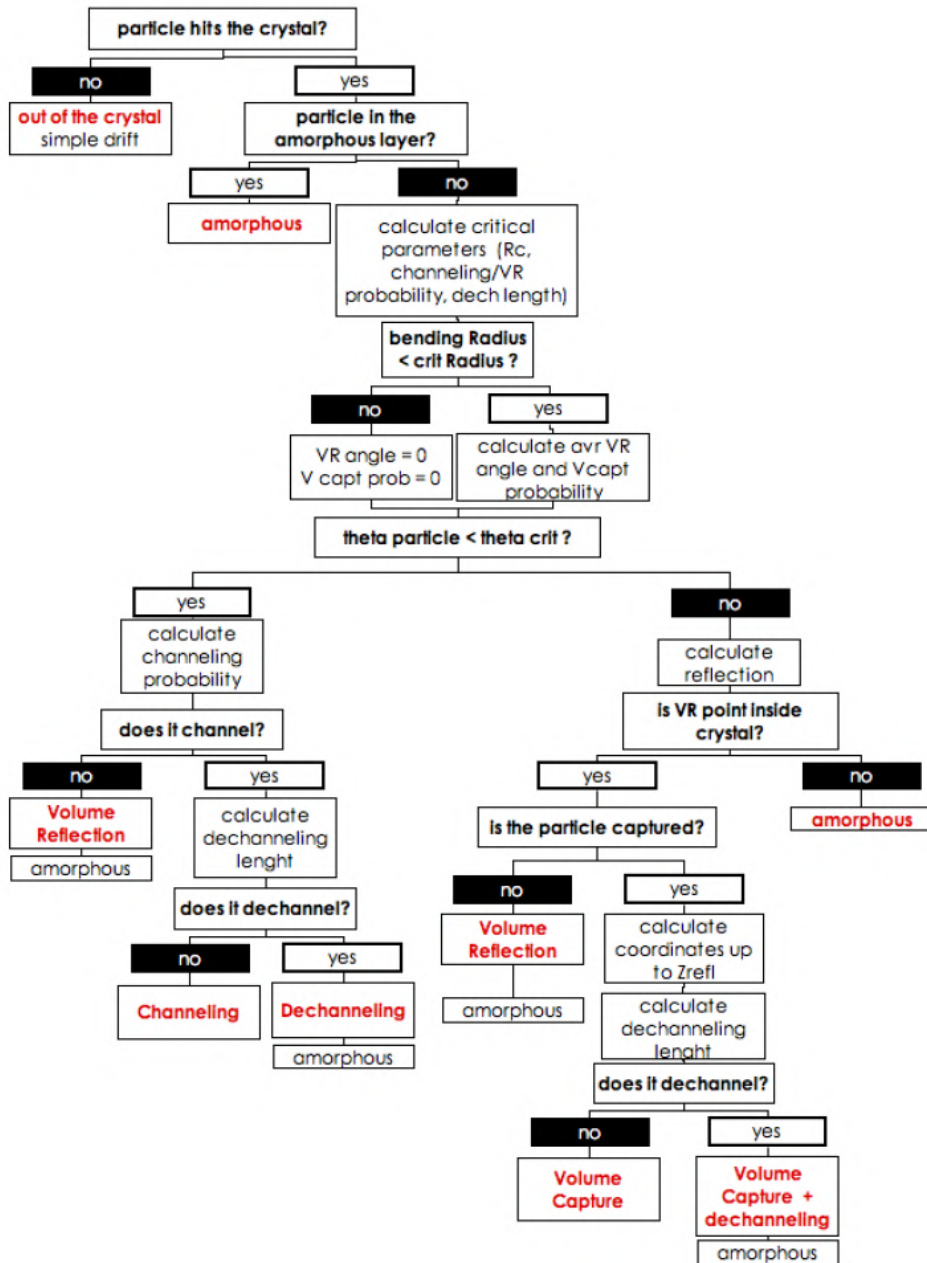- The ability to dynamically allocate arrays for storing data.

Figure 6.2: Crystal routine logic flow. The possible processes experienced by protons when interacting with a crystal are highlighted in red [76].

Table 6.1: Numerical parameters required to define a crystal collimator in the collimator database, following the same order as they are specified in the `SETTINGS` block.

`Bend`	float	Bending radius of the crystal collimator in [m].
`XDim`	float	Transverse dimension along the X axis of the crystal collimator in [m].
`YDim`	float	Transverse dimension along the Y axis of the crystal collimator in [m].
`Thick`	float	Thickness of the amorphous layer of the crystal collimator in [m].
`Tilt`	float	Tilt of the crystal collimator in [rad] with respect to its default orientation (calculated as the divergence of the beam at that location, i.e. optimal orientation for channeling).
`MisCut`	float	Miscut angle of the crystal collimator in [rad].
`Orient`	integer	Used only for Si crystal collimators. Its value is either 1 (strip crystal, 110 planes) or 2 (quasi-mosaic crystal, 111 planes).

- A generally more streamlined structure for the input files to set the parameters of the simulation.

- Various other code optimizations that significantly reduced the time required to run simulations in many scenarios.

These major changes were grouped in a new version of the code, named SixTrack 5 [107]. In the meantime however, since it was never part of an official release, the crystal simulation routine could not profit of these improvements and remained based on SixTrack 4. As part of this thesis, the routine was rewritten and reorganized in order to be fully compatible with SixTrack 5, leading to the inclusion in the officially released code as of version 5.4.1. In this section, the definition of a crystal collimator in the new version of the routine and the structure of the routine itself are presented, along with the results of benchmark tests against the original version.

6.3.1   Definition of a Crystal Collimator in SixTrack 5

First of all, a crystal collimator needs to be defined in the collimator database together with all the other standard collimators. This is where the collimator name, material and length are specified. As of the current version, the only fully supported and benchmarked material for crystal collimators is silicon (Si). Germanium (Ge) is also supported but has never been benchmarked since no experimental data are available.

In order for a collimator to be recognized as a crystal and treated accordingly, additional parameters need to be specified in the `SETTINGS` block of the collimator database. All the parameters related to the geometry and angular orientation of the device are specified here in a single line prefaced by the `CRYSTAL` flag and the name of the selected collimator to be treated as a crystal. The following is an example of the definition of a crystal collimator with the typical parameters of those installed in the LHC:

```
SETTINGS
CRYSTAL  cry.h.b1 80.00 2.0e-3 50.0e-3 0.0 0.0 0.0 1
```

The description of each numerical parameter is given in Tab. 6.1. Additional details can be found in the SixTrack user manual [97].

6.3.2   Structure of the SixTrack 5 Crystal Routine

In order to maintain the crystal routine as independent as possible from the SixTrack collimation code, for easier debugging, all crystal-related physics is contained in its own separate Fortran module, called `coll_crystal.f90`, which is organized in two "setup" subroutines and five physics subroutines.

The first two subroutines are called anytime a crystal collimator is encountered while moving through the machine lattice, and they essentially take care of some initial definitions and calculations:

- The `cry_init` subroutine initializes all material-related crystal parameters, such as the radiation length, nuclear interaction length, interplanar distance and height of the potential well between crystalline planes.

- The `cry_startElement` subroutine performs some preliminary calculations (such as the default orientation of the crystal) and stores the parameters read from the collimator database.

Anytime a particle hits a collimator flagged as a crystal, the K2 scattering routine [108,109], which is used to treat interactions with standard collimators, directly calls a subroutine named `cry_doCrystal` to start the crystal physics treatment. This subroutine shifts the particle coordinates to the crystal reference system mentioned in Sec. 6.2 and then calls the four other subroutines to compute the interaction with the crystal:

- The `cry_interact` subroutine contains the logical tree in Fig. 6.2 and calculates the specific process that the particle experiences in the crystal, along with its final spatial and angular coordinates.

- The `cry_calcIonLoss` subroutine calculates the energy lost by the particle via ionization while traveling through the crystal.

- The `cry_moveAM` subroutine calculates if a particle experiences inelastic interactions while traveling through the crystal as an amorphous material.

- The `cry_moveCH` subroutine calculates if a particle experiences inelastic interactions while being channeled by the crystal.

The coordinates of the particle at the crystal exit are then transported back into the machine reference system by the `cry_doCrystal` subroutine and the tracking can continue within SixTrack.

If the `WRITE_CRYCOORDS` flag is enabled in the `fort.3` input file, up to three special output files can be produced by the crystal routine. The most important one for crystal collimation studies is the `cry_interaction.dat` file, which contains all the relevant information regarding the interaction of the simulated beam with crystal collimators:

- ID number of the interacting particle.

- Turn in which the interaction took place.

- Name of the crystal collimator where the hit was recorded.

- Numeric label which identifies the specific process experienced by the particle in the crystal:

1	Amorphous
2	Volume reflection
3	Channeling
4	Volume capture
5	Deep inelastic (i.e. the particle is "absorbed" in the crystal)
6	Dechanneling
7	Proton-nucleus elastic (PNE)
8	Proton-proton elastic (PPE)
9	Single diffractive
10	Rutherford
15	Absorption while in channeling
17	PNE while in channeling
18	PPE while in channeling
19	Single diffractive while in channeling
20	Rutherford while in channeling

- Numeric label which identifies the previous interaction of the particle if it had already interacted with a crystal before the current interaction, either with the same crystal in a previous turn or with a different crystal (in case no previous interactions were recorded, the displayed value is -1).

- Transverse coordinates and angles of the particle at the crystal entrance face.

- Deflection angle resulting after the interaction with the crystal.

- Energy of the particle before and after the interaction.

- Angular orientation of the crystal in absolute value (i.e. the beam divergence added to the tilt specified in the collimator database).

Additionally, the `cry_entrance.dat` and `cry_exit.dat` files store for each turn the particle distribution at the entrance and exit of the crystal respectively. However, these files can become very large, especially for simulations with the crystal in amorphous orientation, when a large number of turns is required before the particles are lost. For this reason, the `DEBUG` flag also needs to be enabled in order to produce them.

6.4 Benchmark against the Original Version

This section describes the benchmark campaign that was carried out in order to demonstrate that the results produced by the two versions of the routine when simulating the same scenarios are entirely compatible. A comparison of the CPU time required for high statistics simulations with SixTrack 4 and SixTrack 5 is also shown.

6.4.1 H8 Simulation Comparison

The original routine was benchmarked against data gathered during crystal tests at the H8 extraction line, in the CERN North Area [102]. In order to verify that there were no changes in the crystal physics after the implementation in SixTrack 5, a similar setup was chosen to compare the results produced by the two versions of the routine. In the following,

the resolution of the detectors, which is normally considered when comparing simulations to measurements, will not be taken into account, as it is irrelevant for the sake of the direct comparison of the simulation routines.

A double Gaussian distribution of 400 GeV protons is generated using the parameters reported in Tab. 6.2, and a single passage through a silicon crystal placed at the center of the beam line is simulated. The crystal is 2 mm long and its bending angle is 149 μrad. These parameters were chosen in order to reproduce the experimental data that were used for the benchmark of the original routine. The same setup is used for both a strip and a quasi-mosaic crystal. The outcome of the interaction, in terms of the fraction of particles that experience each specific process, is reported in Tab. 6.3 and 6.4, and visually compared in Fig. 6.3. The comparison shows no significant differences, aside from very small variations in the least likely processes that are within the statistical errors (which have been evaluated as $\sqrt{N}$, where N is the number of simulated particles that experienced a specific process).

Table 6.2: Parameters of the proton beam distribution used in benchmark simulations. The values are given in the machine reference system (x, y, s).

Quantity	Horizontal	Vertical
Mean position [mm]	1.5	0.0
R.m.s. width [mm]	0.1	1.0
Mean angle [μrad]	0.0	0.0
Divergence [μrad]	5.0	5.0

Table 6.3: Fraction of simulated 400 GeV protons experiencing each possible process in a single passage through a 2 mm long silicon strip crystal with a bending angle of 149 μrad. 10^7 particles have been simulated using the parameters in Tab. 6.2.

Process	Strip crystal	
	Original	New
Amorphous	$(16.58 \pm 0.01)\%$	$(16.59 \pm 0.01)\%$
Volume reflection	$(33.27 \pm 0.02)\%$	$(33.28 \pm 0.02)\%$
Channeling	$(44.85 \pm 0.02)\%$	$(44.83 \pm 0.02)\%$
Volume capture	$(0.0439 \pm 0.0007)\%$	$(0.0448 \pm 0.0007)\%$
Deep inelastic	$(0.230 \pm 0.002)\%$	$(0.228 \pm 0.002)\%$
Dechanneling	$(4.823 \pm 0.007)\%$	$(4.836 \pm 0.007)\%$
Proton-nucleus elastic (PNE)	$(0.0895 \pm 0.0010)\%$	$(0.0888 \pm 0.0009)\%$
Proton-proton elastic (PPE)	$(0.0181 \pm 0.0004)\%$	$(0.0179 \pm 0.0004)\%$
Single diffractive	$(0.0167 \pm 0.0004)\%$	$(0.0164 \pm 0.0004)\%$
Rutherford	$(0.00018 \pm 0.00004)\%$	$(0.00018 \pm 0.00004)\%$
Absorption while in channeling	$(0.0449 \pm 0.0007)\%$	$(0.0446 \pm 0.0007)\%$
PNE while in channeling	$(0.0164 \pm 0.0004)\%$	$(0.0172 \pm 0.0004)\%$
PPE while in channeling	$(0.0034 \pm 0.0002)\%$	$(0.0038 \pm 0.0002)\%$
Single diffractive while in channeling	$(0.0042 \pm 0.0002)\%$	$(0.0039 \pm 0.0002)\%$
Rutherford while in channeling	$(0.00008 \pm 0.00003)\%$	$(0.00011 \pm 0.00003)\%$

Table 6.4: Fraction of simulated 400 GeV protons experiencing each possible process in a single passage through a 2 mm long silicon quasi-mosaic crystal with a bending angle of 149 μrad. 10^7 particles have been simulated using the parameters in Tab. 6.2.

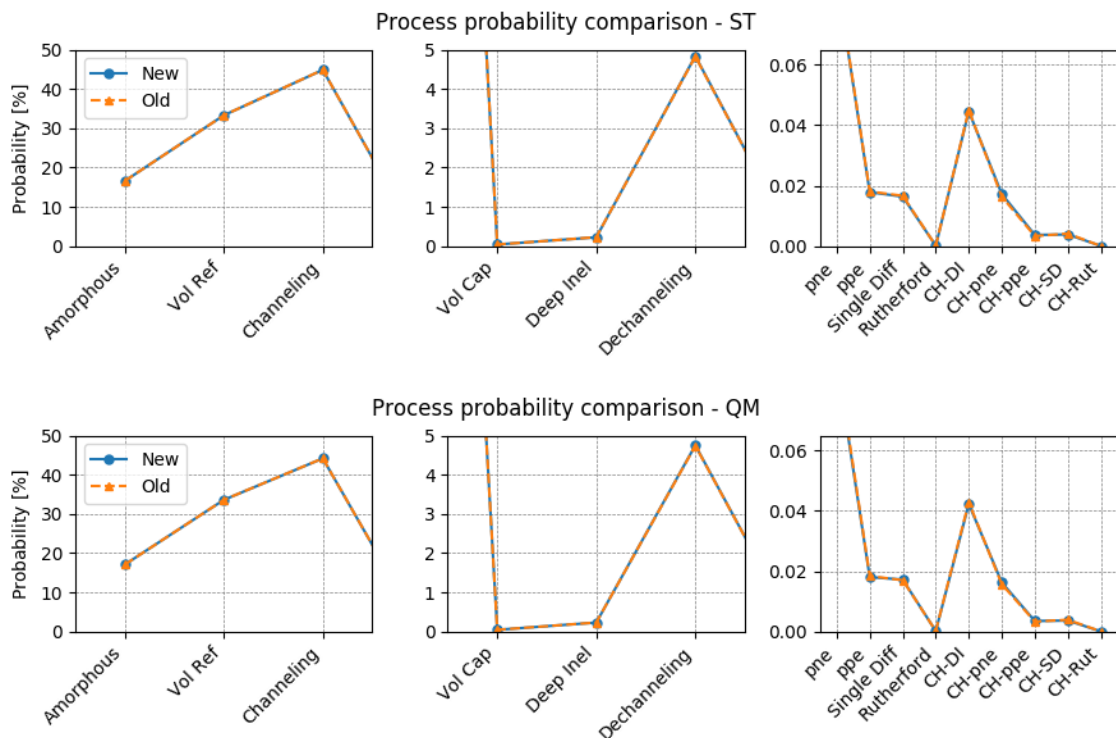| Process	Quasi-mosaic crystal	
	Original	New
Amorphous	$(17.07 \pm 0.01)\%$	$(17.07 \pm 0.01)\%$
Volume reflection	$(33.57 \pm 0.02)\%$	$(33.57 \pm 0.02)\%$
Channeling	$(44.15 \pm 0.02)\%$	$(44.14 \pm 0.02)\%$
Volume capture	$(0.0459 \pm 0.0007)\%$	$(0.0461 \pm 0.0007)\%$
Deep inelastic	$(0.232 \pm 0.002)\%$	$(0.231 \pm 0.002)\%$
Dechanneling	$(4.736 \pm 0.007)\%$	$(4.748 \pm 0.007)\%$
Proton-nucleus elastic (PNE)	$(0.0910 \pm 0.0010)\%$	$(0.0895 \pm 0.0010)\%$
Proton-proton elastic (PPE)	$(0.0184 \pm 0.0004)\%$	$(0.0181 \pm 0.0004)\%$
Single diffractive	$(0.0170 \pm 0.0004)\%$	$(0.0172 \pm 0.0004)\%$
Rutherford	$(0.00023 \pm 0.00005)\%$	$(0.00016 \pm 0.00004)\%$
Absorption while in channeling	$(0.0429 \pm 0.0007)\%$	$(0.0423 \pm 0.0007)\%$
PNE while in channeling	$(0.0157 \pm 0.0004)\%$	$(0.0163 \pm 0.0004)\%$
PPE while in channeling	$(0.0033 \pm 0.0002)\%$	$(0.0035 \pm 0.0002)\%$
Single diffractive while in channeling	$(0.0039 \pm 0.0002)\%$	$(0.0037 \pm 0.0002)\%$
Rutherford while in channeling	$(0.00008 \pm 0.00003)\%$	$(0.00007 \pm 0.00003)\%$

Figure 6.3: Simulated process probability comparison between the newly implemented routine (solid blue) and the original routine (dashed orange) for a strip crystal (top) and a quasi-mosaic crystal (bottom).
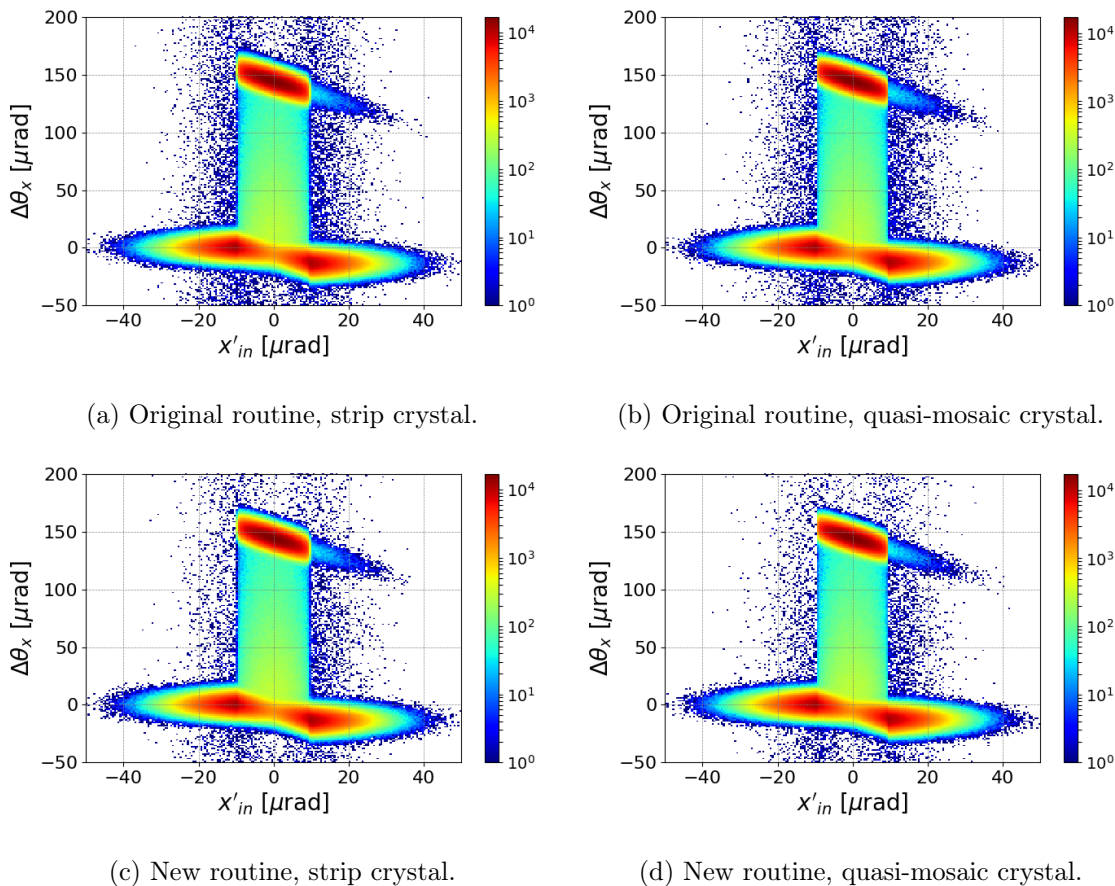
(a) Original routine, strip crystal.

(b) Original routine, quasi-mosaic crystal.

(c) New routine, strip crystal.

(d) New routine, quasi-mosaic crystal.

Figure 6.4: Simulated deflection along the x direction given by the crystal as a function of the entrance angle of the particle. The three main isles reflect the three most likely processes, i.e. channeling (top center of each plot), amorphous (bottom left of each plot) and volume reflection (bottom right of each plot). The parameters of the simulated beam distribution are reported in Tab. 6.2.

To further assess the reproducibility of the results between the two routines, the respective output was also processed to reproduce some of the typical plots used to analyze and display data gathered at the H8 extraction line. One of the most common ways to visualize the results of a single-pass crystal test is to plot the deflection applied to each particle by the crystal along the transverse direction as a function of the entrance angle. The plots produced from the output of the original and newly implemented routine are shown in Fig. 6.4 for both a strip and a quasi-mosaic crystal. This is a more qualitative way to compare the interactions experienced by the simulated particles, and once again no significant differences between the two versions are observed.

Another quantity that can be extracted from measurements and then compared with simulations is the channeling efficiency of the crystal, i.e. the percentage of particles hitting the crystal that actually experience channeling. This quantity can be estimated from the distribution of the deflection angle, typically filtered by selecting only particles whose impact angle falls between $\pm\theta_c$ or $\pm2\theta_c$ (i.e. 5 μrad and 10 μrad respectively for this particular benchmark setup). The channeling efficiency is calculated as the ratio of the integral between 3 σ of a Gaussian function that fits the channeling peak, located around the bending angle of the crystal, and the statistics of the whole distribution [110]. This analysis is per-

(a) 5 μrad cut, strip crystal.

(b) 5 μrad cut, quasi-mosaic crystal.

(c) 10 μrad cut, strip crystal.
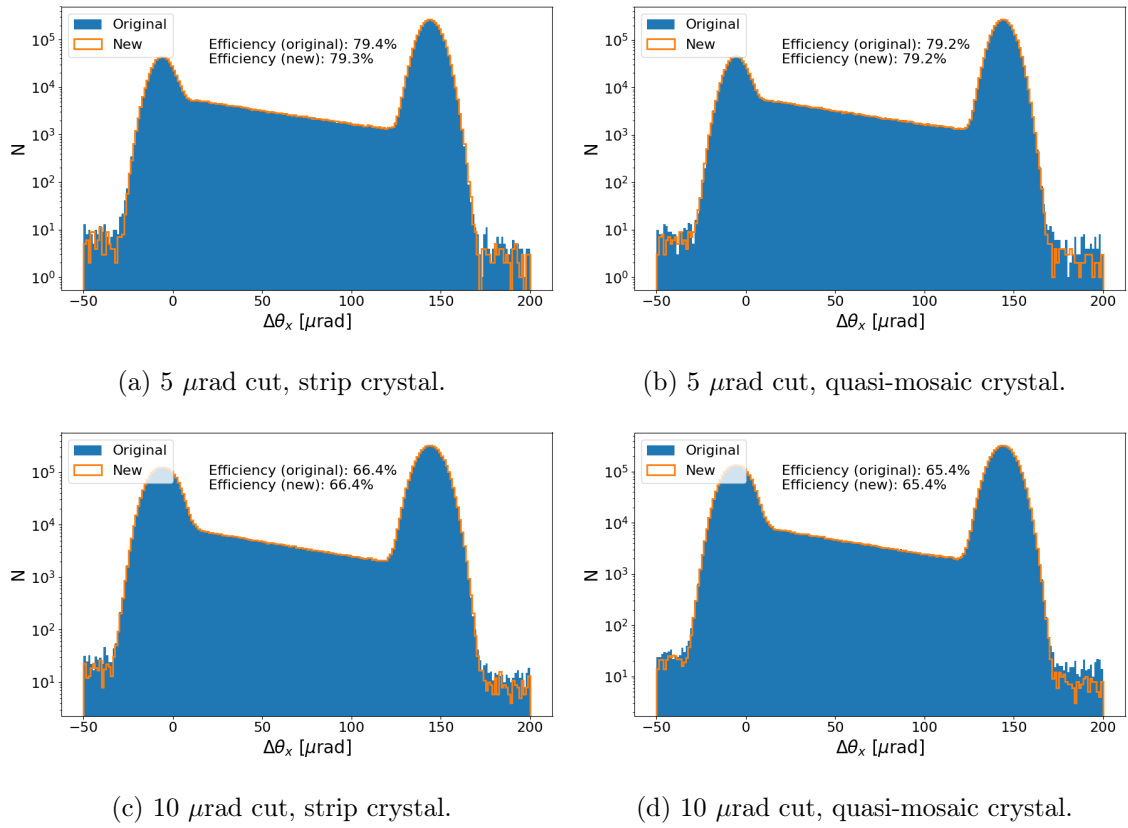
(d) 10 μrad cut, quasi-mosaic crystal.

Figure 6.5: Simulated deflection angle distribution produced by the original routine (blue) and new routine (orange), after the angular cut has been applied. The result of the channeling efficiency calculation for both routines is reported in each plot.
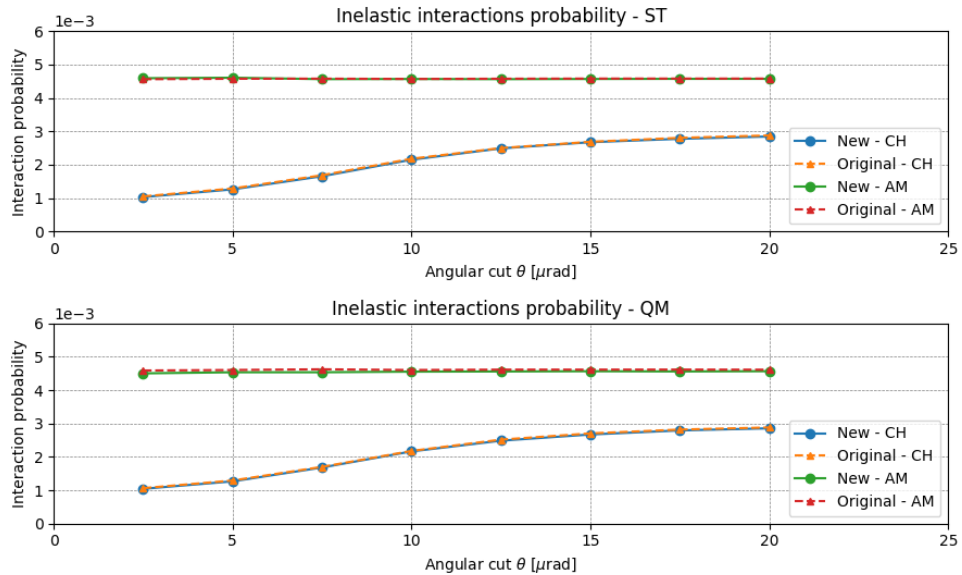

Figure 6.6: Probability of inelastic interactions with the crystal, calculated for the both amorphous and channeling orientations and using both versions of the routine. The same analysis is carried out both for a strip crystal (top) and a quasi-mosaic crystal (bottom).

formed for both a strip and a quasi-mosaic crystal, and the results are shown in Fig. 6.5. The deflection angle distributions produced by the two routines perfectly overlap, and the channeling efficiency calculated with the method described above yields the same values. Finally, another typical quantity estimated from crystal measurements at the H8 extraction line is the probability of inelastic interactions with the crystal, both in channeling and in amorphous orientation. In simulations, this quantity is calculated as the fraction of particles that get absorbed in the crystal or experience a single diffractive interaction, either directly or while in channeling. This is done for various angular cuts applied to the impact angle of the particles, following an approach that was defined for a detailed routine comparison [102]. The simulation setup for the crystal in channeling orientation is the same one that was used to produce previous results, while the crystal is rotated by 200 μrad away from the optimal channeling for the amorphous case. The calculated probabilities are shown in Fig. 6.6 and once again, the two routines show comparable results.

This concludes the first benchmark campaign, which was focused on single-pass simulations and did not show any significant differences between the results produced by the two routines.

6.4.2   LHC Simulation Comparison

The second benchmark campaign was dedicated to understanding the behavior of the new routine for the complex multi-turn simulation setup at the LHC. This was done by simulating angular scans performed with proton beams at the LHC, in order to compare the results of the two routines at higher energy and taking into account multiturn effects. The chosen setup is based on the machine settings used during 2018 crystal tests at the LHC, as reported in Chap. 4, with particular focus on the horizontal strip crystal and vertical quasi-mosaic crystal installed on Beam 1.

The parameters of the two crystals used to define them in simulations are reported in Tab. 6.5. In order to verify that no unexpected behaviors appear when changing the energy of the beam, deflection plots similar to those used for the benchmark reported in Sec. 6.4.1 were produced for simulations at 6.5 TeV. The results are shown in Fig. 6.7. No problematic features are observed in the comparison.

Table 6.5: Parameters of the LHC Beam 1 crystals as defined in simulation.

Crystal	Type	Length [mm]	Transverse dimensions [mm²]	Bending angle [μrad]
Horizontal	Strip	4.0	2.0×50.0	65.0
Vertical	Quasi-mosaic	4.0	5.0×30.0	40.0

Both the LHC injection energy (450 GeV) and flat top energy (6.5 TeV) are chosen as simulation scenarios, and different values of tilt angle with respect to the optimal channeling orientation are applied to both crystals. For each orientation, the ratio of the number of particles absorbed at the crystal and the total number of particles that enter the collimation system (the so-called *first impacts*) is calculated. This allows to reconstruct the familiar profile of local losses as a function of the tilt angle already described in Chap. 4. Finally, the curve is normalized to the level of losses in amorphous orientation, i.e. the mean of the values on the far right and far left areas of the plot. The results for both crystals at both energies are shown in Fig. 6.8. The comparison shows that the two routines produce consistent results, as the profiles overlap very well aside from fluctuations that are within the acceptable range for this kind of setup.

(a) Original routine, strip crystal.

(b) Original routine, quasi-mosaic crystal.

(c) New routine, strip crystal.
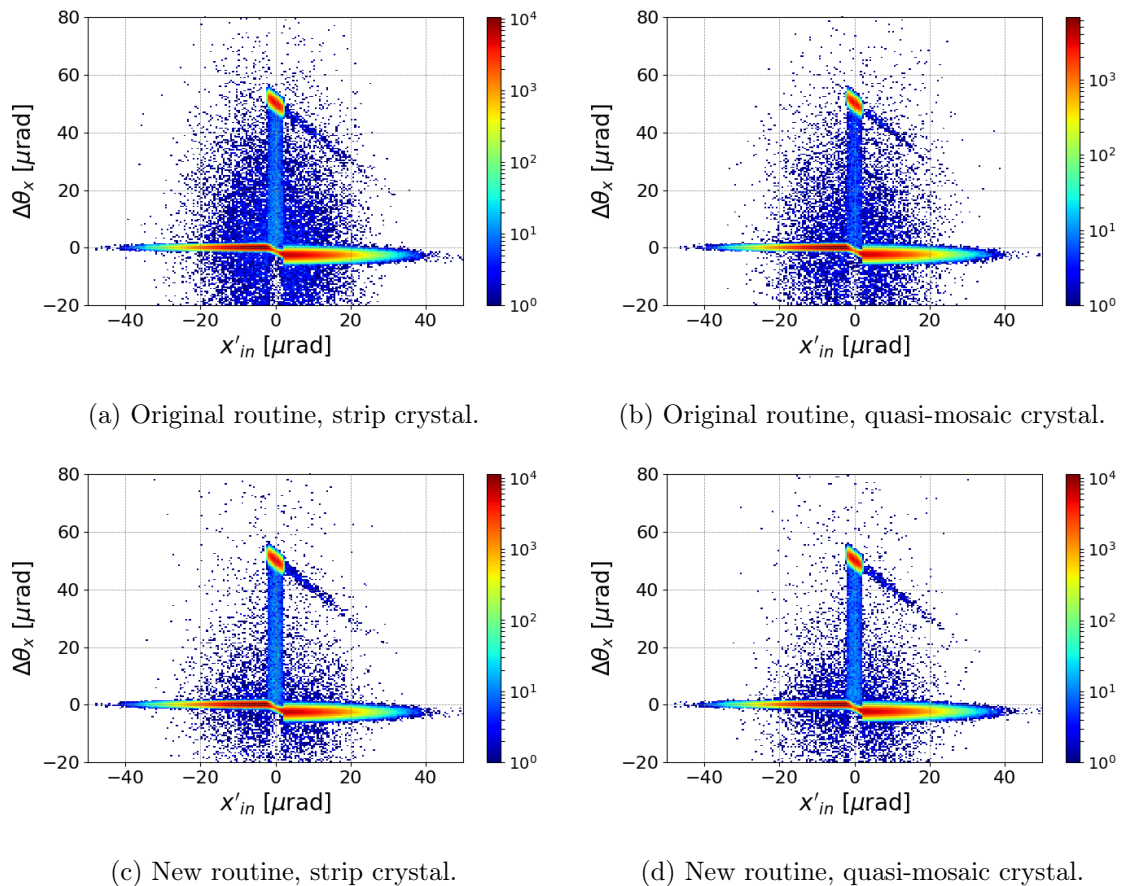
(d) New routine, quasi-mosaic crystal.

Figure 6.7: Simulated deflection as a function of the entrance angle, for simulations of an LHC-type crystal with a 6.5 TeV proton beam.

This completes the benchmark of the newly implemented routine against the original one. As no significant differences were observed, it is safe to say that all the crystal-related physics was maintained intact in the new version.

These simulations were ran on the HTCondor batch system, widely used at CERN for high statistics simulations. The simulation of each angular orientation was split into 10 parallel jobs submitted to an HTCondor cluster at the same time, and the output is merged after all the results have been gathered. This setup offered the opportunity to compare the CPU time needed to complete the simulation of each configuration by the two versions of the routine. To fully understand this comparison it is important to keep in mind a fundamental difference between SixTrack 4 and SixTrack 5, which the two routines are based on respectively:

- SixTrack 4 lacks the "knowledge" of machine aperture, and particles lost on it cannot be removed from the tracking while the simulation is running. Instead, their trajectory needs to be superimposed with the aperture by a separate program called `BeamLossPattern`. This program has to read the file in which the trajectories of all particles are stored, which can occupy several gigabytes, and as such it can take quite a bit of time when the statistics is very high or a large number of turns is simulated. Furthermore, as these "phantom" particles keep being tracked throughout the lattice, they may generate false hits on other elements of the machine that need to be retroactively removed via another program called `CleanInelastic`. For this reason, the total
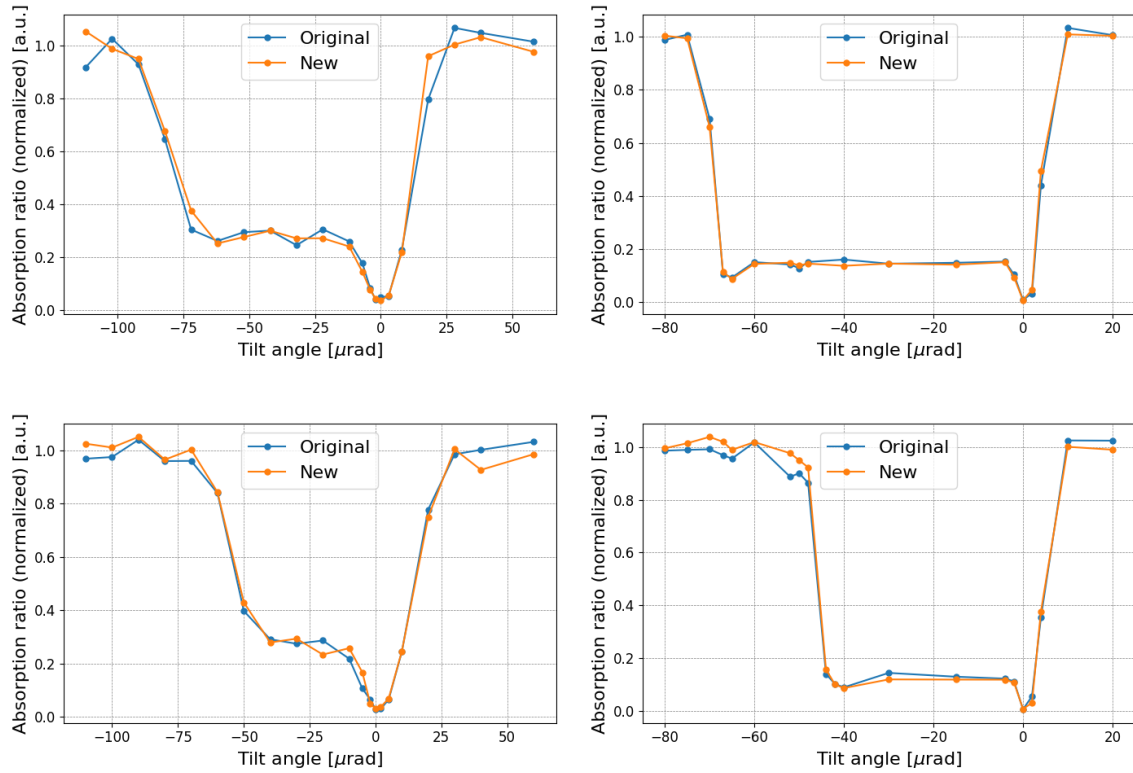
Figure 6.8: Simulated angular scan for the Beam 1 horizontal crystal (top) and vertical crystal (bottom), both at 450 GeV (left) and 6.5 TeV (right).

CPU time required by a simulation with the original routine is the sum of the time spent by SixTrack 4 itself and the time spent by the postprocessing.

- SixTrack 5 implemented the *online aperture check*, a feature that allows to immediately remove particles that hit the machine aperture from the tracking. As a result, not only the number of tracked particles decreases over time as they get lost, but there is no need to read the file containing the simulated trajectories. As writing/reading files is the most time consuming part of a code, this leads to a considerable reduction in the CPU time required for the simulation in many scenarios.

It is also important to note that SixTrack 5 allows to take advantage of LHC@Home, a volunteer computing project that uses internet-connected computers to carry out complex simulations of accelerator physics [111]. SixTrack 4, on the other hand, does not support this feature because of the extremely large trajectory files it generates. This was one of the key motivations, from a technical standpoint, to implement the crystal routine in SixTrack 5.

For the comparison, the mean CPU time across the 10 parallel jobs is calculated for each orientation. Fig. 6.9 shows the ratio between the original and the new version, so a factor higher than 1 indicates that the average CPU time required to run a simulation for that specific orientation is reduced when using the newly implemented routine. A general improvement can be observed at injection and even more noticeably at flat top. The detailed comparison shows the expected results of the migration from SixTrack 4 to SixTrack 5, i.e. the most significant improvements are observed when the crystal is in amorphous orientation. In this configuration, the crystal acts as a very thin primary collimator, so a
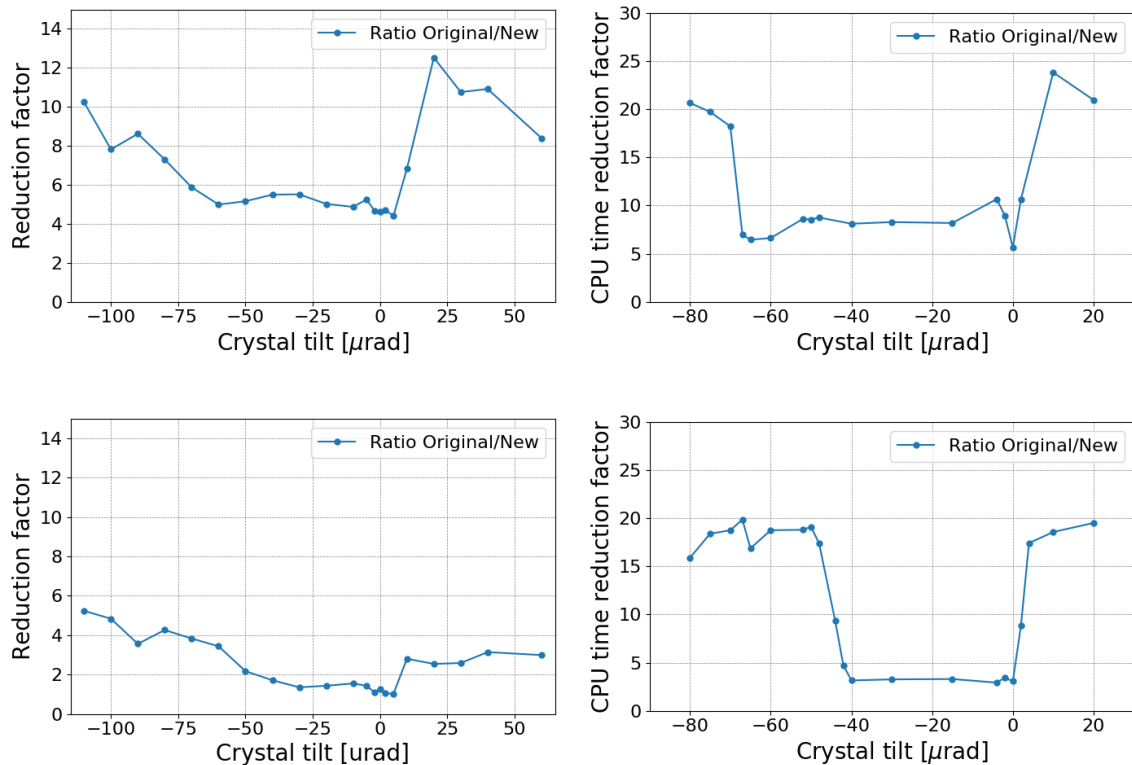
Figure 6.9: CPU time reduction factors between the original and new routine for the Beam 1 horizontal crystal (top) and vertical crystal (bottom), both at 450 GeV (left) and 6.5 TeV (right).

large amount of simulated turns is needed in order to have a statistically significant number of absorptions in the crystal. As a consequence, the time required by the SixTrack 4 postprocessing is massively increased, while SixTrack 5 is not affected as much.

The different gain factors observed for the horizontal and vertical crystals are a consequence of the specific simulation setup used for this comparison. In particular, in simulations for the vertical plane, halo particles spend on average a larger amount of turns in the machine before hitting the crystal, compared to the horizontal plane. As a result, there is an additional time spent tracking particles before the interaction which does not depend on the specific version of SixTrack used, and partially masks the gain in CPU time. Nevertheless, this comparison still gives a good idea of the improvement provided by the migration to SixTrack 5.

6.5 Upgraded Treatment of the Miscut Angle

Crystal collimation simulations normally consider perfectly cut crystals with crystalline planes perfectly aligned to the crystal lateral surface facing the beam. In this case, a channeled particle will always experience a deflection equal to the nominal bending angle no matter its impact parameter $\tilde{b}$, defined as the transverse distance between the lateral surface and the particle impact point in the reduced crystal reference system. However, in reality a non-zero angle between the crystalline planes and the lateral face of the crystal is unavoidable. This is defined as a *miscut angle* (see Fig. 6.10) and causes a series of edge effects that are especially important for particles that hit the crystal at impact parameters
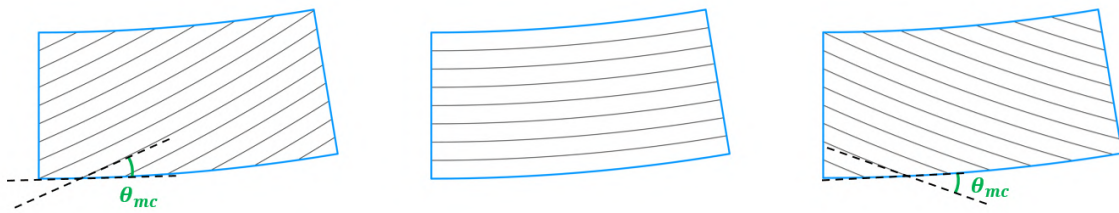
Figure 6.10: Schematic representation of a bent crystal with a positive (left), zero (middle) and negative (right) miscut angle θ_{mc}.

smaller than a certain critical value. Since the relative orientation of the crystalline planes with respect to the incoming beam is altered in this condition, the presence of a miscut angle can hinder the performance of a crystal collimation system and its effects need to be properly evaluated in simulations. For this reason, the design specifics for LHC installations required the miscut angle of crystal collimators to be lower than 40 μrad, based on experience gained at the SPS.

A first treatment of the miscut angle was originally implemented in the crystal simulation routine [76], and with the migration of the routine from SixTrack 4 to SixTrack 5 it was decided to take the chance to also revise and upgrade it. After a brief description of the original model, this section describes the new model that was implemented in the routine, as well as some preliminary simulation results.

6.5.1   Miscut Treatment in the Original Routine

The model implemented in the original routine treats the miscut angle θ_{mc} as an additional tilt applied to the collimator, in order to take into account the different relative orientation between the particle direction and the crystalline planes with respect to a perfectly cut crystal. This covers the interactions of the particles with the bulk of the crystal (green region in Fig. 6.11), while the edge geometry (red region in Fig. 6.11) needs to be treated differently depending on the sign of the miscut angle.

It is important to remember that, after the particle coordinates have been transported into the reduced crystal reference frame used by the routine, the entrance point is always at $s_{cry} = 0$. This means that, for positive miscut angles, the particle always falls within the bulk region of the crystal and as such it travels through the full length of the crystal. In this case, it is enough to add the miscut angle to the particle direction.

For negative miscut angles, on the other hand, two different regions can be identified depending if the impact parameter $\tilde{b}$ is larger or smaller than a critical value $\tilde{b}_c$ which can be found via simple trigonometric considerations:

$$\tilde{b}_c = -l \cdot \tan\theta_{mc}, \tag{6.3}$$

where l is the crystal length in the reduced reference system. The two conditions need to be treated differently:

- If $\tilde{b} \geq \tilde{b}_c$, the particle interacts with the bulk of the crystal and it is enough to add the miscut angle to the particle direction. The length of the path inside the crystal is equal to the length of the crystal itself;

- If $\tilde{b} < \tilde{b}_c$, the particle does not travel through the full length of the crystal and instead exits from the lateral face. The deflection given by the crystal to a channeled particle in
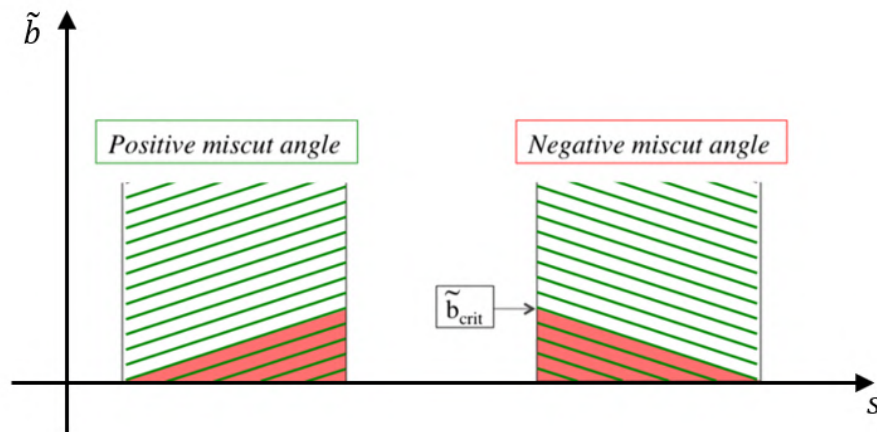
Figure 6.11: Positive and negative miscut angle orientation for the model used by the original routine. The beam moves along the s direction.

this case is lower than the bending angle. The reduced length of the path is calculated in a straight crystal approximation:

$$l_{path} = -\frac{\tilde{b}}{\tan\theta_{mc}}. \tag{6.4}$$

This value is then used to calculate the reduced deflection angle:

$$\theta_{def} = \frac{l_{path}}{R_{curv}}, \tag{6.5}$$

where R_{curv} is the bending radius of the crystal.

This treatment was originally maintained intact along with the rest of the crystal-related physics during the implementation in SixTrack 5. However, some premilinary simulation tests showed that the model needed to be refined, in particular in the way the additional tilt given by the miscut angle was applied to the particle angular coordinates at the entrance and at the exit of the crystal. Fig. 6.12 shows the deflection as a function of the impact angle for single-pass simulations of a 50 μrad bent crystal, with an input distribution of 400 GeV particles hitting exactly at the middle point of the entrance face ($\tilde{b} > \tilde{b}_c$) and a uniform impact angle distribution between -100 μrad and +100 μrad. The channeling isle is correctly shifted along the impact angle axis to coincide with the value of the miscut angle, as that is the angle for which incoming particles are aligned with the tilted crystalline planes. However, the deflection applied to channeled particles changes. This is an artificial feature introduced by this miscut treatment, as in these simulations the impact point is far enough from the edges to allow particles to travel through the whole length of the crystal. Thus, the deflection should be equal to the crystal bending angle no matter the value of the miscut angle (at least for realistic values of a few tens of μrad). Additionally, Fig. 6.12 shows that particles that fall within the channeling range but do not experience channeling have their deflection changed with the miscut angle too, which is another non-physical behavior. These observations sparked the necessity to revise the treatment with particular focus on the consistency of the application of the additional tilt used to describe the miscut. This then lead to a complete rework of the model used to the describe the miscut, in order to
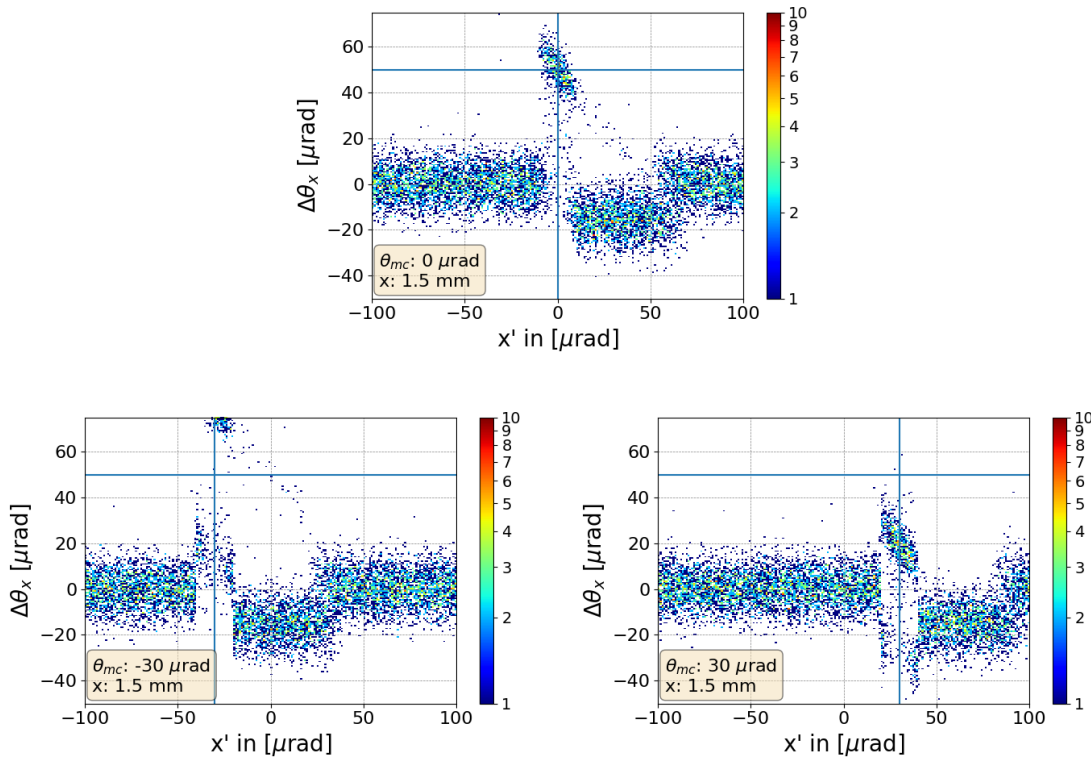
Figure 6.12: Simulated deflection as a function of the impact angle for single-pass interaction of a 400 GeV proton beam. The crystal bending angle is 50 μrad and the entrance face is 3 mm wide along the x direction. The simulated beam hits the middle point of the entrance face, and different values of the miscut angle θ_{mc} are considered with the original treatment. The horizontal and vertical lines in each plot indicate the miscut angle and the bending angle of the crystal, i.e. the area where the channeling isle should be located.

calculate the length of the path inside the crystal and the resulting deflection in a consistent way, which further improved the miscut treatment.

6.5.2   Miscut Treatment in the New Routine

The first upgrade to the miscut treatment for the new routine is a new geometrical model that properly takes into account the curvature of the crystal. This is schematically represented in Fig. 6.13, where the main points that characterize the geometry of the system are shown. Knowing the coordinates of these points in the crystal reference frame allows calculating the direction of a channeled particle when it exits the crystal, as well as the length of its path inside the crystal. The calculation is done before entering the actual physics of the crystal routine and can be summarized in the following steps:

1. The coordinates of P, the center of curvature of the crystalline planes when a miscut angle θ_{mc} is defined, are calculated. If $\theta_{mc} = 0$, this point coincides with R, the center of curvature of the crystal.

2. The coordinates of the exit point F are calculated as the intersection of the crystalline plane centered in P and passing through the entrance point I of the particle with the line defined by the crystal bending angle θ_b. Two different scenarios are considered:

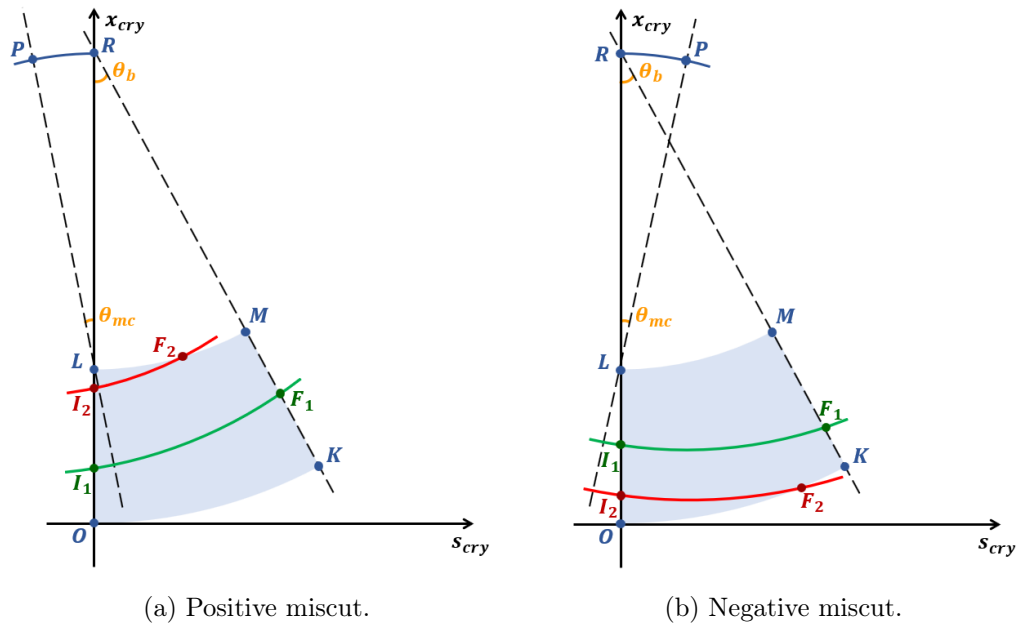(a) Positive miscut.   (b) Negative miscut.

Figure 6.13: Schematic representation of the new miscut model. The bent crystal is represented as a light blue shape in the reduced crystal reference frame. The trajectory of a channeled particle that travels through the full crystal length (green) is shown, along with the trajectory of a channeled particle that exits from the side of the crystal (red).

    a) If F falls within the exit face of the crystal, delimited by M and K, the particle sees the full crystal length and F will be its exit point if it is channeled (green lines in Fig 6.13).

    b) If F does not fall within the exit face, the particle does not see the full crystal length. The exit point F is recalculated as the intersection of the crystalline plane with the lateral face of the crystal, delimited by L and M if the miscut angle is positive or by O and K if the miscut angle is negative (red lines in Fig 6.13).

3. Knowing the coordinates of F and P, the exit angle and path length of the particle in case of channeling are calculated:

$$\theta_{def} = \arcsin \frac{s_F - s_P}{r}, \tag{6.6}$$

$$l_{path} = r \cdot \arccos \frac{2r^2 - [s_F^2 + (x_I - x_F)^2]}{2r^2}, \tag{6.7}$$

where r is the radius of the crystalline plane passing through I.

Afterwards, the physics calculation still uses the relative angle between the direction of the incoming particle and the crystalline planes as in the original treatment, and the path length from the new model is used as the channeling length. Additionally, the dependence of the deflection given by processes other than channeling on the miscut angle was corrected and properly taken into account in the final results. This can be clearly seen in Fig. 6.14, where the deflection plots obtained with the same simulation setup used for Fig. 6.12 are shown. With the new implementation, the miscut angle effectively acts as a shift of the entire plot
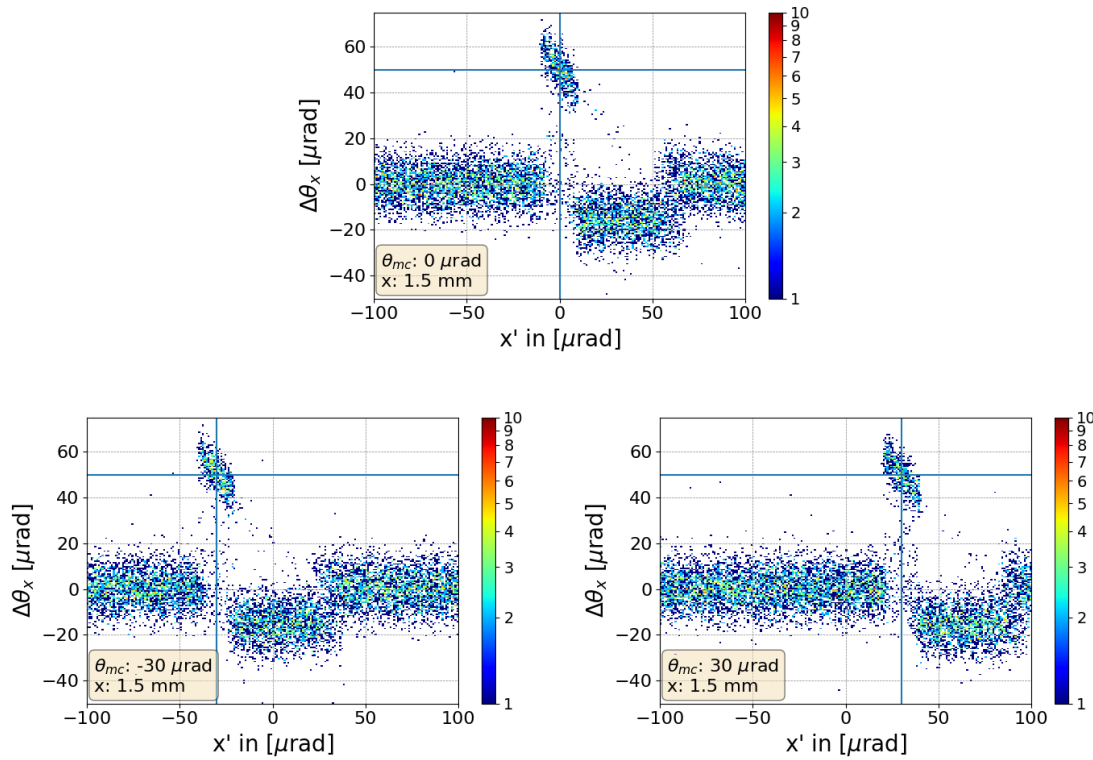
Figure 6.14: Simulated deflection as a function of the impact angle for single-pass interaction of a 400 GeV proton beam. The crystal bending angle is 50 μrad and the entrance face is 3 mm wide along the x direction. The simulated beam hits the middle point of the entrance face, and different values of the miscut angle θ_{mc} are considered with the updated treatment. The horizontal and vertical lines in each plot indicate the miscut angle and the bending angle of the crystal, i.e. the area where the channeling isle should be located.

along the impacting angle with no added effects, which is what is expected if all particles see the full crystal length.

To verify the consistence of the new treatment, it is crucial to simulate also the edge effects that appear when $\tilde{b} < \tilde{b}_c$. For this reason, the new routine was tested in a series of simulations using a similar setup to the preliminary studies described in Sec. 6.5.1 to verify the original model. All simulated particles hit the crystal entrance face in the same spot, but with progressively smaller impact parameter (from 40 nm down to 5 nm in steps of 5 nm). The impact angle is uniformly distributed between -100 μrad and +100 μrad. A negative miscut of -10 μrad is considered. This configuration was chosen as the most significant for crystal collimation studies, where the impact parameter of halo particles on primary collimators is expected to be smaller than 1 μm from diffusion measurements. As shown in Fig. 6.15, channeled particles are progressively less deflected as they hit closer to the edge of the entrance face, reflecting the fact that their path inside the crystal becomes progressively smaller. It is also worth noting that the angular acceptance range of the volume reflection is adjusted to the effective deflection given by the crystal. This is another correction with respect to the original treatment, where the volume reflection range was instead fixed to the crystal bending angle.
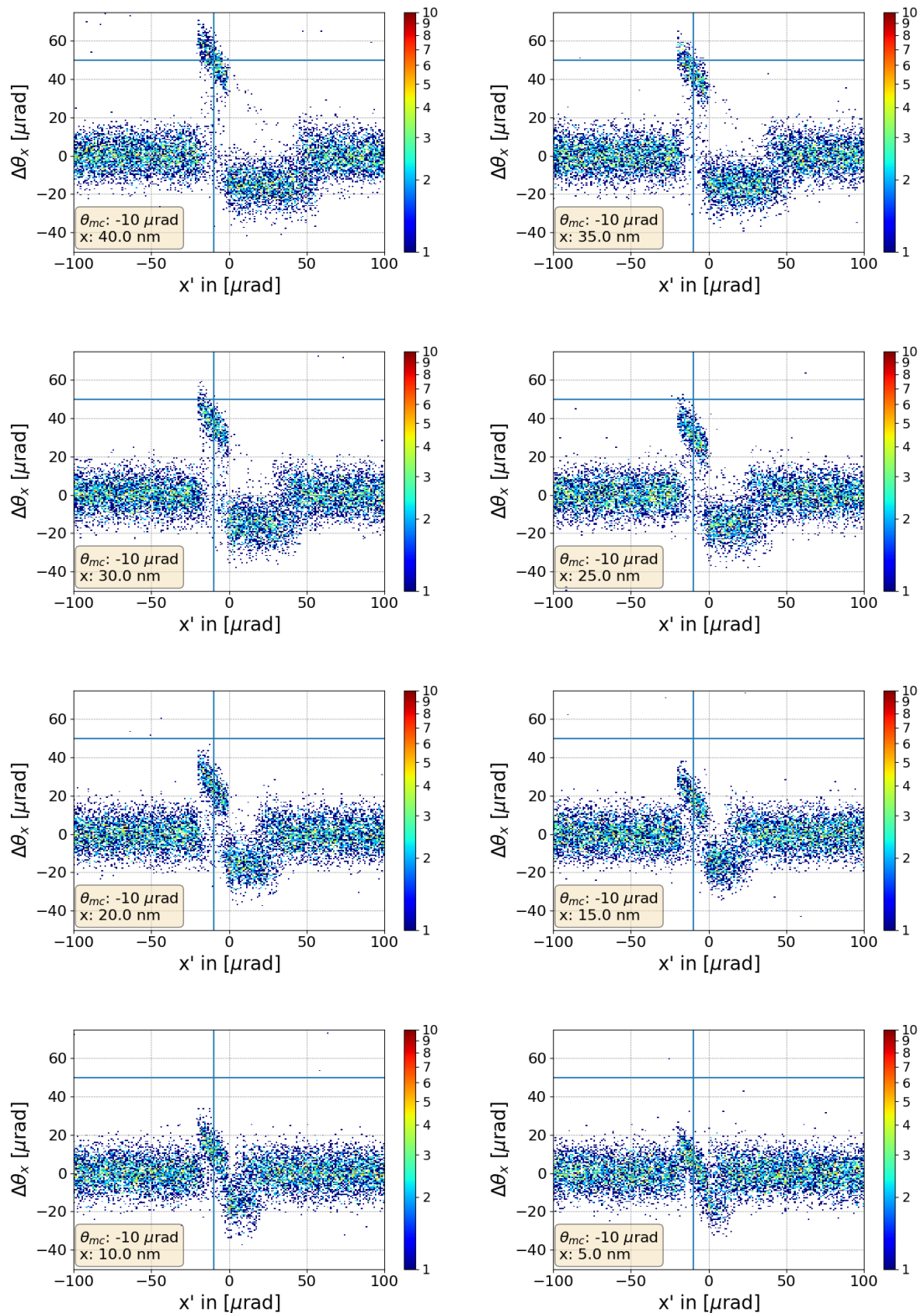
Figure 6.15: Simulated deflection as a function of the impact angle for single-pass interaction of a 400 GeV proton beam. The crystal bending angle is 50 μrad and the entrance face is 3 mm wide along the x direction. The impact parameter of the simulated beam is progressively reduced. The horizontal and vertical lines in each plot indicate the miscut angle and the bending angle of the crystal, i.e. the area where the channeling isle is located if the particles see the full crystal length.

6.5.3   Premilinary Multi-turn Simulation Results

In view of the possible use of crystal collimation in operations at the LHC, it is extremely important to correctly identify tolerance ranges for the design parameters of crystal devices. For this reason, it is planned to exploit the newly implemented miscut treatment in order to evaluate its effects in multi-turn simulation scenarios.

Given the small impact parameters expected when halo particles are intercepted by a collimator, negative miscut values are the most relevant conditions for crystal collimation studies. As described in previous sections, if its impact parameter is smaller than the critical value $\tilde{b}_c$, a channeled particle experiences an effective deflection which is lower than the nominal bending of the crystal, and as a result populates intermediate amplitudes between the primary beam and the fully channeled halo. This effect could be observed in a linear scan with a downstream secondary collimator. As the collimator jaw moves towards the primary beam, a continuous rise in the BLM signal would be observed after the channeled halo has been intercepted.
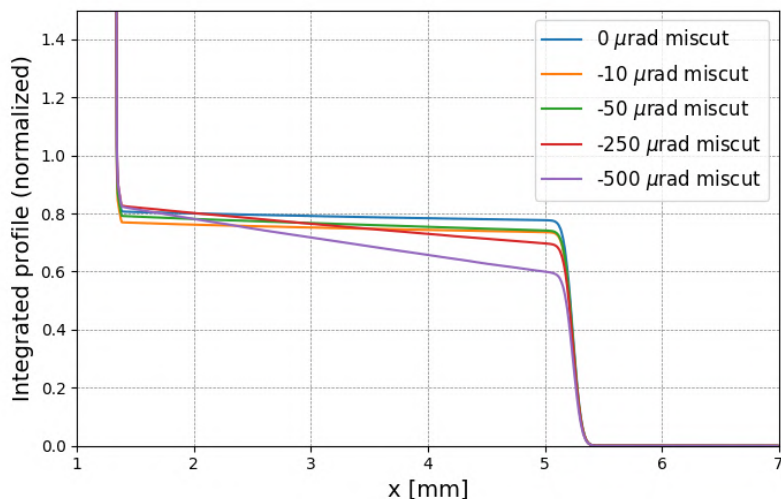

Figure 6.16: Simulated linear scan for the horizontal crystal on Beam 1 at 6.5 TeV. The results for different values of the miscut angle are shown.

As noted in Chap. 4 and 5, a similar effect was observed in crystal collimation tests at flat top energy with the crystal installed on the horizontal plane of Beam 1. The main working hypothesis attributes this behavior to the large bending angle of the crystal, which may lead to an increase in the population of dechanneled particles [11]. However, the possibility of these observations being at least partly related to a miscut angle was explored in a dedicated simulation campaign using the newly implemented treatment. Preliminary results of simulated linear scans for different values of the miscut angle are shown in Fig. 6.16. The effects described above can be clearly seen as a slope in the otherwise flat profiles. However they become significant only in presence of a very high miscut angle (more than 5 times the nominal bending angle), which would be outside of the design specifics by a large margin. This is a consequence of the parameters of the simulated beam halo, which match the same setup routinely used for crystal collimation studies at 6.5 TeV and were chosen in order to have a reasonable computing time [16]. The resulting distribution of impacts at the crystal entrance face is shown in Fig. 6.17. Fig. 6.15 demonstrates that the effects of a negative miscut angle become noticeable only for small impact parameters, of the order of tens of nm.
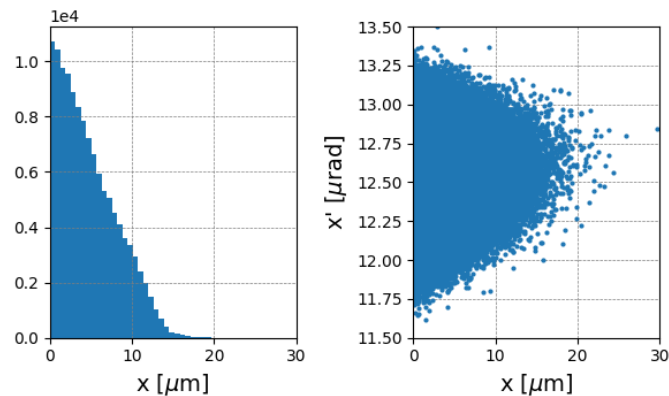
Figure 6.17: Distribution of simulated impacts on the crystal entrance face.

It is clear that with such a wide simulated distribution of impacts, the majority of particles do not experience these edge effects, which become dominant only for very high values of the miscut angle.

These results are not final. Various simulation scenarios will be explored as a follow up to this work, in order to evaluate the effects of the crystal miscut angle with narrower impact distributions. The possibility of benchmarking these results against experimental data will also be considered.

6.6 Simulation Challenges for Crystal Collimation with Ion Beams

As already mentioned, the routine described in this chapter is capable of accurately simulating the interaction of proton beams with crystal collimators. On the other hand, the modeling of ion beams poses significant challenges. In particular, additional ion species are produced in inelastic interactions with matter by fragmentation and dissociation of the impacting ion. These secondary products need to be properly generated, in order to accurately simulate a realistic loss pattern. This factor has to be taken into account also when simulating coherent interactions between ions and crystal collimators. While SixTrack is capable of simulating the interaction of ions with standard collimators [99], the modeling of crystal-specific physics – which requires the detailed knowledge of coherent processes and interactions with the atoms of the crystalline lattice – is still under development.

At present, a simulation environment that is able to treat crystal interactions in a multi-turn tracking setup for ion beams is not available. Various options are currently being explored, by interfacing SixTrack with other codes (such as FLUKA [112–114] or Geant4 [115, 116]) to properly treat the physics of the ion-crystal interaction. However, the development of these tools is beyond the scope of this work.

Chapter 7

Other Applications of Bent Crystals

Bent crystals are mainly studied at the LHC for beam cleaning purposes, as a possible way to improve the performance of the collimation system in view of the HL-LHC upgrade. However, the promising results and the operational experience gathered during Run 2 with this novel collimation technique sparked interest in deploying bent crystals in a wide range of contexts.

This chapter focuses on three setups that were explored at the CERN accelerator complex with proton beams:

- Crystal collimation for reduced detector background during the 2018 special physics run at the LHC at injection.

- Proof-of-concept for a double-crystal channeling setup at the SPS.

- Channeling of higher order beam halos at the LHC.

In all cases, simulation studies were crucial to determine the feasibility of the setup and predict the performance of the system in these unusual settings, as well as understand the outcomes of experimental tests.

7.1 Crystal Collimation for Reduced Background on Forward Physics Detectors

Throughout Run 2 (2015-2018), the LHC was operated with proton beams at the top energy of 6.5 TeV, with typical beam populations of a few 10^{14} particles. In 2018 however, a special run at the injection energy of 450 GeV was requested by the forward physics community, using special optics with high β^*, which translates into a much larger beam size at the interaction points than in standard operations [117].

The main physics motivation was the measurement of the proton-proton elastic cross section and the extrapolation of its nuclear part towards low values of momentum transfer. Dedicated detectors housed in movable Roman Pots (XRPs) are transversely placed very close to the circulating beams in order to intercept particles scattered at small angles as a result of collisions with low momentum transfer. Two sets of four XRP stations are installed on the vertical plane 210 m and 250 m downstream of the collision points in IP1 and IP5, which are operated by the ATLAS (ALFA) [63] and TOTEM [64] collaborations respectively.

The setup of this run posed several challenges from the accelerator physics point of view [65]. In particular, the main constraint from the collimation point of view came from the request of the experiments to keep the XRPs at an aperture of at most 3 σ, smaller than the standard

Table 7.1: Operational settings of the LHC collimation system and Roman Pots during the high-β^* physics run with proton beams in 2018. The crystal collimators are indicated as TCPCV.A6[L/R]7.B[1/2] [106].

Device name	IR	Plane	Standard Collimation [σ]	Crystal Collimation [σ]
TCL.4[R/L]1.B[1/2]	1	H	OUT	OUT
TCL.5[R/L]1.B[1/2]	1	H	OUT	OUT
TCL.6[R/L]1.B[1/2]	1	H	OUT	OUT
XRP.A7[R/L]1.B[1/2]	1	V	3.0	3.0
XRP.B7[R/L]1.B[1/2]	1	V	3.0	3.0
TCTPH.4[L/R]2.B[1/2]	2	H	13.0	13.0
TCTPV.4[L/R]2.B[1/2]	2	V	2.7	13.0
TDI.4[L/R][2/8].B[1/2]	2/8	V	OUT	OUT
TCLIA.4[L/R][2/8].B[1/2]	2/8	V	OUT	OUT
TCLIB.6[L/R][2/8].B[1/2]	2/8	V	OUT	OUT
TCP.6[L/R]3.B[1/2]	3	H	5.3	5.3
TCSG.5[L/R]3.B[1/2]	3	H	6.3	6.3
TCSG.4[R/L]3.B[1/2]	3	H	6.3	6.3
TCSG.A5[R/L]3.B[1/2]	3	S	6.3	6.3
TCSG.B5[R/L]3.B[1/2]	3	S	6.3	6.3
TCLA.A5[R/L]3.B[1/2]	3	V	2.7	2.7
TCLA.B5[R/L]3.B[1/2]	3	H	9.0	9.0
TCLA.6[R/L]3.B[1/2]	3	H	9.0	9.0
TCLA.7[R/L]3.B[1/2]	3	H	9.0	9.0
TCTPH.4[L/R]5.B[1/2]	5	H	13.0	13.0
TCTPV.4[L/R]5.B[1/2]	5	V	2.7	13.0/2.7
TCL.4[R/L]5.B[1/2]	5	H	OUT	OUT
TCL.5[R/L]5.B[1/2]	5	H	OUT	OUT
XRP.D6[R/L]5.B[1/2]	5	V	3.0	3.0
XRP.B6[R/L]5.B[1/2]	5	V	3.0	3.0
TCL.6[R/L]5.B[1/2]	5	H	OUT	OUT
TCDQ.4[R/L]6.B[1/2]	6	H	8.0	8.0
TCSP.A4[R/L]6.B[1/2]	6	H	7.5	7.5
TCP.D6[L/R]7.B[1/2]	7	V	3.2	3.2
TCP.C6[L/R]7.B[1/2]	7	H	4.0	4.0
TCP.B6[L/R]7.B[1/2]	7	S	5.7	5.7
TCSG.A6[L/R]7.B[1/2]	7	S	5.0	5.0
TCPCV.A6[L/R]7.B[1/2]	7	V	OUT	2.5
TCSG.B5[L/R]7.B[1/2]	7	S	5.0	5.0
TCSG.A5[L/R]7.B[1/2]	7	S	5.0	5.0
TCSG.D4[L/R]7.B[1/2]	7	V	5.0	5.0
TCSG.B4[L/R]7.B[1/2]	7	H	5.0	5.0
TCSG.A4[L/R]7.B[1/2]	7	S	5.0	5.0
TCSG.A4[R/L]7.B[1/2]	7	S	5.0	5.0
TCSG.D5[R/L]7.B[1/2]	7	S	5.0	5.0
TCSG.E5[R/L]7.B[1/2]	7	S	5.0	5.0
TCSG.6[R/L]7.B[1/2]	7	H	5.0	5.0
TCLA.A6[R/L]7.B[1/2]	7	V	2.5	2.7
TCLA.B6[R/L]7.B[1/2]	7	H	8.0	8.0
TCLA.C6[R/L]7.B[1/2]	7	V	2.7	2.7
TCLA.D6[R/L]7.B[1/2]	7	H	10.0	10.0
TCLA.A7[R/L]7.B[1/2]	7	H	8.0	8.0
TCTPH.4[L/R]8.B[1/2]	8	H	13.0	13.0
TCTPV.4[L/R]8.B[1/2]	8	V	2.7	13.0
TCTPH.4[L/R]1.B[1/2]	1	H	13.0	13.0
TCTPV.4[L/R]1.B[1/2]	1	V	2.7	2.7/13.0

injection settings of primary collimators (5.7 σ). This translated into much tighter settings than normal operations for the collimation system. The commissioning of the machine in this unusual configuration was simplified by imposing a limit on the beam intensity (up to $6 \cdot 10^{11}$ protons per beam). This limit allowed to avoid lengthy validation steps for such a short run, while being still sufficient to fulfill the requirements of the ALFA and TOTEM experiments. The most limiting factor, however, was the working principle of the standard LHC collimation system, which uses Multiple Coulomb Scattering in amorphous collimators to increase the transverse particle amplitude in a multi-turn cleaning process. The unavoidable background generated on the XRPs, placed extremely close to the primary beam, was deemed too high in initial tests and put the feasibility of the setup in question [118]. To address these issues, after extensive simulation studies, a two-stage collimation scheme was conceived, based around tungsten collimators (chosen for their high absorption efficiency) and featuring the tightest operational margins ever used in the LHC [67].

At the same time, an alternative scheme based on crystal collimator was proposed. The reduced rate of inelastic interactions experienced by channeled particles promises faster cleaning and reduced multi-turn halo population, potentially allowing more relaxed collimation settings. The work presented in this section was dedicated to the initial simulations and beam commissioning that demonstrated the feasibility of such a setup. A detailed description of the outcome of the special physics run is outside the scope of this thesis and can be found in [106].

7.1.1 Preparation of the Special Physics Run

Tab. 7.1 reports the settings of the two proposed collimator schemes. In the two-stage collimation system, referred to as the *standard system* from here on, the primary collimators are set at an aperture of 2.5 σ, with the TCLAs acting as the secondary stage and retracted by 0.2 σ. The XRPs feature an additional retraction of 0.3 σ from the secondary stage, reaching the target settings of 3 σ. Such tight settings make the system very sensitive to even small orbit drifts, which could potentially break the collimation hierarchy and cause a large increase of the background at the XRPs.

These issues lead to the idea of using one vertical crystal per beam as the primary collimation stage, and profiting from the reduced rate of single diffractive events in crystal collimators to achieve faster cleaning and a more stable background level. The secondary collimators are still kept at a 0.2 σ retraction, in order to allow the XRPs to be placed at 3 σ. Semi-analytical studies were carried out, using the matrix formalism introduced in Sec. 3.2 to predict the trajectory of a kicked particle using the high-β^* optics. The results shown in Fig. 7.1 demonstrate that the channeled halo can be safely intercepted by the secondary collimators on both beams even in this extreme configuration.

As part of this thesis work, complete multi-turn tracking simulations with SixTrack were carried out to validate this layout in terms of the expected background at the eight XRP stations, by scoring the number of impacts on the active area of each detector. As a starting point, the hierarchy of all collimator stages was kept similar to the standard system. These studies allowed to optimize and relax the collimator settings, and the final layout features the following differences from the standard system:

- TCTPs in IR2 and IR8 in both beams are opened from 2.7 σ to 13 σ;

- TCTPs in IR5 of Beam 1 and in IR1 of Beam 2 are opened from 2.7 σ to 13 σ.

Fig. 7.2 shows simulated loss maps for the standard two-stage scheme and the crystal scheme with the settings described above. While losses on cold elements of the machine are generally
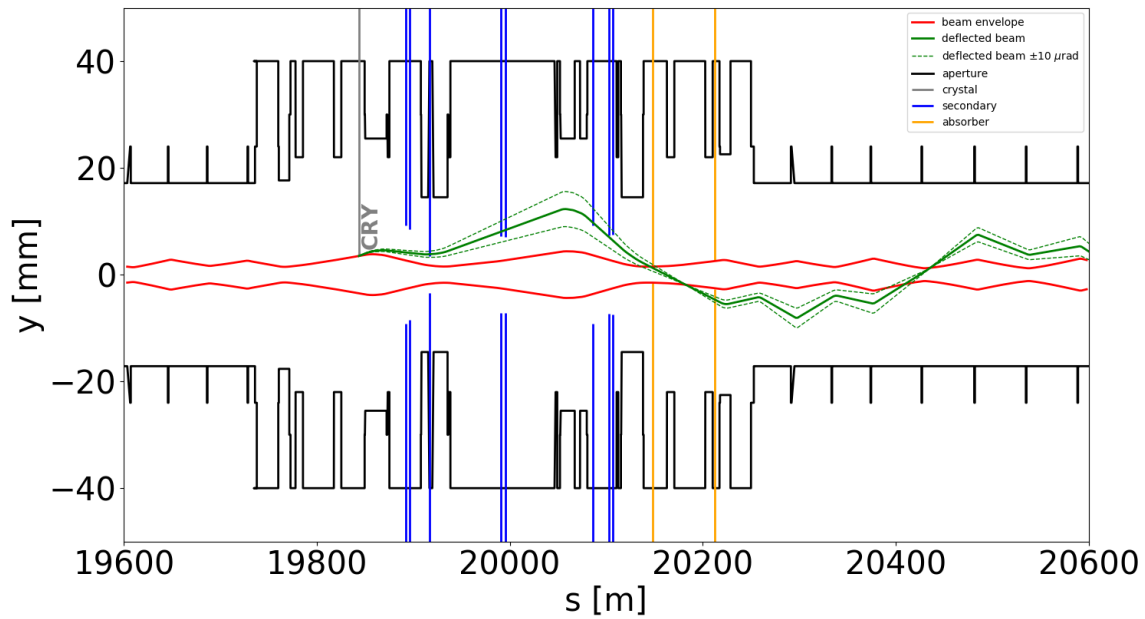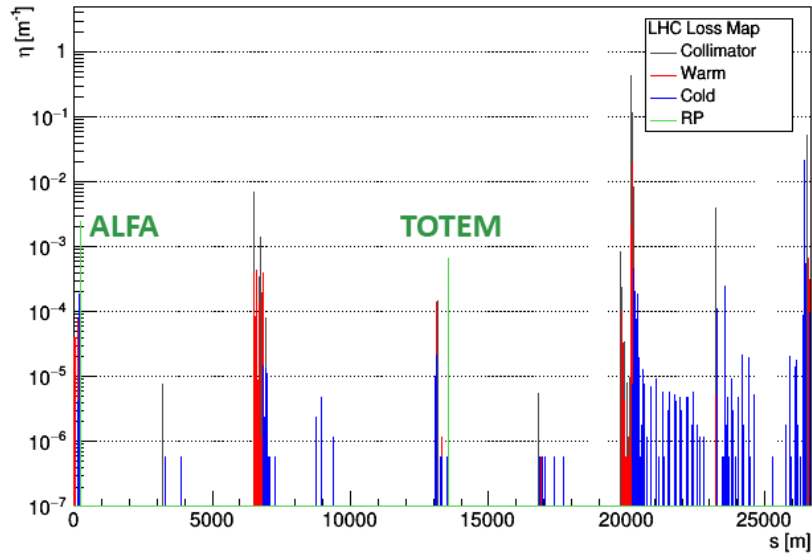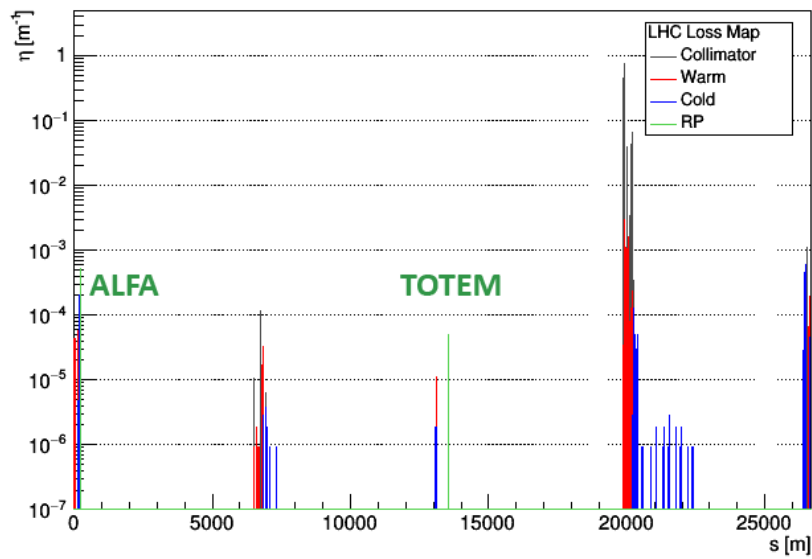
(a) Beam 1.
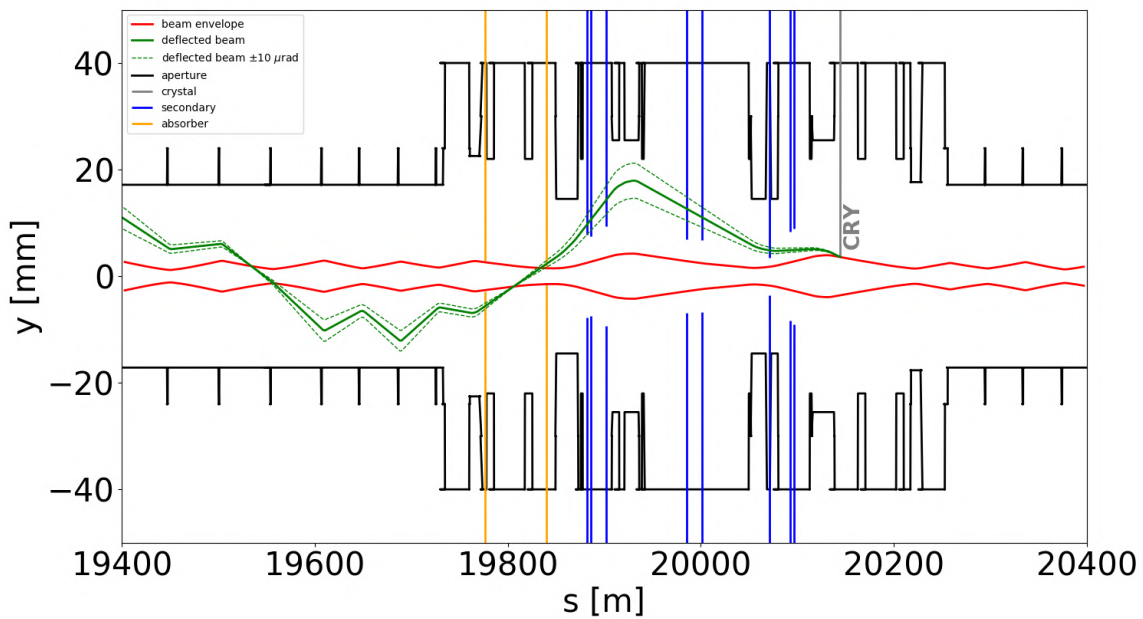
(b) Beam 2.

Figure 7.1: Predicted trajectory of the channeled beam on the vertical plane of Beam 1 (top) and Beam 2 (bottom), using high-β^* optics and settings at 450 GeV. The crystals and the TCSGs used to intercept the channeled halo are set at 2.5 σ and 5.0 σ respectively. The TCLAs are kept at 2.7 σ as in the tight standard system.

(a) Standard collimation scheme.

(b) Crystal collimation scheme.

Figure 7.2: Simulated loss maps for the standard system (top) and crystal system (bottom) for proton beams at 450 GeV with high-β^*. The simulated signal is normalized to the statistics (i.e. the number of particles that entered the collimation system). The XRPs are highlighted in green.

reduced all around the ring when crystals are deployed, this was not the main concern given the very low stored energy of the beams during the special physics run (< 30 kJ). The focus was instead on the simulated signal at the pots (highlighted in green). The ratio between the simulated background with the standard and crystal scheme is shown in Fig. 7.3, where values higher than 1 indicate a reduction of the impacts on the XRPs when crystals are deployed.

The simulation setup used for these studies was aimed at an early qualitative assessment of the performance of the crystal system. As such, a number of approximations were used, including the modelization of the XRPs as black absorbers. A detailed treatment, where the proper composition, orientation and active area of the XRPs are taken into account, is described in [106]. Nonetheless, these promising early results allowed to deploy crystal collimation in preparatory tests.
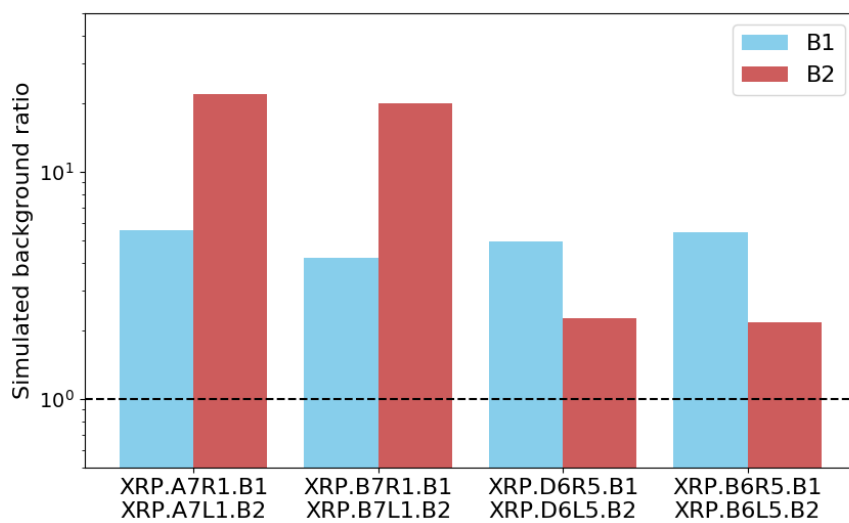
Figure 7.3: Ratio between the background observed in simulations with the standard system and the background observed in simulations with the crystal system at the ALFA and TOTEM XRPs.

7.1.2   Operational Performance

Initial tests were performed on the 2nd October 2018, where promising results were obtained with both the standard and crystal-based schemes. In particular, the expected performance of the crystal system was qualitatively confirmed, leading to the decision to keep this alternative scheme as a viable option for the special physics run. The preparatory run was used to find the alignment position and optimal channeling orientation of both crystals. As shown in Fig. 7.4, the whole setup procedure only took about 25 minutes, thanks to the experience gathered in test with proton beams. For the first time since the installation of the crystal devices, these settings were inserted in an automatic sequence that allowed the deployment of crystals by the operators even without the presence of system experts. An example of crystal insertion during the physics run is shown in Fig. 7.5. The initial loss spike shows that the halo of the circulating beam was touched when inserting the crystal. After the procedure was completed, a small rotation from the final angular settings was performed to verify that the crystal was actually inserted directly in channeling conditions.
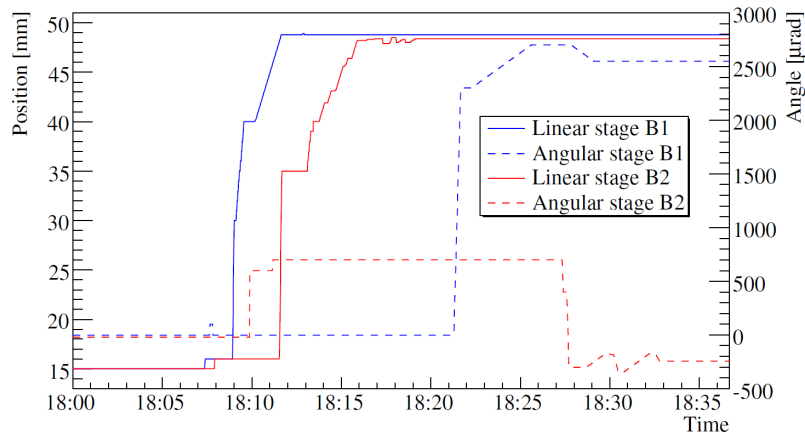
Figure 7.4: Overview of the alignment procedure for the two vertical crystals on Beam 2, performed on the 2nd October 2018 [106].
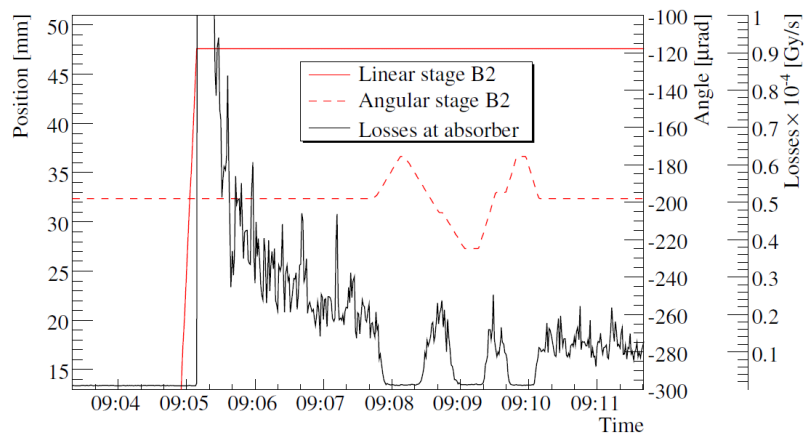

Figure 7.5: Overview of the automatic insertion in channeling orientation and preliminary checks of the crystal in Beam 2 [106].

Indeed, losses at the absorber used to intercept the channeled halo are reduced in the rotation, which means that channeling conditions are lost when the crystal is moved away from the final settings applied by the automatic sequence. This check was performed in all fills in which crystal collimation was used, showing consistent results and demonstrating reliable channeling performance along the entire run [106].

The physics run itself took place from 11th to 13th October 2018. After a first setup fill used to validate the results obtained in previous tests, two fills were dedicated to data taking with the standard and crystal collimation schemes respectively. In both cases, the beams were scraped using vertical primary collimators to reduce their width from 5.7 σ to 2.5 σ, before setting the other collimators and the XRPs to the planned apertures. A strong preference for the standard system was then expressed by ALFA, while TOTEM was satisfied by both schemes, although their data quality was significantly better with crystal collimation. It was then decided to continue with the standard scheme for the following fills, until a re-centering of some collimators was needed in order to maintain the required 0.2 σ margin between the first and second collimation stage. In the fills following this procedure, the data quality was significantly worsened for TOTEM, leading to the decision to alternate between the standard and crystal scheme for the remaining fills. At the end of the run, the standard and crystal collimation schemes had been used for 9 and 3 fills respectively.
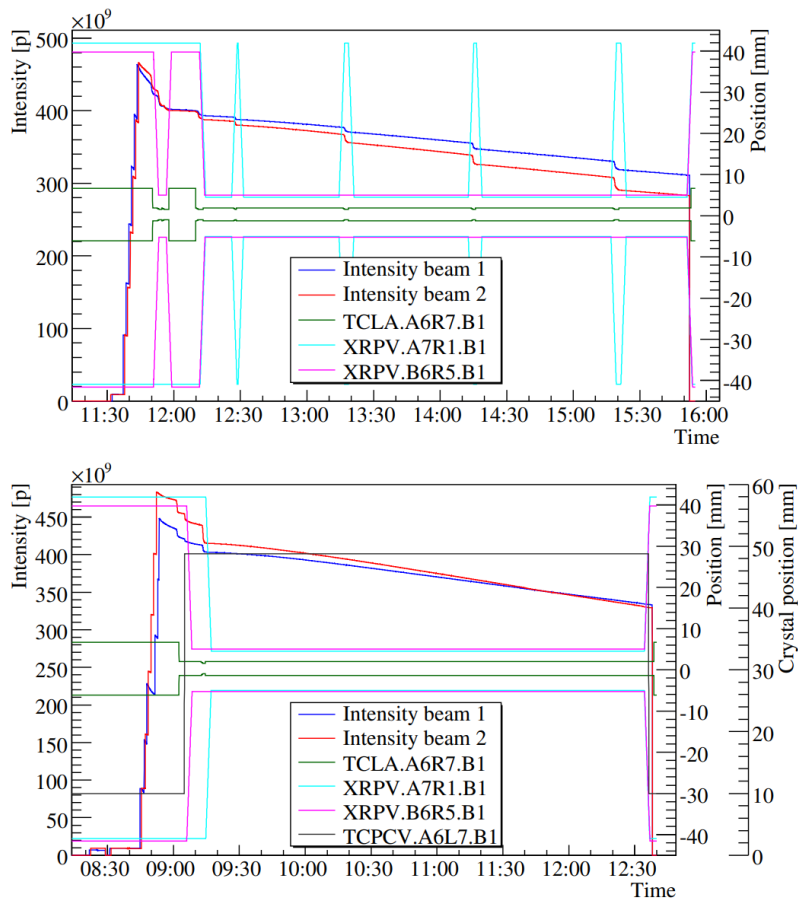
Figure 7.6: Overview of a fill using the standard collimation system (top) and a fill using the crystal collimation system (bottom). TCLA, XRPV and TCPCV are the linear positions of the collimator used for scraping and primary stage (in the case of standard collimation), Roman Pots and crystal respectively. For the crystal, 0 mm corresponds to the completely retracted position, while for double movable objects it corresponds to the geometrical center of the beam pipe [106].

The main observable difference between the two schemes was the speed with which the multi-turn halo was repopulated over time for both experiments, leading to the observed background rate. The multi-turn halo is directly related to the number of turns required on average by particles entering the collimation system to be completely absorbed. If the speed at which particles are removed is lower than the speed at which particles enter the collimation system, then the multi-turn halo grows over time. As can be see in Fig. 7.6, about one re-scraping every hour was needed when using the standard collimation system, in order to prevent the background at the detectors to increase above the acceptable level. On the other hand, this procedure was not needed when crystal collimation was in place, allowing a 10% more efficient data taking with no need to take the pots in and out for ALFA. This can be explained by the fact that the crystal collimation scheme offers a faster halo removal rate, i.e. the vast majority of the particles are removed from the circulating beam in the same turn in which they hit the primary collimation stage. On the other hand, using the standard scheme particles spend on average more turns in the machine before getting absorbed after entering the collimation system. This hypothesis was later confirmed

in simulations. A detailed description of the dynamics is outside the scope of this thesis and can be found in [106].

7.2   Double-Crystal Measurements at the SPS

Particles channeled by a bent crystal can experience a deflection equivalent to the effect of a magnetic field of hundreds of Tesla over the same length. In the context of Physics Beyond Colliders (PBC), it was proposed to explore the possibility of using this property to measure the magnetic dipole moment of short-lived baryons in high energy hadron colliders [5] by inducing the precession of the polarization vector via a double-crystal setup. The first crystal deflects halo particles towards a fixed target, while the second crystal rotates the polarization vector of the baryons produced in the collision and steers them towards a detector [71]. Layouts for the application of this concept at the LHC have been studied, demonstrating their feasibility on paper [119]. The installation of such a complex setup at the LHC, however, poses significant technical challenges. For this reason, a simplified version of the setup was implemented at the SPS, in order to experimentally verify the predicted performance in a safer, low-energy environment.

Part of this thesis work involved the participation in tests of the double-crystal setup carried out at the SPS in 2018 by the UA9 collaboration [120] and to the understanding of the results through multi-turn simulations with the complex double-crystal scheme. This section will only focus on the SPS setup, while studies for the implementation of this concept at the LHC are beyond the scope of this thesis [119].

While the results presented in this chapter are not related to the use of crystal collimation at the LHC, the comparison of simulations against experimental data served as an extremely useful benchmark of the crystal routine. The good agreement between simulations and measurements for such a complex setup, involving collimators and two crystals, reinforces the confidence of the prediction power of the simulation tools that are used for the LHC layouts. As described below, the results of these simulations were also instrumental to identify issues in the SPS experimental setup during these measurements.

7.2.1   UA9 Setup for Double-Crystal Studies at the SPS

The double-crystal setup installed in the SPS [72, 121] is schematically shown in Fig. 7.7, where the two silicon crystals are represented by red boxes labeled as Crystal1 and Crystal2. The main parameters of the two crystals are listed in Tab. 7.2. A double-sided LHC collimator prototype, only one jaw of which is represented as a black box and labeled as Collimator, is used to scrape the beam envelope (blue lines) down to $4\,\sigma$ and allows the beam-base alignment of all movable objects. The first crystal is aligned with the beam envelope and properly oriented to deflect incoming halo particles, producing the single-channeled beam (light green lines). The second crystal is then positioned in order to intercept the particles channeled by the first crystal and apply an additional deflection to them, producing the double-channeled beam (dark green lines). A tungsten absorber, represented by a grey box labeled as Absorber, intercepts both channeled beams. Two Roman Pots, represented by pink boxes labeled as RP0 and RP1, house the Timepix pixel detectors [122] used to monitor the profile of the deflected beams. High sensitivity BLMs record the secondary showers produced in the interactions of the beam particles with the equipment.

During the data taking considered in this section, no target was placed close to Crystal2, as the primary objective of the test was the measurement of the double-channeling process efficiency to verify the feasibility of the setup. A single bunch of 10^{11} protons was accelerated up to 270 GeV and kept coasting. Finding the optimal channeling condition for Crystal1 is
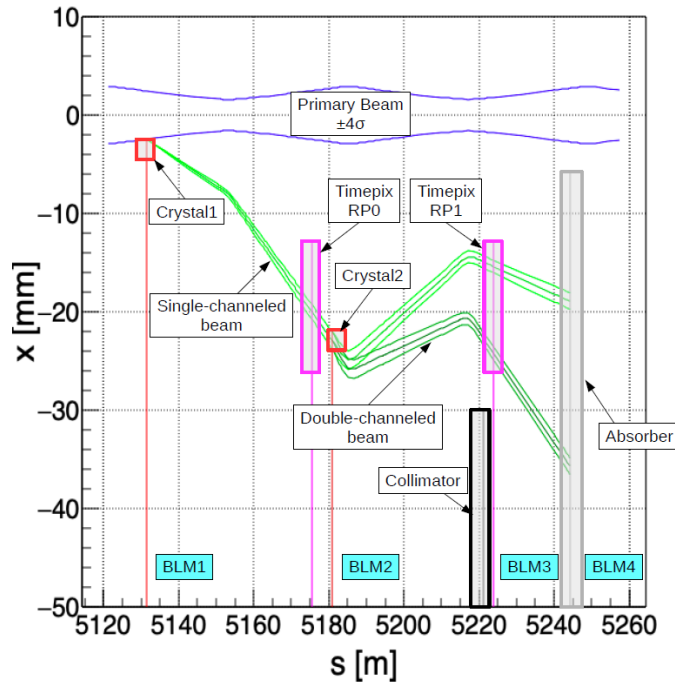
Figure 7.7: Schematic view of the UA9 setup for double-crystal channeling at the SPS [120].

Table 7.2: Parameters of the two crystals used for double-channeling tests at the SPS.

Crystal	Type	Length [mm]	Bending angle [μrad]
Crystal1	Strip	4.0	301.0
Crystal2	Strip	6.0	196.8

a well-established operation [123]. The Timepix housed in RP1 is then used to monitor the profile of the single-channeled beam and detect the shadow cast by Crystal2 during a linear scan. Once the best alignment has been found, Crystal2 is placed on the path of the halo channeled by Crystal1, and an angular scan is performed to find the optimal channeling orientation. This condition can be identified by the appearance of the double-channeled beam spot on the Timepix housed in RP1, as shown in Fig. 7.8.

The data collected with the Timepix were used to evaluate the efficiency of the double-channeling process, by calculating the ratio between the integral of the double-channeled peak (within $\pm 3\sigma$) and the total integrated signal in the entire Timepix frame. Additionally, linear scans were performed both in single- and double-channeling configuration using one of the jaws of the collimator prototype. The signal recorded by the downstream BLM as a function of the transverse position of the jaw allows to reconstruct the profile of the channeled beams, similar to what is done in tests at the LHC, and evaluate the channeling efficiency of each crystal separately. The results are reported in Tab. 7.3, where $\epsilon_{\mathrm{MT}}^{\mathrm{CR1}}$ is the multiturn channeling efficiency of the first crystal, ϵ_{DC} is the double-channeling efficiency and $\epsilon_{\mathrm{SP}}^{\mathrm{CR2}} = \epsilon_{\mathrm{DC}}/\epsilon_{\mathrm{MT}}^{\mathrm{CR1}}$ is the single-pass channeling efficiency of the second crystal [120].
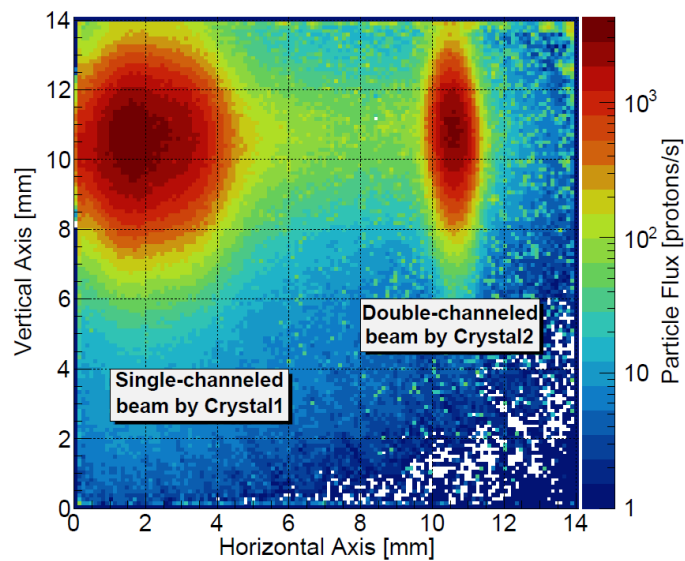
Figure 7.8: Timepix integrated image of the single- and double-channeled beam [120].

Table 7.3: Measured deflection efficiency of the double-crystal configuration at the SPS, compared with simulation results. The first two rows show the values estimated from measurements. The third row shows simulation results for the configuration used during the experiment. The last row shows simulation results for an optimal configuration, with RP0 retracted from the beam line and both crystals in optimal channeling orientation [120].

Method	$\epsilon_{\mathrm{MT}}^{\mathbf{CR1}}$	ϵ_{DC}	$\epsilon_{\mathrm{SP}}^{\mathbf{CR2}}$
Timepix	-	-	0.188 ± 0.001
BLM	0.519 ± 0.028	0.080 ± 0.006	0.154 ± 0.014
SixTrack (experimental)	0.535 ± 0.001	0.081 ± 0.001	0.151 ± 0.002
SixTrack (optimal)	0.929 ± 0.001	0.454 ± 0.001	0.489 ± 0.001

7.2.2 Channeling Efficiency Comparison with Simulations

The measured efficiency reported in Tab. 7.3 is significantly lower than typical values expected for bent silicon crystals. As part of this thesis, an extensive simulation campaign was carried out in order to understand these findings.

Various details of the setup need to be taken into account in order to properly reconstruct the setup used in measurements. First of all, all movable objects present in the beam line need to be accurately modeled in SixTrack. Even though its data turned out to be not usable due to an alignment issue, the Timepix sensor housed in RP0 was left close enough to the beam to intercept the channeled halo coming from the first crystal. The Multiple Coulomb Scattering inside RP0 affects the angular distribution of the beam, increasing its standard deviation. This effect can be clearly seen by monitoring the profile of the single-channeled beam with RP1. The thickness of RP0 in units of radiation length can thus be estimated from the difference in angular standard deviation before and after its insertion in the beam line, resulting in 0.06. In order to introduce an equivalent effect in simulations using one of the materials in the SixTrack database, RP0 was modeled with 0.2 mm of tungsten. The nominal simulation setup clearly includes both crystals in optimal channeling configura-
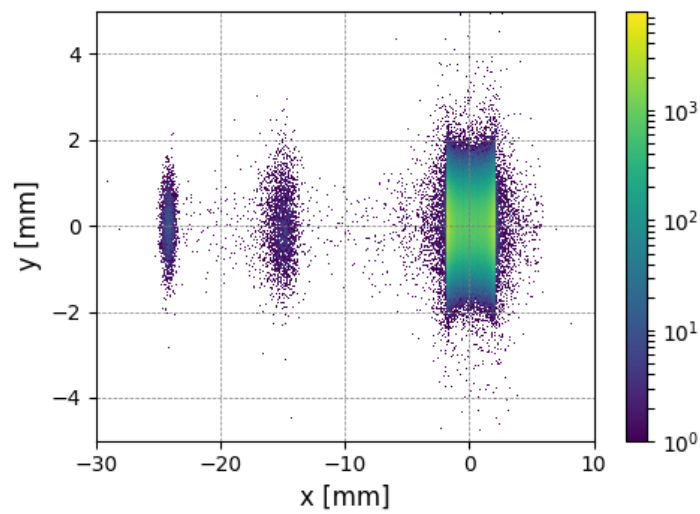
Figure 7.9: Simulated profile at the RP1 location in optimal configuration, i.e. with RP0 retracted from the beam line and both crystals in the best channeling orientation.
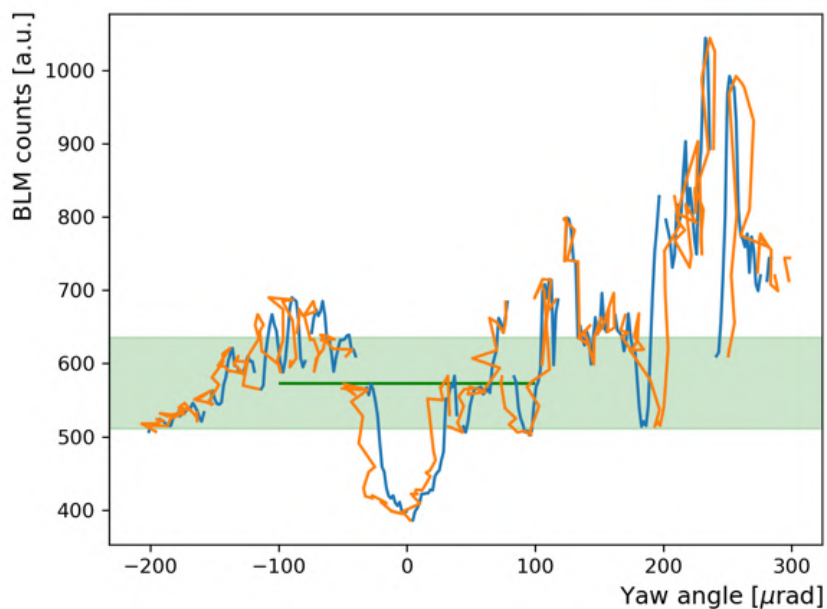

Figure 7.10: Angular scan performed with Crystal1 [78]. The BLM signal is shown as a function of the angular settings given as input to the hardware (orange) and effective angular position measured by the goniometer (blue). A green line indicates the average losses recorded in steady configuration, with the light green band being the standard deviation.

tion, i.e. Crystal1 is oriented as the beam envelope and Crystal2 is oriented as the direction of the single-channeled beam. The resulting profile at the Timepix location is shown in Fig. 7.9. The relative position of the single- and double-channeling spots is compatible with the expected beam trajectory, calculated using the matrix formalism previously introduced and shown in Fig. 7.7. However, this profile was not compatible with the recorded transverse positioning of the two crystals in measurements, giving a first indication that the crystals might not have been oriented in optimal channeling during the data taking. Fig. 7.10 shows the BLM signal at the location of Crystal1 during an angular scan. In complete analogy with crystal characterization at the LHC, the optimal channeling orientation corresponds to the minimum signal recorded by the BLM (around $x = 0$ in the plot). However, even though the optimal orientation of the first crystal was correctly identified, the backlash of the goniometer was not properly compensated while setting the final steady position. The comparison of the angular scan profile with the average BLM signal recorded in this configuration shows that the actual orientation of the crystal is compatible with a tilt of -35 μrad, which is about 3 times larger than the critical angle (12.2 μrad and 270 GeV). It follows that the measured channeling efficiency of Crystal1 is actually the result of a multi-turn process. The Multiple Coulomb Scattering angle caused by the passage through 4 mm of silicon is of about 10 μrad, meaning that halo particles need to traverse the crystal at least 2 or 3 times before having the chance to get channeled. This can be clearly seen in Fig. 7.11, which shows the fraction of simulated particles that experience channeling after a given number of passages through the crystal.
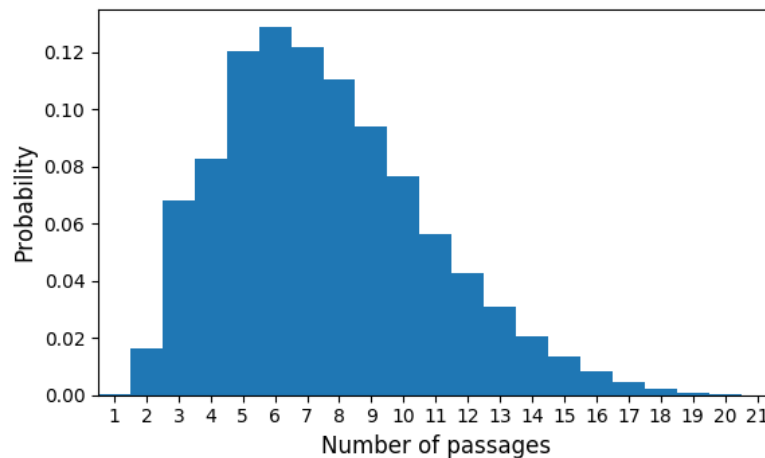

Figure 7.11: Simulated number of interactions with Crystal1 experienced by a halo particle before being successfully channeled.

A similar analysis could not be done for the second crystal. The corresponding BLM detects a high level of losses due to showers generated by the interaction of beam particles with upstream devices, hiding the characteristic decrease of local losses observed in channeling conditions. However, there are two other ways to verify the possibility of a non-optimal orientation of Crystal2. A first indication is given by the distribution of the leftover single-channeled beam, i.e. the particles that experience channeling in the first crystal but not in the second one. If Crystal2 is in optimal channeling conditions, the profile should in principle have a Gaussian shape. However, Fig. 7.8 shows an asymmetry towards lower transverse positions. This indicates a significant contribution from volume reflection by the second
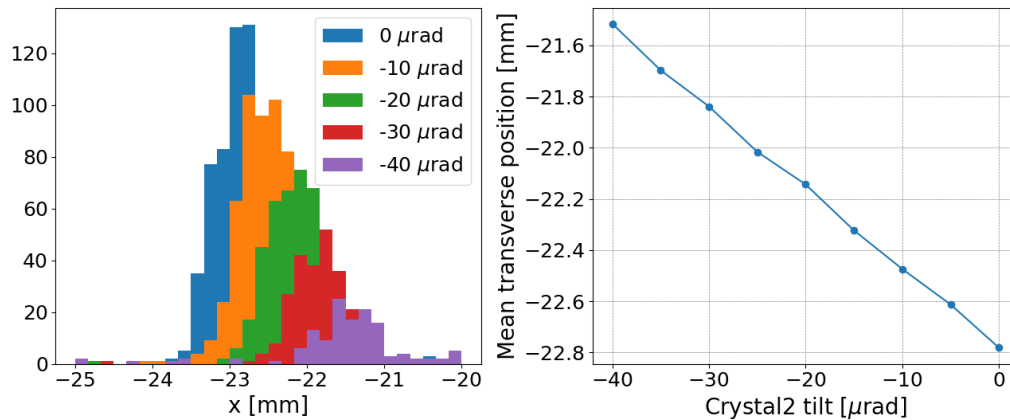
Figure 7.12: Left frame: simulated transverse distribution of the double-channeled beam for different values of angular tilt applied to Crystal2 with respect to the optimal channeling orientation. Right frame: mean transverse position of the simulated double-channeled beam as a function of the tilt applied to Crystal2.
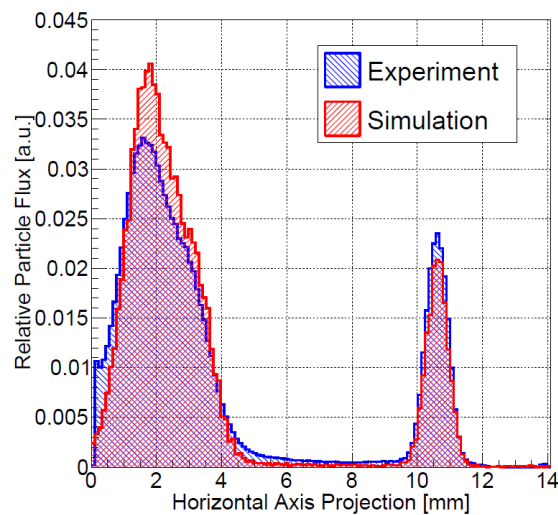

Figure 7.13: Comparison between data (blue) and simulation (red) for the horizontal profile of the single- and double-channeled beam [120].

crystal, supporting the hypothesis of a non-optimal orientation during measurements. The second observable is the transverse position of the double-channeled beam, which, as shown in Fig. 7.12, is significantly affected by a non-optimal orientation of Crystal2.

A simulation campaign was carried out by changing the orientation of Crystal2 in an attempt to find a realistic setup that could reproduce the observed pattern. The results showed that an angular tilt of -20 μrad (about two times the critical angle at 270 GeV) from optimal channeling is the orientation that best reconstructs the observed distribution. As can be seen in Fig. 7.13, the configuration described above leads to a good agreement with the measured profile at the Timepix, further supporting the postulation on the orientation of the two crystals.

Fig. 7.14 shows the recorded BLM signal during a linear scan with the collimator jaw, both for the single- and double-channeling configuration. The good agreement between
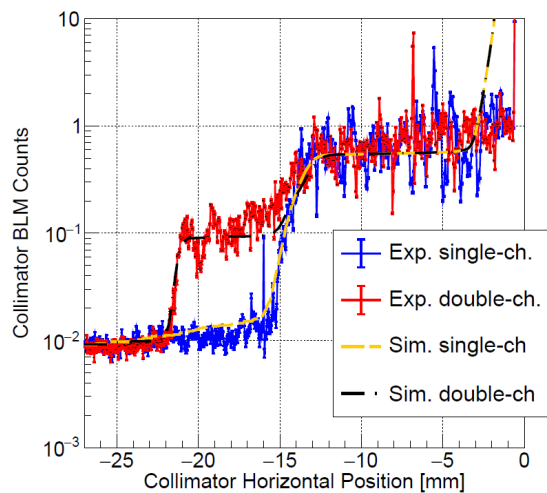
Figure 7.14: BLM signal recorded during linear scans made in single-channeling (blue) and in double-channeling (red), normalized to the beam intensity. The simulation results are shown by the orange dashed and black dot-dashed lines [120].

the simulated and measured efficiency reported in Tab. 7.3 supports the assumptions on the experimental configuration used during the data taking. Furthermore, the same table reports simulated results for an optimized setup, with both crystals properly oriented and without any XRPs altering the angular distribution of the beam coming from the first crystal. These values can be interpreted as an estimation of the maximum efficiency achievable by the SPS double-crystal setup, which is more than a factor 5 higher than what was observed in measurements.

7.3 Channeling of Higher Order Halos at the LHC with Proton Beams

A potential application of the double-crystal channeling setup described in the previous section is the measurement of the magnetic dipole moment of charm baryons produced in fixed target collisions of proton beams at the LHC. The magnetic moment of the Λ_c^+ baryon is of particular interest because it is equal to the magnetic moment of the charm quark [6, 124].

The installation of such a setup poses serious technical challenges. In principle, placing the crystal as a primary collimator could maximize the flux of protons on target for the production of Λ_c^+. This configuration, however, is not feasible due to the high losses generated outside of IR7. For this reason, the possibility of placing the crystal in the shadow of a standard TCP has been considered. In this configuration, the crystal would deflect higher order (i.e. secondary or tertiary) halo particles onto the target, while the primary collimator would mitigate the generated losses and provide protection to the machine [125]. A configuration with a crystal intercepting the secondary halo allows an optimization between the opposite requirements of maximizing the protons on target while minimizing the collimation losses at the location of the double-crystal experiment (IR3 and IR8 are presently under study [119]). Such a configuration has been demonstrated to work in simulations. However, given the complexity of the conditions to be fulfilled to achieve this setup, experimental tests are extremely important for a feasibility assessment. Although the results obtained at
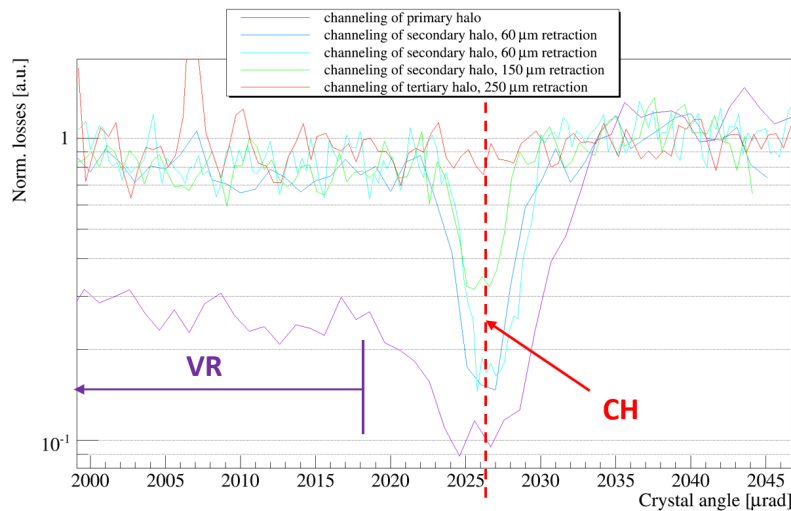
Figure 7.15: BLM signal during angular scans with the horizontal crystal on Beam 1 at different retractions with respect to the primary collimator. The signal is normalized to the amorphous level. The optimal channeling orientation and the volume reflection plateau are highlighted [125].

the SPS are very promising, the setup described in Sec. 7.2 only allows the first crystal to act as a primary collimator.

First tests to assess the feasibility of crystal channeling of higher order halo particles were carried out in July 2017 using the horizontal crystal installed on Beam 1 [125]. The crystal was retracted with respect to the primary collimator, and angular scans were performed in order to verify the possibility to achieve channeling conditions in this configuration. Although this setup does not reproduce the final configuration, which will be even more challenging as the crystal will be located outside of IR7, these measurements are very useful for a first assessment and to provide reference data for simulations. The results are reported in Fig. 7.15 for different retractions of the crystal and show two peculiar behaviors:

- The volume reflection plateau disappears when the crystal is retracted, while the channeling well remains clearly visible.

- The depth of the channeling well decreases as the distance of the crystal from the beam increases, until it disappears completely for a 250 μm retraction.

These tests demonstrated that optimal channeling orientation can be found even if the crystal is in the shadow of the primary collimator, at least for retractions of up to 150 μrad (the exact cutoff value between 150 μm and 250 μm has yet to be determined). To the best of this author's knowledge, this was the very first observation of channeling of higher order halos.

As part of this thesis, these results were compared to a preliminary set of simulations, shown in Fig. 7.16. In the simulated angular scans, the volume reflection plateau vanishes when the crystal is retracted, confirming what was observed in measurements. The origin of this behavior is currently being investigated, but not enough data are available to reach a conclusion. On the other hand, in simulations the depth of the channeling well, while being reduced with respect to the case of primary halo channeling, does not seem to change with the retraction, as opposed to what was experimentally observed.

These results are not final, and further studies are planned to understand this discrepancy. The simulated angular scans are obtained by calculating the fraction of particles
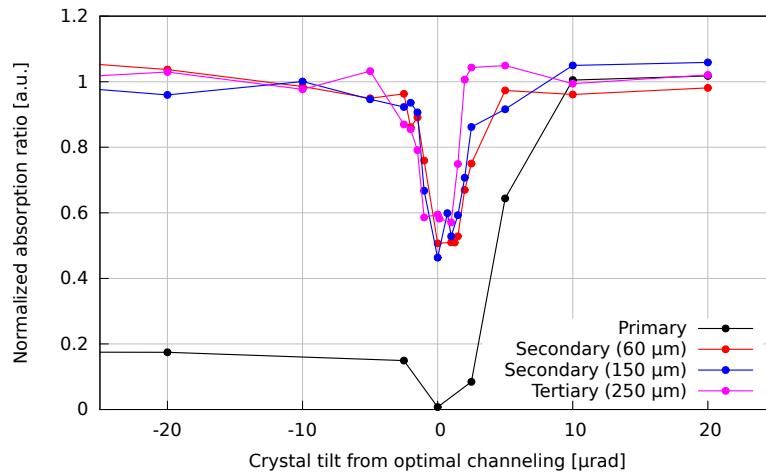
Figure 7.16: Simulated angular scan with the horizontal crystal on Beam 1 at different retractions with respect to the primary collimator. The profiles are centered to the minimum of the channeling well and normalized to the amorphous level.

experiencing inelastic interactions with the crystal for each orientation. This is not directly comparable with the measured BLM signal, since a number of different factors need to be taken into account. For example, channeling could actually be possible even with the crystal retracted by 250 μm, but its effect on local losses may be too small to be detected by BLMs. Energy deposition simulations are needed to reproduce the BLM response for a direct comparison with measurement and verify the validity of this hypothesis. Futhermore, linear scans with a downstream collimator, which could not be performed due to the limited time available, can provide useful data for a direct comparison with SixTrack simulations and shed some light on the observed discrepancy.

Chapter 8

Conclusions

Channeling of high-energy particle beams using bent crystals has great potential for a variety of applications to accelerators and high-energy particle physics. As part of this thesis, different applications were explored with promising results, both in experimental measurements at the CERN accelerator complex and in simulations.

As part of the R&D effort to improve beam collimation for HL-LHC, an extensive campaign of experimental tests and theoretical studies has been carried out to assess the feasibility of crystal collimation of high-intensity hadron beams. This collimation technique uses bent crystals to deflect halo particles towards a single absorber per beam and per plane, as opposed to the present system that relies on a complex arrangement of collimators (38 for the two beams just in the betatron cleaning insertion). At the 2018 HL-LHC Crystal Collimation Day, an important effort was launched to demonstrate the feasibility of this concept for Pb ion beams by the end of Run 2. This effort was successful: the results gathered in 2018 and reported in this thesis demonstrated for the first time the capability of the crystal collimation system to improve the beam cleaning with Pb ion beams at the LHC. In view of the possible deployment during the first year of Run 3, a first proposal of operational settings was elaborated. In this configuration, crystals are adiabatically inserted in the present collimation system, allowing to profit from the improved cleaning performance while still respecting all machine protection requirements. A cleaning improvement of up to a factor ~ 8 in the IR7 Dispersion Suppressor region was observed. Other configurations were explored in dedicated MDs, approaching local gains of a factor 100 at critical locations with more "aggressive" collimator settings that seem feasible, but require more experimental validations before being deployed operationally. Additionally, crystals were used for the first time at the LHC with high-intensity Pb ion beams showing a good performance and no specific drawbacks. These observations indicate the feasibility of the use of crystal collimation in Run 3. These findings were a key component in the decision to include crystal collimation in the baseline program of the HL-LHC upgrade at the end of 2019.

This thesis work also addressed two specific applications of bent crystals to proton beams, namely collimation at tight settings for background reduction in a special forward-physics run at the LHC, and double-crystal studies in the SPS in preparation for a fixed-target program at the LHC. During the 2018 special physics run with proton beams, a crystal collimation scheme was studied in an extensive simulation campaign, leading to the first use of bent crystals in a physics run at the LHC. A low and stable background was observed by the ALFA and TOTEM experiments, and additional runs with this scheme have been requested by TOTEM for the future. With regards to the double-crystal setup, a test layout has been installed in the safer low-energy environment of the SPS by the UA9 collaboration.

Crystal collimation simulations were instrumental in understanding the details of the data collected in 2017-2018, and to assess the achievable efficiency of such a complex setup.

It is clear from the work presented that simulations play a key role in studies involving bent crystals. Part of this thesis was dedicated to the migration of the crystal simulation routine to the newly released version of SixTrack. The new routine was successfully benchmarked against the old one showing that all crystal-related physics was correctly carried over, while enabling an improvement by up to a factor 20 in simulation speed. At the same time, the physics of the routine was improved with the inclusion of a new treatment of the crystal miscut angle, which will be extensively used in future studies to assess its effects on the performance of crystal collimation. Preliminary results with this routine have been included in this thesis as a reference.

At present, the crystal routine has been used for simulations with proton beams with great success. One of the priorities for the imminent future is the preparation of a simulation environment for crystal collimation with ion beams, by coupling SixTrack with other codes (like Geant4 and FLUKA). This setup would be extremely important to study in detail the performance of this system in operational scenarios, even though the possibility of a successful deployment for collimation of ion beams is strongly supported already by the solid experience gathered in Run 2. The support of simulations, coupled with the new campaign of experimental tests that will take place after the CERN accelerator complex resumes its activities, will allow to define final operational settings for the use of crystal collimation with high-intensity ion beams in Run 3.

Bibliography

[1] O. S. Brüning et al. *LHC Design Report*. CERN, 2004.

[2] O. Brüning and L. Rossi. *The High Luminosity Large Hadron Collider*. World Scientific, 2015.

[3] R. Assmann et al. The final collimation system for the LHC. In *10th European Particle Accelerator Conference*, page 986, 2006.

[4] R. Assmann, S. Redaelli, and W. Scandale. Optics study for a possible crystal-based collimation system for the LHC. In *10th European Particle Accelerator Conference*, 2006.

[5] L. Burmistrov et al. Measurement of Short Living Baryon Magnetic Moment using Bent Crystals at SPS and LHC. Technical report, CERN, 2016. CERN-SPSC-2016-030.

[6] A. S. Fomin et al. Feasibility of measuring the magnetic dipole moments of the charm baryons at the LHC using bent crystals. *Journal of High Energy Physics*, 2017(8), 2017.

[7] K. Wille. *The physics of particle accelerators: an introduction*. Oxford University Press, 2000.

[8] D. A. Edwards and M. J. Syphers. *An introduction to the physics of high-energy accelerators*. Wiley, 1993.

[9] S. Redaelli. Beam cleaning and collimation systems. In *CERN Yellow Report*, volume 2, 2016.

[10] J. Rossbach and P. Schmüser. Basic course on accelerator optics. In *CAS - CERN Accelerator School: 5th General Accelerator Physics Course*, pages 17–88, 1994.

[11] R. Rossi. *Experimental assessment of crystal collimation at the Large Hadron Collider*. PhD thesis, La Sapienza, Rome, 2018.

[12] B. J. Holzer. Introduction to transverse beam dynamics. In *CAS - CERN Accelerator School: Superconductivity for Accelerators Course*, pages 21–40, 2014.

[13] J. Buon. Beam phase space and emittance. In *CAS - CERN Accelerator School: 5th General Accelerator Physics Course*, pages 89–116, 1994.

[14] J. Buon. Transverse beam dynamics. In *CAS - CERN Accelerator School: 5th General Accelerator Physics Course*, pages 131–158, 1994.

[15] J. Le Duff. Longitudinal beam dynamics in circular accelerators. In *CAS - CERN Accelerator School: 5th General Accelerator Physics Course*, pages 289–312, 1994.

[16] D. Mirarchi. *Crystal collimation for LHC*. PhD thesis, Imperial College, London, 2015.

[17] B. Auchmann et al. Testing beam-induced quench levels of LHC superconducting magnets. *Physical Review Special Topics - Accelerators and Beams*, 18:061002, 2015.

[18] R. Schmidt. Introduction to Machine Protection. In *2014 Joint International Accelerator School: Beam Loss and Accelerator Protection*, pages 1–20, 2016.

[19] J. Wenninger. Machine Protection and Operation for LHC. In *2014 Joint International Accelerator School: Beam Loss and Accelerator Protection*, pages 377–401, 2016.

[20] G. Valentino et al. Beam diffusion measurement using collimator scans in the LHC. *Physical Review Special Topics - Accelerators and Beams*, 16:021003, 2013.

[21] K.-H. Mess and M. Seidel. Collimators as diagnostic tools in the proton machine of HERA. *Nuclear Instruments and Methods in Physics Research Section A: Accelerators, SPectrometers, Detectors and Associated Equipment*, 351(2):279–285, 1994.

[22] Particle Data Group et al. Review of Particle Physics. *Progress of Theoretical and Experimental Physics*, 2020(8), 2020.

[23] H. A. Bethe. Molière's Theory of Multiple Scattering. *Physical Review*, 89:1256–1266, 1953.

[24] S. Meroli. *Interaction of radiation with matter: from the theory to the measurements*. 2015.

[25] R. Assmann. Collimators and cleaning, could this limit the LHC performance? In *12th Chamonix LHC Performance Workshop*, pages 163–170, 2003.

[26] M. Seidel. The proton collimation system of HERA. Master's thesis, 1994. DESY-94-103.

[27] R. Assmann et al. Equilibrium Beam Distribution and Halo in the LHC. In *8th European Particle Accelerator Conference*, page 1326, 2002.

[28] J. B. Jeanneret. Optics of a two-stage collimation system. *Physical Review Special Topics - Accelerators and Beams*, 1:081001, 1998.

[29] H. Wiedemann. Wake Fields and Instabilities. In *Particle Accelerator Physics – Fourth Edition*, chapter 22. Springer, 2015.

[30] N. Mounet. *The LHC Transverse Coupled-Bunch Instability*. PhD thesis, EPFL Lausanne, 2012.

[31] A. M. Taratin. Particle channeling in a bent crystal. *Physics of Particles and Nuclei*, 29(5):437–462, 1998.

[32] V. M. Biryukov et al. *Crystal channeling and its application at high energy accelerators*. Springer, 1996.

[33] J. Stark and G. Wendt. Über das Eindringen von Kanalstrahlen in feste Körper. *Annalen der Physik*, 343(10):921–940, 1912.

[34] J. Lindhard. Influence of crystal lattice on motion of energetic charged particles. *Kongelige Danske Videnskabernes Selskab*, 34(14), 1965.

[35] R. A. Carrigan Jr and J. A. Ellison. *Relativistic channeling.* Springer, 2013.

[36] L. H. Thomas. The calculation of atomic fields. *Mathematical Proceedings of the Cambridge Philosophical Society*, 23(5):542—548, 1927.

[37] E. Fermi. Un metodo statistico per la determinazione di alcune proprietà dell'atomo. *Rendiconti dell'Accademia Nazionale dei Lincei*, 6(6):602–607, 1927.

[38] G. Molière. Theorie der Streuung schneller geladener Teilchen I. Einzelstreuung am abgeschirmten Coulom-Feld. *Zeitschrift für Naturforschung A*, 2:133–145, 1947.

[39] J. Lindhard and M. Scharff. Energy Dissipation by Ions in the keV Region. *Physical Review*, 124:128–130, 1961.

[40] Y. M. Ivanov et al. Volume reflection of a proton beam in a bent crystal. *Physical Review Letters*, 97(14), 2006.

[41] A. M. Taratin and V. A. Vorobiev. Volume reflection of high-energy charged particles in quasi-channeling states in bent crystals. *Physics Letters A*, 119(8):425–428, 1987.

[42] W. Scandale et al. Volume Reflection Dependence of 400 GeV/c Protons on the Bent Crystal Curvature. *Physical Review Letters*, 101:234801, 2008.

[43] W. Scandale et al. Observation of nuclear dechanneling for high-energy protons in crystals. *Physics Letters B*, 680(2):129–132, 2009.

[44] W. Scandale et al. Observation of nuclear dechanneling length reduction for high energy protons in a short bent crystal. *Physics Letters B*, 743:440–443, 2015.

[45] Y. A. Chesnokov et al. Volume reflection and volume capture of ultrarelativistic particles in bent single crystals. *Physical Review Special Topics - Accelerators and Beams*, 18(11), 2015.

[46] D. Mirarchi, S. Redaelli, and W. Scandale. Crystal implementation in SixTrack for proton beams. In *ICFA Mini-Workshop on Tracking for Collimation in Particle Accelerators*, 2018.

[47] W. Scandale, A. M. Taratin, and A. D. Kovalenko. Experiments with crystal deflectors for high energy ion beams: Electromagnetic dissociation probability for well channeled ions. *Physical Review Special Topics - Accelerators and Beams*, 16:011001, 2013.

[48] S. Timoshenko and J. N. Goodier. *Theory of elasticity.* McGraw-Hill, 1970.

[49] G. Germogli, A. Mazzolari, V. Guidi, and M. Romagnoni. Bent silicon strip crystals for high-energy charged particle beam collimation. *Nuclear Instruments and Methods in Physics Research Section B: Beam Interactions with Materials and Atoms*, 402, 2017.

[50] Y. M. Ivanov et al. Observation of the elastic quasi-mosaicity effect in bent silicon single crystals. *JETP Letters*, 81(3):99–101, 2005.

[51] S. Redaelli et al. Installation in IR7 of Primary Crystal Collimators (TCPC) on Beam 2. Technical report, 2016.

[52] R. Bruce, D. Mirarchi, and S. Redaelli. Functional and operational conditions of the crystal primary collimators. Technical report, 2019.

[53] S. Montesano et al. Installation of the LUA9 Equipment in IR7 of the LHC. Technical report, 2014.

[54] S. Redaelli, R. Assmann, R. Losito, and A. Masi. Final Implementation and Performance of the LHC Collimator Control System. In *23rd Particle Accelerator Conference*, page FR5REP007, 2009.

[55] A. Masi et al. Goniometer and controls. Presented at the HL-LHC Crystal Collimation Day, 2018.

[56] G. Apollinari et al. *High-Luminosity Large Hadron Collider (HL-LHC): Technical Design Report*. CERN Yellow Reports: Monographs. CERN, 2017.

[57] LHC Collimation Review, 2013.

[58] International Review of the HL-LHC Collimation System, 2019.

[59] High Luminosity LHC website. `https://hilumilhc.web.cern.ch/`.

[60] C. Bahamonde, A. Lechner, and R. Rossi. Crystal channeling of ions on different TCSG materials. Presented at the LHC Collimation Upgrade Specification Meeting, 2018.

[61] O. S. Brüning. Private communication.

[62] F. Savary et al. Status and Test Results of the 11 T Magnets. In *10th HL-LHC Collaboration Meeting*, 2020.

[63] S. A. Khalek et al. The ALFA Roman Pot detectors of ATLAS. *Journal of Instrumentation*, 11(11):P11013, 2016.

[64] G. Anelli et al. The TOTEM experiment at the CERN Large Hadron Collider. *Journal of Instrumentation*, 3:S08007, 2008.

[65] H. Burkhardt. High-Beta Optics and Running Prospects. *Instruments*, 3(1):22, 2019.

[66] G. Antchev et al. First determination of the ρ parameter at s=13 TeV: probing the existence of a colourless C-odd three-gluon compound state. *The European Physical Journal C*, 79:785, 2019.

[67] R. Bruce et al. Special collimation schemes for reduced background during high-β tests at injection. In *LHC Machine Committee Meeting*, 2018.

[68] N. Doble, L. Gatignon, and P. Grafström. A novel application of bent crystal channeling to the production of simultaneous particle beams. *Nuclear Instruments and Methods in Physics Research Section B: Beam Interactions with Materials and Atoms*, 119(1):181–191, 1996.

[69] M. A. Fraser et al. Experimental results of crystal-assisted slow extraction at the SPS. In *8th International Particle Accelerator Conference*, 2017.

[70] J. Jaeckel, M. Lamont, and C. Vallée. The quest for new physics with the physics beyond colliders programme. *Nature Physics*, 16:393–401, 2020.

[71] V. G. Baryshevsky. Spin rotation and depolarization of high-energy particles in crystals at Hadron Collider (LHC) and Future Circular Collider (FCC) energies and the possibility to measure the anomalous magnetic moments of short-lived particles. 2015.

[72] S. Montesano. Testing the Double-Crystal Setup for Physics Beyond Colliders Experiments in the UA9-SPS Experiment. In *9th International Particle Accelerator Conference*, 2018.

[73] A. Natochii. *Detectors developments for the UA9 experiment at the CERN SPS*. PhD thesis, Université Paris-Saclay, 2019.

[74] B. Dehning et al. The lhc beam loss measurement system. In *22nd Particle Accelerator Conference*, pages 4192–4194, 2007.

[75] G. Valentino et al. Semiautomatic beam-based lhc collimator alignment. *Physical Review Special Topics - Accelerators and Beams*, 15:051002, 2012.

[76] V. Previtali. *Performance evaluation of a crystal-enhanced collimation system for the LHC*. PhD thesis, EPFL Lausanne, 2010.

[77] R. Bruce, R. Assmann, and S. Redaelli. Principles for Generation of Time-dependent Collimator Settings during the LHC Cycle. In *2nd International Particle Accelerator Conference*, 2011.

[78] R. Rossi. Private communication.

[79] R. Rossi et al. Crystal Collimation with protons at injection energy. CERN-ACC-NOTE-2016-0035.

[80] R. Rossi et al. Crystal Collimation with protons at flat top energy. CERN-ACC-NOTE-2017-0021.

[81] R. Rossi et al. Crystal Collimation Cleaning Measurements with Proton Beams in LHC. CERN-ACC-NOTE-2018-0024.

[82] R. Rossi et al. Crystal Collimation During the LHC Energy Ramp. CERN-ACC-NOTE-2018-0053.

[83] R. Rossi et al. Beam 2 Crystal Characterization Measurements with Proton Beams in the LHC. CERN-ACC-NOTE-2018-0067.

[84] M. D'Andrea et al. Crystal Collimation Tests with Proton Beams. CERN-ACC-NOTE-2019-0022.

[85] M. D'Andrea et al. Operational Aspects of Crystal Collimation with Proton Beams. CERN-ACC-NOTE-2019-0023.

[86] B. Salvachua. Overview of proton-proton physics during Run 2. In *9th LHC Operations Evian Workshop*, 2019.

[87] N. Fuster et al. Run 2 Collimation Overview. In *9th LHC Operations Evian Workshop*, 2019.

[88] R. Rossi et al. Crystal Collimation with Lead Ion Beams at Injection Energy in the LHC. CERN-ACC-NOTE-2018-0004.

[89] R. Rossi et al. Crystal Collimation Cleaning Measurements with Lead Ion Beams in LHC. CERN-ACC-NOTE-2018-0077.

[90] M. D'Andrea et al. Crystal Collimation Tests with Pb Ion Beams. CERN-ACC-NOTE-2019-0024.

[91] M. Schaumann et al. First Xenon-Xenon Collisions in the LHC. In *9th International Particle Accelerator Conference*, 2018.

[92] J. Jowett and M. Schaumann. Overview of heavy ions in LHC Run 2. In *9th LHC Operations Evian Workshop*, 2019.

[93] P. D. Hermes et al. LHC Heavy-Ion Collimation Quench Test at 6.37Z TeV. 2016. CERN-ACC-NOTE-2016-0031.

[94] D. Mirarchi, G. Hall, S. Redaelli, and W. Scandale. Design and implementation of a crystal collimation test stand at the Large Hadron Collider. *The European Physical Journal C*, 77, 2017.

[95] SixTrack release version 5.4.1. `https://github.com/SixTrack/SixTrack/releases/tag/v5.4.1/`.

[96] SixTrack website. `http://sixtrack.web.cern.ch/SixTrack/`.

[97] F. Schmidt et al. *SixTrack User's Reference Manual.* Version 5.4.3.

[98] G. Ripken and F. Schmidt. A symplectic six-dimensional thin lens formalism for tracking. 1995. CERN-SL-95-12-AP, CERN-SL-95-12(AP), DESY-95-063, DESY-95-63.

[99] P. D. Hermes. *Heavy-Ion Collimation at the Large Hadron Collider: Simulations and Measurements.* PhD thesis, 2016. CERN-THESIS-2016-230.

[100] N. Fuster et al. Simulations of heavy-ion halo collimation at the cern large hadron collider: Benchmark with measurements and cleaning performance evaluation. *Physical Review Accelerators and Beams*, 23:111002, 2020.

[101] MADX website. `http://mad.web.cern.ch/mad/`.

[102] D. Mirarchi et al. A crystal routine for collimation studies in circular proton accelerators. *Nuclear Instruments and Methods in Physics Research Section B: Beam Interactions with Materials and Atoms*, 355, 2015.

[103] D. Mirarchi, S. Redaelli, and W. Scandale. *Crystal implementation in SixTrack for proton beams.* CERN Yellow Reports: Conference Proceedings. CERN, 2018.

[104] W. Scandale et al. Observation of strong leakage reduction in crystal assisted collimation of the SPS beam. *Physics Letters B*, 748:451–454, 2015.

[105] W. Scandale et al. Study of inelastic nuclear interactions of 400 GeV/c protons in bent silicon crystals for beam steering purposes. *The European Physical Journal C*, 78(6):505, 2018.

[106] D. Mirarchi et al. Reducing beam-related background on forward physics detectors using crystal collimation at the Large Hadron Collider. *Physical Review Applied*, Submitted, 2020.

[107] R. De Maria et al. SixTrack Version 5: Status and New Developments. *Journal of Physics: Conference Series*, 1350:012129, 2019.

[108] G. Robert-Demolaize, R. Assmann, S. Redaelli, and F. Schmidt. A new version of sixtrack with collimation and aperture interface. In *21st Particle Accelerator Conference*, 2005.

[109] N. Catalan Lasheras. *Transverse and longitudinal beam collimation in a high-energy proton collider (LHC)*. PhD thesis, Universidad de Zaragoza, 1998. CERN-THESIS-2000-019.

[110] R. Rossi et al. Measurements of coherent interactions of 400 gev protons in silicon bent crystals. *Nuclear Instruments and Methods in Physics Research Section B: Beam Interactions with Materials and Atoms*, 355:369–373, 2015.

[111] J. Barranco et al. LHC@Home: a BOINC-based volunteer computing infrastructure for physics studies at CERN. *Open Engineering*, 7, 2017.

[112] FLUKA website. `http://www.fluka.org/fluka.php/`.

[113] L. S. Esposito et al. FLUKA4 Crystal module. Presented at the 132nd Collimation Upgrade Specification Meeting, 2020.

[114] R. Rossi et al. Benchmark of the FLUKA 4 Crystal Module. Presented at the 132nd Collimation Upgrade Specification Meeting, 2020.

[115] Geant4 website. `https://geant4.web.cern.ch/`.

[116] L. Nevay et al. Update on Crystal Simulations and Loss Maps. Presented at the 132nd Collimation Upgrade Specification Meeting, 2020.

[117] H. Burkhardt. High-Beta Optics and Running Prospects. *Instruments*, 3(1):22, 2019.

[118] H. Garcia Morales et al. Special Collimation System Configuration for the LHC High-Beta Runs. In *9th International Particle Accelerator Conference*, 2018.

[119] D. Mirarchi, A. S. Fomin, S. Redaelli, and W. Scandale. Layouts for fixed-target experiments and dipole moment measurements of short-living baryons using bent crystals at the LHC. *The European Physics Journal C*, In press, 2019.

[120] W. Scandale et al. Double-crystal measurements at the CERN SPS. *Nuclear Instruments and Methods in Physics Research A*, Submitted, 2020.

[121] W. Scandale et al. The UA9 setup for the double-crystal experiment in CERN-SPS. *Nuclear Instruments and Methods in Physics Research Section A: Accelerators, Spectrometers, Detectors and Associated Equipment*, 975:164175, 2020.

[122] A. Natochii. Use of a hybrid semiconductor pixel detector as a precision beam monitor at CERN accelerator facilities. *Journal of Instrumentation*, 14:P03018, 2019.

[123] W. Scandale et al. First results on the SPS beam collimation with bent crystals. *Physics Letters B*, 692(2):78–82, 2010.

[124] A. S. Fomin et al. The prospect of charm quark magnetic moment determination. *The European Physical Journal C*, 80(5), 2020.

[125] D. Mirarchi, S. Redaelli, and R. Rossi. Update on crystal tests relevant for PBC-FT. Presented at the LHC Fixed Target Working Group, 2017.

Acknowledgements

- Giorgia Bonetto, for always standing by my side even when living apart miles away, for keeping me sane during the most critical times of this experience and for choosing to live the adventure of life with me.

- My friends and family back in Italy, for their everlasting support and for constantly reminding me that there is someone cheering for me outside the walls of my apartment.

- Aphra, the latest addition to the family, for keeping me company and taking good care of me during isolation times.

Marco